Testing non-standard neutrinos properties with Borexino: from [8]B solar neutrino rate measurement to the characterization of the [144]Ce source for the SOX experiment.

Thibaut Houdy

Thèse de doctorat

préparée à l'Université Paris–Diderot
pour obtenir le grade de Docteur de l'Université Paris Sorbonne Cité

Testing non-standard neutrinos properties with Borexino

From ^{8}B solar ν_e rate measurement to characterisation of the ^{144}Ce source for testing the sterile hypothesis in the SOX experiment.

par

Thibaut Houdy

Thèse dirigée par MM. Davide Franco et Thierry Lasserre.

Soutenue publiquement le 18 septembre 2017 devant le jury composé de :

Pr. Alessandra Tonazzo (Université Paris-Diderot) . . . . Présidente du jury
Dr. Davide Franco (CNRS) . . . . Directeur de thèse
Dr. Gautier Hamel de Monchenault (CEA) . . . . Examinateur
Dr. Thierry Lasserre (CEA) . . . . Directeur de thèse
Dr. Anselmo Meregaglia (CNRS) . . . . Rapporteur
Pr. Stefan Schönert (TUM) . . . . Rapporteur
Dr. Laurent Simard (Université Paris-Sud) . . . . Examinateur

Aux amis qui illuminent,

Remerciements

Que les remerciements apparaissent au début d'un manuscrit n'est pas dû au hasard, c'est pour rectifier au plus vite l'approximative attribution d'un travail à un seul auteur quand son essence est éminemment collective.

Je tiens donc en premier lieu à remercier mes directeurs de thèses: Thierry Lasserre pour nos longues discussions sur la physique et le reste, pour m'avoir encouragé et poussé dans les moments obscurs qui ont ponctué ces 3 ans, Davide Franco pour la rigueur qu'il a su m'imposer et l'expertise dont j'ai pu bénéficier grâce à lui durant cet apprentissage.

Le Service de Physique des Particules de l'Irfu (CEA) ainsi que le laboratoire AstroParticules et Cosmologie (Université Paris-Diderot/CNRS), dirigés respectivement par Anne Isabelle Etienvre puis Gautier Hamel de Montchenault et Stavros Katsanevas m'ont permis de rencontrer beaucoup de chercheurs formidables, d'engager des discussions exaltantes et de poursuivre mon travail en toute sérénité, je tiens à les en remercier.

Merci à Anselmo Meregaglia et Stefan Schönert d'avoir accepté de relire ma thèse. Merci à Laurent Simard pour les fructueuses conversations et la rigoureuse lecture de mon manuscrit pendant ses vacances. Merci à Gautier Hamel de Montchenault et Alessandra Tonazzo d'avoir accepté de participer à mon jury.

Parce que tout n'est pas rose durant une thèse mais que Léa Jouvin a toujours su apporter de la couleur à la grisaille parisienne, merci. D'avoir acquis une amie et un titre, tu sais bien ce dont je suis le plus fier.

Je remercie mes co-bureaux Paolo Agnes, Adrien Hourlier, Andrea Scarpelli et Hector Gomez pour n'avoir rien dit quand je chantais -mal- et Romain Roncin pour avoir chanté avec moi -mal aussi-. Merci à mes colocataires Lucile, Stéphanie, Lise et Lorenzo, pour à peu de choses près les mêmes raisons.

Un grand merci à Jonathan Gaffiot pour ces jours passés ensemble à patiemment apprendre, coder, corriger, lire, relire, chercher la virgule, la faute d'orthographe ou la petite bête. Merci à tous ces "grands frères" de thèse qu'ont été Vincent Fischer, Romain Roncin, Matthieu Durero et grâce à qui j'ai compris qu'on pouvait faire de la recherche en s'amusant et même que c'était sans doute la meilleure façon d'en faire. Un bon courage à Victoria Wagner qui reprend la charge honorifique, à laquelle je ne pourrais plus participer à mon grand dam, de remplir le germanium.

Merci à Michel Cribier d'incarner la Recherche à mes yeux: bougonne et orageuse, humble, honnête et brillante.

Merci aux neutrinistes (et aux autres) qui ont partagé avec moi leur passion et leurs connaissances: Mathieu Vivier, Guillaume Mention, Antoine Kouchner, Bruny Baret, Quentin Riffard, Jaime Dawson, Thomas Patzak.

Merci à Birgit Neumair et Simon Appel pour les discussions à Munich, Paris, Milan et ailleurs ainsi que pour m'avoir poussé à déguster des spécialités bavaroises dans un Biergarten bien camouflé.

Contents

Introduction

Neutrino physics has been built upon experimental anomalies. Neutrino is a fascinating particle because of its nuances: massive but surprisingly light, flavoured but oscillating, over abundant but hard to detect. This field of study has emerged as a combination of nuclear science, particle physics as well as astrophysics and cosmology.

First postulated to explain the β spectrum, decades were needed to finally observe some of them, coming out of a nuclear reactor. Later on, our understanding has gradually grown by solving the solar and atmospheric sector problems. If the Sun enabled physicists to indubitably observe neutrino oscillations, the increase of statistics and sensitivity in modern detectors allows now neutrino to be used as Sun interior messenger. Although most of the oscillation parameters have now been measured, some experimental anomalies still remain unexplained.

Following the first measurement of neutrino-nucleus scattering this year, next years will be critical for our global understanding of neutrino physics. In 5 years from now, the sterile hypothesis will be answered by source experiment and short baseline reactor detectors, enabling the ^{235}U $\overline{\nu_e}$ spectrum measurement. Direct mass measurement using giant spectrometer will reach sensitivity addressed by cosmology and a generation of detector using a completely different approach (cyclotron radiation) is already under development. CP-phase and mass hierarchy might be determined by the next generation of long-baseline experiments. Huge instrumented volume for high energy neutrino spectroscopy comes into play. Finally, large collaborations investigate theoretical nature of the neutrino using double beta decay.

Borexino celebrates its 10-years anniversary of low energy neutrino observation in 2017. The detector calibration and the well constrained simulations enable to make precise measurements over a long period of time despite detector ageing process. The first direct observation of pp-neutrino and the geoneutrinos rate measurement are two impressive results for instance.

Among solar neutrinos, ^8B spectrum is a key measurement because it lies in between the two Mikheyev–Smirnov–Wolfenstein effect regimes: the vacuum and matter domination one's. A precise measurement of the energy spectrum would help getting rid of exotic oscillation models testing the MSW transition area, as well as addressing solar metallicity controversy.

At the same time as metallicity controversy, new measurements led to a re-evaluation of the reactor antineutrino fluxes enhancing a clear deficit of the observed flux with respect to the expected ones. Light sterile neutrino is one of the global solution to the Reactor Antineutrino Anomaly as well as Gallium experiment calibration discrepancies.

This work is articulated around 7 chapters.

The first chapter highlights the historical need of postulating and proving the neutrino existence. Experimental techniques used in the 50's are almost the same than the one used nowadays in Neutrino physics, describing them is therefore still of first interest. Atmospheric, Reactor and Solar sectors are described with a natural accent on the Standard Solar Model as well as current issues regarding solar abundances. The second chapter focus on theoretical frame of particle physics. The standard Model is introduced as well as neutrino oscillation in vacuum and in matter. The mass generation mechanism and sterile neutrinos are particularly detailed.

The third chapter describes the Borexino detector, from the design to the electronics. A global view of the solar program and previous results of Borexino are depicted. Finally the SOX experiment principles are described and the choice of the source is discussed.

The fourth chapter exposes the ^{8}B analysis, from the selection of the data to the calibration. Background tagging, suppression and estimation of residues is investigated. The residual backgrounds are described and final measurement is presented.

The fifth chapter is dedicated to the SOX ^{144}Ce source production, transport and storage. In particular, the Cerium extraction from the spent nuclear fuel using Displacement Complexing Chromatography columns is detailed. Characteristics of the Tungsten shield and certifications are also detailed.

The sixth chapter is devoted to description of the calibration and simulation of the detector developed for SOX source γ spectroscopy. Apparatus is described as well as the characterisation of the crystal.

The seventh chapter summarizes the on-going effort for characterising the Cerium source using γ but also β, mass and α spectroscopy. It derives competitive limits on sensitivity to source contamination with respect to contractual constrains.

Chapter 1

Neutrinos in nature

"You must have chaos within you to give birth to a dancing star." Zarathustra

Contents

1.1 Odyssey of the discovery

1.1.1 β-spectrum or an evidence of the invisible

By discovering on May 1896 that uranium salts emit radiations imaging photographic plates without external excitation, H. Becquerel opened a completely new field of study: nuclear physics or understanding the elementary matter compounds. This spontaneous emission is then extensively studied by P. and M. Curie leading to identification of new radioactive elements such as thorium, polonium and radium [1, 2].

Few years later, E. Rutherford was able to separate two of the "uranique radiation" using a magnetic field. He called them using the two first letters of the Greek alphabet α and β [3]. He

then observed transmutation of elements induced by those radiations [4]. P. Villard identified more penetrating radiation emitted by uranium salt, that he clearly identified to the very same nature than X-rays [5]. It will be called after Rutherford system, γ radiation.

In 1914, J. Chadwick worked with a magnetic spectrometer and a counter to evaluate the β emission velocity, scanning different velocity by varying the intensity of the magnetic field [6]. The result was a surprising continuous shape together with monoenergetic lines. Previous experiment done by O. Hahn and L. Meitner in Berlin were consistent with β lines of well defined energy, in agreement with the quantified orbital introduced by N. Bohr in 1913 [7] and consistent with observed α and γ lines.

Many interpretations overlapped. Rutherford in 1914 expressed the idea that the smoothness of the spectrum was due to collision of the primary emitted electrons with outer atomic electrons, loosing energy in the process [8]. The Bohr-Kramers-Slater theory [9] was breaking energy and momentum conservation. L. Meitner developed the idea that the emission of an electron induced a γ emission which would carry part of the β energy while remaining unseen by the magnetic spectrometer.

To test those hypothesis, C. Ellis and W. A. Wooster set-up a calorimeter to measure the total energy released. If the measured heat is the maximum energy of the spectrum, the continuous shape is the consequence of a monoenergetic electron loosing somehow part of its energy. If the released heat corresponds to the average of the energy spectrum, it means that the β decay is a direct emission of a continuous spectrum. The result published in 1927 [10], later confirmed by L. Meitner and W. Orthmann [11], indicates clearly the fundamental aspect of the continuous spectrum: the heat measured per decay is the averaged energy of the β spectrum. The L. Meitner and E. Rutherford interpretations are now refuted. The main explanation left at that time was the BKS theory, the energy is conserved only statistically.

On December 1930, in total disagreement with the break of energy conservation, W. Pauli postulates the existence of a new particle in an open letter addressed to the physicists of the Tübingen meeting: "Lieben Radioaktiven Damen und Herren". A 3-body decay would easily solve the momentum distribution of the β-spectrum provided that the third particle escapes the measurement. W. Pauli detailed characteristics needed by this new particle: spin 1/2, electromagnetically neutral, small mass ($< 1\%$ proton) . First called neutron, it will be re-baptised neutrino by E. Fermi during the famous 1933 Brussels Solvay meeting. Indeed, in 1932 Chadwick discovered the "neutral proton", called from now on neutron.

Following the excitement of new inputs in the matter understanding, Fermi published a complete β theory. This theory was needed for important fundamental differences with α decay. Unlike α emission described by barrier penetration probability, in the β decay, the electron and the neutrino are not present inside the nucleus before the decay process. Besides, both emitted particles have to be treated relativistically and the continuous distribution of the electron have to be predicted [12]. Illustrated by the very long characteristic lifetime (~ 1 s) of β decay with respect to ordinary nuclear processes ($\sim 10^{-19}$ s), Fermi's theory is based on the idea that the interaction causing the β transition is weak with respect to nuclear forces and he succeeded in explaining correctly the shape of β decay. G. Gamov and E. Teller extended the Fermi's theory by adding axial-vector currents for explaining the possible change of one unit of isospin in β decay [13, 14].

Using simple consideration, H. Beth and R. Peierls compute one of the first neutrino cross section

with a nucleus [15]. Finding an upper limit of $\sigma < 10^{-44}$ cm^2 they conclude: *"one can conclude that there is no practically possible way of observing the neutrino"*.

1.1.2 Neutrino comes out

First trials of direct detection were using radiochemical experiment. in 1939, H.R. Crane realised the first of this type using 1.5 kg of NaCl irradiated by a 37 MBq ^{228}Ra source [16]. He was looking for ^{16}S, produced through the reaction: ^{35}Cl + $\overline{\nu_e} \to$ ^{35}S + e^+ but was only able to set a limit on the $\overline{\nu_e}$ cross section ($\sigma < 10^{-30}$ cm^2). Knowing the cross section is so low, the first preoccupation of neutrino physicist precursors was to get the most intense neutrino flux. At this time, the most obvious intense source for nuclear physicists was nuclear bombs, before realising the sensitivity would be too low with respect to expected background [17]. Emerging atomic piles were appealing alternatives. G. Pontecorvo suggested experiments on ^{37}Cl in 1946, attempted by R. Davis and L. Alvarez at Brookhaven (1949) and Savannah River (1955) reactor sites with no successes. Scintillation of organic liquids newly discovered in 1950 allowed to look for cubic meters target scale and real-time neutrino interaction. Aside from radiochemical experiment, a new detection idea using the inverse beta decay (IBD):

$$\overline{\nu_e} + p \to n + e^+ \tag{1.1}$$

This reaction enables to master the background in such way that monitoring a nuclear reactor is made possible. The fact that two particles are emitted with different absorption time gives a clear signature of this interaction. Figure 1.1b is displaying a typical IBD signal as seen by the Reines experiment in Savannah River: one signal from e$^+$ annihilation and the following γ emitted by the n-capture.

The first attempt in the Handord site, a plutonium producing reactor, was encouraging: if not significant, an hint of a neutrino signal was observed [18]. It leads to the Savannah River site where a 700 MW compact heavy water moderated reactor had been built for hydrogen bomb material production. The laboratory room was 12 m underground and at 11 m from the core of the reactor. Three scintillating liquid tanks filled with 1400 L of triethylbenzene were used to tag γ. Between these 3 tanks, two reservoirs of 200 L of water, in which 40 kg of CdCl$_2$ were dissolved, were used as proton target for the IBD reaction and neutron capture target. Figure 1.1a sketches the original detection principle. ^{113}Cd is used because of its high neutron absorption cross section correlated with a 558 keV γ emission. In 1956 they finally reported the first neutrino signal detection [20], concluding the long hunt for proving the existence of this particle and on the same time opening a totally new field of study for nuclear, particle and astrophysics science.

1.1.3 A handed and flavoured neutrino

Parity violation The Parity is a symmetry standing for switching direction up to down, right to left, like a reflect in a mirror. This fundamental symmetry was standing for electromagnetism and strong interaction, making it hard to consider that it should be tested for the weak force. The "Wu experiment" conducted in 1956 by C.S. Wu and theorised by T.D. Lee and C. N. Yang [21] established that weak interaction is indeed violating Parity symmetry. The experiment was using ^{60}Co β-decay into ^{60}Ni. ^{60}Co can be polarized if cold enough ($\sim$3 mK) using a strong magnetic field . Looking at electron angular distribution, C.S. Wu found a modified distribution depending on the ^{60}Co polarization, meaning emitted electrons are sensible to the nuclear spin. If not expected,

(a) *Detection principles with the origin of the coincidence illustrates: positron annihilation followed by the neutron capture on ^{113}Cd [19],*

(b) *Characteristic record of the three scintillating tank signal. One can see the e^+ annihilation followed by the typical, 5.5 μs delayed, larger neutron capture pulse [18]*
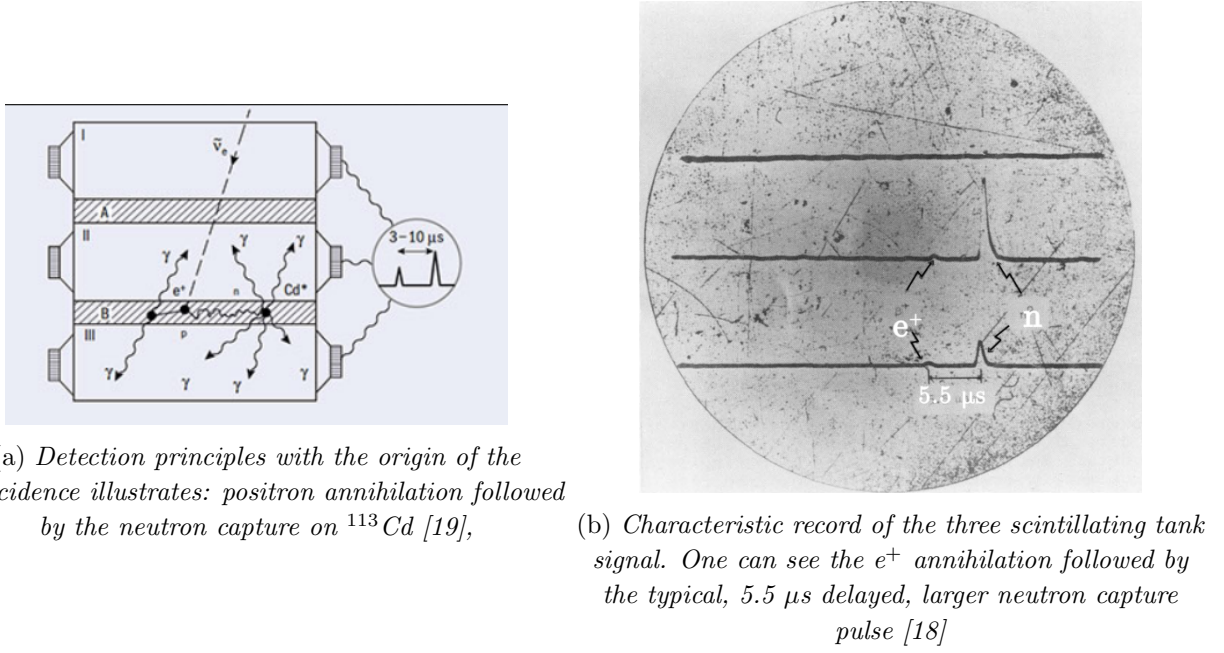
Figure 1.1: *Illustration of the Reines and Cowan experiment*

observed maximal P-violation in the weak force brought R. Feynman and M. Gell-Man to introduce the V-A theory and neutrinos to have left and right handed components [22].

A year later the "Goldhaber experiment" measured the polarization of the neutrino using electron capture on ^{152m}Eu:

$$^{152m}\text{Eu} + e^- \rightarrow ^{152}\text{Sm}^* + \nu_e \rightarrow ^{152}\text{Sm} + \gamma + \nu_e \tag{1.2}$$
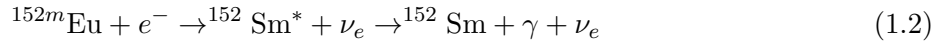
Measuring the helicity of the emitted γ ray one can directly measure the ν_e helicity. The experiment concluded that neutrinos/antineutrinos are massless and left-handed/right-handed [23].

In 1973 the "Gargamelle experiment" seeing neutrino scattering concludes to the existence of neutral current in the weak interaction. The UAI detector directly observed the neutral current using quark-quark interaction. Discovery of the W interaction gauge bosons in 1983 at CERN confirmed the Glashow-Weinberg-Salam model [24].

ν_μ **discovery** The absence (or the suppression of the branching ratio) of the reaction $\mu \rightarrow e + \gamma$ is considered the first indication that a new quantity might be differentiating "muonic" neutrino from "beta" neutrinos [25]. In 1962, L. Lederman, M. Schwartz and J. Steinberger realised the first accelerator neutrino experiment in the Brookhaven National Laboratory using the newly installed AGS (Alternating Gradient Synchrotron) facility. The experiment is composed of a 15 GeV proton beam hitting a Beryllium target. Pions and Kaons are produced in a well known quantity during the collision enabling precise estimation of the neutrino flux. A 13.5 m thick iron shield and a concrete wall are separating the target from the 10-tons aluminium spark chamber suppressing any hadronic part of the beam. The detector is shielded from cosmic rays using 5.5 m of concrete. Figure 1.2 is showing a map of the installation. The aluminium spark chamber is filled with a gas mixture of about 70% neon and 30% helium. A thin layer of scintillator surrounding the detector is actively shielding it for cosmic rays or beam induced muons events. If $\nu_e = \nu_\mu$ one should see as many electrons as muons inside the spark chamber by charged currents. However, the experiment reported 34 single

muon events (5 being potentially cosmic-ray background) for 6 electron-like events, advocating for the existence of two different neutrinos species: the one produced by β decay not being similar to the one produced by μ decay [26]. It is the first highlight of ν_μ existence and of leptonic number conservation.
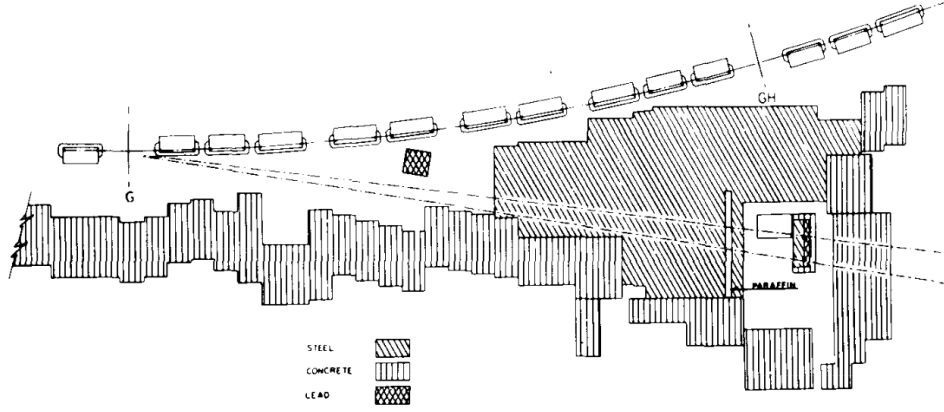
Figure 1.2: *Illustration of the A.G.S neutrino experiment in Brookhaven National Laboratory [26]. The steel, concrete and lead shields are represented as well as the expected neutrino beam direction.*

ν_τ **discovery**   The question of the existence of a third family rose when the τ lepton was discovered by M. Perl at SLAC-LBL in 1975. The DONUT (Direct observation of the nu tau) experiment successfully detected ν_τ in few months of running using the Fermilab Tevatron 800-GeV proton beam. The DONUT detector was located at 36-m from the beam dump. The primary source of ν_τ (~ 85 %) was the leptonic decay of D_S. The active target was composed of a mixture of bulk (emulsion only modules) and sandwich of emulsion and stainless steel layers. Each emulsion module was interleaved with scintillating fibre planes for vertex position reconstruction. These BrAg emulsion are acting like photographic plates: they record everything passing through them but are integrating the signal over time, not allowing any time reconstruction interaction. The main idea of DONUT was observing a ν_τ interacting via charged current with an iron nucleus producing a τ. This charged lepton decays fastly ($\tau = (290.6 \pm 1.0) \times 10^{-15}$s) but long enough to travel 2 mm from the first source vertex. Decaying mainly ($\sim 86\%$) in one charged particle, the 2 mm displacement (called a kink) can be observed between the two vertices if position is well reconstructed. This is the signal the DONUT experiment was looking for in the pictures given by the emulsion modules after all. From April to September 1997 they observed 4 ν_τ events [27] concluding do the discovery of the last piece of the neutrino family as nowadays known.

1.1.4   The end of the family?

A legitimate question is why only 3 neutrinos? The four LEP experiments ALEPH, DELPHI, L3 and OPAL at CERN analysed the Z decay modes. The Z decay has to preserve any charge and energy conservation: the final state has to be neutral and lighter than the Z mass, eliminating the top quark. The final state can be divided into three decay paths:

- leptonic, Θ_{lept} : Z→e$^+$e$^-$, Z→ $\mu^+\mu^-$ or Z→ $\tau^+\tau^-$,
- hadronic, Θ_{had} : Z→ q$\overline{\text{q}}$ ($\times 5$),

- invisible, $\Theta_{\mathrm{inv}} = N_\nu \Theta \nu$, $\Theta \nu$: $Z \to \nu \bar{\nu}$,

with N_ν being the number of Z-coupled neutrinos lighter than 45.6 GeV.c^{-2} (half of the Z mass). Following the relativistic Breit-Wigner distribution, the probability distribution of the measured energy of a particle width is larger if the decay is short and the time life of the boson is linked to the number of accessible states. Measuring the Z-boson decay width Θtot, one can deduce:

$$\Theta \text{tot} = \Theta \text{lept} + \Theta \text{had} + \Theta_{\mathrm{inv}} \tag{1.3}$$
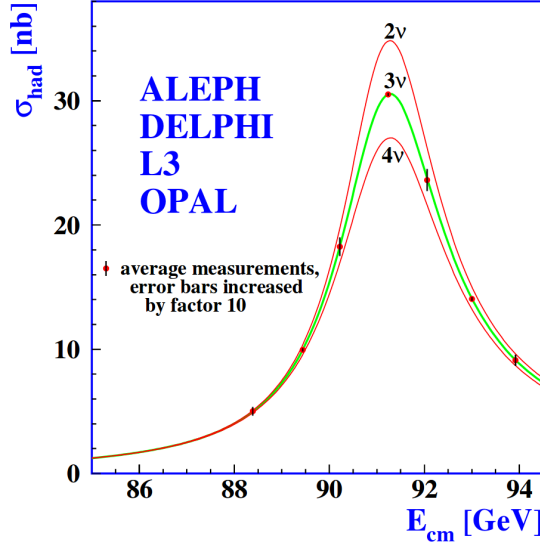
Figure 1.3: *Measurement of the Z-boson decay width at the LEP, CERN. Θinv is fitted giving $N_\nu \sim 2.98$ [28].*

In order to reduce the dependency to the Standard Model, one can derive the ratio $R_{\mathrm{th}} = (\Theta_{\mathrm{lept}}/\Theta_\nu)_{\mathrm{th}}$ instead of Θ_ν directly. Then, N_ν can be extracted using: $N_\nu = R_{\mathrm{th}} \times \Theta_{\mathrm{inv}}/\Theta_{\mathrm{lept}}$ with Θ_{inv}, Θ_{lept}, Θ_{had} experimentally measured [28]. Figure 1.3 shows the very convincing result obtained by the collaborations leading to the result of $N_\nu = 2.9840 \pm 0.0082$, excluding a priori any extra active neutrino (except if very heavy).

1.1.5 A global picture

Neutrino is an abundant particle in the Universe. Many sources are producing neutrinos covering a wide energy range: from meV to EeV, from human nuclear reactor to cosmic rays and Supernovae. Figure 1.4 shows this diversity of sources as well as the covered orders of magnitude.

Following sections are focusing on some of these sources: solar neutrinos are explored in section 1.2, contextualising the ^{8}B rate measurement reported in chapter 4, then atmospheric and accelerator neutrinos in section 1.3 and finally a brief review of reactor based experiments 1.4.
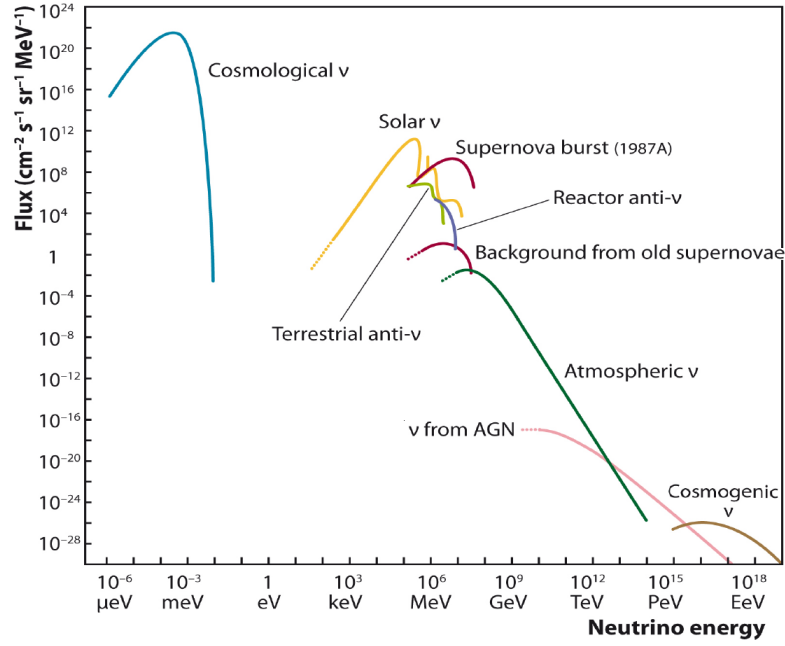
Figure 1.4: *Illustration of the wide energy spectrum and order of magnitude of neutrino sources.*

1.2 Solar neutrinos

The two violent antagonists of a star equilibrium are gravitation which tends to collapse the accreted mass and the nuclear reactions which counterbalance the collapse by activating fusion chain reactions. Mainly composed of hydrogen ($\sim 90\%$) and helium ($\sim 10\%$) at start, fusion enriches the star with heavier elements in processes described in the first section 1.2.1. The second part focus on heliosismology (1.2.2, 1.2.3) and solar neutrino emission (1.2.4) as cross checks of the model while the last part describes experimental efforts to hunt them down (1.2.5).

Until the middle of the century, informations about the Sun would not allow a deep understanding of its internal dynamic. From the 3rd Kepler's law and knowing the period of Earth rotating around the Sun, mass of the Sun can been determined ($M_\Theta \sim 2 \times 10^{30}$ kg), leading to $\sim 1.3 \times 10^{57}$ protons. The radius is deduced from apparent diameter $R_\Theta \sim 7 \times 10^8$ m. The age of the Sun (4.55×10^9 y) is assessed from meteoritic dating measurements, assuming the Solar system was formed in the same time than the Sun. Besides, temperature, composition and motions of the surface layers (mainly using black body model knowing luminosity, spectroscopic observations and meteoritic analysis) were roughly estimated. Despite Sun's discretion, it is the best known star and any Solar Model modification impacts stellar physics. In the late 60s however two powerful new techniques have emerged enabling for testing model of the Sun's core: helioseismology and solar neutrinos.

1.2.1 The Standard Solar Model

If for a long time the source of the Sun energy was a mystery, fusion processes fuelling the Sun has been postulated in 1926 by Eddington [29]. No other known energy source would be able to fuel the Sun for such a long time. His theory was mocked when published because of the Sun temperature

too low for protons forcing the Coulomb barrier ($\frac{3}{2}k_\text{B}\text{T} > \frac{e^2}{r_{\text{p-p}}}$) which arises for $\text{T} > 6.8 \times 10^{10} K$. The Sun interior temperature being estimated to $1.5 \times 10^7 K$, this reaction should be highly suppressed. Discovery of tunnel effect enabled back to consider *thermonuclear reactions as the heat source* explaining Sun light emission [30]. This is the first hypothesis of the Standard Solar Model (SSM) continuously developed since 1960. Fusion in the sun is realised through ^{4}He production by proton consumption. The principal process, counting for $\sim$98% of the solar fusion, is the *pp-chain*. It consists on ^{4}He generation by fusion of 4 protons followed by enrichment of ^{4}He through different chains described in 1.6a. An other contribution is called *CNO-cycle* [31], illustrated in 1.6b. It consists of producing ^{4}He through catalysed fusion of 4 protons by ^{12}C. This cycle is thought to be responsible of only $\sim$(1-2%) of the Sun fusion induced energy but can be dominant in massive, or ageing stars (see Fig. 3 in [32]).

A star is by definition a self gravitating ball of gas and as previously stated, *respecting the equation of hydrostatic equilibrium*, meaning equilibrating pressure with gravitational contraction:

$$\frac{dP}{dr} = -\frac{Gm(r)\rho}{r^2} \tag{1.4}$$

The total pressure is made of three contributions: thermal pressure (ideal gas law, $\text{P}_\text{th} = nk_BT$), quantum pressure from Heisenberg principle ($\text{P}_\text{Q} = \frac{1}{5}(3\pi^2)^{2/3}(\frac{N}{V})^{5/3}\frac{\hbar^2}{m}$, main contribution from e^- because $\text{P}_\text{Q} \propto 1/m$) and radiation pressure from photon ($\text{P}_\text{r} = \frac{\pi^2}{45}\frac{(kT)^4}{(\hbar c)^3}$) [33]. In the case of the Sun however, the small mass of the star induces a negligible contribution of P_Q with respect to P_th and P_r even at low radius and high density. The equation of state 1.4 is the second SSM assumption. It is known to be a good approximation for time evolution of the star [34]. When the pressure due to fusion increases, the proton-proton distance augments leading to less fusion, cooling down the system. Conversely, if the gravitation collapse get stronger, the distance proton-proton being reduced, the temperature will increase, making easier to cross the Coulomb barrier. These "respiration" effects are also happening in the fission process of a nuclear reactor. They both contribute to the stability of the system. Assuming this equilibrium valid at any radius inside the star, one can build a pressure profile depending on the temperature and the solar mass distribution.

The third hypothesis of the SSM is the *energy transport can be modelled using only convective and radiative (photon) motions*. Therefore the energy transport depends only on the temperature and the opacity (which can be seen as a resistance to radiative or convective motion) [34]. Two regions can be distinguished: the inner part where the dominant energy transport is radiative process while convection is dominant in the envelope. The radiative zone is a zone where the mean path of an emitted photon before scattering on electrons is $\sim$ 2 cm. The radius at which the convection begins to be dominant, R_CZ, is a free parameter of the SSM varying between $0.7146 \times \text{R}_\odot$ [35] and $0.7289 \times \text{R}_\odot$ [36]. Neutrinos and heliosismology are two independent techniques to test solar model based on those assumptions.

1.2.2 Heliosismology

Heliosismology is the observation of the Sun's vibration to deduce its inner structure. Using Doppler shift of solar atmospheric absorption lines, one can map the small deviation from spherical shape of the Sun surface. The most commonly used oscillating mode is the p-mode, looking at sound velocity modification due to density evolution inside the Sun. The s-mode widely employed in Earth

seismology can not be exploited in heliosismology because of the liquid phase of the Sun. Figure 1.5a is the simulation of p-wave propagation inside the Sun, showing the modification induced on the surface. Figure 1.5b is a picture taken by the GONG group of Doppler effect at the surface of the Sun. Comparing both one can extract oscillation mode resulting from the different layers of the Sun.
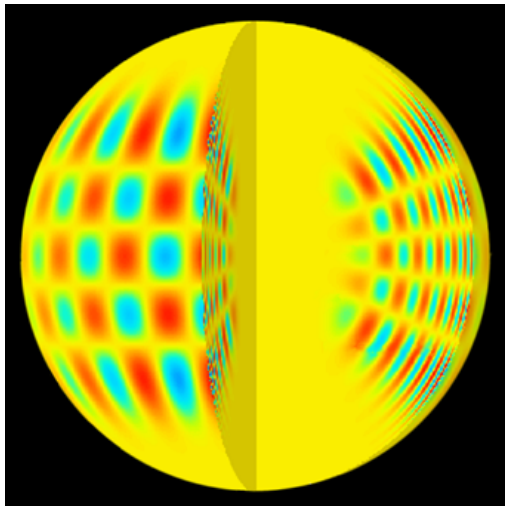
(a) *Computer generated illustration of P-mode vibration propagating on the Sun's surface.*
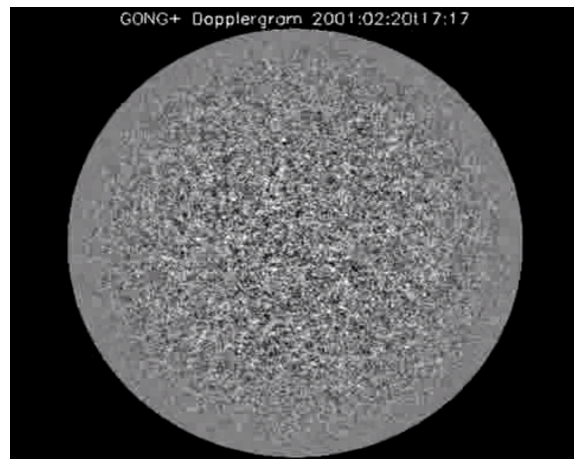
(b) *Observation of the Sun's surface Doppler shift in real time (dopplergrams). From GONG/NSO/AURA/NSF.*

Figure 1.5: *Simulation and observation of P-mode vibration propagation through the Sun's interior using Doppler effect on the surface.*

1.2.3 The Solar Abundance

The standard solar model is based upon few equation of states, neglecting any energy loss during its life and being constrained by the boundary conditions, namely the surface layers limited informations. Key parameters of the Sun are the abundance of Hydrogen (noted X), Helium (noted Y) and the abundance of heavier elements (called metallicity, noted Z). There are two possibilities to measure those abundances: analysis of meteorites in terrestrial laboratories and spectral absorption lines from the photosphere. Both relies on questionable assumption.

The meteoritic analysis is the most precise measurement because all the chemical composition can be extracted, included the isotopic composition. However, the most important compound of the Sun mass (hydrogen, helium, oxygen, nitrogen, neon) are volatile elements meaning that they are depleted in meteorite with respect to Sun composition [37]. Inferring the Sun composition with meteorite measurement is therefore a though task.

Using the spectroscopic measurement, one has to infer the internal composition from the solar photosphere. It is assumed that the initial Sun composition is within 10% the composition of the photosphere [37]. Despite uncertainties, the agreement between the SSM derived from those abundance [38] and internal structure tests using heliosismology was excellent [32]. This good agreement was a strong argument to question neutrino physics during the Solar Neutrino Problem leading to the neutrino oscillation observation.

Recently, a complete revision of the solar abundances has been realised [39] due to development of three dimensional hydrodynamics models and improvement in the spectroscopic measurements. In particular, the metallicity has been lowered from Z=0.0229 X [38] to Z=0.0178 X [37] modifying opacity. This revision leads to contradiction between heliosismology measurement and predictions of the SSM [40]. This solar abundance problem weakens the SSM ability to predict solar neutrino fluxes, making solar neutrino measurement of great importance.

1.2.4 Solar neutrinos emission

The main component of fusion energy in the Sun (*pp-chain*) is also the main neutrino emitter through processes described in figure 1.6a. The *CNO-cycle* is emitting neutrinos as well as illustrated in figure 1.6b.

(a) *Solar pp-chain [41],*

(b) *Solar CNO cycle [14],*
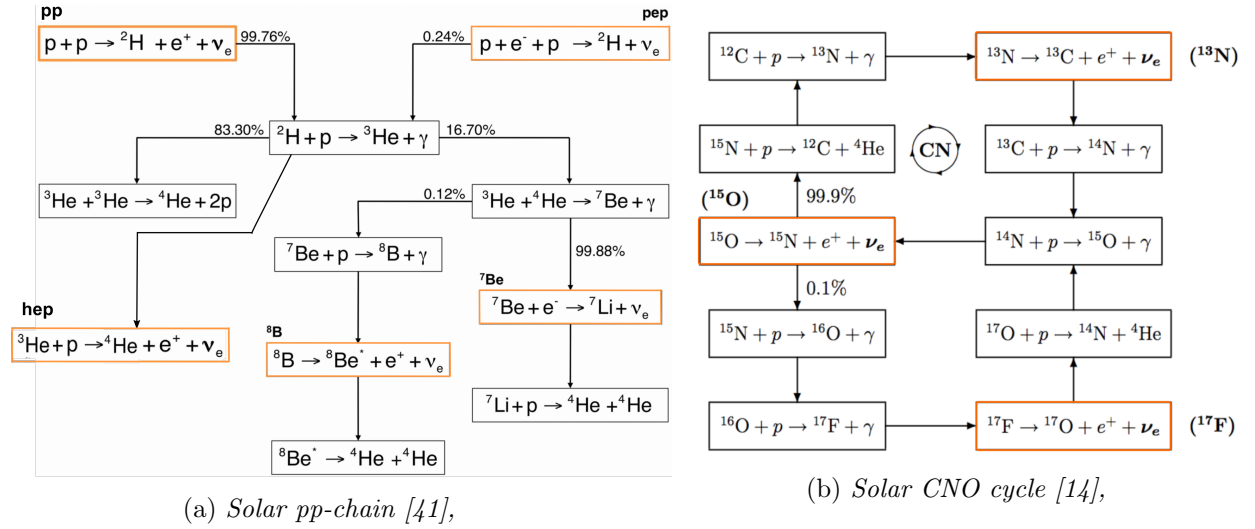
Figure 1.6: *Fusion cycle fuelling the Sun's core. In orange the neutrino emissions.*

pp-chain The *pp-chain* releases neutrino through 5 processes called (*pp*), (*pep*), (*hep*), ^{7}Be and ^{8}B. The major process for heat production and for neutrino flux, is called the (*pp*) process:

$$p + p \rightarrow {}^2He + e^+ + \nu_e \qquad (pp) \tag{1.5}$$
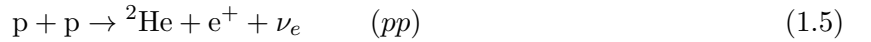
Although the most abundant solar neutrino, (*pp*) low energy makes them hard to detect. Knowing that the main proton-proton fusion branch provides an energy of Q_{pp}=26.7 MeV and two neutrinos, one can roughly estimate the total neutrino flux on Earth [33]:

$$\phi = 2 \times \frac{\mathcal{L}}{Q_{pp} 4\pi R^2_{\text{Sun-Earth}}} \approx 6.3 \times 10^{10} \text{cm}^{-2}.\text{s}^{-1} \tag{1.6}$$

From Deuterium to Helium, the other neutrinos emitters are:

$$p + p + e^- \rightarrow {}^2H + \nu_e \qquad (pep) \tag{1.7}$$

$$p + {}^3He \rightarrow {}^2He + e^+ + \nu_e \qquad (hep) \tag{1.8}$$

$$^7Be + e^- \rightarrow {}^7Li + \nu_e \qquad (^7Be) \tag{1.9}$$

$$^8B \rightarrow {}^8Be^* + e^+ + \nu_e \qquad (^8B) \tag{1.10}$$
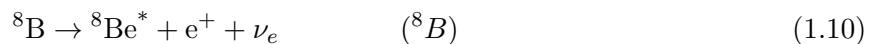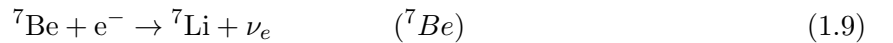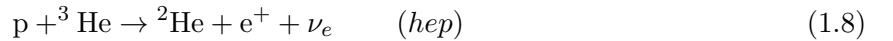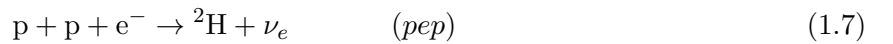
The CNO cycle, illustrated in Figure 1.6b generates ν_e via three channels:

$$^{13}\text{N} \rightarrow ^{13}\text{C} + \text{e}^+ + \nu_e \qquad (^{13}N) \qquad (1.11)$$

$$^{15}\text{O} \rightarrow ^{15}\text{N} + \text{e}^+ + \nu_e \qquad (^{15}O) \qquad (1.12)$$

$$^{17}\text{F} \rightarrow ^{17}\text{O} + \text{e}^+ + \nu_e \qquad (^{17}F) \qquad (1.13)$$

As illustrated in Figure 1.7, the *(pp)*, (^8B), *(hep)*, (^{13}N), (^{15}O), (^{17}F) have a continuous spectrum in energy due to momentum distribution with the charged lepton emitted in the same reaction. *(pep)* and (^7Be) are monoenergetic peaks. The *pp-chain* neutrino shapes were subject of extensive
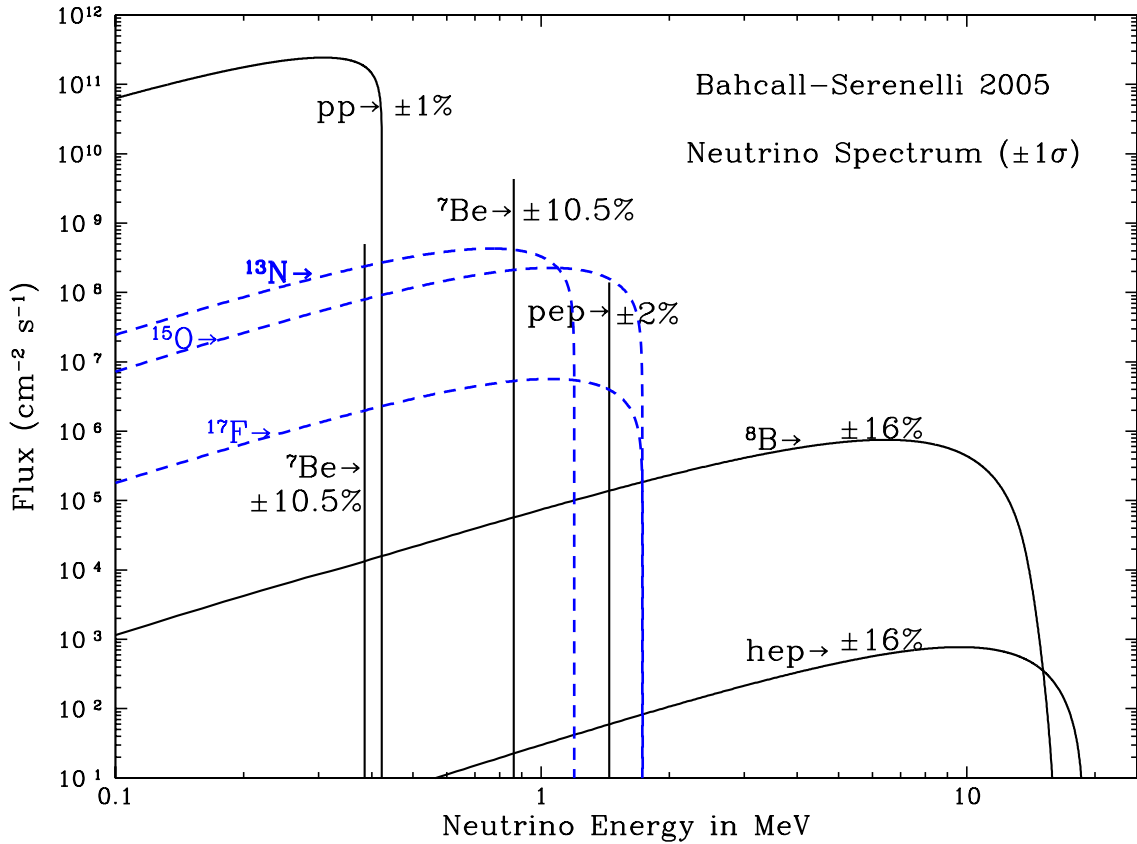
Figure 1.7: *Solar neutrino energy spectrum extracted for the solar model BS05 [36].*

study but their normalization depends on the chosen Standard Solar Model and can not be derived only from the Sun luminosity [42]. The flux estimation relies on assumption made on many SSM parameters such as the solar abundance evolution (initial and present chemical composition), the distance from the core where the convective behaviour become dominant, and the convective mixing length [36]. Table 1.1 shows neutrino flux predictions for the same SSM (B16 [40]) applied on high (GS98 [38]) and low (AGSS09 [37]) metallicity models. Some model-independent constraints on solar neutrino fluxes are derived from luminosity measurement [43].

From table 1.1, it is clear that ^{8}B and CNO neutrinos are the most sensitive neutrinos to the

Flux	B16-GS98[38, 40] High metallicity	B16-AGSS09 [37, 40] Low metallicity	Unit
(pp)	5.98 ± 0.04	6.03 ± 0.03	10^{10} cm^{-2}s^{-1}
(pep)	1.44 ± 0.01	1.46 ± 0.013	10^{8} cm^{-2}s^{-1}
(hep)	7.98 ± 2.4	8.25 ± 2.5	10^{3} cm^{-2}s^{-1}
^{7}Be	4.93 ± 0.30	4.50 ± 0.27	10^{9} cm^{-2}s^{-1}
^{8}B	5.46 ± 0.66	4.50 ± 0.54	10^{6} cm^{-2}s^{-1}
^{13}N	2.78 ± 0.42	2.04 ± 0.29	10^{8} cm^{-2}s^{-1}
^{15}O	2.05 ± 0.39	1.44 ± 0.23	10^{8} cm^{-2}s^{-1}
^{17}F	5.29 ± 1.06	3.26 ± 0.59	10^{6} cm^{-2}s^{-1}

Table 1.1: *Estimation of the solar neutrino fluxes depending on the abundancy distribution. From [40].*

metallicity problem. The CNO flux is 40% higher in the high metallicity than in low metallicity models [44], allowing a clear discrimination.

1.2.5 Solar neutrinos measurements

1.2.5.1 Radiochemical experiments

The main idea of any radiochemical experiments is to exploit reverse electron capture in order to measure neutrino interaction with matter as suggested by B. Pontecorvo in 1946. Transforming a nucleus A into B using reverse electron capture, B is then chemically separated from A solution and counted. For its higher density and to optimize the extraction of the resulting compound, the target volume is liquid. The observed flux is necessarily integrated on energy due to the technique itself in which the signal is a number of transformed nucleus. The threshold of the reaction is therefore an important parameter to understand the expected fluxes.

The Solar Neutrino Unit (SNU) was introduced for radiochemical detectors such as Homestake with the value of: 1 SNU = 10^{-36} ev.atom^{-1}.s^{-1}. This unit is target-dependent as it takes into account the cross section of the neutrino on an atomic target. Comparing two measurements in this unit is meaningless and it is only used for comparison between SSM estimation and experimental measurements.

Chlorine experiments The first neutrino radiochemical experiment was realised in 1955 by R. Davis in Brookhaven reactor for $\overline{\nu_e}$ observation [45]. The Davis' experiment was based on the principle that if ^{37}Ar naturally decays by electron capture on ^{37}Cl, this process can be reversed. A neutrino interacting with a ^{37}Cl neutron can undergo the following reaction:

$$\nu_e + ^{37}\text{Cl} \rightarrow ^{37}\text{Ar} + e^-$$

(1.14)

Two tanks (200 L and 3900 L) filled with carbon tetrachloride (CCl$_4$) were placed at approximately 9 meters from the 25 MW reactor center. At this distance, $\sim 3 \times 10^{11}$ $\overline{\nu_e}$.cm^{-2}s^{-1} are expected at the detector position. The argon produced by neutrino capture was removed using helium flushing the liquid volume. The argon was extracted from the helium gaz using cold charcoal trap. Geiger-Müller counters were finally used for measuring ^{37}Ar activity. The experiment was aiming

at observing reaction 1.14 realised with antineutrino to probe neutrino/antineutrino differ in their interactions [45]. Failing to see any differences between the ON/OFF phases of the reactor, he derived a limit on antineutrino capture cross section.

The Homestake experiment is based on the same principle only being more massive, looking at solar neutrino, and located deep underground for cosmic-rays shielding. A 378-m^3 tank of per-chorethylene (C_2Cl_4) was installed in the Homestake Gold Mine at Lead (South Dakota, USA) 1478 m below the surface ($\sim$ 4200 m.w.e.). J. Bahcall predicts the solar fluxes for such an experiment [46] to 4 to 11 solar neutrino events per day for a background rate of 0.2 [47]. With a 0.81 MeV reaction threshold, the main component of the solar flux is coming from ^{8}B ($\sim$ 75%) and ^{7}Be ($\sim$ 25%). In 1968, the Homestake chlorine observed flux was only a third of the Bahcall's prediction ($\phi_{obs} \leq 3$ SNU with respect to $\phi_{pred} = 20 \pm 12$ SNU [48]). This deficit was later confirmed by the Homestake collaboration after several tests and additional measurements. After 25 years of data taking, the Homestake chlorine detected 2200 ^{37}Ar atoms leading to a measured solar neutrino flux of about $2.56\pm0.16_{stat}\pm0.16_{syst}$ SNU [49] for a prediction of $7.6^{1.3}_{1.1}$ SNU [32] or 8.5 ± 1.8 SNU [35].

Gallium experiments   Homestake was not the only radiochemical experiment hunting down solar neutrinos. The GALLEX/GNO and SAGE collaborations used Gallium target for neutrino detection following the reaction:

$$\nu_e + ^{71}Ga \rightarrow ^{71}Ge + e^- \tag{1.15}$$

With a threshold of 0.233 MeV, these experiments were aiming at measuring the pp neutrino flux, dominant at this energy (pp: 54%, ^{7}Be: 27%, ^{8}B: 9% from [14]).

Like for the Chlorine channel, the Gallium collaborations extracted ^{71}Ge from the liquid target, converted to germane ($^{71}GeH_4$) and then observing the ^{71}Ge decay: NaI detectors measuring the 10.4 and 1.2 keV lines emitted by ^{71}Ge decay. The expected flux for Gallium is: $\phi_{pred} \sim 128$ SNU.

- SAGE, the Soviet-American Gallium Experiment is located in the Baksan Neutrino Observatory below the Mt. Andyrchi (4700 mwe) in the Caucasus, Russia, running from Dec., 1989 to Dec., 2007. The target is a 50 t metallic gallium heated (30 °C) so the gallium remains molten [50]. The solar neutrino measurement is: $\phi_{obs} = 65.4 \pm 4.1$ SNU.

- Gallex ran between 1991 and 1997 in the Laboratori Nazionali del Gran Sasso in Italy (3200 mwe). From 1998 to 2003, the experiment has changed its name to the Gallium Neutrino Observatory (GNO). The target is a 54-m^3 detector tank filled with 101 t. gallium liquid-chloride solution (30.3 t. of gallium) [51]. The combined Gallex+GNO(I+II+III) solar neutrino measurement is: $\phi_{obs} = 69.3 \pm 5.5$ SNU.

The calibration issues encountered by those two experiments are discussed in the sterile neutrino section 2.4.1.1. A careful combined analysis of the two gallium experiments leads to 66.1 ± 3.1 SNU [50]. It is about half of the SSM prediction but observed pp neutrinos for the first time.

1.2.5.2   Cerenkov detector

With respect to Radiochemical experiments, Cerenkov detection techniques enables directional, spectral and real-time observation of solar neutrinos [52]. Indeed, the light produced by charged particle Cerenkov effect is emitted in a cone of aperture θ_C following $\cos(\theta_C) = (\beta n)^{-1}$ with $\beta = v/c$

and n the refractive index of the medium, directly linked with the particle velocity direction. The number of visible Cerenkov photons is about: $N \approx 5 \times 10^4 \sin(\theta_C)^2$ m^{-1} [33].

The main detectors for solar neutrinos are located in Japan: Kamiokande, Super-Kamiokande and in Canada: Sudbury Neutrino Observatory. They both rely on Cerenkov emission in water (light or heavy). Solar neutrino energy is not high enough for inducing charged current with μ or τ emission (see section 2.1.3). The only possible interaction of solar neutrino with matter is via electron scattering (see 2.1).

Kamiokande/Super-Kamiokande The Kamioka Nucleon Decay Experiment built an underground laboratory in the Mozumi mine of the Kamioka mining company. The Kamiokande detector is located under 1000 m of rock, shielded from the cosmics by 2600 mwe. Kamiokande ran from 1983 to 1996 when Super-Kamiokande started. The Kamiokande detector was a cylindrical 3000-t tank filled with pure water. Aiming at detecting proton decay and cosmic neutrinos, the first energetic threshold was 100 MeV not enabling any solar neutrino measurement [14]. An upgrade of the detector happened in 1986 in order to reach 10 MeV [53], enlarging the detector for active shielding and reducing the radioactive background. Kamiokande detects neutrinos coming from the supernovae SN1987A [54]. During several upgrades (KM-I, KM-II, KM-III), Kamiokande reaches 9 MeV [55], and 7 MeV energy threshold. For the solar analysis the Kamiokande collaboration used a 680 tons fiducial mass.

The Kamiokande collaboration detected 597 ± 41 solar ν_e events for 2079 days of KM-II and KM-III data. Measuring a flux of $2.80 \pm 0.38 \times 10^6$ cm^{-2}s^{-1}, the discrepancy with the SSM was going from 49% to 64% [56]. This totally new experiment with respect to the radiochemical ones, confirmed the Solar Neutrino Problem.

Super-Kamiokande is located 500 m far from the position of Kamiokande (where now stands the experiment KamLAND). It is taking data since 1996. The detector is a cylinder of 50 kt ultra pure water. This cylinder is then divided between the inner detector (ID) and the active shield called outer detector (OD). The ID is a 33.8 m(diameter)x36.2 m(height) cylinder, representing a 32.5 kt ultra-pure Cerenkov imaging detector. The OD ($\sim$ 2.5 m water layer between wall and ID) is an active veto against external penetrating particles as well as passive shielding against neutron and γ rays from the surrounding wall. Figure 1.8a is a sketch of the Super-Kamiokande detector site.

Super-Kamiokande divided data taking in four different phases:

- SK-I, April 1996 to November 2001, 11,146 PMTs, 4.49 MeV threshold [57],
- SK-II, December 2002 to October 2005, 5182 PMTs, 6.49 MeV threshold [58],
- SK-III, October 2006 to 2008, 11,129 PMTs, 3.99 MeV threshold [59],
- SK-IV, September 2008 to February 2014, 11,129 PMTs, 3.49 threshold [60].

The water has to be purified (60 tons.h^{-1}) and temperature of the reinjected water is well controlled to avoid convection inside the tank which would bring radon to the most inner part of the detector. Each PMT is giving integrated charge and time of events. Selection and coincidence is then made online using software [60]. Super-Kamiokande can detect solar neutrino via elastic scattering. Looking at the Cerenkov cone reconstruction, the velocity of the electron, the deposited energy and

the direction can be measured. Figure 1.8b shows the angular distribution of solar neutrino like events. Super-Kamiokande has a clear signal coming from the Sun and exploits directionality for background rejection.

The Super-Kamiokande collaboration released a solar flux measured above 6.5 MeV (^{8}B) in 1998

(a) *Illustration of the detector geometry [61],*

(b) *Angular distribution of the events between 3.49 and 19.5 MeV [60] shows a clear distinction between solar neutrino (dark grey) and background (light grey).*
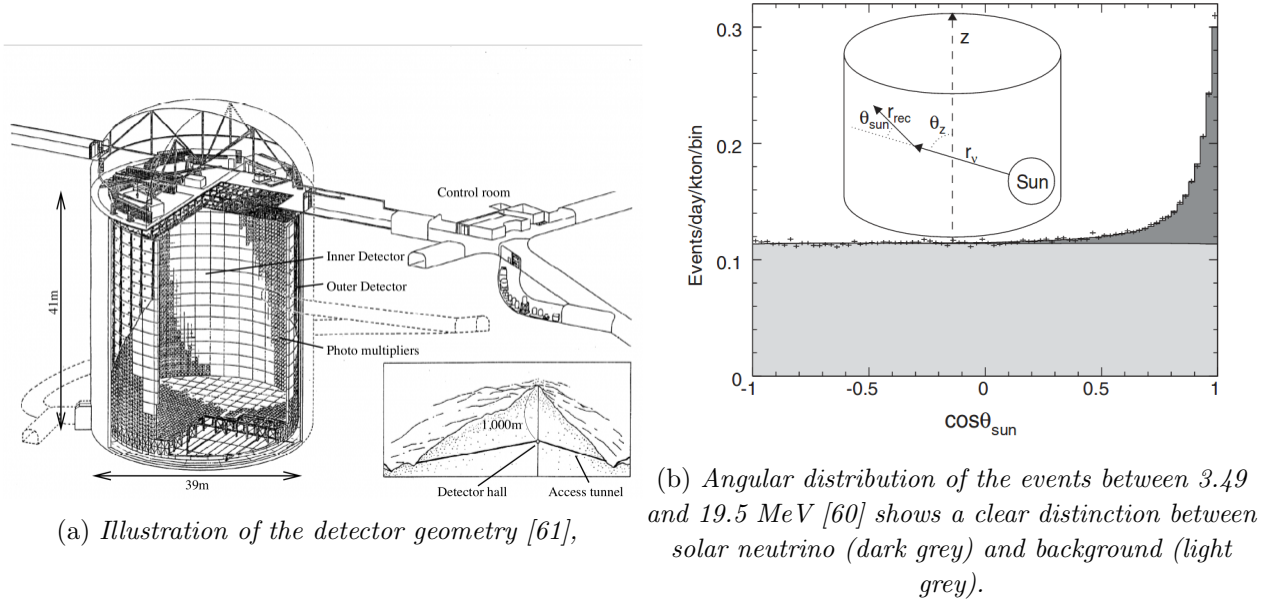
Figure 1.8: *The Super-Kamiokande experiment.*

consistent with Kamiokande: $2.42^{+0.12}_{-0.09}$ [62] and confirming the Solar Neutrino Problem (36% of the expected solar flux [62]). The same year they observe oscillation of the atmospheric neutrinos (see section 1.3).

The Sudbury Neutrino Observatory and the resolution of the Solar Neutrino Problem
The Sudbury Neutrino Observatory (SNO) is a real-time heavy-water Cerenkov detector located in the Creighton mine, near Sudbury, Ontario, Canada. The underground laboratory is 2092 m depth, shielding the facility with 6010 mwe. The geometry is a 34-m high, 22-m diameter cavity filled with ultra pure light water (H_2O) acting as a passive shield. A 17.8 m diameter stainless steel geodesic filled with light water is suspended in the center. 9456 20-cm PMTs are monitoring the active part of the detector: a 12 m diameter nylon vessel sphere filled with 1 kton of D_2O [63].

SNO detects solar neutrino through three different channels: Charged Current (CC), Neutral Current (NC) and Elastic Scattering (ES) described in section 2.1.3. (CC) and (NC) reactions are possible only for neutrino energy above 1.442 MeV and 2.224 MeV respectively. However due to high activity background the neutrino energy threshold enables SNO to measure only ^{8}B solar fluxes [65]. Equations 1.16,1.17 and 1.18 describe the reactions used in the SNO experiment to observe solar neutrinos.

$$\text{CC:} \quad \nu_e + d \rightarrow p + p + e^- \tag{1.16}$$

$$\text{NC:} \quad \nu_\alpha + d \rightarrow p + n + \nu_\alpha \tag{1.17}$$

$$\text{ES:} \quad \nu_\alpha + e^- \rightarrow \nu_\alpha + e^- \tag{1.18}$$
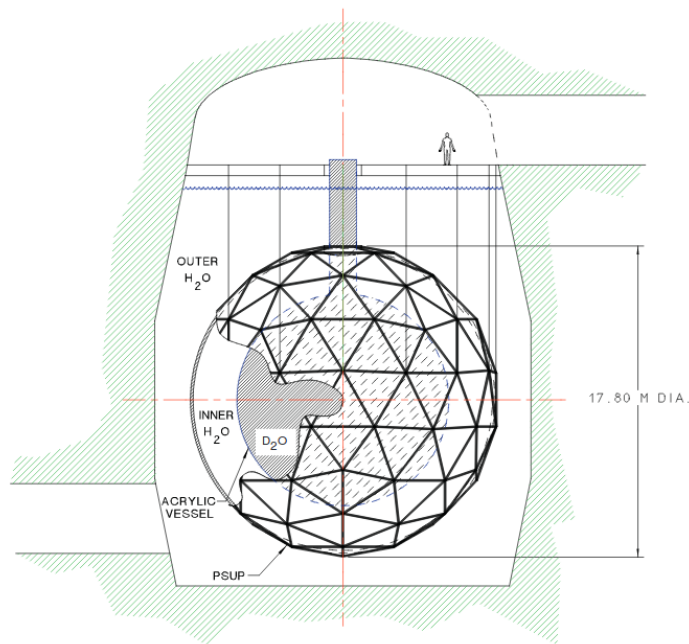
Figure 1.9: *Sketch of the SNO detector [64].*

with $\alpha = e, \mu, \tau$.

The Radiochemical experiments as well as Kamiokande and Super-Kamiokande all shared the same observation: a high deficit ($R = N_{\mathrm{obs}}/N_{\mathrm{predict}} \sim 30 - 50\%$) of measured solar neutrinos fluxes with respect to prediction from the SSM. The key point of this experiment is the capacity of observing the same phenomenon (solar neutrino) via parallel channels. As described in equation 1.16, the (CC) channel is sensible only to ν_e while (NC) and (ES) are detecting ν_e, ν_μ and ν_τ (with different weights though). SNO data analysis has been divided in three parts:

- SNO-I : Nov. 1999 to May 2001, D_2O only,
- SNO-II, *salt phase*: July 2001 to Aug. 2003, D_2O+NaCl,
- SNO-III: Nov. 2004 to Nov. 2006, D_2O+array of ^{3}He proportional counter.

During the SNO-I phase (NC) neutrons were tagged using the n-capture on deuterium leading to the emission of one 6.25 MeV γ. Adding the NaCl in SNO-II enhanced the efficiency of the neutron identification using n-capture on ^{35}Cl. The higher cross section and the several high energy γ emissions ($\sim$ 5-8 MeV) more than double the efficiency on the neutron capture [66].

The results of SNO measurement published in 2001 [67] reveals that if the derived (ES) flux is in agreement with the Super-Kamiokande and radiochemical measurements, the (NC) flux is in agreement with the SSM. The Sun producing almost exclusively electronic flavoured neutrino, this means that electronic neutrino changes flavour during propagation, neutrinos are oscillating. Figure 1.10 summarizes the different measurements of the Solar Neutrino Problem. The difference in the observed ν_e fluxes is depending on the energy threshold. Experiments with the lower threshold have a higher measured-over-expected ratio due to the MSW effect described in section 2.3.2.2. SNO solves the Solar Neutrino Problem: Sun is shinning about the right number of ν_e, they simply oscillate in the in-between.

Total Rates: Standard Model vs. Experiment
Bahcall—Serenelli 2005 [BS05(OP)]
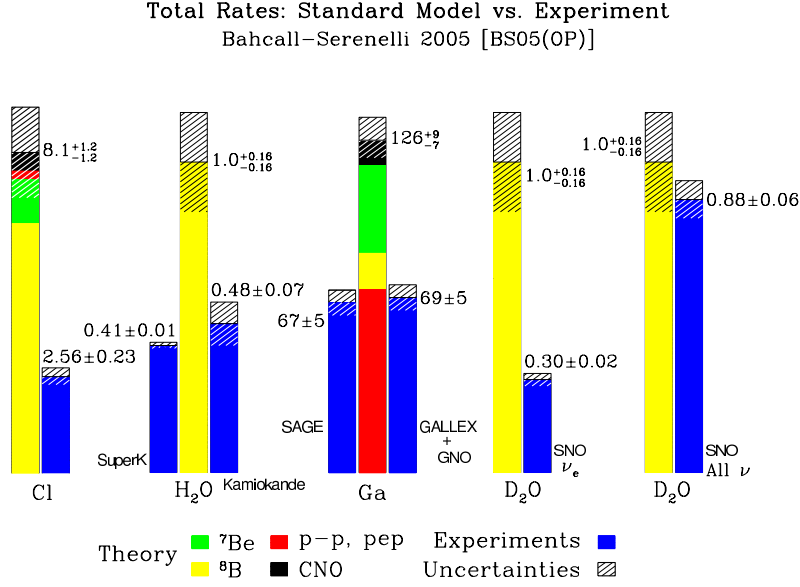
Figure 1.10: *Summary of the solar neutrino measurement done before 2002 and the resolution of the anomaly thanks to the SNO experiment [68].*

1.3   Atmospheric and accelerator neutrinos

Cosmic rays are high energetic extraterrestrial particles entering atmosphere. Mainly composed of protons ($\sim$90%) with a tiny fraction of heavy elements and electrons. Entering the atmosphere, cosmic rays interact with atmospheric nuclei, inducing hadronic and electromagnetic showers. In the shower induced by the incident primary particle, a lot of mesons will be created, mainly: π^+,π^-,π^0, $\kappa^+,\kappa^-,\kappa_R^0,\kappa_L^0$. These mesons will fast decay to μ and e^- producing $\overline{\nu_e}$, and $\overline{\nu_\mu}/\nu_\mu$.

Neutrinos production is dominated by the two processes:

$$\pi^+ \rightarrow \mu^+ + \nu_\mu \qquad \mu^+ \rightarrow e^+ + \overline{\nu_\mu} + \nu_e \tag{1.19}$$

The ratio of the number of $\nu_\mu + \overline{\nu_\mu}$ over the number of $\nu_e + \overline{\nu_e}$, $N_{\mu/e}$, is expected to be two, according to equation 1.19. Figure 1.11 is the calculated $N_{\mu/e}$ depending on ν energy for three different models [69]. Important feature of atmospheric neutrinos is the wide range of length roamed by neutrinos from their production site: from about 10 km to 12700 km. Beside their energy spread around 10 GeV [69].

The observable in the atmospheric neutrino experiment is R= $(N_{\mu/e})_{\text{DATA}}/(N_{\mu/e})_{\text{MC}}$. Two experiments reported the first observation of atmospheric neutrinos in 1965 by the Kolar Gold Field collaboration [70] and the Case-Wits-Irvine experiment [71]. Both were located deep underground (> 8000 mwe cosmic shielding). Many experiments looking for the proton decay detected atmospheric neutrinos, considering it as a background. Kamiokande and IMB, large underground Cerenkov detectors, both measure with good precision the atmospheric fluxes [72, 73] but lower than the one from estimation by respectively (30 ± 10) and $(31 \pm 11\%)$. This discrepancy will stand for years being called the Atmospheric neutrino anomaly. During the same period, other experiments (Fréjus [74], NUSEX [75]) were seeing no deficit, making this anomaly subject to controversy in the

27
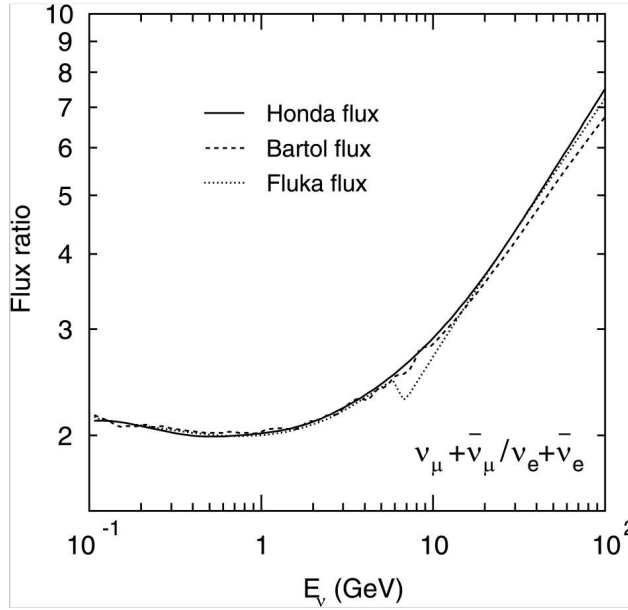
Figure 1.11: *Evolution of $N_{\mu/e}$ with the energy for three different models [69].*

scientific community [14]. If neutrino mixing was expected since the discovery of the CKM matrix in the quark sector [76], it was not believed to be with a large mixing angle [69].

Thanks to upgrade of the detector (using high energetic produced muons crossing the detector: Partially Contained events), Kamiokande could observe the zenith-angle distribution of multi-GeV events [77]. This result confirms the atmospheric neutrino anomaly (R= 0.57 ± 0.08) and is the first solid hint of new physics lying under the anomaly. Super-Kamiokande saw a consistent discrepancy by comparing upward and downward going atmospheric neutrinos ($\nu_\mu \sim$ GeV) [78]. Figure 1.12a is illustrating the neutrino path across the Earth or not. This up-down asymmetry was giving the first evidence of neutrino flavour oscillation with travel distance and energy as shown in Figure 1.12b.

Atmospheric sector can be explored by any beam of GeV ν_μ and a baseline of several hundred kilometres. The source production can be either the atmospheric pions and kaons decaying, either anthropogenic through accelerators-based experiments.

The K2K experiment [80] was a long baseline neutrino experiments using 12 GeV protons beam accelerated in the KEK-PS and directed toward Super-Kamiokande. They observed 112 events instead of the $158.1^{+9.2}_{-8.6}$ expected in a model without oscillations. The K2K observed indeed ν_μ oscillation disappearance with 4.3σ [81]. The MINOS experiment (2005-2012) used a near and a 735 km far detectors located in the Soudan mine. The source was a 120 GeV proton beam from the Fermilab Main injector, with an option to modulate the neutrino beam energy by moving the target with respect to the horn and the ability to enhance ν_μ or $\overline{\nu}_\mu$ production in the final mixture. Being able to distinguish on an event-by-event basis ν_μ and $\overline{\nu_\mu}$, MINOS confirmed the ν_μ disappearance and reported the first $\overline{\nu_\mu}$ disappearance [82].
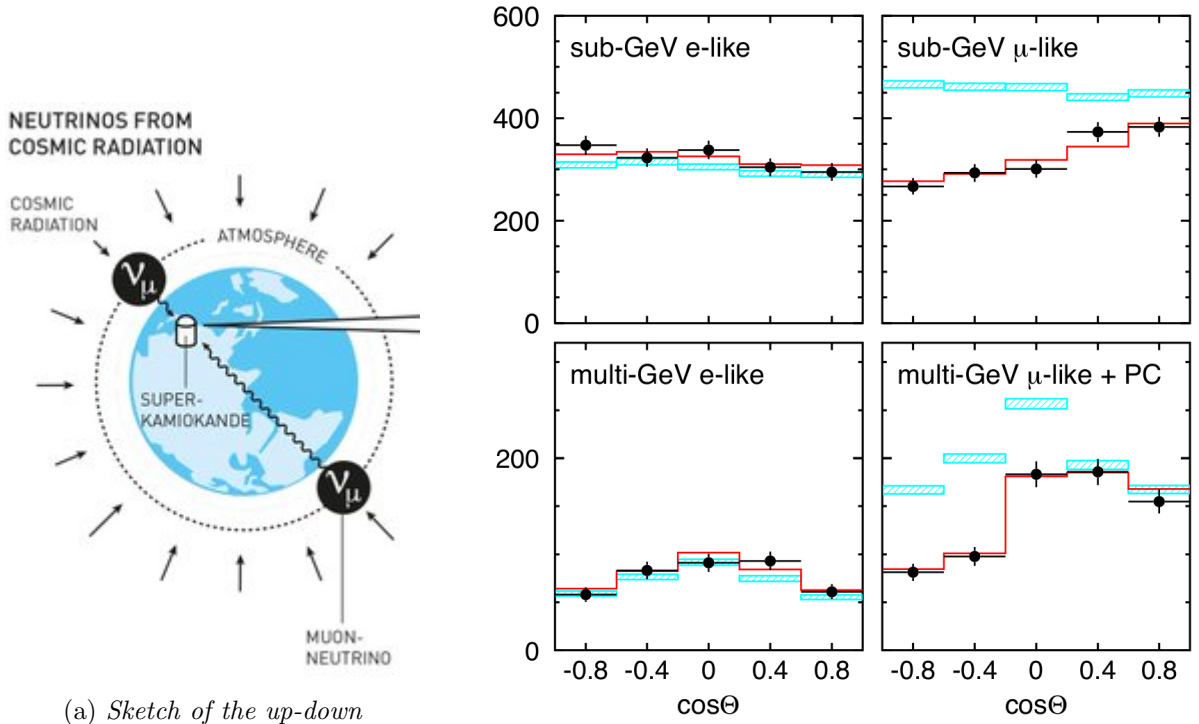
(a) *Sketch of the up-down atmospheric neutrino comparison*

(b) *Zenith angle distribution of events (black dots) in Super-Kamiokande with momenta below and above 1.33 GeV. Blue boxes is expectation from MC with no oscillation while red curve is the fit with oscillation.*

Figure 1.12: *Illustration of the evidence of atmospheric neutrino oscillation in the Super-Kamiokande detector [79].*

1.4 Reactor neutrinos

Nuclear reactors are intense sources of neutrinos. About 5% of the total heat released by fissions is escaping through neutrino emissions. Fission product are neutron rich and undergo β^- reactions to reach stability by converting them in proton, emitting $\overline{\nu_e}$. This is the reason why reactor neutrinos are pure $\overline{\nu_e}$ emitter.

Reactor neutrino experiments aim at observing neutrino exiting a reactor core. CHOOZ, taking place in the late 1990 used Gadolinium doped scintillating liquid for neutron capture and was locate ~ 1 km from the reactor core. Using a comparison of flux and spectrum between a close to the core measurement and after several meters of propagation, reactor neutrino experiments can test the oscillation model as well. The benchmark was predicted flux using heat balance of the core extrapolated to neutrino rate and spectrum. The detector was a 5 t Gd-doped scintillator in a 5.5 m tall, 5.5 m diameter cylinder. Photomolutiplier tubes, immersed in a buffer liquid, collected light from the innermost region. The detector was surrounded by an active veto muon detector [83].

The absence of observed oscillation in the CHOOZ experiment leads to the construction of a new generation of reactor neutrino experiment. Bigger and more precise, they are all buit on the same principle. Using the inverse beta decay close to the core, constituted of at least two detectors for comparing spectrum with less assumption on the emitted flux. Double-Chooz [84], Daya-Bay [85]

and RENO [86] were built in France, China and South Korea respectively. Distribution of reactors and detectors is specific to each experiment.

They all observed oscillation from the core. Figure 1.13 is showing oscillation observed by Double Chooz and Daya Bay.
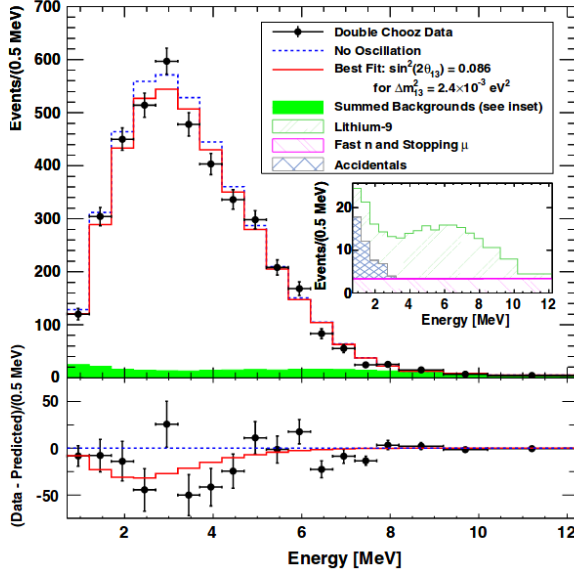
(a) *Double Chooz result of the far detector [87]*
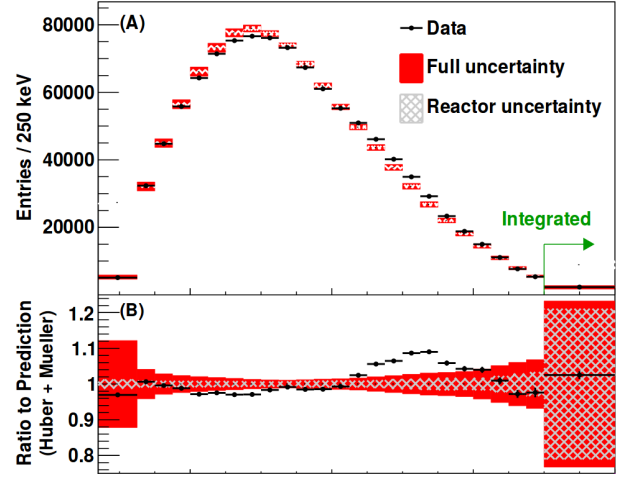
(b) *Daya Bay result [88]*

Figure 1.13: *Reactor neutrino experiments results.*

Conclusion

Neutrinos have come a long way since physicist first observed them. If the first idea to overcome the infinitesimal interaction cross section of neutrinos was to use nuclear bomb, a lot of sources are now settled enabling scientists to play with energy and distance as well as matter or not in their trajectory. From one massless and invisible particle, six have now been observed, oscillating and "feeling" matter. Together with experimental discoveries, new models have enabled to include step by step all the long live standing anomalies inside a coherent theory, confining and delineating *what is a neutrino* in a smaller trap.

Chapter 2

Nature of the neutrino

"Where man is not, nature is barren." W.Blake

Contents

2.1 The neutrino and the Standard Model

As far as we know, neutrino is a fundamental particle (no size, no substructure, can not be excited or broken up). Because they form different statistics, spin is a good way of dividing fundamental particles into two species: boson (integer unit spin) and fermion (semi integer unit spin). Force carriers are bosons while particles interacting and constituting common matter are fermions. Table 2.1 is listing fermions while Table 2.2 is giving properties of known bosons.

	Generations (mass)			EM charge	strong	EM	weak
Quarks Up	u $(2.3^{+0.7}_{-0.5}$ MeV)	c (1.28 GeV)	t (173 GeV)	2/3	✓	✓	✓
Quarks Down	d $(4.8^{+0.5}_{-0.3}$ MeV)	s (95±5 MeV)	b (4.7 GeV)	-1/3	✓	✓	✓
Charged leptons	e (511 keV)	μ (106 MeV)	τ (1.78 GeV)	-1	x	✓	✓
Neutral leptons	ν_e	ν_μ	ν_τ	0	x	x	✓

Table 2.1: *Summary of fermions and their interactions [89, 81].*

Force	name	number	EM charge	spin	mass
Strong	Gluons (g)	8	0	1	0
EM	Photon (γ)	1	0	1	0
Weak	W$^\pm$	2	±1	1	80.4 GeV
Weak	Z	1	0	1	91.2 GeV
-	Higgs	1	0	0	125 GeV

Table 2.2: *Summary of bosons [89, 81].*

2.1.1 Gauge theory

Relativistic fermions can be described as a function ψ using the Dirac equation:

$$i\hbar\gamma^\mu\partial_\mu\psi - mc\psi = 0 \tag{2.1}$$

with γ_μ respecting $\{\gamma^\mu, \gamma^\nu\} = 2g^{\mu\nu}$ ($g^{\mu\nu}$ being the Minkowski metric), and $\gamma^0\gamma^{\mu+}\gamma^0 = \gamma^\mu$ (for momentum conservation). This equation is built from the Schrödinger equation and compatibility with the Klein-Gordon equation leads to the presence of the γ matrices. One of the simplest representation of the γ matrices is the Dirac representation in equation 2.2 using Paul matrices (σ^i) [90].

$$\gamma^0 = \begin{pmatrix} 1 & 0 \\ 0 & -1 \end{pmatrix}, \gamma^i = \begin{pmatrix} 0 & \sigma^i \\ -\sigma^i & 0 \end{pmatrix} \tag{2.2}$$

ψ solution of equation 2.1 is a four-elements vector called bi-spinor or Dirac spinor. The γ matrices are the reason why this four-element column does not behave as a four-momentum vector: for a particle at rest ($\iff$ $(\gamma^\mu) = \gamma^0$), γ^0 in equation 2.2 implies necessarily that the solution of the Dirac equation will be two plane waves propagating with opposite sign energy[1]. This leads to the interpretation of bi-spinor as particle and antiparticle solutions [90].

The Lagrangian density derived from the Dirac equation is given by varying the action and can be written as:

$$\mathcal{L} = i\hbar\overline{\psi}\gamma^\mu\partial_\mu\psi - mc\overline{\psi}\psi \tag{2.3}$$

Standard Model is then generating gauge field by looking at global symmetry of this Lagrangian.

For instance, the *global phase transformation* ($\psi(x) \to e^{i\theta}\psi(x)$, U(1)) is not modifying equation 2.3. However, applying a *local transformation* ($\theta \to \theta(x)$) does not let the Lagrangian invariant. The power of Gauge theory is to demand the Lagrangian to be invariant under global and local transformation. Through a complex process, described in [90], demanding this invariance under local transformation leads to add a new field (A_μ, latter recognized as the electrostatic potential) for absorbing the modification induce by the local phase transformation. This local invariance transforms equation 2.1 into:

$$\mathcal{L} = [ic\hbar\overline{\psi}\gamma^\mu\partial_\mu\psi - mc^2\overline{\psi}\psi] - \frac{F^{\mu\nu}F_{\mu\nu}}{16\pi} - (q\overline{\psi}\gamma^\mu\psi)A^\mu \tag{2.4}$$

Besides, the Noether's theorem implies that this symmetry is due to conservation of a current j^μ: $\partial_\mu j^\mu = 0$. This consideration and equation 2.4 lead to conservation of the electromagnetic current, meaning $j_\mu = q\overline{\psi}\gamma^\mu\psi$, and of the electromagnetic charge (q) as well as the classical electrodynamics (two of the Maxwell equation can be derived from the last terms of 2.4). Every interaction is then defined by the "gauge invariance" applied to the Lagrangian, extending it from global to local, generating gauge field.

A lot of efforts were invested between 1961 and 1967 on the unification of electromagnetism and weak force by theoreticians. Among them S. Glashow, A. Salam and S. Weinberg developed what is now known as the electroweak interaction. After spontaneous symmetry breaking of the electroweak interaction and Higgs mass acquisition, 4 bosons were induced: $W^\pm$, Z^0 and γ. The final Lagrangian density of the Standard Model is then describing the electroweak interaction (SU(2)×U(1)) and the strong force (SU(3)).

2.1.2 Neutrino nature

Neutrinos are produced through weak processes. This interaction only plays with left-handed (/ right-handed) ν_l(/$\overline{\nu_l}$), breaking the parity (see section 1.1.3). Chirality (left or right handedness) is an intrinsic property of the particle defined for Dirac fermions through the operator γ^5. The weak interaction acts as a left-handed projector for particle: $P_L = \frac{1+\gamma^5}{2}$ ($P_R = \frac{1+\gamma^5}{2}$ for antiparticle) [22].

Helicity is a much easier concept to understand: it is the projection of the particle spin on its momentum direction. Consequently, its value is either +1/2 or -1/2. Unlike chirality, helicity is not an intrinsic property of massive particle as the momentum direction will depend upon observatory

---

[1]Eqn 2.1 becomes $i\hbar\gamma^0\frac{\partial}{\partial t}\psi = mc\psi \to \begin{cases} \psi_{\text{up}}(t) = e^{-imc^2t/\hbar}\psi_{\text{up}}(0) \\ \psi_{\text{down}}(t) = e^{+imc^2t/\hbar}\psi_{\text{down}}(0) \end{cases}$

frame. One can always think of a frame going faster than the particle in which the momentum is reversed, switching the helicity value. For massless particle travelling at light speed, this operation is not possible and helicity is therefore the same as chirality.

When neutrino is produced, it is left-handed with a mixture of two helicity ($\pm 1/2$) but with very different ratio. In the laboratory frame, the main component for ν_l is -1/2. +1/2 is suppressed proportionally to m(ν_l)/E$_\nu$ [81], hence the parity violation observation done by C.S.Wu [91] and the neutrino helicity measurement done by the Goldhaber experiment [23].

Besides, all Standard Model interactions preserve so far the lepton number (L=L$_e$+L$_\mu$+L$_\tau$ is conserved). It is assumed to be an accidental and not fundamental global symmetry of the Standard Model [92]. Experiment about checking the exact conservation of lepton flavour (L$_e$,L$_\mu$, L$_\tau$ individually) are discussed below.

2.1.3 Interaction with matter

Weak interaction can be described by the use of two conserved currents:

$$j_W^\mu = -\frac{ig_W}{2\sqrt{2}}\overline{u}\gamma^\mu(1-\gamma^5)u \tag{2.5}$$

$$j_Z^\mu = \overline{u_l}\gamma^\mu(g_V^l - g_A^l\gamma^5)u_l \tag{2.6}$$

with $\gamma^5 \equiv i\gamma^0\gamma^1\gamma^2\gamma^3$. Equation 2.5 describes the exchange of a charged boson (W$^\pm$)(Charge Current, (CC)) while Equation 2.6 describes the exchange of a Z^0 (Neutral Current, (NC)).

The weak interaction is weak at low energy because the cross section depending on the neutrino momentum squared is:

$$\frac{d\sigma}{dq^2} \propto \frac{1}{(q^2-M^2)^2} \tag{2.7}$$

with M mass of exchange particle. Z and W being massive, the probability of "spontaneously" creating such a particle is low ($\Delta E\Delta t > \hbar/2$).

2.1.3.1 Neutrino-Electron Scattering

Neutrino can interact with electron using Neutral Current (NC) or Charged Current (CC). The interaction will be called elastic scattering (ES) if the leaving and entering particles are the same and Quasi-Elastic Scattering (QES) if a lepton is produced during the process.

Elastic Scattering: $\nu + e^- \rightarrow \nu + e^-$

Neutrino can interact with charged leptons (l) via elastic scattering: $\nu + l \rightarrow \nu + l$. This process does not have any energy threshold, elastic scattering being a redistribution of the total interacting momentum. The charged leptons composing matter being electron, ES on electrons is one of the main channel to observe nuclear or solar neutrino. If ν_μ and ν_τ undergo ES with e$^-$ via neutral current (see figure 2.1a), ν_e can interact as well with charged current, as illustrated in figure 2.1b. This additional possibility of interaction of with matter induces a substantial higher cross section for MeV ν_e with respect to other flavour and is a crucial point for the MSW effect discussed in section 2.3.2.

(a) *Elastic Scattering via (NC),*

(b) *Elastic Scattering via (CC),*
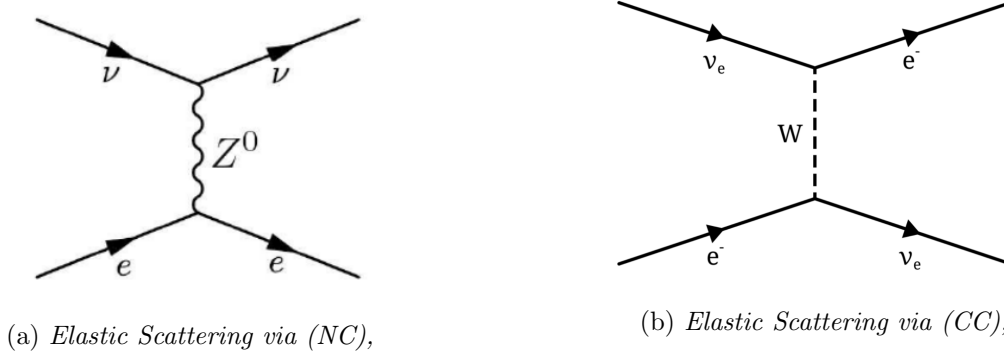
Figure 2.1: *Neutrino-Electron scattering via neutral current (NC) and charged current (CC).*

Assuming E_ν large with respect to m_e, the cross section can be written as [14]:

$$\sigma(E\nu) \approx 2G_F^2 m_e \frac{E_\nu}{\pi}(g_1^2 + \frac{g_2^2}{3})$$ (2.8)

with g_1 and g_2 depending on the Weinberg angle and the nature of the neutrino; their values are listed in table 2.3.

(g1,g2)	e	μ	τ
ν	(0.73,0.23)	(-0.27,0.23)	(-0.27,0.23)
$\overline{\nu}$	(0.23,0.73)	(0.23,-0.27)	(0.23,-0.27)

Table 2.3: *Value of the g-factor depending on characteristics of the neutrino.*

The ratio between total cross section of $\nu_l + e^- \rightarrow \nu_l + e^-$ is then:

$$\sigma_{\nu_e} : \sigma_{\overline{\nu_e}} : \sigma_{\mu,\tau} : \sigma_{\overline{\mu,\tau}} = 1 : 0.42 : 0.16 : 0.14$$ (2.9)

with σ_{ν_e} being on the order of 9.5×10^{-45} cm^{2}E$_\nu$/MeV for E$_\nu \gg 511$ keV.

Quasi-Elastic Scattering: $\nu + e^- \rightarrow \nu + l$
Neutrino can also interact via QES using CC: $\nu_{l'} + l \rightarrow \nu_l + l'$. Figure 2.1a is giving the elastic scattering interactions while Figure 2.1b using CC is called quasi-elastic because of the momentum and charge exchange in the process. For the $\nu_e + e \rightarrow \nu_e + e$ interaction it is not possible a priori to disentangle CC and NC interaction. One important effect is that ν_μ/ν_τ are not able to interact through CC with electrons except if bringing enough kinetic energy to create μ/τ (respectively 106 MeV and 1.8 GeV). This leads to total suppression of this channel for those flavours in the MeV scale.

2.1.3.2 Neutrino-Nucleon Scattering

Neutrino can interact with nucleons via QES and ES reactions but also Nuclear Resonance Production and Deep-Inelastic Scattering (DIS). Figure 2.3 is illustrating the importance of each process depending on the neutrino energy for charge-current interaction.
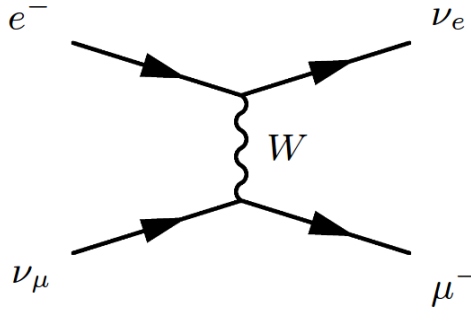
Figure 2.2: *Inverse muon decay, CC-QES.*
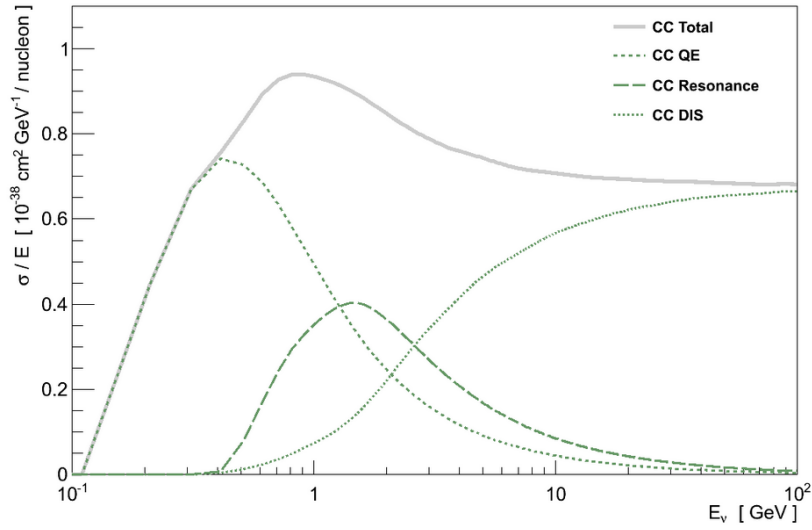
Figure 2.3: *Cross section of Neutrino-nucleus CC interaction [93].*

Working at low energy ($E_\nu \sim 1 MeV$), only ES and QES can be observed. Especially, below 50 MeV, the neutrino can excite coherently the nucleus itself. This is called the Coherent neutrino-nucleus elastic scattering. Resonance production and DIS are beyond the scope of this thesis and will not be discussed.

Elastic Scattering   The Neutral Current can happen with a nucleon or a nucleus. At low energy (< 50 MeV), the Coherent Neutrino-Nucleus Scattering (CNNS) $\nu + A \to \nu + A$ is dominant over neutrino-nucleon scattering. However this signal is very hard to see as the recoil of the nucleus is very small. It is considered as an irreducible background for WIMP search for now but some experiments aim at observing this interaction (COHERENT [94], RICOCHET [95]). It is target dependent but for illustration, the cross section on Germanium is expected around 3.82×10^{-42} cm^2 [95]. At the time of writing this manuscript, the COHERENT experiment announces the first observation of coherent scattering [96].

The NC elastic scattering on nucleons, as for electrons, is letting the nuclei intact and is just an exchange of momentum: $\nu + N \to \nu + N$ (N being a proton or a neutron). Typically, the cross section on free nucleon is $\sigma_{\nu n \to \nu n} \approx 9.3 \times 10^{-48}$ m$^2(\frac{E_\nu}{MeV})^2$ and $\sigma_{\nu p \to \nu p} \approx 6.0 \times 10^{-50}$ m$^2(\frac{E}{MeV})^2$ [97].

Quasi-Elastic Scattering Quasi-Elastic charged-current reactions consists of induced neutron and inverse beta decay written in equations 2.10 and 2.11 respectively.

$$\nu_l + n \rightarrow p + l^- \tag{2.10}$$

$$\overline{\nu_l} + p \rightarrow n + l^+ \tag{2.11}$$

Both reactions demand the creation of a lepton therefore have a threshold depending on the nuclei environment. For illustration, assuming a $\overline{\nu_e}$, the inverse beta decay threshold on free protons is 1.81 MeV, while induced neutron decay thresholds on ^{37}Cl and ^{71}Ga are 0.82 MeV and 0.23 MeV respectively. This interaction is dominant over NC ES for ν_e and ν_μ below 1 GeV [93].

2.2 The neutrino mass

The neutrino mass is still an open question of modern physics. Mechanism of mass generation as well as the absolute mass of the neutrinos are under investigation. The Standard Model does not predict any mass neither oscillation properties of the neutrino. The intriguing theoretical question is precisely: *why are they so light*? It is not the scope of this thesis to answer this question. Many experiments are aiming and might in the next decade, measure the absolute mass of the neutrino as well as highlight existence or not of a sterile state, fuelling the understanding of the fundamental nature of neutrino. This is only an introduction to the theoretical framework.

2.2.1 Mass generation in SM

Weinberg and Salam introduced the electroweak unification using the quantum fields theory of gauge fields. Coupling the weak charge of SU(2) and U(1), the four bosons induced are massless as enforce by chirality [98]. However in nature only the photon is a massless gauge field, the weak force being a short range interaction due to the high mass of the Z and W bosons. In order to generate mass of those bosons, it is needed to break the SU(2)xU(1) symmetry. To do so, the Higgs mechanism was proposed [99, 100] introducing a new scalar field ϕ such as:

$$\phi = \begin{pmatrix} \phi^+ \\ \phi^0 \end{pmatrix} \tag{2.12}$$

with ϕ^+ a charged complex scalar field and ϕ^0 a neutral scalar field. Applying the SU(2)xU(1) gauge transformation to this scalar field, a Higgs part is derived in the Lagrangian:

$$\mathcal{L}_{\text{Higgs}} = (D_\mu \phi)^\dagger (D^\mu \phi) - V(\phi) \qquad \text{with} \qquad V(\phi) = \lambda(\phi^\dagger \phi - \frac{v^2}{2})^2 \tag{2.13}$$

From equation 2.13 one can see that the minimum of the potential (which can be called the vacuum) is not null: $\phi^\dagger \phi = \frac{v^2}{2}$. This non-zero value of the vacuum expectation has to come from the neutral part of the Higgs field (ϕ^0) in order to conserve vacuum electrical neutrality. The Higgs field is then:

$$< \phi >= \frac{1}{\sqrt{2}} \begin{pmatrix} 0 \\ v \end{pmatrix} \tag{2.14}$$

This field is invariant under U(1) transformations, guaranteeing the existence of a massless gauge boson associated with the photon but coupling the Z and the W inducing their mass: $m_W = \frac{g\,v}{2}$ and

$m_Z = \frac{g\,v}{2cos(\theta_W)}$ as well as the Higgs mass itself: $m_H = \sqrt{2\lambda v^2}$. The first observation and the mass measurement of the Higgs bosons ($m_H = 125 \pm 0.4$ GeV [81]) recently at CERN by the Atlas [101] and CMS [102] collaboration is a great achievement for the Standard Model and for experimentalists.

Fermions are described by the Dirac equation as explained in section 2.1.1. The field solution of the Dirac equation are the so called Dirac spinor, bi-spinor or chiral fermion fields composed of two fields: $\psi = \psi_L + \psi_R$. This is the smallest irreducible representation of the Lorentz group [14]. The Dirac equation can then be rewritten as:

$$i\gamma^\mu \partial_\mu \psi_{L/R} = m\psi_{R/L} \tag{2.15}$$

One can already notices that equation 2.15 involves simultaneously ψ_R and ψ_L with the mass m. The fermions masses generation is then a consequence of Yukawa coupling with the Higgs doublet:

$$\mathcal{L}_H = -(\frac{v+H}{\sqrt{2}})\overline{l_L}Y^l l_R \tag{2.16}$$

with Y^l the Yukawa coupling matrix, l_R and l_L the charged lepton fields right and left-handed. Presence of left and right handed part of the Dirac spinor is a demand of the gauge transformation (one can already see it in equation 2.15). The mass of the fermions is then: $m_\alpha = \frac{y_\alpha^l v}{\sqrt{2}}$ with v the Higgs vacuum expectation value and y_α^l the Yukawa matrix elements. Those matrix elements can not be predicted by the Standard Model but can be derived from mass measurements.

The mechanism generating mass for the neutrino is still not understood. It is highly depending on the neutrino nature. For now, two main interpretation coexist in theory: Dirac and Majorana.

2.2.2 Dirac mass

The most intuitive idea to explain neutrino mass is to extend the already existing Higgs mechanism to the Dirac neutrino. The simplest way of doing it is to introduce a right-handed component to the neutrino field, generating a mass term in the Lagrangian with the same form as equation 2.16:

$$\mathcal{L}_H = -(\frac{v+H}{\sqrt{2}})[\overline{l_L}Y^l l_R + \overline{\nu_L}Y^\nu \nu_R] \tag{2.17}$$

The mass term is then given as $m_k = \frac{y_k^\nu v}{\sqrt{2}}$ with the y_α^l the Yukawa coupling matrix elements. It is a complete mystery why this coupling is so small for neutrinos with respect to leptons and quarks. It is one of the reason for the introduction of the see-saw theory explained below. Besides, explaining the neutrino mass using Higgs mechanism forces to introduce right-handed neutrinos, never observed in nature. Such neutrinos would not be interacting via weak interaction and would be only sensible to gravitation, they are therefore called *sterile*. The number of sterile right-handed neutrino fields is not constrained by the theory. In the minimally extended Standard Model, three sterile neutrinos are coupled with three active neutrino to generate the mass term described above.

2.2.3 Majorana mass

E. Majorana in 1937 [103] realises that ψ_L and ψ_R may not be independent and may be related by: $\psi_R = \xi C(\psi_L)^T$ with ξ an arbitrary phase. Using this mix between left and right handed part, one can rephrase 2.15 as:

$$i\gamma^\mu \partial_\mu \psi_L = m\mathcal{C}\overline{\psi_L}^T \tag{2.18}$$

leading to the Majorana condition: $\psi = \psi^C$ meaning that particle and antiparticle must be the same. A direct consequence of such condition is that only neutral particle can be described by Majorana fields. Using this condition, neutrino can be described by only two independent components [14]. The Majorana mass term can then be derived in the same mechanism than Dirac one but using $\overline{\nu_L^C}$ as the right-handed field. The mass term is then:

$$\mathcal{L}_m = -\frac{1}{2}m(\overline{\nu_L^C}\nu_L + \overline{\nu_L}\nu_L^C) \tag{2.19}$$

If the Majorana theory for the neutrino can be seen as more elegant, it has non trivial consequences. One of them is that the Majorana neutrino field is no more invariant under global U(1) gauge transformation, leading to breaking the lepton number conservation.

Revealing the nature of the neutrino is the reason of huge effort in scientific community. Experiments (SuperNEMO, CUORE, GERDA, KamLand-Zen) are trying to observe $\beta\beta0\nu$ process to prove that neutrinos are Majorana fields. Only limits on the reaction rate depending on the nuclei have been settled so far and the Majorana/Dirac problem remains unsolved.

2.2.4 The see-saw mechanism

The see-saw mechanism aims at explaining the so small mass of the active neutrinos ν_L. If we suppose that neutrinos are Dirac fermion fields, it must exist a right-handed neutrino N_R. The symmetry and gauge invariance allows to think of adding a Majorana mass term (M) associated with N_R. This woud be forbidden for ν_L because it would break isospin conservation. We can write the mass matrix $\mathcal{M}$ such that:

$$\mathcal{L}_{\text{mass}} = -\frac{1}{2}M\overline{N_R}N_L^C - m\overline{N_R}\nu_L \tag{2.20}$$

knowing that $N_L^C = \overline{\nu_L}$, equation 2.20 can be written:

$$\mathcal{L}_{\text{mass}} = -\frac{1}{2}(\overline{\nu_R^C}\ \overline{N_R})\mathcal{M}\begin{pmatrix}\nu_L\\N_L^C\end{pmatrix} \qquad \text{with} \qquad \mathcal{M} = \begin{pmatrix}0 & m\\m & M\end{pmatrix} \qquad \text{and} \tag{2.21}$$

with a Dirac mass, m, and M the Majorana mass. The matrix 2.21 has to be diagonalised in order to access to the effective mass: $m_{\text{eff}} = \frac{1}{2}(M \pm \sqrt{M^2 + 4m^2})$. If now we decide $M \gg m$, we have two very different effective masses:

$$m_{\text{heavy}} \sim M \qquad \text{and} \qquad m_{\text{light}} \sim \frac{m^2}{M} \tag{2.22}$$

This model enables to think that neutrinos are not peculiar in the standard model, their mass scale would be in the same order of magnitude than leptons or quarks, depending on M. In this model, a 0.1 eV active neutrino would be coupled to a ~ 2.6 TeV right-handed neutrino. This effect will be discussed further when introducing sterile neutrinos in section 2.4.2.

2.2.5 Mass measurements

2.2.5.1 Hierarchy

Oscillation measurements (see section 2.3.1.2) are sensitive to squared mass difference between mass eigenstates (Δm^2). Oscillation measurements is one way to evaluate Δm^2 depending on the

mixing angles. Figure 2.4 is showing the sensitivity plot of the mass measurement in a global joined oscillation analysis [104].

(a) Δm_{3l} is Δm_{32} in case of Inverted hierarchy and Δm_{32}^2 in case of Normal hierarchy.

(b) Δm_{21}^2
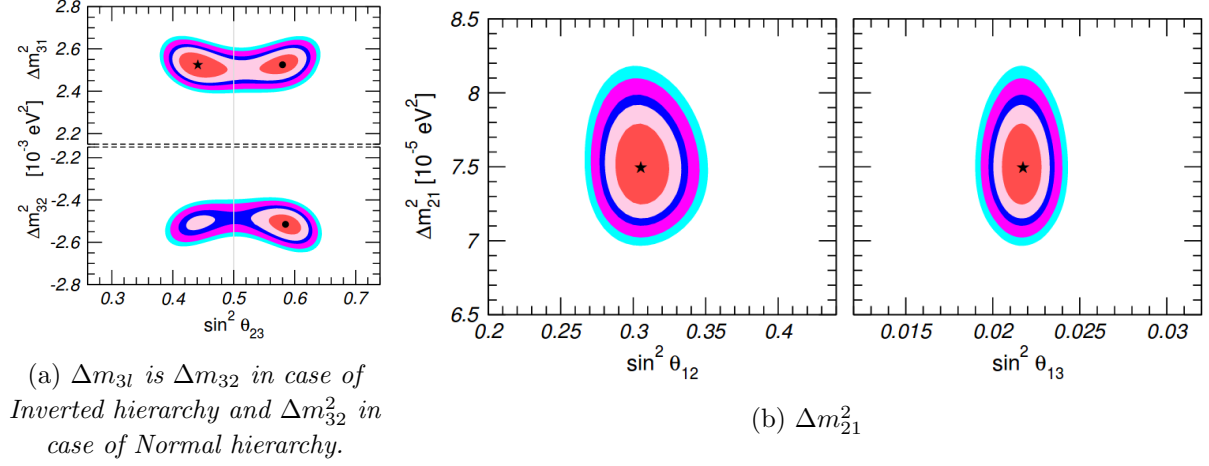
Figure 2.4: *Sensitivity plot of the Δm^2 measurement extracted from a global analysis [104].*

The so called mass hierarchy problem stems from the incapacity of knowing mass eigenstates ordering only from Δm^2. From solar sector, we know that $\Delta m_{3j}^2 \gg \Delta m_{21}^2$. Figure 2.5 is summarizing the two left possibilities concerning mass ordering: Normal (two lights and one "heavy") or the Inverted (two heavy and one light) mass hierarchy. One can see that determining the hierarchy and measuring the absolute scale of the neutrino masses are two different questions. Indifferently of the
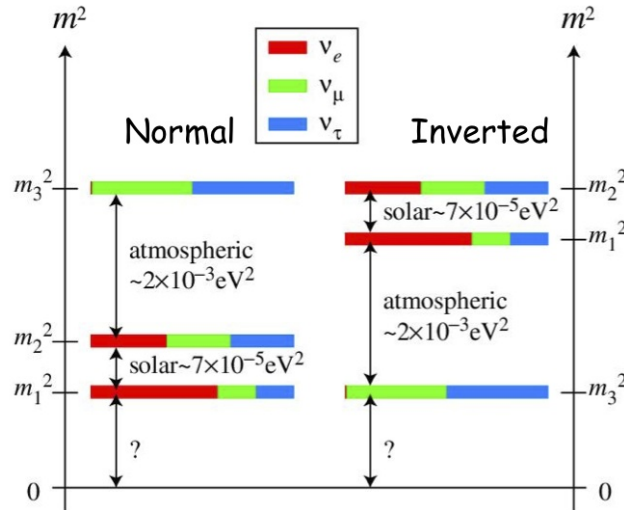
Figure 2.5: *Neutrino mass eigenstates distribution in the case of normal and inverted hierarchy as well as flavour composition.*

hierarchy, from figure 2.4 it is clear that at least one neutrino is heavier than 2.5×10^{-3} eV, hence the considerable effort to reach such sensitivity.
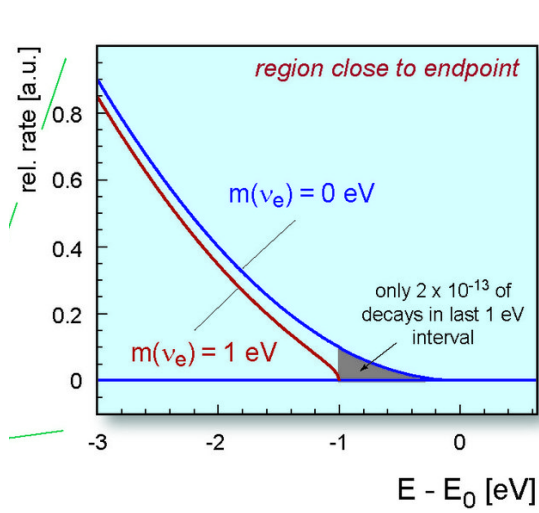
(a) β spectrum comparison for $m_\nu = 1$ eV. Credit to KATRIN collaboration.
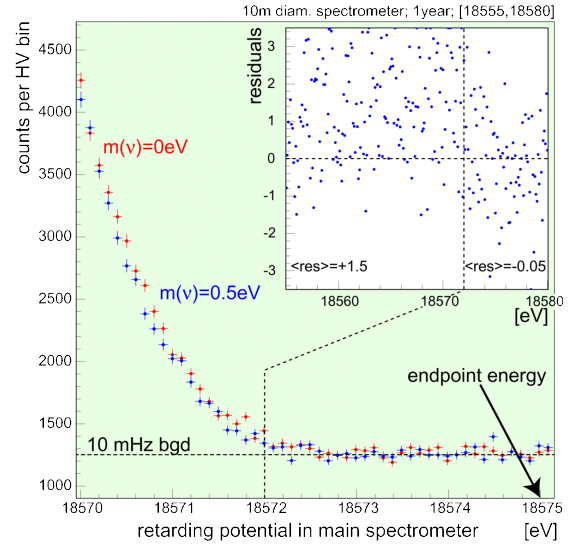
(b) β spectrum comparison for $m_\nu = 1$ eV. Credit to KATRIN collaboration.

2.2.5.2 Absolute mass measurement

β **measurement** Since the work done by C. Ellis and W.A.Wooster [10], L. Meitner and W. Orthmann [11], in 1927, the β spectrum measurement has been carefully and extensively studied. In particular, observing the end point of the spectrum gives a limit of m_{ν_e}. Indeed, the Q_β being shared by the electron and the neutrino, in the rare case where electron is taking all the kinetic energy, the difference between the available and the electron energy is the neutrino mass as illustrated in Figure 2.6a. The concern of such research is then to obtain the most precise β tail spectrum. As discussed, $\overline{\nu_e}$ is not a mass eigenstate. $m_{\overline{\nu_e}}$ is indeed designing the $\overline{\nu_e}$ effective mass, $m_{\overline{\nu_e}} = \sum_k |U_{ek}|^2 m_k^2$.

The most precise ground experiments constraining the absolute mass of the neutrinos are using electrostatic spectrometer. In such devices, the β emitter used is tritium (^{3}H). The choice of tritium is a consequence of its long half-life time ($\sim$ 12.3 y.) guaranteeing stability of the measurement during the experiment and its low energy Q_β (18.6 keV) enabling to use electrostatic spectrometer [105]. Such source must be produced with high specific activity to avoid any layer effect on the β emission and finally, the super-allowed transition of ^{3}H$\rightarrow^3$He enables precise derivations (low nuclear effects). This leads to the most stringent upper limit on $\overline{\nu_e}$ mass by the Troitzk collaboration [81, 105] :

$$m_{\overline{\nu_e}} < 2.05 \text{ eV.c}^{-2} \qquad (95\% \text{ Confidence Level})$$

and the Mainz collaboration [106]:

$$m_{\overline{\nu_e}} < 2.3 \text{ eV.c}^{-2} \qquad (95\% \text{ C.L.})$$

The KATRIN experiment is the next generation of detector based upon the same principles. It is running, and the expecting sensitivity after three years of experiment is 0.2 eV.c^{-2} [107]. Figure 2.6b is showing a simulation of the expected signal from the KATRIN experiment.

To increase the sensitivity of KATRIN by one order of magnitude would demand a 300 m diameter spectrometer [108], which is not realistic. To challenge the limit settled by cosmology,

other techniques have to be developed. New angle has been found using electron spectroscopy via relativistic cyclotron radiation in Project8 [109].

Cosmological constraints In parallel to ground experiment, constraints can be derived from Cosmic Microwave Background measurements. The WMAP and the Planck collaboration gave an upper limit on the sum of the three mass eigenstates in the ΛCDM model: $\sum_i m_i < 0.66eV$. Adding the data from the Baryon Acoustic Oscillations [110], the upper limit is then:

$$\sum_i m_i < 0.23eV \qquad (95\% \text{ C.L.}) \tag{2.23}$$

This limit can even be improved by adding Lyman-α forest constrained on structure formation [111]:

$$\sum_i m_i < 0.12eV \qquad (95\% \text{ C.L.}) \tag{2.24}$$

2.3 Neutrinos oscillations

2.3.1 Neutrino oscillation in vacuum

From the Super-Kamiokande observation of atmospheric neutrino oscillation and SNO observation of solar neutrino mixing flavour, it is clear that neutrinos oscillate in flavour during propagation. In order to get the time evolution of the quantum state $|\nu_\alpha\rangle$, the Evolution operator is used in the Schrödinger equation:

$$H |\psi(t)\rangle = i\hbar \frac{\partial}{\partial t} |\psi(t)\rangle \tag{2.25}$$

If H is independent on time, one can write the solution as a plane wave:

$$|\psi(t)\rangle = e^{-iHt/\hbar} |\psi(0)\rangle \tag{2.26}$$

This is a great simplification as real particles can not be rigorously described as plane wave but should be described by localized wave packet. However this allows us to well-described oscillation phenomenon. Extensive descriptions and derivations in the wave packet formalism can be found in [14]. Using 2.26 in 2.25 leads to $H |\alpha\rangle = E_\alpha |\alpha\rangle$ with E_α the energy of the particle α if $|\alpha\rangle$ is an eigenstate of the Hamiltonian. As we know that flavours are evolving with time, flavour eigenstate can not be an eigenstate of the Hamiltonian. Hence the idea to rewrite flavour states in the Hamiltonian eigenstate basis.

2.3.1.1 Mixing convention

The vacuum mixing is the hypothesis that flavour states do not coincide with mass eigenstates. One can write any flavour eigenstate as a linear combination of mass eigenstates and vice versa. The unitary 3x3 complex matrix parametrizing this mixing is the $\text{U}_{\text{P-MNS}}$ matrix called after Pontecorvo, Maki, Nakagawa and Sakata.

$$\begin{pmatrix} \nu_e \\ \nu_\mu \\ \nu_\tau \end{pmatrix} = \text{U}_{\text{P-MNS}} \begin{pmatrix} \nu_1 \\ \nu_2 \\ \nu_3 \end{pmatrix} \tag{2.27}$$

This matrix can be parametrized by 3 independent angles and one phase δ_{CP} (allowing CP violation in the leptonic sector). The convention is to decompose the P-MNS matrix in 3 rotation matrices (for the three sectors at which angles were measured) and a complex phase, called the CP phase .

$$U_{P-MNS} = \begin{bmatrix} 1 & 0 & 0 \\ 0 & c_{23} & s_{23} \\ 0 & -s_{23} & c_{23} \end{bmatrix} \begin{bmatrix} c_{13} & 0 & s_{13}e^{-i\delta} \\ 0 & 1 & 0 \\ -s_{13}e^{i\delta} & 0 & c_{13} \end{bmatrix} \begin{bmatrix} c_{12} & s_{12} & 0 \\ -s_{12} & c_{12} & 0 \\ 0 & 0 & 1 \end{bmatrix} \tag{2.28}$$

with c_{ij} standing for $\cos(\theta_{\text{ij}})$ and s_{ij} standing for $\sin(\theta_{\text{ij}})$. θ_{23}, θ_{12} and θ_{13} are respectively identified to the atmospheric, the solar and the reactor sectors. Using the P-MNS matrix ($U_{\alpha,i}$), one can write each flavour eigenstate ($\alpha \in [e, \mu, \tau]$) on the mass eigenstates basis ($i \in [1, 2, 3]$):

$$|\nu_\alpha\rangle = \sum_i U_{\alpha,i} |\nu_i\rangle \qquad\qquad |\nu_i\rangle = \sum_\alpha U_{i,\alpha}^* |\nu_\alpha\rangle \tag{2.29}$$

2.3.1.2 Oscillation probability

By construction, we know that $(|\nu_i\rangle)_i$ is an orthogonal basis of mass eigenstates, meaning that:

$$H |\nu_i\rangle = E_i |\nu_i\rangle \tag{2.30}$$

with $E_i^2 = p_i^2 + m_i^2$. However weak processes are producing weak eigenstate: flavour. In order to get the time evolution of the quantum state $|\nu_\alpha\rangle$ one has to propagate each mass eigenstates using equations 2.25 and 2.29:

$$|\nu_i(t)\rangle = e^{-iE_i t} |\nu_i\rangle \qquad \Rightarrow \qquad |\nu_\alpha(t)\rangle = \sum_i U_{\alpha,i} e^{-iE_i t} |\nu_i\rangle \tag{2.31}$$

and in the flavour basis:

$$|\nu_\alpha(t)\rangle = \sum_i (U_{\alpha,i} e^{-iE_i t} \sum_\beta U_{\beta,i}^* |\nu_\beta\rangle) \tag{2.32}$$

$P_\alpha(t)$ the survival probability of a flavour α as being $P_\alpha(t) = |\langle\nu_\alpha(t)|\nu_\alpha\rangle|^2$ and $P_{\alpha\rightarrow\beta}(t)$ the probability of oscillation from α to β as $P_{\alpha\rightarrow\beta}(t) = |\langle\nu_\alpha(t)|\nu_\beta\rangle|^2$. Knowing that $\langle\alpha|\beta\rangle = \delta_{\alpha,\beta}$ (the flavour states are orthogonal):

$$\langle\nu_\beta|\nu_\alpha(t)\rangle = \sum_i U_{\alpha,i} e^{-iE_i t} U_{\beta,i}^* \tag{2.33}$$

leading to:

$$P_{\alpha\rightarrow\beta}(t) = \sum_i (U_{\alpha,i} e^{-iE_i t} U_{\beta,i}^*) \sum_j (U_{\beta,j}^* e^{iE_j t} U_{\alpha,j}) = \sum_{i,j} (U_{\alpha,i} U_{\beta,i}^* U_{\beta,j}^* U_{\alpha,j} e^{i(E_j - E_i)t}) \tag{2.34}$$

Considering $E_i = \sqrt{p_i^2 + m_i^2}$ and for relativistic neutrinos $E_i \sim p_i$. Taylor expanding $E_i \simeq p(1 + \frac{1}{2}\frac{m_i^2}{p^2}) = E_i + \frac{m_i^2}{2E_i}$. Consequently, $(E_j - E_i) \simeq \frac{m_j^2 - m_i^2}{2E} = \frac{\Delta m_{ji}^2}{2E}$.
Besides, assuming neutrino is ultra-relativistic, one can replace the time (t) by the distance (L) with convention $c = \hbar = 1$. Finally, for clarity of the expression, we will call $A_{i,j}^{\alpha,\beta} = U_{\alpha,i} U_{\beta,i}^* U_{\beta,j}^* U_{\alpha,j}$. These transformations lead to:

$$P_{\alpha\rightarrow\beta}(t) = \sum_{i,j} (A_{i,j}^{\alpha,\beta} e^{-i\frac{\Delta m_{ij}^2 L}{2E}}) \tag{2.35}$$

One phase of the oscillation is depending on L/2E; hence the varying baseline experiments looking for energy spectrum for measuring oscillation angle. Developing the expression 2.35 (see [14]):

$$P_{\alpha\rightarrow\beta}(t) = \delta_{\alpha,\beta} - 4\sum_{i>j}(\text{Re}[A_{i,j}^{\alpha,\beta}]\sin^2(\frac{\Delta m_{ij}^2 L}{4E})) + 2\sum_{i>j}(\text{Im}[A_{i,j}^{\alpha,\beta}]\sin(\frac{\Delta m_{ij}^2 L}{2E})) \qquad (2.36)$$

Figure 2.7 is the oscillation evolution of an electronic neutrino depending on L/E.
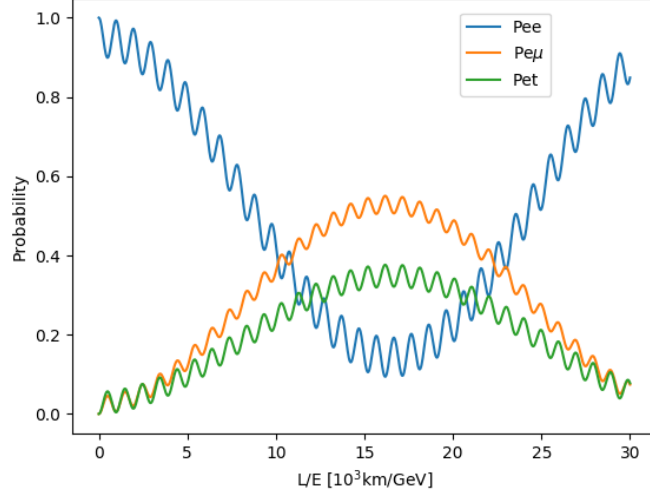
Figure 2.7: *Oscillation pattern for a ν_e with L/E using equation 2.36 with $(\theta_{12}, \theta_{23}, \theta_{13}, \delta_{CP})$=(33.36°, 41.6°, 8.46°, 270) and $(\Delta m_{21}^2, \Delta m_{31}^2 \sim \Delta m_{32}^2)$=(7.5 × 10⁻⁵eV², 2.5 × 10⁻³eV²).*

Similarly for antineutrinos with $\widetilde{A}_{i,j}^{\alpha,\beta} = U_{\alpha,i}^* U_{\beta,i} U_{\beta,j} U_{\alpha,j}^*$:

$$P_{\overline{\alpha}\rightarrow\overline{\beta}}(t) = \delta_{\alpha,\beta} - 4\sum_{i>j}(\text{Re}[\widetilde{A}_{i,j}^{\alpha,\beta}]\sin^2(\frac{\Delta m_{ij}^2 L}{4E})) - 2\sum_{i>j}(\text{Im}[\widetilde{A}_{i,j}^{\alpha,\beta}]\sin(\frac{\Delta m_{ij}^2 L}{2E})) \qquad (2.37)$$

These formulae enable physicists to think about test of symmetry, namely CP and CPT. It is clear that the Time reversal symmetry is simply switching back the two flavours: $P_{\alpha\rightarrow\beta} \xrightarrow{T} P_{\beta\rightarrow\alpha}$ while CP symmetry is: $P_{\alpha\rightarrow\beta} \xrightarrow{CP} P_{\overline{\alpha}\rightarrow\overline{\beta}}$ and CPT: $P_{\alpha\rightarrow\beta} \xrightarrow{CPT} P_{\overline{\beta}\rightarrow\overline{\alpha}}$. Symmetry CPT is widely believed to be conserved. However, CP breaking symmetry in the leptonic sector should lead to observation of non null $P_{\alpha\rightarrow\beta} - P_{\overline{\alpha}\rightarrow\overline{\beta}}$. Indeed, from equations 2.36 and 2.37:

$$P_{\alpha\rightarrow\beta} - P_{\overline{\alpha}\rightarrow\overline{\beta}} = 4\sum_{i>j}(\text{Im}[\widetilde{A}_{i,j}^{\alpha,\beta}]\sin(\frac{\Delta m_{ij}^2 L}{2E})) \qquad (2.38)$$

This is the reason why the imaginary part of the P-MNS matrix is called the CP phase. It is then a convention to put that weight on the smallest mixing angle: the reactor sector.

2.3.1.3   Two-flavours oscillation case

A common illustration is using a simplification of the process assuming only two flavours and two mass eigenstates. This is a valuable exercise as depending on the baseline, one oscillation is

dominant. Indeed, in two-flavour hypothesis, one can write:

$$\begin{pmatrix} \nu_\alpha \\ \nu_\beta \end{pmatrix} = \begin{pmatrix} \cos\theta & -\sin\theta \\ \sin\theta & \cos\theta \end{pmatrix} \begin{pmatrix} \nu_1 \\ \nu_2 \end{pmatrix} \tag{2.39}$$

leading to $|\nu_\alpha\rangle = \cos\theta\,|\nu_1\rangle + \sin\theta\,|\nu_2\rangle$. One can use the Schrödinger equation in the flavour eigenstates basis to introduce the Hamiltonian H_0:

$$i\frac{d}{dt}\begin{pmatrix} \nu_\alpha(t) \\ \nu_\beta(t) \end{pmatrix} = Ho\begin{pmatrix} \nu_\alpha(t) \\ \nu_\beta(t) \end{pmatrix} \qquad \text{with} \qquad H_0 = U\begin{pmatrix} E1 & 0 \\ 0 & E2 \end{pmatrix}U\dagger \tag{2.40}$$

Using formula derived in equation 2.35, for two flavours oscillation:

$$P_{\alpha\to\beta}^{\beta\neq\alpha}(t) = 4\sin^2(\theta)\sin^2(\theta)\sin^2(\frac{\Delta m_{ij}^2 L}{4E}) = \sin^2(2\theta)\sin^2(\frac{\Delta m_{ij}^2 L}{4E}) \tag{2.41}$$

$$P_{\alpha\to\alpha}(t) = 1 - P_{\alpha\to\beta,\beta\neq\alpha}(t) = 1 - \sin^2(2\theta)\sin^2(\frac{\Delta m_{ij}^2 L}{4E}) \tag{2.42}$$

2.3.2 Neutrino oscillation in matter

From sections 2.1.3 and 2.3.1 one can wonder if matter modify the oscillation in vacuum model. L. Wolfenstein did in 1978 and highlighted the effect of coherent forward scattering [112]. This "matter effect" due to neutrino interactions with electrons and nucleons of the medium can be divided in Neutral and Charged current. Due to their low energy (<20 MeV), only ν_e undergoes (CC).

2.3.2.1 The MSW effect

The effect can be modelled using two matter potentials on the Hamiltonian of the system depending on the exchange boson and on the target (electron, proton or neutron). If (NC) can happen with every fermions composing the matter, in fact the number of protons and electrons being the same, effects cancel each others [14]. The matter effect is then only (NC) on neutrons for every flavours and (CC) on electrons for $\overline{\nu_e}$ only. One can write it as:

$$V_{NC} = -\frac{1}{2}\sqrt{2}G_F n_n \qquad V_{CC} = \sqrt{2}G_F n_e \qquad \Rightarrow \qquad V_{\text{matter}}^\alpha = \delta_{\alpha,e}V_{CC} + V_{NC} \tag{2.43}$$

with n_n and n_e respectively the neutron and electron densities.

Potentials of equation 2.43 should be added to the Hamiltonian of equation 2.40. In presence of matter, H_0 becomes H_m following: $H_m = H_0 + V_{\text{matter}}^\alpha$. However the (NC) current is not modifying oscillation probability. Indeed, adding V_{NC} to H_m corresponds to add a global phase shift as the terms are symmetrical and diagonals [112]. The (CC) in an other hand is sensible to ν_e only, acting like a refractive index for ν_e. If the medium has a constant density, the matter effect consists in the replacement of the vacuum mass eigenstates (E_1 and E_2 in equation 2.40) by new matter mass eigenstates (E_1^m and E_2^m) and θ by θ_m. $P_{\alpha\to\beta}$ is then transformed in [92]:

$$P_{\alpha\to\beta}(t) = \sin^2(2\theta_m)\sin^2(\frac{(E_2^m - E_1^m)t}{2}) \tag{2.44}$$

$$\sin(2\theta_m) = \frac{\sin(2\theta)}{A(n_e)} \tag{2.45}$$

45

$$E_2^m - E_1^m = \frac{\Delta m^2}{2E} A(n_e) \tag{2.46}$$

with:

$$A(n_e) = \sqrt{\sin^2(2\theta) + \cos^2(2\theta)(1 - \frac{n_e}{n_\text{res}})^2} \quad \text{and} \quad n_\text{res} = \frac{\Delta m^2 \cos(2\theta)}{2\sqrt{2}G_\text{F}E} \tag{2.47}$$

The MSW (Mikhee-Smirnov-Wolfenstein) resonance is realised when $\sin(2\theta_m) = 1 \iff n_e = n_\text{res}$. This resonance effect can be described in three regimes [92]:

- low density ($n_e \ll n_\text{res} \Rightarrow A(n_e)$=1). $\sin(2\theta_m) = \sin(2\theta)$, similar to vacuum oscillation;

- resonance ($n_e = n_\text{res} \Rightarrow A(n_e) = \sin(2\theta)$). $\sin(2\theta_m) = 1$, oscillations are maximal.

- high density ($n_e \gg n_\text{res}$), $\sin(2\theta_m) < \sin(2\theta)$ oscillations are suppressed.

If neutrinos are produced in high density regime, θ_m is close to 90°meaning that $\nu_e = \cos(\theta_m)\nu_1 + \sin(\theta_m)\nu_2$ are produced in a quasi pure mass eigenstate ν_2. Considering the electronic density variation adiabatic, the neutrino will leave the medium in a pure vacuum eigenstate ν_2: $\nu_2 = \sin(\theta)\nu_e + \cos(\theta)\nu_m u$. It induces that if the vacuum mixing angle is small, $\cos(\theta) \sim 1$ and the oscillation $\nu_e \leftrightarrow \nu_\mu$ is maximal.

2.3.2.2 Consequences on Solar neutrinos

Solar neutrinos are produced in the solar core. Figure 2.8a shows the simulated radial distribution of *(pp-chain)* neutrinos production inside the Sun.
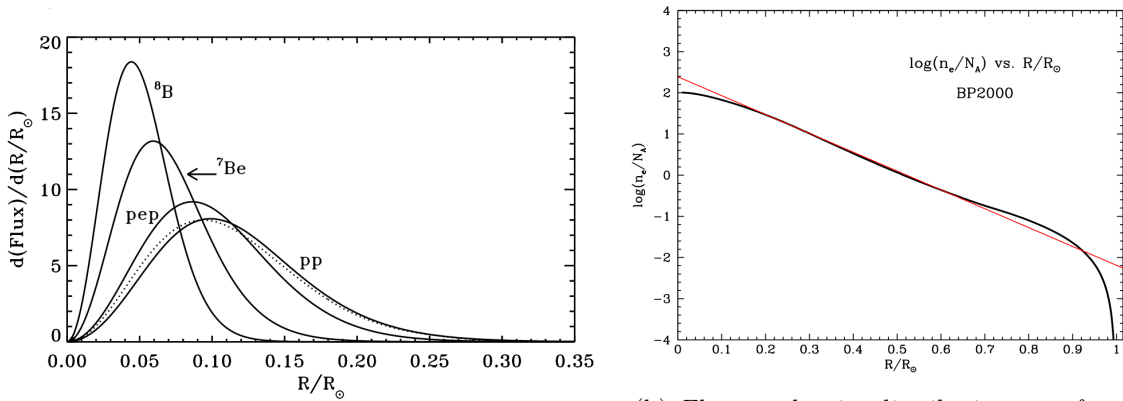
(a) *(pp)-chain $\overline{\nu}_e$ production distribution depending on their radial position inside the Sun. The integral of each contributor is normalized to one.*

(b) *Electron density distribution as a function of the Sun radius. Blakc curve is from BP00 [32] model computation while red line shows the approximation $n_e = 245e^{-10.54R/R\ominus}\mathcal{N}_\mathcal{A} \ cm^{-3}$.*

Figure 2.8: *Report of results of the BP00 [32] model simulation concerning the neutrinos matter effect.*

The MSW resonance effect can be observed if n_e at production site is higher than n_res. From [32], we have:

$$\frac{n_\text{res}}{\mathcal{N}_\mathcal{A}} = 66\cos(2\theta_{12})\frac{\Delta m_{12}^2}{10^{-4}\text{eV}}\frac{10 \text{ MeV}}{E} \tag{2.48}$$

with $\mathcal{N}_\mathcal{A}$ the Avogadro number. From figure 2.8b, the n_res is reached for a 10 MeV neutrino already at r~0.5 R_θ. Figure 2.8a shows the radius at which *pp-chain* neutrinos are produced. ^{8}B neutrinos

for instance are produced around r$\sim$ 0.05 R$_\theta$ up to 15 MeV. From equation 2.48, they will therefore undergo a MSW effect resonance if $\Delta m_{12}^2 \cos(2\theta) < 10^{-4}$ eV^2.

The neutrino experiments measured Δm_{12}^2 and $\tan(\theta_{12})$ in oscillation experiments. Five areas as potential $(\Delta m_{12}^2, \tan(\theta_{12})^2)$ solution were observed: four of them for a mixing angle far from zero (by decreasing Δm^2 order, from 7$\times$10^{-4} to $\sim 10^{-11}$: LMA, LOW, QVO, VAC) and one with a $\tan^2(\theta_{12}) \sim 10^{-3}$ (SMA).

The Large Mixing Angle (LMA) hypothesis (7$\times$10^{-5} eV^2,0.4) was confirmed by KamLAND collaboration in 2003 [113]. Knowing the solar vacuum mixing angle, one can derive the expected matter effect [114] on P$_{ee}$ the ν_e survival probability:

$$P_{\text{ee}} = 1 - \sin^2(2\theta_{12}^m)\sin^2(\frac{(E_2^m - E_1^m)t}{2}) \tag{2.49}$$

Far from the resonance range, the effect is low energy-dependent while the transition is energy-dependent. Knowing that $L_{\text{osc}} = 1.27\frac{\Delta m^2}{eV^2}\frac{L}{km}\frac{GeV}{E}$, the observation of neutrino on Earth are not sensible to Δm^2 and can be averaged.

$$P_{ee}(vacuum) \simeq 1 - \frac{1}{2}\sin^2(2\theta_{12}) \simeq 0.58 \tag{2.50}$$

$$P_{ee}(matter) \simeq \sin^2(\theta_{12}) \simeq 0.3 \tag{2.51}$$

From figure 2.8a, the different solar neutrinos branches are not produced in the same radius. Modifying the radial position influence the electron density and therefore the transition between vacuum and matter dominated area. Indeed, the typical transition energy for ν_{8B} is 1.8 MeV while it is 3.3 MeV for ν_{pp} [114]. ν_{pp} are not produced at such high energy (see section 1.2.4). This is the reason why ^{8}B solar neutrinos are interesting to test MSW resonance effect in the Sun.

Figure 2.9 is showing the solar neutrino results obtained from SNO, SK and Borexino. It confirmed the hypothesis of the MSW effect.
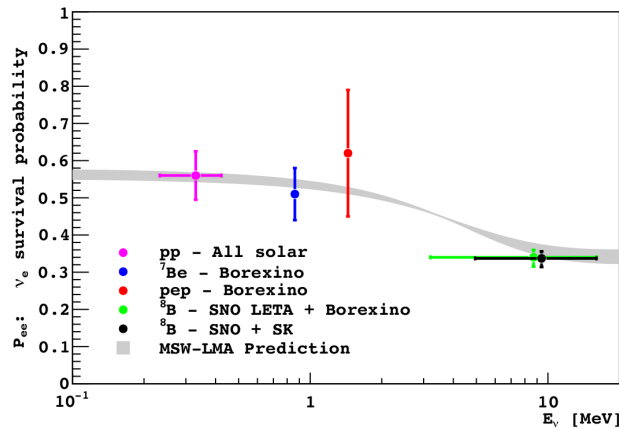
Figure 2.9: *Solar neutrino measurement of the ν_e survival probability depending on the energy [115].*

2.3.3 State of the art

As explained in section 2.3.1.2, three mixing angles (θ_{12},θ_{23},θ_{13}), two mass squared differences Δm_{ij}^2 and one phase (δ_{CP}) are the free parameters of the neutrino oscillation playground. It is of great luck for physicist, the mass squared differences have two order of magnitude separating them.

Indeed, the typical oscillation length is given by: $L_{\text{osc}} = \frac{4\pi E}{\Delta m^2}$, meaning that by observing neutrino oscillation of same energy at different baseline one can disentangle some of the parameters.

Three features can be observed:

- L$\ll L_{\text{osc}}$, the experiment will not be sensible to the corresponding Δm_{ij}^2 as the oscillation will not have time to develop,

- L$\gg L_{\text{osc}}$, the finite energy resolution "average" the oscillation. The experiment is only sensible to $\sin^2(2\theta)$,

- L$\sim L_{\text{osc}}$ the oscillation due to Δm^2 is visible.

Many efforts have been invest in measuring the oscillation parameters in the last decades. Figure 2.10 is giving the last global fit from [104].

NuFIT 3.0 (2016)

	Normal Ordering (best fit)		Inverted Ordering ($\Delta\chi^2 = 0.83$)		Any Ordering
	bfp $\pm 1\sigma$	3σ range	bfp $\pm 1\sigma$	3σ range	3σ range
$\sin^2\theta_{12}$	$0.306^{+0.012}_{-0.012}$	$0.271 \to 0.345$	$0.306^{+0.012}_{-0.012}$	$0.271 \to 0.345$	$0.271 \to 0.345$
$\theta_{12}/°$	$33.56^{+0.77}_{-0.75}$	$31.38 \to 35.99$	$33.56^{+0.77}_{-0.75}$	$31.38 \to 35.99$	$31.38 \to 35.99$
$\sin^2\theta_{23}$	$0.441^{+0.027}_{-0.021}$	$0.385 \to 0.635$	$0.587^{+0.020}_{-0.024}$	$0.393 \to 0.640$	$0.385 \to 0.638$
$\theta_{23}/°$	$41.6^{+1.5}_{-1.2}$	$38.4 \to 52.8$	$50.0^{+1.1}_{-1.4}$	$38.8 \to 53.1$	$38.4 \to 53.0$
$\sin^2\theta_{13}$	$0.02166^{+0.00075}_{-0.00075}$	$0.01934 \to 0.02392$	$0.02179^{+0.00076}_{-0.00076}$	$0.01953 \to 0.02408$	$0.01934 \to 0.02397$
$\theta_{13}/°$	$8.46^{+0.15}_{-0.15}$	$7.99 \to 8.90$	$8.49^{+0.15}_{-0.15}$	$8.03 \to 8.93$	$7.99 \to 8.91$
$\delta_{\text{CP}}/°$	261^{+51}_{-59}	$0 \to 360$	277^{+40}_{-46}	$145 \to 391$	$0 \to 360$
$\dfrac{\Delta m_{21}^2}{10^{-5}\ \text{eV}^2}$	$7.50^{+0.19}_{-0.17}$	$7.03 \to 8.09$	$7.50^{+0.19}_{-0.17}$	$7.03 \to 8.09$	$7.03 \to 8.09$
$\dfrac{\Delta m_{3\ell}^2}{10^{-3}\ \text{eV}^2}$	$+2.524^{+0.039}_{-0.040}$	$+2.407 \to +2.643$	$-2.514^{+0.038}_{-0.041}$	$-2.635 \to -2.399$	$\left[\begin{array}{c}+2.407 \to +2.643\\-2.629 \to -2.405\end{array}\right]$

Figure 2.10: *Summary of the last mixing parameters determination using a global fit described in [104].*

2.4 Toward a sterile neutrino?

2.4.1 Experimental Anomalies

Neutrino theory has been built upon anomalies: from the β spectrum, to the Solar and the Atmospheric problems. All those anomalies lead to great discoveries from the existence of the neutrino

to matter effect and neutrino oscillations. It is not to say that discoveries lie in every discrepancy between model and data. However each and every anomaly should be carefully investigated. Many anomalies in the neutrino sector can be explained by adding a light sterile neutrino.

2.4.1.1 Gallium anomaly

During its calibration campaigns, GALLEX (refer to section 1.2.5.1) used two intense ^{51}Cr sources (more than 60 PBq) produced by neutron irradiation on ^{50}Cr. ^{51}Cr decays through electron capture, emitting: 750 keV ν_e (90%) or 430 keV ν_e + 320 keV γ, with an half-life of about 27.7 days. The activity after irradiation of the two sources was checked using γ spectroscopy in four different laboratories. The entire source was then inserted in a calorimeter for heat measurement before being installed inside the detector. The second source was obtained by reirradiation of the first chromium source a year later. The measured activity of the two sources were respectively $63.4^{+1.1}_{-1.6}$ PBq and $69.1^{+3.3}_{-2.1}$ PBq. The result of the comparison between expected and observed signal for the two sources, R_1^{51Cr} and R_2^{51Cr}, are [116]:

$$\textbf{GALLEX} \qquad R_1^{51Cr} = 1.01^{+0.12}_{-0.11} \qquad R_2^{51Cr} = 0.84^{+0.12}_{-0.11} \qquad (2.52)$$

In parallel, the SAGE collaboration (refer to section 1.2.5.1) used a ^{51}Cr ($\sim$ 19 PBq) and a ^{37}Ar (($\sim$ 15 PBq). ^{37}Ar decay to ^{37}Cl through electronic capture emitting 813 keV (90.2%) or 811 keV(9.8%) ν_e. It offers the advantage of an almost monoenergetic ν_e line and has a longer half-life (35 days). Besides, production can be made almost free of radioactive impurities (important for calorimetric measurement of the activity). As for the GALLEX experiment, the result of the comparison between expected and observed signal for the two sources, R^{51Cr} and R_2^{37Ar}, are [117]:

$$\textbf{SAGE} \qquad R^{51Cr} = 0.95 \pm 0.12 \qquad R^{37Ar} = 0.79^{+0.09}_{-0.10} \qquad (2.53)$$

Combining the two deficits, the ratio is then: 0.88 ± 0.05.

Some interpreted this result as an evidence that ^{71}Ga(ν_e,e$^-$)^{71}Ge cross section is lower than expected. In particular, contribution from ^{71}Ge excited states via Gamow-Teller transition to the total cross section is discussed [118]. If R is lower than 0.95 (no contribution from excited state to ^{71}Ge production), the deficit is automatically more consistent with the data [117]. However, new analysis of the Gallex data using recent analysis techniques confirmed the anomaly at 1.5 σ [119].

2.4.1.2 Accelerator anomalies

The LSND (Liquid Scintillator Neutrino Detector) operated from 1993 to 1998. It was a 167 tons liquid scintillator detector located 30 m away of the LAMPF accelerator. LAMPF was a 798 MeV proton beam running at Los Alamos, producing low energy neutrinos on water (1993-1995) and high-Z (1996-1998) targets. The most abundant produced particle was π^+ decaying into μ^+ and e$^+$ with emission of ν_μ, ν_e and $\overline{\nu_\mu}$. π^- are height time less produced than π^+ and the relative yield of $\overline{\nu_e}$ is 5×10^{-4} with respect to $\overline{\nu_\mu}$ from the positive channel [120] for neutrino energy between 20 MeV and 52.8 MeV. This means that any excess above this rate is due to $\overline{\nu_\mu}$ to $\overline{\nu_e}$ oscillation.

LSND detected $\overline{\nu_e}$ through IBD on ^{12}C. Not able to distinguish e$^+$ from e$^-$ an energy threshold of 36 MeV was settled on the prompt signal for reducing ν_e-induced accidental background [121].

The LSND collaboration observed an excess of $\overline{\nu_e}$ at 3.8σ with respect to $\overline{\nu_\mu}$ to $\overline{\nu_e}$ expected oscillation. This excess is inconsistent with the model and the actual mixing angles measured. In parallel the KARMEN collaboration did not observe any excess, located at 17.7 m from a 800 MeV protons beam. Both experiments are not inconsistent, KARMEN gives constraints on potential new oscillation angle observed by LSND [122].

The MiniBooNE experiment was designed to test the LSND anomaly. Looking for signal 500 m from the Fermilab Booster accelerator, it is designed as a 800 tons liquid scintillator detector. The emitted $\overline{\nu_\mu}$ energy is up to 3 GeV, comparing the same L/E parameter than the one used by the LSND experiment. The MiniBooNE collaboration observed an excess of ν_e (ν_μ disappearance) at low energy only and an excess of $\overline{\nu_e}$ ($\overline{\nu_\mu}$ disappearance) consistent with the LSND observation. A combined analysis increases the significance of those excesses to 3.4σ [123].

MicroBooNE is addressing this excess at low energy using a 170 tons liquid argon detector. The MicroBooNE experiment is taking data since end of 2015 and should review results in middle 2017.

2.4.1.3 Antineutrino Reactor Anomaly

Antineutrino Reactor experiments are using estimation of neutrino production spectrum to look at short baseline oscillation. The final reactor antineutrino spectrum is composed of the sum of the ^{238}U, ^{235}U, ^{239}Pu and ^{241}Pu fission products spectra. Each of those spectrum is the sum of the different β branches weighted with their branching ratios. The ab initio method is one of the method used to predict antineutrino spectrum for oscillation measurement. In this method, considering each and every β branches, the antineutrino energy $E_{\overline{\nu_e}}$ is easily deduced from the electron energy E_e and the Q_β of the reaction by $E_{\overline{\nu_e}} = Q_\beta - E_e$ when no radiations is emitted. This is not the case when fitting the spectrum with virtual branches. The very low energy of the β spectrum however is not continuous as the emitted electrons will have to undergo Coulomb deceleration protons induced when leaving the nucleus: it leads to a sharp step at the high energy edge of the antineutrino spectrum. To take this into account, Fermi function is correcting the β spectrum at low energy. The final antineutrinos spectrum, summed over all the branches will have steps and discontinuities because of this effect.

The re-evaluation done in [124] is based on the sum of all the known branches listed in ESDF and JENDL nuclear database: 845 nuclei and 10 000 β-branches. From ab initio calculus on this data set, authors were able to predict the fission antineutrino spectra above 1.8 MeV at 10%. Measurement done at ILL [125, 126] allowed a conclusive comparison with ^{235}U, ^{239}Pu and ^{241}Pu total spectra. ^{238}U has not been measured yet. Even this dataset is not complete and $\sim$10% of the β spectra measured at ILL is not explained by known β transitions. 4 virtual β branches have then to be added for fitting the unknown transitions. This new method, using the most recent dataset, is less model dependent and better handle systematics of the electron-neutrino conversion procedure. The result was a +3.5% shift in the normalization of Uranium and Plutonium antineutrinos spectra [124] with respect to previous predictions [125, 126].

This antineutrino reactor spectra re-evaluation leads to reconsider the reactor neutrino experiments done in the past. Correcting for neutron lifetime, IBD cross section and emission spectrum, a discrepancy between observed and expected neutrino of 0.943 ± 0.023 is measured. It is the so called

Reactor Antineutrino Anomaly [127]. Figure 2.11 shows the fit of the reactor neutrino experiment in a 3+1 model.
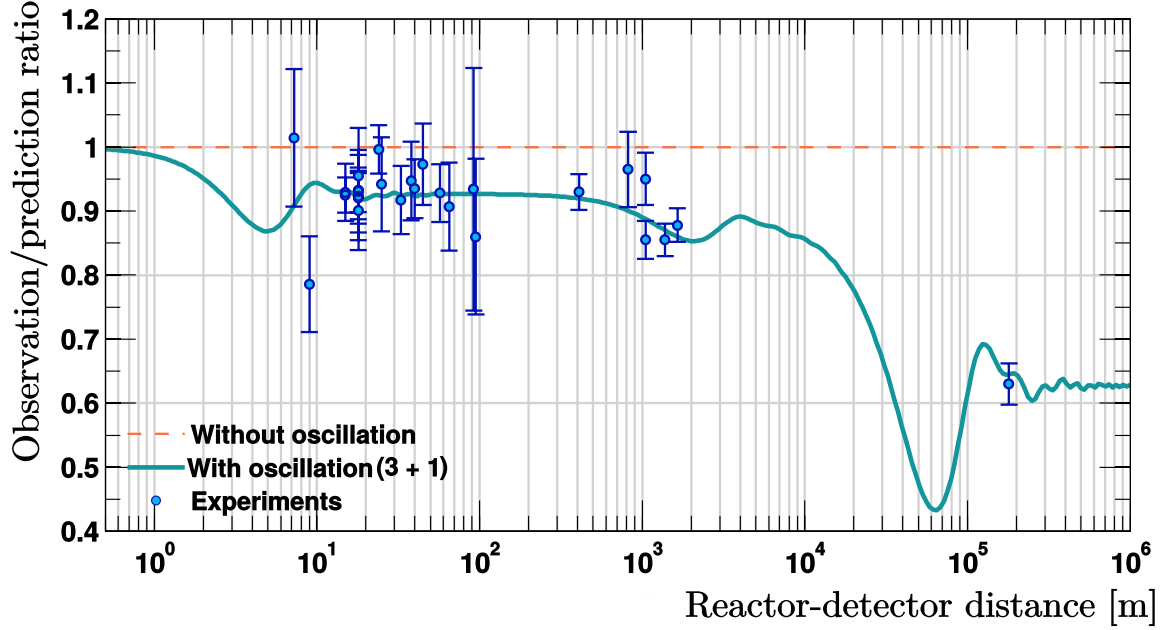
Figure 2.11: *The Reactor Neutrino Anomaly fitted with and without sterile neutrino. Credits to T.Lasserre.*

Recent results [88] from Daya Bay confirms the reactor antineutrino anomaly, measuring a 0.946 ± 0.020 measured over prediction ratio with respect to Huber-Mueller model [124, 128] but offer another explanation than the existence of a sterile neutrino. By observing evolution of their observed flux, the collaboration was able to fit provenance of the antineutrinos among ^{235}U or ^{239}Pu, the first one being consumed while the second rising from ^{238}U enrichment. They report that ^{235}U might be the primary contributor the reactor antineutrino anomaly [129]. This together with the 5 MeV bump in the reactor antineutrino spectra is subject of intense researches and discussions.

2.4.2 Theoretical aspect

A sterile neutrino is a neutral lepton not coupled to the weak interaction. Theoretically, those particle can have any mass. If the see-saw mechanism use a very heavy sterile neutrino (see section 2.2.4), the standing anomalies would accommodate for a light sterile neutrino because of the relatively high mixing with active species.

It is possible considering that one of the Majorana mass added in the see-saw mechanism is not high enough for suppressing oscillations between left-handed neutrino and left-handed antineutrino.

Considering the oscillation case of only one active neutrino, if $M > m$ but not $M \gg m$, equation 2.21 leads to two mass eigenstates ν_1 and ν_2 as:

$$\begin{pmatrix} \nu_1 \\ \nu_2 \end{pmatrix} = \begin{pmatrix} 1 & -\frac{m}{M} \\ \frac{m}{M} & 1 \end{pmatrix} \begin{pmatrix} \nu_L \\ \overline{\nu_L} \end{pmatrix}$$ (2.54)

Equation 2.54 means that considering a m~0.1 eV, oscillation from ν_L to $\overline{\nu_L}$ is possible if $M \sim 1eV$ for instance. $\overline{\nu_L}$ can not interact via weak interaction as only $\overline{\nu_R}$ is weakly coupled. This oscillation would lead to a sterile neutrino production. However one has to remember that the theoretical interest of introducing the see-saw mechanism was to explain the small neutrino mass by adding a suppressive term M. In the case where M and m are relatively close (to have visible oscillation effect), one looses this theoretical justification. This mechanism is easily explaining the existence of a sterile state in a small theoretical framework. A theory with 2 heavy sterile neutrinos and 1 light sterile neutrino is a possibility. In this idea, we are introducing only 1 sterile state as 2 heavy sterile neutrinos would be not observable.

Considering only one sterile state, the P-MNS matrix can be rewritten as a 4×4 unitary matrix such that [92]:

$$\nu_\alpha = \sum_{i=1}^{4} U_{\alpha i} \nu_i \qquad \text{with} \qquad \alpha = e, \mu, \tau$$ (2.55)

It means that this sterile state is produced in any β decay with an angle depending on the flavour produced. The probability of oscillation is then modified by this new term:

$$P_{\nu_\alpha \to \nu_\beta} = \sin^2(2\theta_{\alpha\beta}) \sin^2(\frac{\Delta m_{41}^2 L}{4E}) \qquad \text{with} \qquad \sin^2(2\theta_{\alpha\beta}) = 4|U_{\alpha 4} U_{\beta 4}|^2$$ (2.56)

2.4.3 Testing the sterile hypothesis

Explaining the reactor antineutrino anomaly using a sterile state leads to consider the disappearance of $\overline{\nu_e}$ due to Δm_{41}^2:

$$P_{\overline{\nu_e} \to \overline{\nu_e}} = 1 - \sin^2(2\theta_{ee}) \sin^2(\frac{\Delta m_{41}^2 L}{4E})$$ (2.57)

with favoured parameters $\sin^2(2\theta_{ee})$ and Δm_{41}^2 as displayed in figure 2.12.

2.4.3.1 Short Baseline experiments

All the short baseline experiments testing the sterile neutrino are using the IBD technique. Apart from this similarity, they use different detection techniques, size of the reactor core, baseline and composition of the fuel.

STEREO The STEREO experiment [130] is tracking $\overline{\nu_e}$ from 3 to 8 MeV produced in the compact (~40 cm) reactor core of Institut Laue-Langevin, France. The detector is 2.2 m long segmented in 6 cells filled with Gd-doped scintillator. $\overline{\nu_e}$ are detected through IBD interaction in the liquid, n-capture on Gadolinium enabling for a 8 MeV γ cascade. Four photomultiplier tubes (PMT) are collecting light at the top of each cell, separated from the scintillator by acrylic buffers. A water-Cerenkov veto is placed above the detector for muon rejection. The detector is actually running and first results are expected fall 2017.
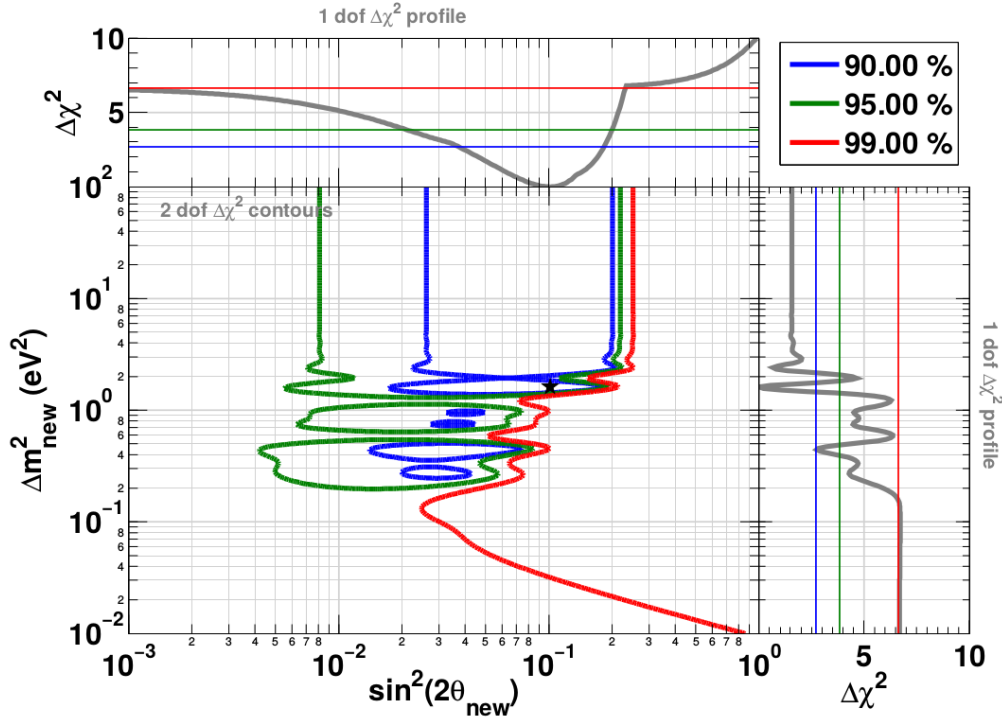
Figure 2.12: *Allowed regions for sterile oscillation parameter using reactor neutrino data in the 3+1 hypothesis [127].*

Neutrino-4 The Neutrino-4 experiment [131] is based on a moveable detector from 6 to 11 m detection $\overline{\nu}_e$ from the SM-3 reactor (Dimitrovgrad, Russia). The detector is composed of 16 rectangular sections for 0.4 m^3 as active target filled with 350 l of mineral oil doped with Gadolinium. Each section is equiped with 4 PMTs. External events are rejected thanks to an upper active shielding and an extra layer of plastic scintillator surrounding the detector. Finally, a passive shielding is settled covering the 5 m way of the detector. The first reported measurement in 2015 [131] was inconclusive due to a high cosmic background and small size of the detector.

SoLid The SoLid experiment [132] is located at 5.5 m from a compact (diameter 40 cm) research reactor BR2, Belgium. The detector design is constituted of $24 \times 24 \times 40$ cubes of 125 cm^3 of plastic scintillator. A 250 μm layer of Lithium based material. The IBD signature is a positron annihilation in the plastic scintillator followed by the neutron capture on ^{6}Li nuclei. Scintillation light is collected by wavelength shifting optical fibres through silicon photomultipliers. Results are expected by the end of 2017.

PROSPECT The PROSPECT project [133] will be located at the Oak Ridge National Laboratory, United-States, 7-12 m from the High Flux Isotopes Reactor core. The reactor core is 42 cm diameter and the fuel is highly enriched ^{235}U ($>94\%$ of $\overline{\nu}_e$ coming from ^{235}U). The detector is based on rectangular unit segment of 119 cm$\times$14.6 cm$\times$14.6 cm filled with 25 L of lithium-loaded liquid scintillator. PMTs at both end of the unit are collecting scintillating light. The IDB induced neutron is captured on ^{6}Li decaying in tritium and alpha.

(a) *Data over prediction (3-ν). Prompt energy spectra in the NEOS experiment [134]*

(b) *Preliminary prompt energy spectra in the DANSS experiment [137] compared with a 3-ν Monte Carlo model.*
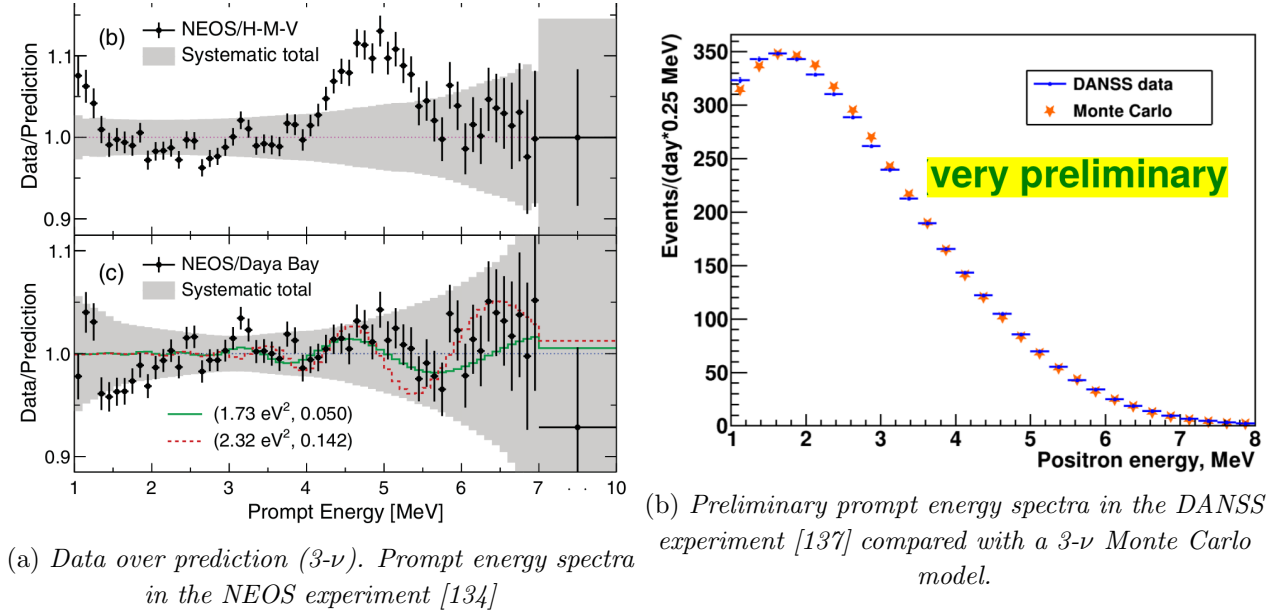
Figure 2.13: *Preliminary results of short baseline reactor experiments.*

NEOS   The NEOS experiment [134] is installed 23.7 m from the center of the reactor 5 core, Hanbit, Korea. The nuclear reactor complex is the same than the one used in the RENO experiment. The detector is using Gd-doped liquid scintillator in a 1 m diamater, 1.2 m length stainless steel cylinder. PMTs are packed in mineral oil buffers separated from the scintillator by a 6 cm thick of transparent plastic. Plastic scintillator are used as muon veto surrounding the detector and lead layers act as neutron and gamma passive shield. NEOS published results in 2017 [134] were no strong evidence of oscillation was observed, excluding part of the reactor antineutrino anomaly. Figure 2.13b shows the oscillating spectrum depending on the flux normalization. The 5 MeV bump already reported by [135, 136, 88] is clearly visible when using the Hubert-Mueller computational flux.

DANSS   The DANSS experiment is located 10.7-12.7 m from a PWR-1000 reactor core (3.7 m height, 3.1 m diameter) in the Kalin Nuclear Power Plant installation, Russia. The fuel is composed of highly enriched Uranium (58-69% of ^{235}U, 21-30% ^{239}Pu, 7%^{238}U). The $\overline{\nu_e}$ detection is based on segmented plastic scintillator with Gadolinium additive [138]. Light is transmitted through wavelength shifter optical fibres to SiPMs. The detector is surrounded by active and passive veto. Taking data since April 2016, 170 days of reactor-ON data have been analysed [137] with a statistics of around 5000 $\overline{\nu_e}$ candidates per day. No oscillations were observed and large area of the reactor antineutrino anomaly was excluded. The 5 MeV bump seems not visible but more detailed analysis should be reported by the collaboration in the next months.

2.4.3.2   Source experiments

At the time of this thesis, two projects of bringing a very radioactive source close to a detector are known: SOX and BEST. The SOX project is detailed in section 3.3. The BEST project [139] aims at producing a 3 MCi ^{51}Cr source. The source hold in a 9 cm diameter and 10 cm height cylinder is encased in a 0.66 m radius sphere filled with homogeneous liquid gallium ^{71}Ga. This

sphere is inserted in a cylinder (1.1 m radius, 2.2 m height) filled with the same liquid. They plan to extract ^{71}Ga liquid separatetly for each volume any 9 days for 10 extractions at last. Counting the number of ^{71}Ge produced, BEST can test ν_e disappearance by comparing the number of interaction undergone in each volume. They aim at beginning the source production in 2017.

2.4.3.3 β decay measurement

The existence of a fourth neutrino mass states could be seen by any beta decay measurement as a kink in the electron shape depending on the mass of this extra eigenstate. The KATRIN experiment could test the eV-keV sterile mass scale using this technique but many technical issue must be first addressed like supporting the high rate of electrons at higher energy [140].

Chapter 3

Borexino

Contents

Borexino is a neutrino detector taking data since 2007. Borexino was originally designed to measure low energy solar neutrinos rates, from ^{7}Be (monoenergetic 872 keV line) in real-time to CNO and to distinguish between the different solar mixing angles (LOW vs SMA/LMA) using day/night effect [141, 142].

It detects solar neutrino via elastic scattering on electrons in an organic scintillator. The main technological challenge of Borexino was to reach high accuracy in the background control and very high level of radiopurity inside the detector. The extraordinary radiopurity achieved in Borexino allowed to extend the physics potential to other neutrino sources as geoneutrinos and to extend its research to sterile oscillation with an intense antineutrinos source, namely the SOX experiment.

3.1 The Borexino detector

The detector is located deep underground in the Hall C of the Laboratori Nazionali del Gran Sasso (LNGS), Italy. The minimum rock depth of 1400 m (3800 m.w.e) reduces the muon flux by a factor of 10^6.

3.1.1 Detector design

The Borexino detector is sketched in figure 3.1. The onion structure of Borexino is composed by the Outer Detector (OD) filled with water and by the Inner Detector (ID) filled with buffer liquid and scintillator. The Inner Volume (IV) is the innermost part of the detector containing only the scintillator.
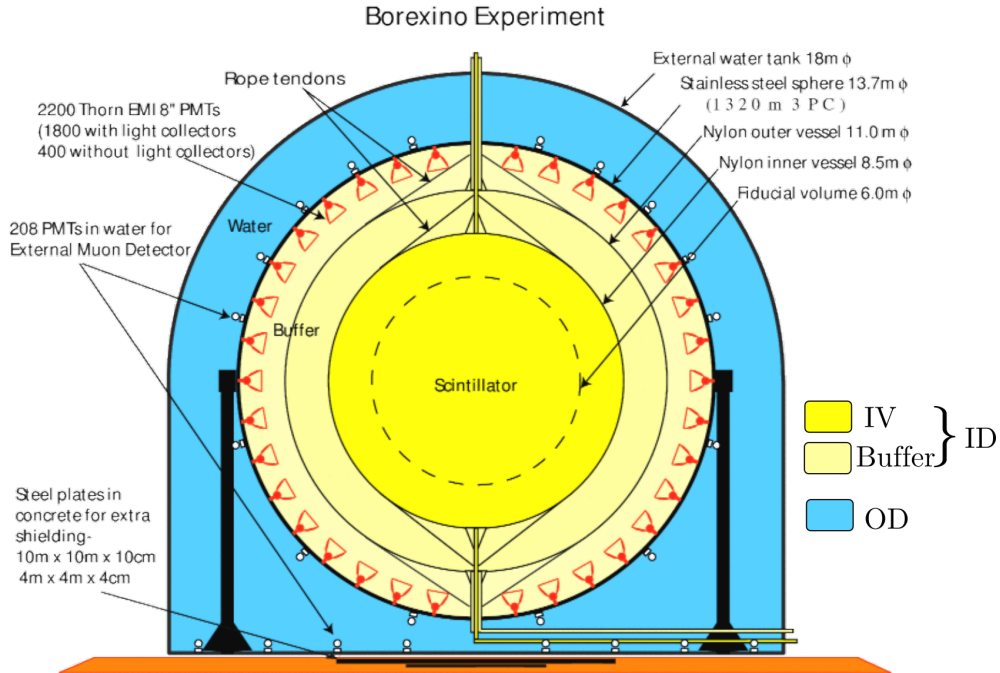
Figure 3.1: *The Borexino detector geometry [143].*

The Water tank   The OD is made of a steel dome whose size is 18 m-diameter and 16.9 maximum height filled with 2100 tons of water. Thus it provides a 2.5 m thickness shield of water around the ID. The OD volume is surrounded by 208 PMTs looking at Cerenkov light from cosmic muons. It acts as an active veto against muons and as a passive veto against neutrons from the rock. In the lowest part of the detector, this water shielding is only of 1 m. To counterbalance this thickness reduction, two steel plates, equivalent to 1.5 m of water shielding, have been added. The muon veto efficiency has been estimated to be $> 99.992\%$ [144].

The Stainless Steel Sphere   Inside the Water Tank, a 6.85 m radius Stainless Steel Sphere (SSS) of $\sim$8 mm thick is suported by 20 steel legs. This massive (45 tons) structure supports the 2212 Photomultiplier Tubes (PMTs) oriented toward the center of the detector. The SSS also absorbs the buoyant force due to density difference between water and scintillator.

3.1.1.1   Scintillator

The main component of the scintillating mixture is Pseudocumene ($C_6H_3(CH_3)_3$, 1,2,4-Trimethylbenzene). It is an aromatic hydrocarbon constituted of benzene rings. Their inner symmetry gives rise to a π-e^- structure in which delocalised electrons can be excited to collective excited states (singlet of spin 0 or triplet of spin 1). The first singlet excited state is around 3 or 4 eV. The de-excitation of singlet state leads to prompt ($\sim$ 1-10 ns) fluorescence photon emission while triplet state de-excites through phosphorescence, a much longer light emission (1 μs up to 1 ms). Some crossing between singlet and triplet states may induce a delayed fluorescence from about 100 ns to 1 ms [145, 146].

The inner vessel is filled with 270 tons of Pseudocumene (PC) doped with 1.5 g/L of a fluor called PPO (2,5-diphenyloxazole). Pseudocumene (PC) is the target. When excited, PC emits around 290 nm with a 22 ns characteristic decay time. PPO will then absorb this radiation until 380 nm, re-emitting at 400 nm by prompt fluorescence with a 80% efficiency and a 1.6 ns time decay. PPO is needed for matching the quantum efficiency of the PMTs as well as decrease the light attenuation. The light attenuation length in PC ranges from $\sim$1 cm at 360 nm to 8 m at 400 nm .

For low ionization densities (γ and β), the main process is excitation of singlets while for high ionization densities (α and protons), more triplet states are excited leading to different deexcitation times. The different scintillation time profiles enable to distinguish low and high ionization particles, as described in section 3.1.3.4. Besides this timing effect, depending on the particle crossing the detector, the transferred energy from deposited energy to light is different. If electrons and gammas convert around 5% of their deposited energy in light, this ratio is around 0.5% for alpha and proton [147], see section 3.1.3.2 describing this quenching effect. Aside from the scintillation light, relativistic electrons in the scintillator will emit Cerenkov radiation discussed in section 3.1.3.3. Besides, intrinsic radioactivity of the scintillator can mimic a neutrino signal. In order to master this background, a huge effort was developed for purification. Tested on the CTF detector [148], the system is using gas removal, water extraction, distillation and solid column chromatography reaching a residual contamination of $(3.5\pm1.3)\times10^{-16}$ g/g in ^{238}U, $(4.4\pm1.5)\times10^{-16}$ g/g in ^{232}Th and $(1.94\pm0.09)\times10^{-18}$ ^{14}C/^{12}C in the scintillator [149].

The absorptions, re-emissions and fluorescence processes imply an isotropic light at the end of the light production.

Buffer liquid The scintillator is shielded by ~ 2 m thickness of non-scintillating PC (buffer) and by extra nylon vessel. The buffer must not scintillate but be transparent to light from the scintillator. It is composed of PC doped first with 5g.L^{-1} of dimethyl phthalate (DMP) to quench the scintillation yield of the buffer by a factor 20. It was diminished to 2 g.L^{-1} of DMP due to leakage described in section 3.1.4.1.

Nylon Vessels Inside the SSS, two nylon vessels (0.125 mm thick of Nylon-6 B73ZP polymer) physically delimit liquid interfaces. Nylon has been chosen for its refractive index close to the scintillator, its transparency, its chemical compatibility and its radiopurity. A 5.5 m radius nylon vessels separate the buffer liquid close to the scintillator from the buffer liquid in contact with the PMT. This structure shields the inner part of the detector against diffusion of radioactive elements from the PMTs. The second vessel, 4.25 m radius, encases the fiducial volume and avoid any mixing between buffer and scintillator.

3.1.1.2 Photomultipier tubes

The scintillating light is detected by 2212 8" ETL9351 photomultipliers (PMTs) mounted on the SSS surface. The front part of each PMT is immersed in the buffer liquid (PC+DMP) while the back is in contact with the water of the OD. Chemical compatibility is guaranteed by the encapsulation in stainless steel cylinder, as well as the impermeability thanks to isolation by phenolic resin. The PMTs are alimented with high voltage tension around 1600 V for a typical gain of 10^7.
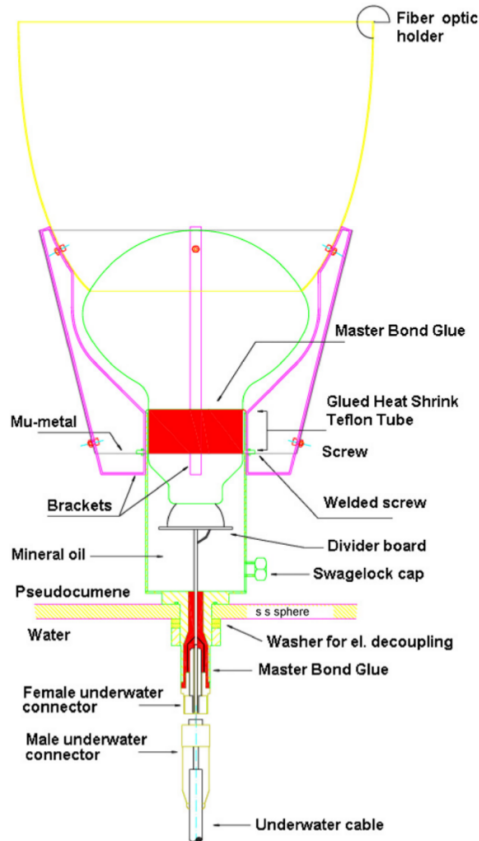
Figure 3.2: *Schematics of one photomultiplier used in Borexino [143].*

1839 PMTs are equipped with light concentrators, aluminium cone (23 cm height, radius from 9.5 cm at the PMT glass to 16 cm at the entrance). The light concentrators are designed to maximise the light collection on event in the 3 m innermost sphere and to protect the PMTs from light produced in the buffer. It induces a small decrease of the light collection close to the vessel. The PMTs without light concentrators helps to discriminate buffer event mainly induced by cosmic rays from IV events.

The 2212 PMTs provide an optical coverage of 30% with a nominal quantum efficiency of 26% at 420 nm. The light yield in the center normalized to 2000 working PMTs is about 500 pe/MeV [143]. PMTs work in single photoelectron regime because of the ^{7}Be energy region (665 keV) for which Borexino was designed. Saturation of the amplifier begins at 35 pe per channel. The front-end electronics saturated at $\sim$8.6 pe per channel (in a 80 ns interval) [143] which corresponds to an energy of more than 35 MeV deposited by an electron in the center of the detector. Hence this effect does not affect the Borexino physics goals. Figure 3.2 gives the scheme of one photomultiplier tube.

Due to its large size, PMT is affected by the Earth's magnetic field. A μ-metal conic foil shields the tubes against this effect.

3.1.2 Electronics

3.1.2.1 Front end electronics

Specific electronics are designed for the ID and the OD. This section describes only the ID electronics.

Each PMT supplies one channel which divides the signal in two parts: one is feeding a time-digital-converter (TDC) and one an analogue-digital-converter (ADC). The time signal will be used for position reconstruction while charge signal and the number of hits will be used for energy determination. Single photoelectron signals have on average an amplitude of 1 mV mean and a width of 15 ns.

The analogue signal used in the TDC is first amplified by a low-noise fast amplifier with a gain of 20 before being discriminated to obtain signal time with a resolution of 0.5 ns. The signal of each channel is saved in a buffer if the tension in the discriminator is larger than $\sim$ 0.2 pe. The board is defining such a signal as a *hit*. When the TDC registers a hit, it is disabled for 140 ns in order to inter alia avoid false retrigger [146].

The analogue signal used in the ADC is integrated on a gateless charge integrator. If the TDC is activated at t_0, the charge signal is integrated between t_0 and t_0+80 ns. The ADC and TDC combination implies consequently a 60 ns dead-time during which the photoelectron signal is lost. It is determinant mostly concerning delayed scintillation processes.

3.1.2.2 Triggers

When the Borexino Trigger Board (BTB) is fired, all the channels are active for 16.5 μs. Each trigger is followed by a dead-time of 2.5 μs. The BTB is activated if:

- Standard Event: in the ID, at least N_{ch} channels (PMTs) register hits within 60 ns window time. N_{ch} is around 20 nowadays and 25 in the past ($\approx$ 50 keV deposit), varying with the

number of alive PMTs and the aim of the analysis.

- the Muon Trigger Board (MTB) is fired. The MTB requires at least 6 channels fired within 150 ns in the OD.

- the Neutron Trigger: if the MTB is activated a gate is opened for 1.6 ms looking for n-capture.

Other specific triggers exist concerning the laser calibration or electronics analysis (random trigger, pulse from a generator sent to the electronics). These technical triggers are used for synchronising time signal between PMTs and are activate with a 0.5 Hz rate during data taking [44].
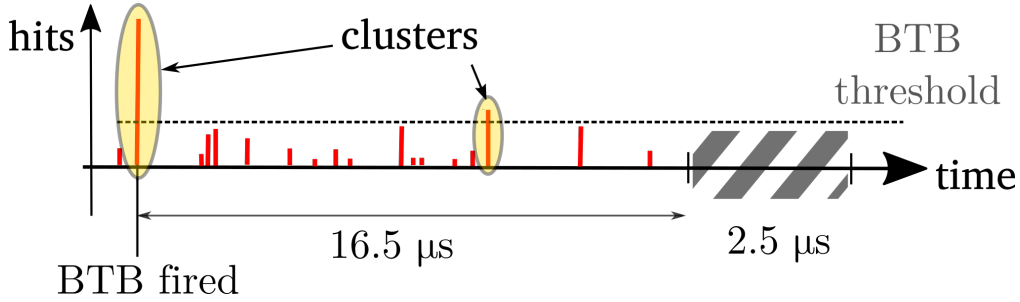
Figure 3.3: *Illustration of the standard Borexino event trigger and clusterisation using Echidna.*

3.1.3 Reconstruction and calibration

The data are handled by Echidna, the official data reconstruction code developed in C++ by the Borexino collaboration. Echidna uses laser calibration informations for each runs, to better discriminate the dark noise. The program is looking for correlation in time between hits in the 16.5 μs window calling it a cluster. In most of the situations, only one cluster is found but for fast coincidence several clusters can be found in one time window as illustrated in Figure 3.3.

As the Borexino signature relies on the identification of energy spectral shapes, an optimal comprehension of the energy variable and position reconstruction is necessary.

3.1.3.1 Event reconstruction

Schematically, Borexino records two primary characteristics for one signal in each PMT: charge (ADC) and time (TDC). From those two informations position and energy are reconstructed.

The position reconstruction algorithm uses a likelihood method. Assuming one hit in PMT i, the coordinate $(x_i^{\mathrm{PMT}}, t_i^{\mathrm{PMT}})$ is the position of this PMT with respect to the center of Borexino and the time of recorded signal. Considering a point-like scintillation event, the true position, (x^0, t^0), is the difference between the observed position $(x_i^{\mathrm{PMT}}, t_i^{\mathrm{PMT}})$ and the time-of-flight t_i^f. t_i^f is depending on the distance between x^0 and x_i^{PMT} (d_i) as well as the refractive index of the scintillator, n, in the following way $t_i^f = \frac{d_i n}{c}$. The true position (x^0, t^0) is then determined minimizing the likelihood adjusting the time-of-flight for each PMT knowing $(x_i^{\mathrm{PMT}}, t_i^{\mathrm{PMT}})$:

$$\mathcal{L}((x^0, t^0)|(x_i^{\mathrm{PMT}}, t_i^{\mathrm{PMT}})) = \prod_i f(t_i^{\mathrm{PMT}} - t_i^f - t_0) \tag{3.1}$$

with $f(t_i^{\mathrm{PMT}} - t_i^f - t_0)$ the probability density function of hits on PMTs for one point-like event in the center of the detector. Varying the true position, the reconstructed position is the set of (x^0, t^0) minimizing the likelihood of equation 3.1. Because the position reconstruction is based upon hit distribution, it is energy dependent. At low energy correction can be applied due to single photoelectron probability to appear below the pedestal while at high energy volume effects arises because of dead-time on photoelectron time arrival. Therefore the PDFs have been adjusted during the calibration campaign.

The deposited energy is in first approximation proportional to the number of observed photons. However some processes such as quenching or light collection efficiency (absorption, reemission, scattering ...) introduce non-linearity in the conversion of npe to energy. Besides those physical effect, the non uniform distribution of PMT in time and in the volume, position dependency due to the light concentrator, can also affect the conversion.

A Monte-Carlo approach is then the best way to understand the energy reconstruction inside the detector. Calibration of the Monte-Carlo has been done using γ sources such as ^{57}Co(122 keV, 136.5 keV), ^{139}Ce(166 keV), ^{203}Hg(279 keV), ^{85}Sr(514 keV), ^{54}Mn(834 keV), ^{65}Zn(1.1 MeV), ^{40}K(1.4 MeV) and ^{60}Co (2.5 MeV). Figure 3.4a shows the excellent agreement (0.2%) between Monte Carlo and data in the center of the detector. A neutron source was deployed for calibrating the simulation at higher energy (from 2.2 MeV to 9.3 MeV) and at large radius. It is discussed in section 4.2.2.

^{222}Rn contamination was used to test position reconstruction and energy resolution via the ^{214}Bi and ^{214}Po decay coincidence (see ^{222}Rn decay chain in A.1). Resolution in position was found to be about 16 cm and 7% in energy.

(a) *Comparison MC/data for the calibration sources in the center of the detector, from [150].*

(b) *Photoelectron production as a function of the initial γ energy in the center of the detector for 6 different γ sources, from [146].*
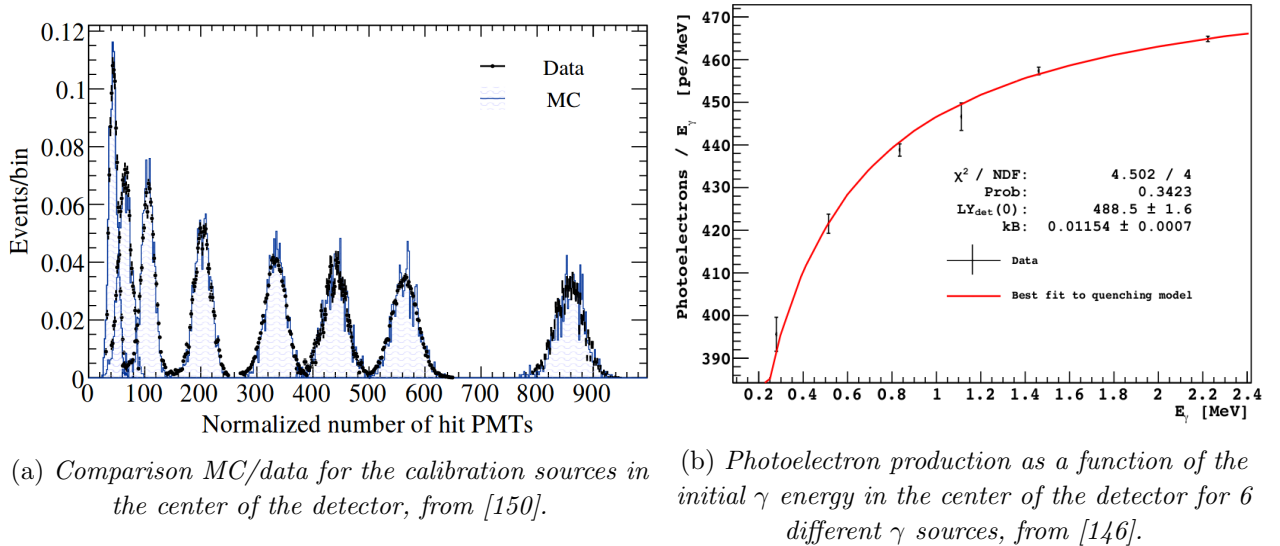
Figure 3.4: *Energy calibration in Borexino using γ sources.*

3.1.3.2 Quenching effect

The amount of light produces in the scintillation process depends on the charged particle crossing the detector, the so called ionization quenching effect. The number of photoelectrons N_{pe} can be described by the empirical Birk's formula depending on the specific energy loss for the charged

particles dE/dx:

$$N_{pe}(E) = \int_0^E \frac{LY_0 \, dE}{1 + k_B dE/dx} \tag{3.2}$$

with LY_0 the scintillation light yield when $E \to \infty$ and k_B the quenching parameter. Equation 3.2 can be rewritten:

$$N_{pe} = Q_e \, LY_0 \, E \qquad \Rightarrow \qquad Q_i(E) = \frac{N_{pe}}{LY_0 \times E} \tag{3.3}$$

calling Q_i the quenching factor, depending on the energy and the particle i.

Quenching is minimal for high energy electrons since dE/dx is sufficiently small for having $Q_e \sim 1$ [145]. The quenching effect is stronger however on low energy electrons. γ in an other hand is not directly emitting scintillation light. Passing through the liquid, it induces Compton electrons which scintillate in the detector. The quenching effect is then the superposition the quenching of several low energy electrons. This leads to a stronger quenching effect for γ than for primary produced electrons. Q_γ is depending on the γ energy and varies from 0.8477 at 300 keV to 0.9867 at 2 MeV.

Finally, heavy particles such as α have a maximal quenching effect as their dE/dx is high with respect to electron one. The Q_α values spread from around 0.0789 at 5.31 MeV to 0.1249 at 8.78 MeV [146]. This factor 13 between the quenching effect on α and β/γ is of great importance as α's fall in the region of interest for ^{7}Be ν when converted in the electron equivalent energy scale. As we will see, this effect shifts away any α contamination for the ^{8}B rate measurement.

3.1.3.3 Cerenkov effect

The Cerenkov effect is highly depending on the energy and nature of the particle. The fraction of observed light emitted by Cerenkov radiation is around few percent with respect to scintillation. This is taken into account in the simulation. As an example, a 3 MeV γ is inducing 8 pe while a 3 MeV electrons will induce around 12 pe by Cerenkov radiation.

3.1.3.4 α/β discrimination

α and β/γ induce different scintillation time profiles. The α charge signal spectrum shape is broader in time due to more delayed scintillation with respect to β/γ scintillation. Based on this intrinsic difference in scintillation pulse shapes, discrimination methods were investigated: Gatti parameter [151], tail to total ratios, Kolmogorov tests etc (see [152] for details). The Gatti discriminant resulted the more powerful in the energy range of interest. It is a learning algorithm. A radon source was used for calibrating the α/β discrimination.

Let's $\alpha(t)$ and $\beta(t)$ be the time probability density distribution of respectively α and β. In reality these spectra are discretized leading to the binned distribution α_i and β_i with i from 0 to N. Ev_i is the time distribution of one event, binned in the same way. The Gatti parameter is then defined as:

$$g = \sum_i^N \left(Ev_i \times \left(\frac{\alpha_i - \beta_i}{\alpha_i + \beta_i} \right) \right) \tag{3.4}$$

Following equation 3.4, each observed bin Ev_i is weighted with the power to discriminate α with respect to β. Having a positive Gatti parameter implies that the event shape is closer to the α PDF

than β one. Figure 3.5 shows this parameter value for the ^{214}Bi and ^{214}Po measurement that were used as reference shapes.
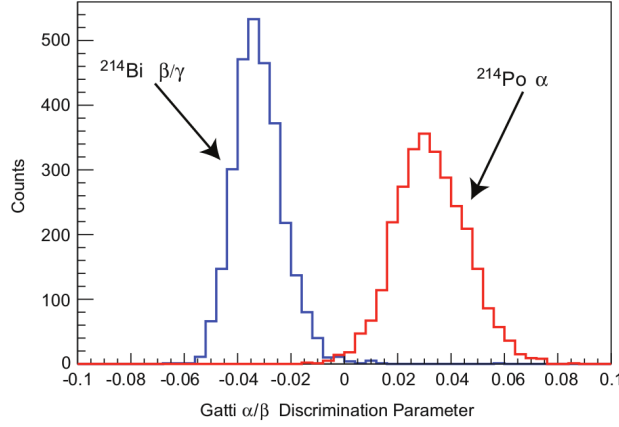
Figure 3.5: *Gatti parameter spectrum for the ^{214}Bi-^{214}Po events analysis [143]. The discrimination is clearly visible.*

3.1.4 Target volume

3.1.4.1 Buoyancy and leaking

At 15 °C, the scintillator density is estimated to be $d_{PC+PPO} = 0.8802 \pm 0.0004$ g.L^{-1} while buffer is $d_{PC+DMP} = 0.8810 \pm 0.0004$ g.L^{-1}, a force is therefore pushing upward the inner nylon vessel with an intensity of $\sim$2.5 kN. The thermal difference between top/bottom is of 5 °C maximum, inducing a limit on the upward or downward force of 13 kN [153]. In April 2008 a change in the IV volume was measured due to a leak between the IV and the inner buffer. This leak estimated at 15.96 m^3/month was contained by changing the DMP doping inside the buffer from 5 g.L^{-1} to 2 g.L^{-1}. This decrease of the DMP concentration diminishes the buoyancy force from 2.5 kN to 250 N and the leak to 1.5 m^3/y [146]. Besides, thermal insulation of the whole Borexino detector was achieved in 2016.

3.1.4.2 Vessel shape

Due to the buoyancy force described above, the Nylon inner vessel was deformed. This is a critical aspect in the ^{8}B analysis which consider the whole active volume as the fiducial volume as well as for the SOX experiment to calculate the number of proton targets.

Six cameras were deployed originally for calibration source position measurement, a seventh added to monitor trapped gas pocket at the top of the vessel during filling. The accuracy demanded on reconstructing position was 2 cm. All of the cameras are settled on the SSS, taking picture at R=660 cm. The cameras are CCD Cameras Kodac DC290 with fish eye lens for having a 183°field of view. Their radioactive contaminations in ^{238}U and ^{232}Th is negligible with respect to PMT. Taking picture requires to illuminate the whole detector, and hence turning off the high voltage of the PMTs. This turn on/off effect is deteriorating PMTs. Figure 3.6a is displaying the picture taken by one camera in 2017. Technique to reconstruct a three-dimensional coordinates from two-dimensional photographies is called photogrammetry. This technique have been widely studied

in [154]. Considering a spherical distribution with z being the vertical, we have three spherical coordinates: the radius R, and two angles: the inclination (θ as z= $\cos(\theta)$) and the azimuth (ϕ). The user has to point with a cursor the hallow vessel border. The task is arduous as the vessel has been built for being transparent. The algorithm is then reconstructing the (R,θ) position from the selected pixel in the picture. Borexino is assumed to be symmetrical around the vertical axis as no force is supposed to deform a side with respect to an other side. From Figure 3.6b, 36 points (R,θ) are extracted constituting the "official" vessel shape. The vessel shape is then described as a R(θ) distribution.
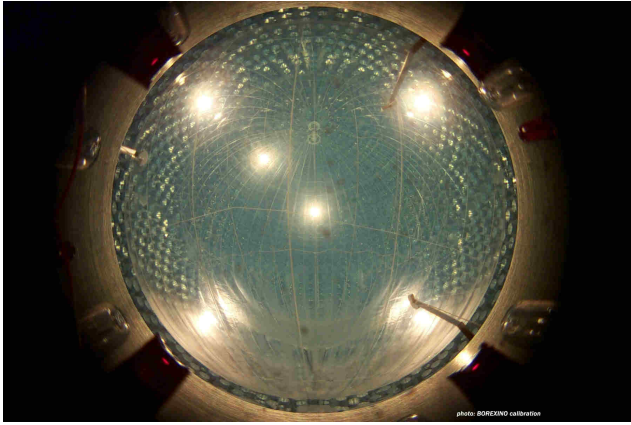
(a) *Photo from one CCD camera taken in 2017. The vessel position is extrapolated from the pixel location of the vessel border as determined by the user.*
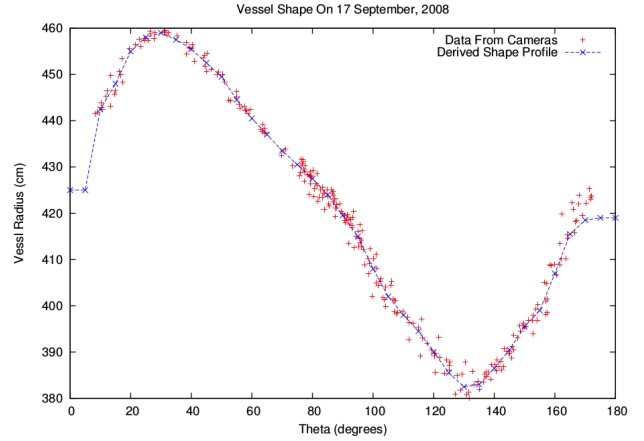
(b) *The vessel shape is the average of positions defined by the users. It is always described as a R(θ) function, the distribution being symmetrical with respect to z or ϕ.*

Figure 3.6: *Vessel shape determination using the CCD Cameras from [154].*

Independently on this method, the vessel shape is given by the surface radioactive background measurement. The ^{210}Bi decays is used as an indicator of the vessel surface. Assuming azimuthal symmetry, the R(θ) distribution is fitted with high-order polynomial function with a vessel Gaussian width. The end-points are fixed to R=4.25 m because of rope fixation. This method does not need to turn off the PMTs, allowing to weekly estimate the shape without degrading the photomultipliers. This method has been cross checked by the CCD camera measurement during the calibration phase of the detector and the precision is of the order of 1%.

3.1.4.3 Volume estimation

The distribution is integrated, divided in North and South poles with a special care for extreme points ($\theta = 0$ and $\theta = 180$). The main error on this measurement is assumed on the determination of the edge of the vessel within 2 cm (approximately 2 pixels). Adding this error on each experimental points, the volume can be determined within 1.5%.

Besides, from density measurement, the number of electrons/free protons in the target volume N_e/n_p is estimated to be [44]:

$$N_e = (3.307 \pm 0.003) \times 10^{31} \text{ e}^-/100 \text{ tons} \tag{3.5}$$

$$N_p = (6.1) \times 10^{30} \text{ free proton}/100 \text{ tons} \tag{3.6}$$

3.2 Solar program

3.2.1 Signal

As described in section 1.2 solar neutrinos are ν_e emitted up to 15 MeV. Borexino detects them using elastic scattering on electrons. Elastic scattering (ES) allows to investigate low energy netrinos because of the absence of energy threshold. ES is sensitive to any active neutrinos, with cross section depending on the flavour as shown in Figure 3.7.
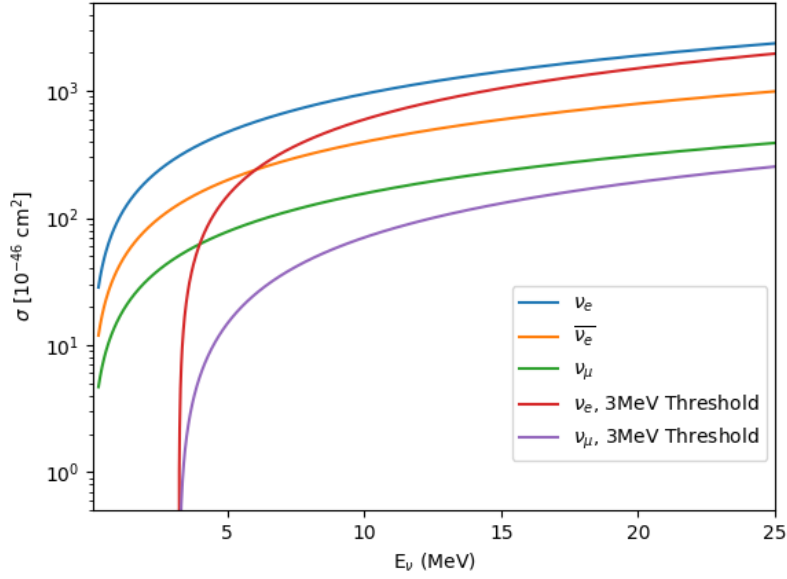
Figure 3.7: *Elastic scattering cross section depending on the neutrino energy E_ν. The cross section is given without any threshold and with a 3 MeV threshold on the recoiled electron (threshold for the ^8B analysis).*

The rate expected in the Borexino detector is the product of the electrons density (N_e) by the cross section ($\sigma_\alpha(E)$) and the neutrino flux $\phi(E)$. Figure 3.7 is giving the cross section for two neutrino flavour, depending on E_ν [14].

$$R = N_e \int \phi(\sigma_e P_{ee}(E) + \sigma_{\nu_{\mu,\tau,s}}(1 - P_{ee}(E))\mathrm{dE} \tag{3.7}$$

Observing neutrino, the visible energy in Borexino, E_{vis} is not directly the neutrino energy E_ν but the recoil energy of the electron excited by ES:

$$E_{\mathrm{vis}} = \frac{E_\nu^2(1 - \cos(\theta))}{m_e c^2 + E_\nu(1 - \cos(\theta))} \tag{3.8}$$

with θ the angle of scattering of the incoming neutrino. The maximal transferred momentum is then:

$$E_{\mathrm{vis}}^{\mathrm{max}} = \frac{2E_\nu^2}{m_e c^2 + 2E_\nu} \tag{3.9}$$

The observed rate is depending on the energy threshold of the experiment. This threshold is applied on the visible energy, therefore on the scattered electrons. As shown in figure 3.7, setting a 3 MeV

threshold in the visible energy does affect the measurement of 10 MeV neutrinos.

The solar flux on Earth of ^{7}Be is 4.5×10^9cm^{-2}s^{-1} and the ES cross section for $^7Be\nu_e$ on electrons is 5.9×10^{-45} cm^2 [155] leading to around 26 events expected per day between 250 and 665 keV for a 100 t fiducial volume. This expected rate is making it a challenge. The expected flux for different metallicity are listed in section 1.2. Table 3.1 lists the maximal energy following equation 3.9 and the signal expected given flux, cross section and energy spectra. The expected signature on any

ν_e	pp	^{7}Be*	pep	^{8}B	^{13}N	^{15}O	^{17}F
E_{vis}^{max} [MeV]	0.264	0.665	1.22	16.34	0.983	1.51	1.52
ϕ_{HM} [38]	131.1 ± 2.4	46.0 ± 2.9	2.7 ± 0.1	0.46 ± 0.01	2.3 ± 0.4	2.6 ± 0.4	0.07 ± 0.01
ϕ_{LM} [37]	132.2 ± 2.4	42.0 ± 2.6	2.8 ± 0.1	0.38 ± 0.05	1.7 ± 0.2	1.8 ± 0.3	0.04 ± 0.01

Table 3.1: *Solar neutrino expected flux [cpd/100t] in Borexino depending on the high (HM) or low metallicity (LM) model as well as the maximal visible energy. Extracted from [44, 156].*

solar neutrino measurement is the energy shape. Many different backgrounds pollutes all energetic range of Borexino observations.

3.2.2 Background

The background can be divided depending on the its origin: external, internal and surface contamination.

External

The onion layers structure of Borexino had been developed in order to tag any external contamination entering the Inner Vessel.

Muons, although highly depleted by the rock shielding, have a residual flux in Hall C of 1.2 μm^{-2}h^{-1} [157]. This background is tagged with a 99.992% efficiency or higher using the Outer Detector. However, muons are inducing irreducible backgrounds by spallation process when they cross the detector. Neutrons and cosmogenics are produced along the track of the muons. Neutron capture is well constrained and can be veto inside the detector.

Cosmogenics are radioactive nuclei produced by spallation when cosmic muons are crossing the detector. The most abundant cosmogenic is ^{11}C (β^+, Q$_\beta$=1.98 MeV, T$_{1/2}$=1222 s) followed by ^{7}Be(EC, E$_\gamma$=477 keV, T$_{1/2}$=53.2 days) and ^{10}Be (β^-, Q$_\beta$=556 keV, T$_{1/2}$=1.51$\times 10^6$ y.) [158, 159]. ^{12}N, ^{12}B, ^{8}He, ^{9}C, ^{9}Li, ^{8}B, ^{6}He,^{8}Li,^{11}Be,^{10}C are expected as well [160]. Some of them have a lifetime longer than few seconds implying an unrealistic dead-time if decision would be made to apply strict veto on the whole detector. This critical aspect was partially solved by applying three fold coincidence (TFC), pulse shape analysis, discriminations on such events. The TFC requires a good reconstruction of the muon track inside the detector.

External neutron can come from either muon interactions in the rock or in the detector material or by (α,n) reactions from natural radioactivity of the rock walls of the LNGS. Cosmogenic neutrons have a wide energy spectrum from few eV to GeV [161] as illustrated in figure 3.8 while neutrons from the rock are mainly thermal and epithermal. Neutrons are passively shielded by the Outer

(a) *Comparison of the cosmogenic neutron flux depending on the underground laboratory,*

(b) *Neutron flux emitted by (α,n) reaction in the LNGS rock,*
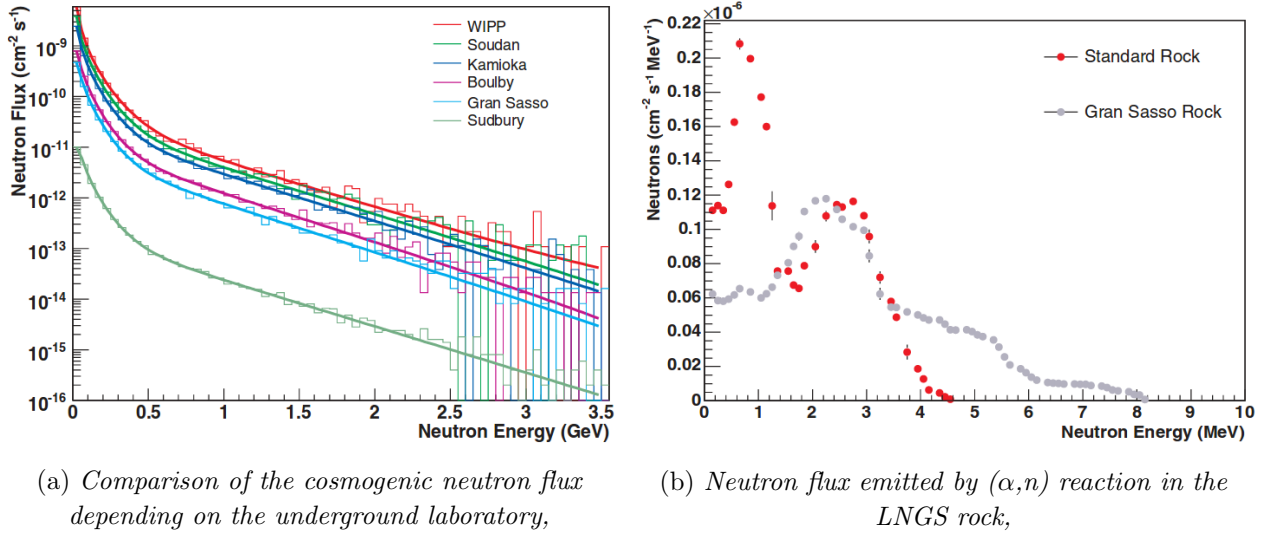
Figure 3.8: *Estimation of the epithermal neutron flux depending on their energy, from [161].*

Detector. Thermal neutron are efficiently captured in water reducing this neutron flux by a 8 order of magnitude. 2 m of water and 2 m of buffer thermalised most of the fast neutrons before they reach the IV.

Internal

Internal background is mainly composed of intrinsic radioactive contamination of detector materials.

^{14}C (β^-, $T_{1/2}$=4700 y. and Q_β=156 keV) is produced by muon spallation on ^{14}N via ^{14}N(n,p)^{14}C. The relative abundance of this isotope in nature is around 1.2×10^{-12}g/g. This contamination is very important as the scintillator of Borexino is made of carbon-based chains. Its strong presence would induce pile-up on any measured charge. To decrease this background to the 10^{-18} g/g reached in Borexino, the oil was extracted in underground reservoirs where most of the ^{14}C has decayed [157].

^{238}U and ^{232}Th chains (see A.2, A.1) are natural radioactive isotopes present in every material. One of the main achievement of Borexino was the purification of these contaminations. The 10^{-16} g/g requirements were over-satisfied with respectively 10^{-17} g/g and 10^{-18}g/g of ^{238}U and ^{232}Th assuming secular equilibrium. Out of the ^{238}U and ^{232}Th chains, ^{222}Rn and ^{220}Rn are emitted. They are both dangerous element as they form an inert gas diffusing in air and in liquid. Continuous purification of the air enables reducing the contamination from 2 kBq.m^{-3} to 100 Bq.m^{-3} [157]. Radon, in particular, is more soluble in pseudocumene than in air, forcing Borexino to be completely airtight. The radon can emanate from any surface, decaying in liquid in contact with the material, hence the second nylon vessel to contain any PMT emanating radon solved in the buffer.

^{40}K is part of the natural radioactive contamination decaying either by β decay (89%) with a Q_β of 1.32 MeV or by electronic conversion (11%) emitting a 1.46 MeV gamma. The concentration of natural potassium in Borexino scintillator has been estimated to be 10^{-14}g/g.

Finally ^{85}Kr and ^{39}Ar are radioactive isotopes present in the hall C air. They are both β emitter and can easily mix with air exposed liquid. ^{85}Kr is an important contaminant for the ^{7}Be measurement has its Q_β of 690 keV is very close from the maximal visible energy of ^{7}Be. Figure 3.9b illustrates the importance of the low ^{85}Kr contamination for any ^{7}Be neutrino measurement.

Surface

The surface contamination is due to the intrinsic radioactivity of Uranium and Thorium in the nylon vessel membrane. This contamination is used for determining the shape of the vessel using the events identified as ^{210}Bi signal in the 800-900 keV region [44].

3.2.3 Results

^{7}**Be** Borexino collaboration published in 2008 the first observation of ^{7}Be solar neutrino spectrum [162]. At such low energy, the main issue was to strongly confine background. The ^{14}C(β^-, Q_β =156 keV) cosmogenic defined the low energy threshold for the ^{7}Be analysis. Irreducible radioactive contamination in this range is due to ^{210}Bi (β^-, Q_β =1.16 MeV) (fitted) and ^{210}Po (α, 5.41 MeV) (subtracted). The low level of ^{210}Bi enables to be sensible to the ^{7}Be shoulder as this illustrated in Figure 3.9b. The ^{210}Po emanates from ^{222}Rn and the induced α is subtracted on an event by event basis and result is displayed in figure 3.9a. Finally, ^{85}Kr contamination was observed. ^{85}Kr is an anthropogenic fission product [156] and is a potential show stopper as its energy spectrum is superimposed with the ^{7}Be as displayed in figure 3.9b. The first measurement published in 2008

(a) *Effect of the fiducial cut in the final neutrino spectrum between as well as the quenching on the α contaminant.*

(b) *Measurement of the ^{7}Be spectrum by fitting the different components at this range [162].*
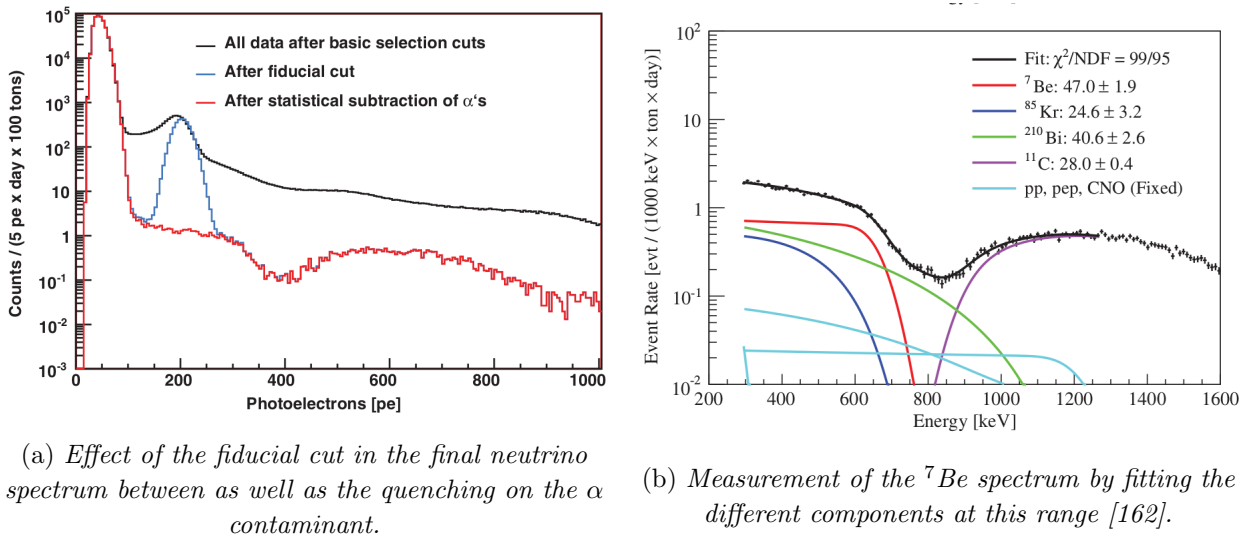
Figure 3.9: *The ^{7}Be solar neutrino measurement realised in Borexino.*

and based upon 192 live days is 49 ± 5cpd/100t, confirmed in 2011 (for 740 live days) at 46.0 ± 2.1. This corresponds to a ^{7}Be solar flux, $\phi_{^7Be}$:

$$\phi_{^7Be} = (4.84 \pm 0.24) \times 10^9 \mathrm{cm}^{-2}\mathrm{s}^{-1} \tag{3.10}$$

The total uncertainty on this measurement is less than 5% which is smaller than the theoretical uncertainty on the Standard Solar Model prediction.

^{8}**B** In 2010, the collaboration released the first result of ^{8}B solar neutrinos shape measurement in scintillator [163]. Based upon 345.3 days live-time, unlike other experiments, the final spectrum is not fitted. Indeed, one of the key point of the ^{8}B measurement is to test MSW effect in the transition regime. To achieve this goal, no spectrum should be inferred. The strategy is to remove on an event-by-event basis most of the radioactive, cosmogenic and external background and to subtract the

residuals. The fiducial volume is 100 t with a radial cut at 3 m and the energy threshold is 3 MeV. One of the purpose of this thesis is to discuss ^{8}B measurement and background, therefore only the result of the 2010 analysis will be reported (above 3 MeV):

$$\phi_{8B} = (2.4 \pm 0.5) \times 10^6 \text{cm}^{-2}\text{s}^{-1} \tag{3.11}$$

Figure 3.10 is displaying the comparison of the measured flux with the two most common use metallicity models.
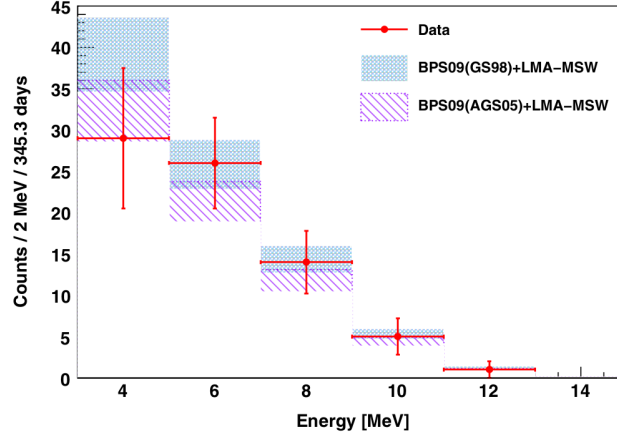
Figure 3.10: *Comparison of the ^8B measured spectrum with two different standard solar models (high metallicity GS98 [38] and low metallicity [39]).*

pp   The pp neutrinos measurement was done during Borexino phase II [41], after an intense purification phase in 2010 and 2011 reducing ^{210}Bi and ^{85}Kr. The pp contribution is fitted at low energy, [150,600] keV, as illustrated in Figure 3.11a.

The measured rate is 144±16 cpd/100 t leading to a rate of:

$$\phi_{pp} = 6.6 \pm 0.7 \times 10^{10} \text{cm}^{-2}\text{s}^{-1} \tag{3.12}$$

The high flux measured is the evidence that proton-proton fusion is at the origin of the sun fusion process. This is in agreement with the SSM predictions but the error is too large to distinguish among metallicity models which predicts respectively $5.98 \pm 0.04 \times 10^{10}$cm^{-2}s^{-1} [38] and $(6.03 \pm 0.03) \times 10^{10}$cm^{-2}s^{-1} [37].

pep   The pep neutrinos are produced in a monoenergetic line of 1.44 MeV. Due to elastic scattering on electrons, the expected spectrum is a Compton shape with an end point at 1.22 MeV. As for the ^{7}Be measurement, the most significant contribution is the shoulder of the pep spectrum, but the expected flux is 40 times smaller than with respect to ^{7}Be. The main backgrounds in this energy range are ^{210}Bi and ^{11}C as displayed in figure 3.11b. ^{11}C, decaying via β^+, is produced by muon spallation and the production rate in Borexino is 28.5±0.7 cpd/100t which is ten times higher than the expected *pep* rate. No purification is possible on this element because of its insitu production and low lifetime. The Three Fold Coincidence was developed in order to identify ^{11}C on an event-by-event basis. It relies on the coincidence between the muon track, a neutron emission and the ^{11}C decay, correlated in space and time. This technique enable to reduce by one order of magnitude

(a) *pp-rate measurement with Borexino by fitting the pp contribution in the low energy spectrum [41].*

(b) *pep-rate measurement with Borexino by fitting the pep contribution (bottom) after background identification and subtraction (top) [115].*
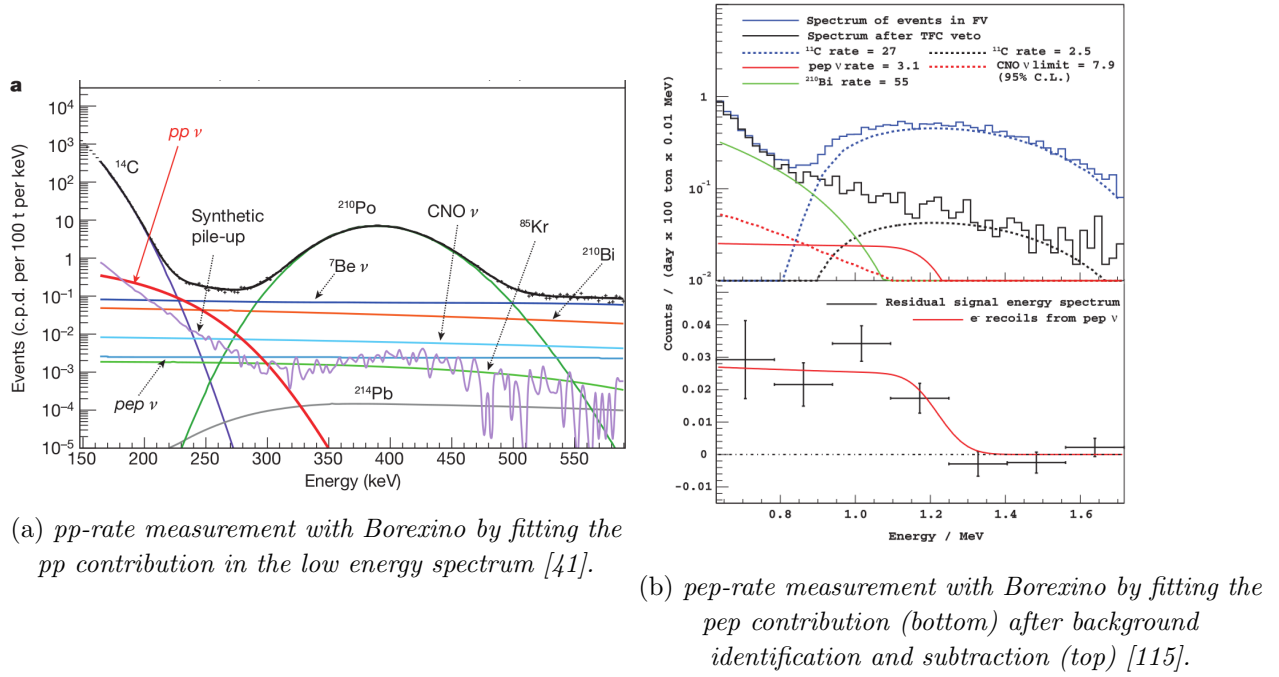
Figure 3.11: *Illustration of the pp and pep flux measurement and backgrounds.*

the ^{11}C contamination with a 51.5% loss of exposure. Finally, pulse shape discrimination was used knowing that positron prior to annihilation can form positronium (electron-positron bound state). Positronium has two possible ground states called ortho and para-positronium. If para-positronium has a very short lifetime (~ 125 ps in vacuum), ortho-positronium decays constant is longer (142 ns in vacuum) [44]. In Borexino scintillator, the ortho-positronium mean life-time has been measured to be ~ 3 ns with a formation probability of ~ 50 % [164]. This effect induces different scintillation light shape between electron and positron, opening the way to pulse shape discrimination. The measured rate in Borexino for two years of data taking [115] is 3.1 ± 1.1 cpd/100 t leading to neutrino flux of:

$$\phi_{pep} = 1.6 \pm 0.3 \times 10^8 \text{cm}^{-2}\text{s}^{-1} \tag{3.13}$$

3.3 The SOX experiment

The Short Oscillation baseline neutrino experiment in BoreXino (SOX) aims at testing the light sterile hypothesis ($\Delta m_s^2 \sim 0.1$ to 5 eV^2) by bringing a very intense radioactive source below Borexino. Sterile neutrino hypothesis is invoked to explain standing anomalies in neutrino oscillation experiments (see section 2.4.1).

3.3.1 Principle

The Gallium and Reactor anomalies could be explained in a (3+1) model with a light sterile neutrino with typically $\Delta m^2 > 1.5$ eV^2 and $\sin^2(2\theta_{14}) \sim 0.14 \pm 0.08$ [127] as displayed in Figure 3.12a. A global fit including the ν_e and $\overline{\nu_e}$ disappearance experiments plus the constraints derived from β measurement in Mainsk and Troitsk highlight narrow widths with $\Delta m^2 \sim 1 - 2.4$ eV^2 [165] illustrated in Figure 3.12b. Using a radioactive emission, the energy of the neutrino is of the order

of 1 MeV. At this energy, scanning the region: $\Delta m^2 \sim 0.1 - 5$ eV^2 demands to set the source from 1 to 10 m to the detector.

(a) Δm^2-$\sin^2(2\theta_{14})$ plane. Allowed region derived from the Gallium (ν_e) and the Reactor ($\overline{\nu_e}$) anomalies [127].

(b) Δm^2-$\sin^2(2\theta_{14})$ plane. Allowed region derived from the Gallium, Reactor anomalies combines with the limit given by Mainz and Troitsk using β spectrum measurement [165].
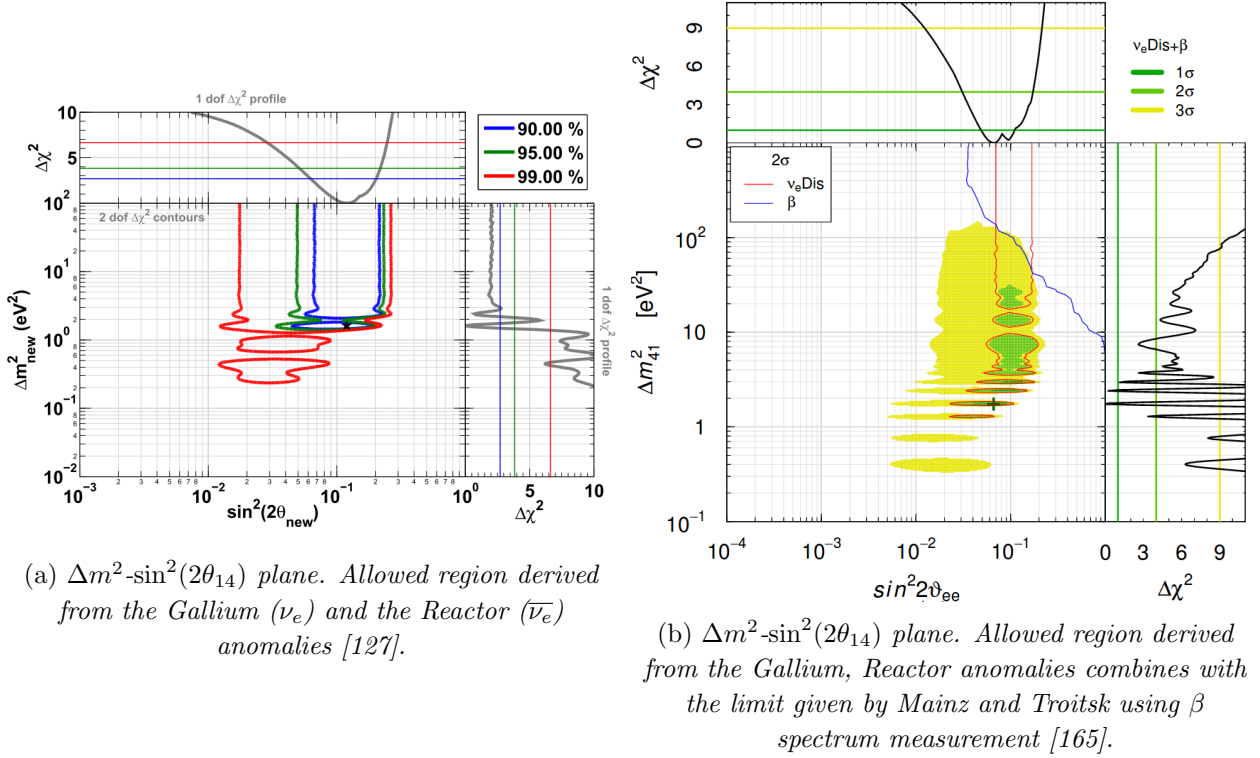
Figure 3.12: *More favorable allow regions for a light sterile hypothesis based on experimental measurement.*

There is no production site of radioactive elements located near to the detector. Due to the very low interaction rate of neutrinos, one needs a very high activity during measurement. For few 10^4 $\overline{\nu_e}$ detected, a PBq source is needed. It will be located in a tunnel under Borexino, 8.4285 m from the center of the detector.

3.3.2 Source candidates

As overlined above, ν_e and $\overline{\nu_e}$ could both be candidates and were eratically investigated in litterature [166, 167, 168]. Some are monochromatic ν_e producer such as ^{37}Ar, ^{65}Zn or ^{51}Cr while others are β continuous spectrum ^{152}Eu, ^{144}Pr, ^{90}Y, ^{42}K or ^{106}Rh.

ν_e candidates

PBq sources of ^{37}Ar and ^{51}Cr have already been successfully used in the Gallium experiments (see section 2.4.1.1). They are indeed both good candidates for source experiments [169].

^{37}Ar has an half-life of 35.0 days and decays through electronic capture into ^{37}Cl. This clean reaction produces exclusively 814 keV ν_e. ^{51}Cr is decaying in ^{51}V via electronic capture as well ($\tau_{1/2} =$27.7 days), emitting four monoenergetic ν_e: 746 keV (81%), 751 keV (9%), 426 keV (9%) and 431 keV (1%) [168] and one 320 keV γ (10%).

Such sources can be produced by neutron irradiation in a nuclear core. ^{51}Cr is produced via ^{50}Cr(n,γ)^{51}reaction. Irradiation of ^{50}Cr can be realised by using enriched chromium as done by the Gallex collaboration [168]. ^{37}Ar is produced via ^{36}Ar(n,γ)^{37}Ar or ^{40}C(n,α)^{37}Ar reactions. Irradiation of ^{36}Ar with thermal neutron is hardly achievable due to the need of inserting ^{36}Ar in pressurized hot gaz or cold liquid phase [170]. The (n,α) reaction, if less probable and demanding fast neutron, has many advantages as the possibility to use dense metalic calcium as a target. The extraction is relatively easy. The source is very safe and without any impurities [117]. One potential disadvantage is the closeness of ^{7}Be ν_e monoenergetic line.

The ^{51}Cr is a serious option considered by the Borexino collaboration and extensively studied [171]. Assuming the source to be 370 PBq and 100 days of data taking, most of the anomaly region would have been covered [166]. The main issue rises from the short lifetime of such source and the absence of nuclear reactor for irradiation close to the detector.

$\overline{\nu_e}$ candidates

With the geoneutrinos measurements [172], Borexino demonstrates its capability on measuring low flux of $\overline{\nu_e}$: 77 $\overline{\nu_e}$ events in 2055.9 days of data with an expected background of 0.73. Therefore, a $\overline{\nu_e}$ source can be considered.

The source decay lifetime has to be long enough for staying very active after few months of transports and production and having a Q_β larger than the IBD threshold: 1.806 MeV. These requirements make the identification of the source challenging as the Q_β and the lifetime are anti-correlated. This problem was solved by identifying couple of radioisotopes. The first nucleus (^A_ZX) should have a long lifetime while the daughter nucleus of reaction ($^A_{Z\pm1}$Y) will have a shorter lifetime and a higher Q value. The first nucleus must have a long lifetime (most probably due to weak interaction). The second reaction releases a neutrino and consequently is due to weak interaction.

$$^A_Z X \rightarrow {}^A_{Z\pm1}Y + e^\pm + \nu_e/\overline{\nu_e}$$
$$^A_{Z'} Y \rightarrow {}^A_{Z'+1}Y + e^+ + \overline{\nu_e} \quad \text{with } Q_{value} > 1.8 \text{ MeV}$$
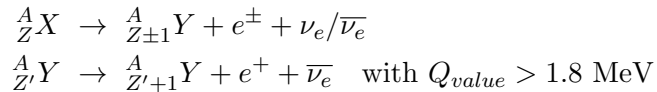
From [169, 173], 4 couple candidates can be identified and are listed in table 3.2.

isotopes	lifetime	Q_β	Cumulative FY [%]	
			^{235}U	^{239}Pu
^{42}Ar-^{42}K	33 y.	3.53 MeV	-	-
^{90}Sr-^{90}Y	28.9 y.	2.28 MeV	5.78	2.1
^{106}Ru-^{106}Rh	372 d.	3.55 MeV	0.401	4.35
^{144}Ce-^{144}Pr	285 d.	3.00 MeV	5.7	3.74

Table 3.2: *Potential candidates for SOX source extracted, [169].*

^{42}Ar can be produced through neutron irradiation of ^{41}Ar. ^{41}Ar has a very short half-life of 109 ms leading to produce ^{42}Ar through double neutron capture from ^{40}Ar [173]. Cross section for a double capture is low and ^{42}Ar candidate has been rejected. ^{144}Ce, ^{106}Ru and ^{90}Sr are common fission products from nuclear reactors. The more abundant product among them is ^{90}Sr, closely

followed by ^{144}Ce. However, the ^{144}Ce higher Q$_\beta$, increasing the statistics of observed events above the IBD threshold, makes ^{144}Ce a better candidate than ^{90}Sr. Finally, ^{144}Ce is easier to extract from reactor ore than ^{106}Ru, though ^{144}Ce-^{144}Pr has been chosen as the best candidate to realise an antineutrino source for short baseline experiment.

3.3.3 Ce/Pr source

^{144}Ce is decaying in ^{144}Pr via β decay with a half-life of 285 days. ^{144}Pr is then decaying into ^{144}Nd via β decay emitting the $\overline{\nu}_e$ that will be observed in Borexino, with a half-life of 17 min. ^{144}Nd is nearly stable. The ^{144}Pr short decay means that ^{144}Ce and ^{144}Pr are always considered in secular equilibrium. The decay process is summarized in figure 3.13.
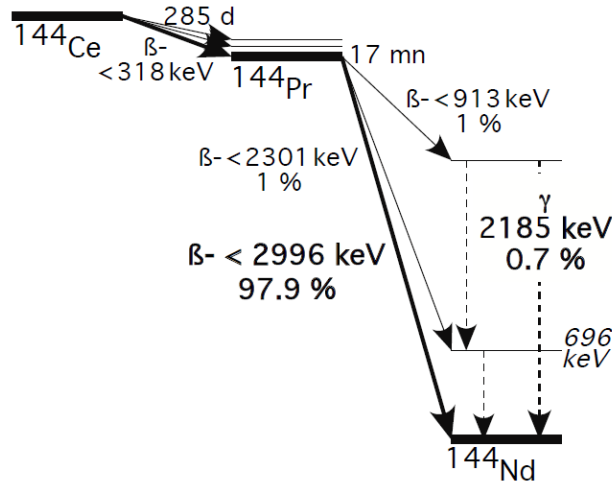
Figure 3.13: ^{144}Ce - ^{144}Pr source decay scheme

^{144}Pr emits a 2.185 MeV gamma emission in 0.7% of the case. Considering a PBq source, this gamma emission induces potential background in Borexino and demands an extra biological protections developed in section 5.5.2.

The knowledge of the mean energy per decay of ^{144}Ce and ^{144}Pr as well as the low energy ^{144}Pr beta shape are important for the SOX measurement, measuring the source from calorimetric measurement as well as predicting the IBD rate inside the detector. Beta spectrum can be partially predicted using theory first developed by Fermi. In this framework, beta transitions are classified following nuclear spin change (ΔI) and parity modification ($\Delta \pi$). Transitions with $\Delta \pi = 0$ are called allowed with respect to forbidden one. During forbidden transion, the electron or the neutrino leaving the nucleus must carry angular momentum. Among the allowed transitions: $\Delta I = 0$, via vector current, is the specific case treated by Fermi at his time and is called "super-allowed". Transitions are then ordered depending on the angular momentum they carry l and depending on vector (Fermi-like) or axial (Gamow-Teller like) transition. Table 3.3 and 3.4 list the different beta branches, Q$_\beta$ and transition for ^{144}Ce and ^{144}Pr.

The three ^{144}Ce branches as well as the two dominant ^{144}Pr branches are forbidden, meaning $\Delta \pi = \pm 1$ and first non unique or first unique, meaning respectively $\Delta J = 0, \pm 1$ or $\Delta J = \pm 2$. For this purpose, the first branch of ^{144}Pr is the highest contributor to the released heat as well as responsible of about 99.8% of the detected neutrino in Borexino due to the IBD threshold [174].

Branch	Branching ratio [%]	Q_β[keV]	transition
^{144}Ce - 1	76.5	318.7	First non unique forbidden
^{144}Ce - 2	3.9	238.6	First non unique forbidden
^{144}Ce - 3	19.6	185.2	First non unique forbidden

Table 3.3: ^{144}Ce beta decay branches from ground 0^+

Branch	Branching ratio [%]	Q_β[keV]	transition
^{144}Pr - 1	97.9	2996.9	First non unique forbidden
^{144}Pr - 2	1.04	2300.4	First unique forbidden
^{144}Pr - 3	1.05	811.8	Allowed
^{144}Pr - 4	0.67	913	First non unique forbidden
^{144}Pr - 5	0.14	1436.5	First unique forbidden

Table 3.4: Main ^{144}Pr beta decay branches ($\mathcal{B}_R > 10^{-3}$) from ground 0^-

The ideal beta shape is derived from the Fermi Golden Rule derived from the phase space accessible for final state [12]. The Fermi function, $F(Z, p)$, is taking into account Coulomb interaction between emitted electron and protons of the nuclei. The expected shape from Fermi theory can be written [12]:

$$N(W) \propto pW(Q - W + m_e)^2 F(Z, W)C(W) \qquad (3.14)$$

with p the electron momenta, W the total beta energy (p+) and C(p,q) an additional shape factor taking into account forbidden transitions and nuclear matrix elements. Those corrections take into account finite size effect on electromagnetism and weak interaction, screening effect, radiative corrections, etc. Full description can be found in [175]. The Fermi function can be derived theoretically. It has already been computed numerically for discrete values [176] and modelled [177, 178]. The shape factor can be empirically described as:

$$C(W) \propto 1 + aW + \frac{b}{W} + cW^2 \qquad (3.15)$$

with (a,b,c) parameters experimentally measured. In a first non-unique forbidden transition however, a and c are not theoretically motivated. Six independent measurements of the first ^{144}Pr branch shape factor have been done from 1956 to 1973 and are summarized in [178, 174]. They are not fully consistent with each others. Figure 3.14a is showing the variation of the shape factor depending on the set of data used. Figure 3.14b is showing the comparison of the expected IBD events depending on the shape factor used. The variation between the two extremes IBD events predictions is 9% while the prediction on the heat release vary from 206.6 W/PBq to 213.4 W/PBq, leading to a 3% discrepancy depending on measurement. This is not acceptable as the calorimetric measurement is expected to be precise in the 1% level. Independent new measurements have to be done for the SOX experiment. One of this potential experiment is described in section 7.4.
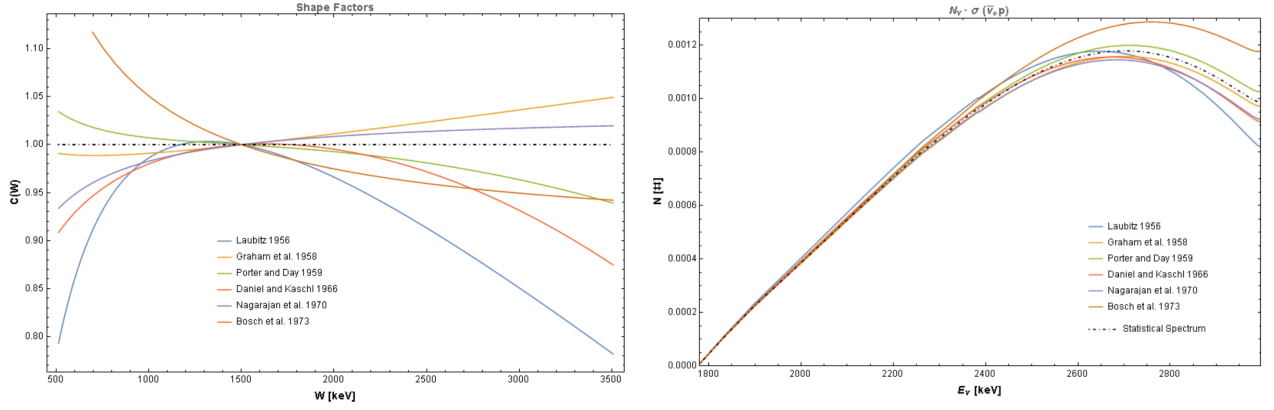
(a) *Shape factor variations depending on measurement normalized to be one at 1500 keV,*

(b) *Expected rate seen in Borexino convolving ^{144}Pr spectrum measurements and IBD cross section,*

Figure 3.14: *Variation of the ^{144}Pr spectrum depending on past measurements, study made in [178]*

3.3.4 Sensitivity

The expected number of events (N) in a small detector volume (d^3x) at a distance L considering a point-like source with an initial activity A_0 [173] is:

$$\frac{\mathrm{d}N}{\mathrm{d}t\mathrm{d}E\mathrm{d}^3x} = A_0 e^{-\frac{t}{\tau_{Ce}}} \frac{\rho_p}{4\pi L^2} \sigma_{\mathrm{IBD}}(E) S_{\mathrm{Ce}}(E) P_{ee}(L,E) \tag{3.16}$$

with ρ_p the free proton density, S_{Ce} the ^{144}Pr neutrino emission spectrum, σ_{IBD} the IBD cross section, $P_{ee}(L,E)$ the survival probability of $\overline{\nu_e}$, assuming a two flavour oscillation case (see section 2.3.1.3):

$$P_{ee}(L,E) = 1 - \sin^2(2\theta_{ee})\sin^2\left(\frac{\Delta m_{41}^2 L}{4E}\right) \tag{3.17}$$

Reconstructing the position and the energy of the event within Borexino, the typical oscillation spectrum for two different Δm_{41}^2 and a comparison with a no oscillation scenario is displayed in figure 3.15a. The SOX experiment scans the light sterile phase space by rate and shape measurements.

- Rate analysis is based on the total number of events (N_ν) with respect to the predicted one from activity measurement,

- Shape analysis is based on observing evolution of the number of events depending on L/E inside the detector.

Both method can be used in the same time to increase the sensitivity of the SOX experiment to the Reactor Antineutrino Anomaly. The three technics are compared in figure 3.15b.

3.3.5 Source activity

The activity of the source will be measured using two calorimeters developed respectively by CEA-Saclay and TUM/INFN collaborations. The source will release between 750 and 1000 W (100-130 kCi). The power is the product of the activity by the mean energy released by ^{144}Ce decaying to ^{144}Nd. If the only visible $\overline{\nu_e}$ in the detector are those emitted by ^{144}Pr due to the IBD
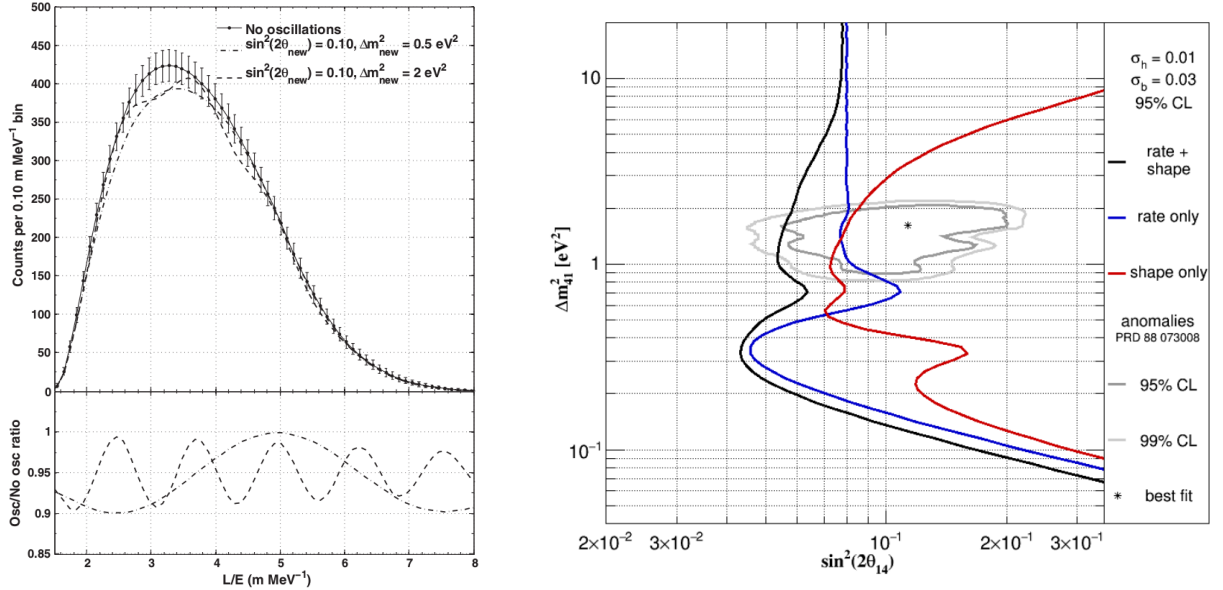
(a) *Oscillation spectrum in L/E for different sterile parameters corresponding to 1.5 y of data taking with a 3.7 PBq source, from [173].*

(b) *Sensitivity plot on the ($\sin^2(2\theta_{14}$, Δm_{41}^2) phase space. The rate+shape analysis covers the reactor antineutrino anomaly at 95% confidence level [179].*

Figure 3.15: *The SOX expectation*

threshold, the mean energy of the ^{144}Ce β decay is playing a role in this conversion factor.

Both calorimeters relie on converting a thermal elevation (ΔT) of a circulating fluid (water) into a power (P) using:

$$P = \phi c \Delta T \tag{3.18}$$

with ϕ the water flow and c its heat capacity. Each calorimeter is designed to measure the power within 1%. Figure 3.16 is displaying the evolution of the SOX sensitivity to the sterile neutrino with respect to the precision on the heat measurement.

As described in section 5.5.1, for biological protection, the tungsten shield surrounding the source capsule is 19 cm thick. The calorimeters will measure heat coming out of this tungsten layer.

Genoa-Munich calorimeter

The apparatus of the Genoa-Munich calorimeter is displayed in Figure 3.18. The heat exchanger is a 20 mm thick copper cylinder surrounding the source shield. It is encapsulated in a stainless steel vacuum tank. The tank is not sealed to avoid any overpressure in case of water leaking from the heat exchanger to the tungsten shielding. The cover is installed at the top of the tank on a O-ring and the recquired vacuum is 10^{-7} bar. The radiation loss is minimized by using two radiation shields between the heat exchanger and the vaccum tank. Water circulation is settled in the heat exchanger.

From calibration measurement, blind tests were realised in which injected power was measured with a 0.2% precision for a 900 W source.
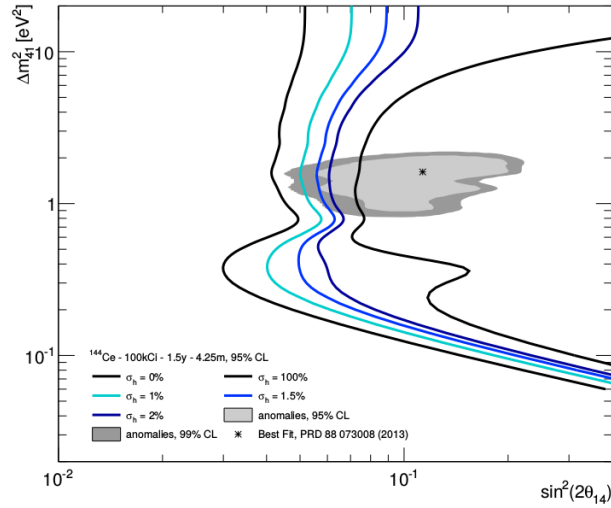
Figure 3.16: *Sensitivity shape depending on error done on the activity measurement. If the error is of 100%, the experiment is then only shape sensible [180].*
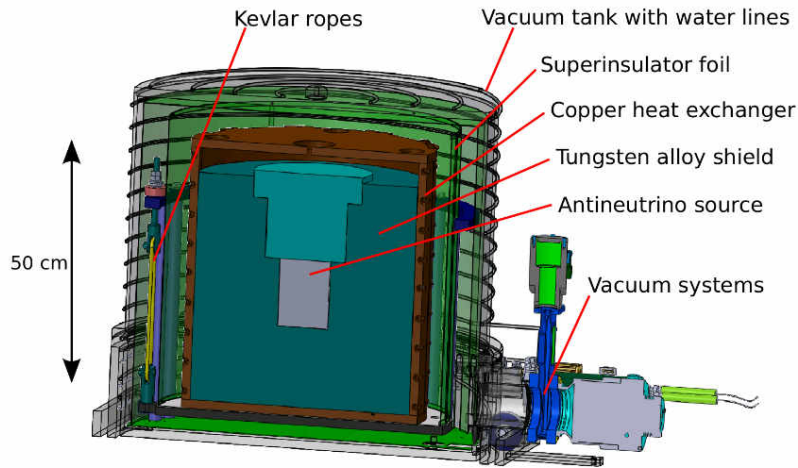
Figure 3.17: *Genoa-Munich calorimeter using heat exchanger under vacuum [181].*

Saclay calorimeter

The Saclay calorimeter heat exchanger is the cooling liquid. The tungsten shield is directly immersed in water. Water is contained in an aluminium shield suspended in a vacuum tank. The water is then circulating for temperature and flux measurement.
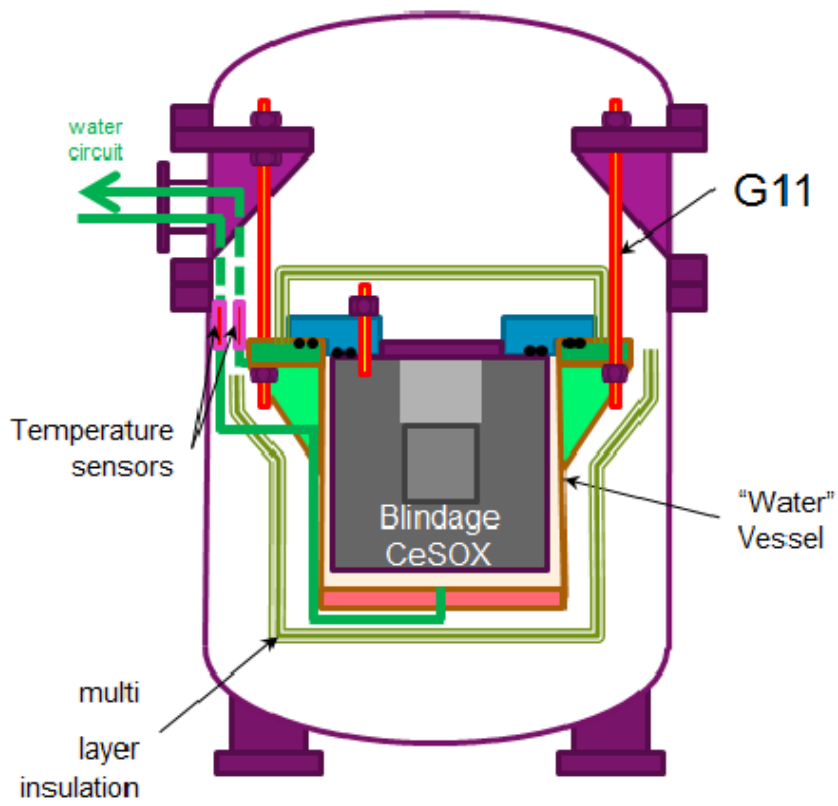
Figure 3.18: *Saclay calorimeter using heat exchanger in water.*

Chapter 4

^{8}B ν_e rate measurement

Contents

This chapter describes the solar ^{8}B ν_e rate measurement above 3 MeV in the entire active volume and on the data from January 13th, 2008 to December 18th, 2016. The total exposure is 1506.48 t.y.

The first measurement of ^{8}B ν_e by the Borexino collaboration was published in 2010 [163]. The fiducial volume was set to the innermost 3 m sphere ($\sim$100 tons) and the analysis was based on 488 livedays from July 2007 to August 2009. The total exposure was of 133.61 t.y. As in the previous analysis, we set a 3 MeV threshold to get rid of the gamma from ^{208}Tl contamination

present in the detector periphery (PMTs). Specific problems at large radii (i.e. close to the vessel) are discussed. The strategy of the selection criteria is the same than the one developed in [163].

The background can be divided in three main classes: *internal* (natural radioactive contamination in the active volume), *external* (cosmics and neutron/γ in external part of the detector) and *surface* (events from the nylon vessel). A review of the expected background rate above 3 MeV [163] is listed below.

- muons (1500 counts per day /100 t)
- neutrons (25 cpd/100 t)
- cosmogenics (2.1 cpd/100 t),
- radioactive background inside the vessel (1 cpd/100 t),
- external background (0.05 cpd/100 t).

Alpha radioactive contaminants are not an issue in our energy scale because they lie below 3 MeV due to the light quenching effect for heavy particles, explained in section 3.1.3.2. The expected ^{8}B rate is $\sim$0.25 cpd/100 t.

Some of the backgrounds can be tagged and removed on an event by event basis (see section 4.3) while others (see section 4.4) must be statistically subtracted after the selection cuts (section 4.5).

4.1 Data selection

The data used in this analysis was acquired from January 2008 to December 2016. Periods were removed from the final data set because of radon penetration (2010-2011), trigger issue (2013) and new trigger calibration (2016). The removed periods are listed in table 4.1.

Period	Live time [d]	Reasons
22nd, May 2016 to 10th, July 2016	37.76	new trigger
20th, June 2010 to 21st August 2011	275.11	radon purification $\rightarrow$ high rate of ^{212}Bi-^{212}Po
17th, February 2013 to 31st, March 2013	28.63	removed from official list

Table 4.1: *Excluded period during the 2008-2016 ^{8}B analysis data set.*

4.1.1 Data selection strategy

The Outer Detector (OD) allows for the identification of cosmic rays. A high energy particle crossing the OD is immediately recognized as a muon. If it crosses the Inner Detector (ID) as well it is called internal muon, external otherwise. Crossing detector materials, a muon produces neutrons and radioactive nuclei by spallation. Section 4.3.1 discussed this identification.

Cosmogenic neutrons can travel meters from the muon track before being captured, inducing signals in the active volume. The neutron capture time in Borexino was measured and is equal to 256 μs. A 2 ms veto, the "*neutron cut*", is applied to the entire detector after any external muon.

All cosmogenics above 3 MeV have a lifetime lower than 1.21 s (^{8}Li lifetime) except for ^{10}C and ^{11}Be which are treated separately. A 6.5 s veto, the *"cosmogenics cut"*, is applied to the entire detector after any internal muon.

^{10}C is a long lifetime (τ=27.8 s) cosmogenic produced mainly in coincidence with a neutron. Its lifetime prevents from using a veto on the entire volume after every muon entering the detector as done for the *"cosmogenics cut"*. A three fold coincidence cut is applied, the *"^{10}C cut"*: when an internal muon is detected in coincidence with a neutron, a 0.8 m radius sphere is vetoed during 120 s to get rid of this contamination.

These vetoes induce a dead-time which is detailed in section 4.1.2. Cut inefficiencies are discussed in sections 4.3.2, 4.3.3 and 4.3.4 respectively.

Beside the muon induced vetoes, coincidences are used to select radioactive contamination within the active volume. ^{214}Bi and ^{212}Bi are identified through the BiPo coincidence. ^{214}Bi contamination (Q_β=3.27 MeV) is therefore removed and this selection is discussed in section 4.3.5. ^{212}Bi does not directly threaten our measurement as it decays through β emission with a Q_β lower than 3 MeV but it is an indicator of ^{208}Tl. This is discussed in section 4.4.4.

Removing those elements and asking for events with more than 500 photoelectrons ($\sim$1 MeV), we are left with about 1.1 cpd/100 t of neutrino candidate.

4.1.2 Dead-time

The live time extracted from Echidna data file is $\tau_l = 2063.147$ days. The first 6.5 s of each run are removed in case of muon crossing the detector before the beginning of the data taking. This cut reduces the livetime to $\tau_l = 2062.38$ days.

The previous analysis exploited a different technique to measure cosmogenics and neutron cuts induced dead-time. An uncorrelated sample of ^{210}Po was extracted to estimate ^{10}C cut induced dead-time. The new method described here uses Monte-Carlo technique with fake events in real sample of data.

First, the entire set of data for the ^{8}B time period was scanned to save position and time of external, internal muons and cosmogenic neutrons. Then, fake events were simulated with a fixed rate (5 Hz), uniformly distributed in time and space. Fake events are chronologically sorted and inserted within the data. Cuts were applied to the fake events as for the data. By comparing the number of survived fake events with respect to the all fake events, we extracted the residual live-time. The advantage of this method is to easily take into account overlaps between vetoes.

Figure 4.1 shows the mixing of fakes events (in red) within real muons and neutron distribution (black). The removed fake events are in blue. Considering this example of a cosmogenic neutron, blue events correspond to events correlated in space and in time with the cosmogenic neutron, consequently identified as ^{10}C candidate. 9.39×10^8 events were simulated, leading to the result displayed in Table 4.2.

Figure 4.2a shows the contributions of the different cuts to the final dead-time. The cosmogenics cut for internal muons is the major contributor. Figure 4.2b shows the evolution in time of the total dead-time. The seasonal modulation of the muon flux is clearly visible, following the pattern showed in figure 4.9.
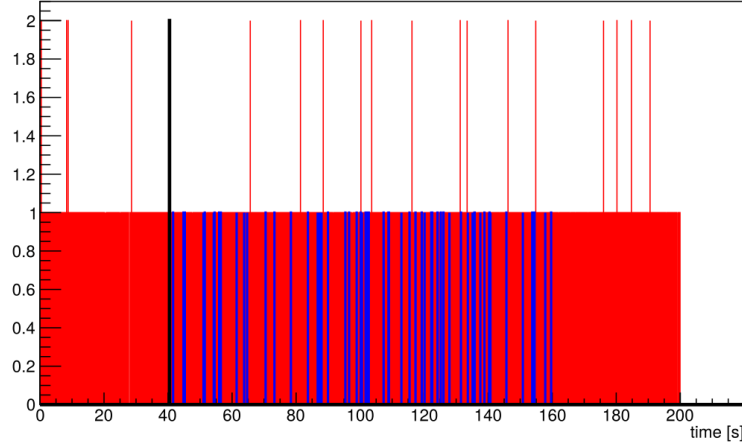
Figure 4.1: *Time distribution of fake (red) and real events (black). The event is a cosmogenic neutron. Fake events are identified as ^{10}C (blue) if correlated in space and time with the cosmogenic neutron. The ratio of the number of blue events over red events, is then the dead time induced by the ^{10}C cut on the final selection.*

Veto	external muons	internal muons	μ+n	total
Fake events eliminated	2.15×10^3	2.578×10^8	6.86×10^6	2.58×10^8
dead time induced (%)	2.3×10^{-4}	27.4496	0.073	27.5169

Table 4.2: *Dead time measurement using fake events.*

With a dead-time of 27.52 % and a livetime of 2062.38 days, the effective time is then 1494.8 days. The volume has been estimated to be 302 m^3, and the density to 0.8802 g.cm^{-3} [44]. It leads to a total exposure of:

$$\text{exposure} = 1088 \text{ t.y} \tag{4.1}$$

At high energy where no z-cut is applied, this is an increase by more than a factor 11 of the exposure with respect to the previous analysis.

(a) *Comparison of the dead-time contributions,*

(b) *Weekly evolution of the total dead-time,*
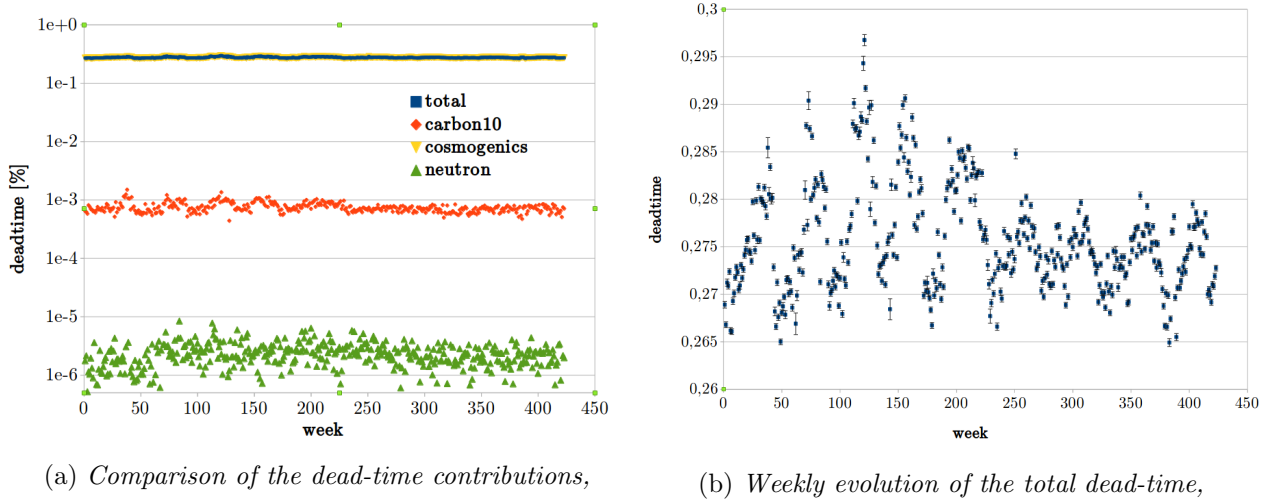
Figure 4.2: *Dead-time measurements and evolution on time.*

4.1.3 The z-cut

Figure 4.3 is showing spatial distribution (with $\rho = \sqrt{x^2 + y^2}$) of selected events at the top edge of the vessel. Generating 3 MeV electrons in the whole active volume, the corresponding charge seen by the detector can be mapped. This map defines the charge threshold corresponding to a 3 MeV electron deposit as a function of (ρ,z) and can be applied to the data selection. Figure 4.3a shows the distribution of selected events. A clear excess of events at the North hemisphere of the detector (z>0) and overlapping the vessel is visible. Figure 4.3b is the spatial distribution of events above a fix charge threshold of 1650 pe. This excess is believed to be due to the scintillator leak in the buffer.

(a) *Applying the map cut. The leak is visible as an excess of event close to the vessel.*

(b) *Applying a fix charge cut at 1650 pe ($\sim$ 3.3 MeV), the excess is still visible.*
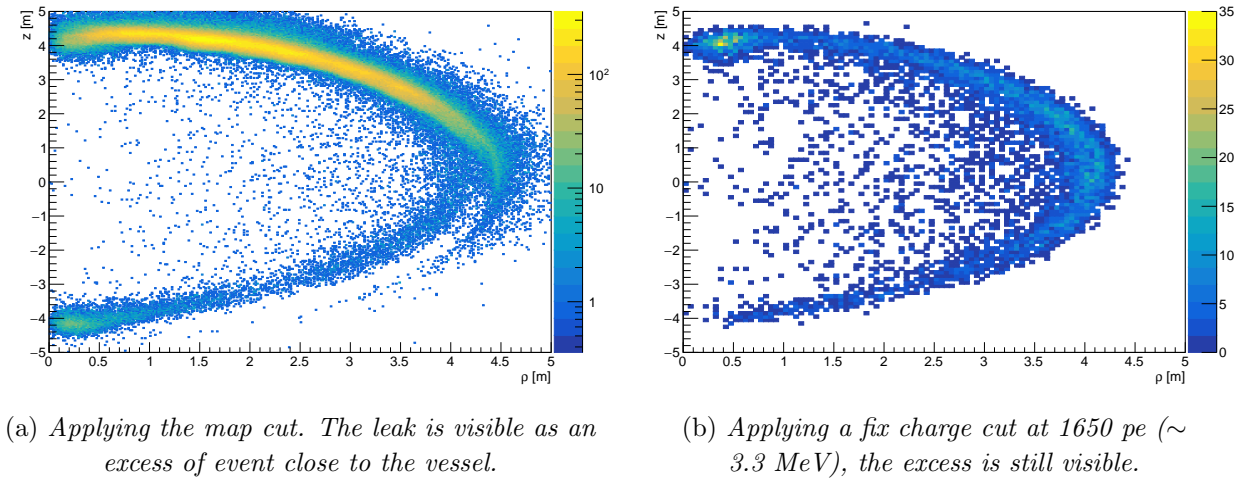
Figure 4.3: *^8B events distribution depending on the energy threshold ($\rho = \sqrt{x^2 + y^2}$).*

Selecting the excess in the (ρ,z) plan in figure 4.3a, figure 4.4 shows the time distribution of the excess events. For comparison, figure 4.4b shows the time distribution of all events but the one from the excess. The evolution of the leak events seems in agreement with the operations of Borexino as detailed in section 3.1.4.1.

(a) *Excess events ($\sim$ leak),*

(b) *All but excess events ($\sim \overline{leak}$),*
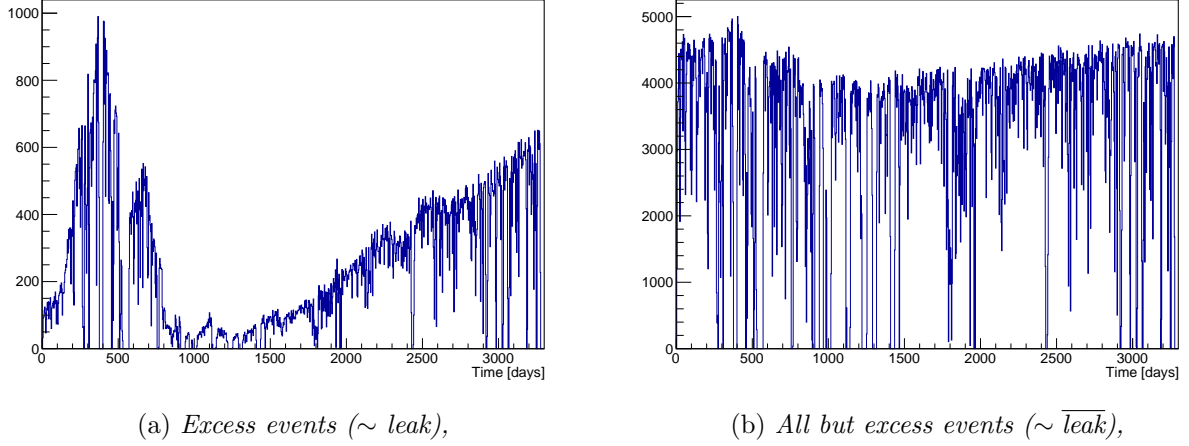
Figure 4.4: *Time distribution of event rate in absolute time scale depending on their selection.*

Leak events are mostly gamma contamination from PMTs and buffer impurities. Figure 4.5 displays the spatial distribution of events above 1650 ($\sim$ 3.3 MeV) and above 2950 pe ($\sim$ 5.7 MeV). To remove this excess, a z-cut is set at 2.5 m.

(a) *Above 1650 pe ($\sim$3.3 MeV), the z-cut is the red line.*

(b) *Above 2950 pe ($\sim$5.9 MeV), no excess is visible.*
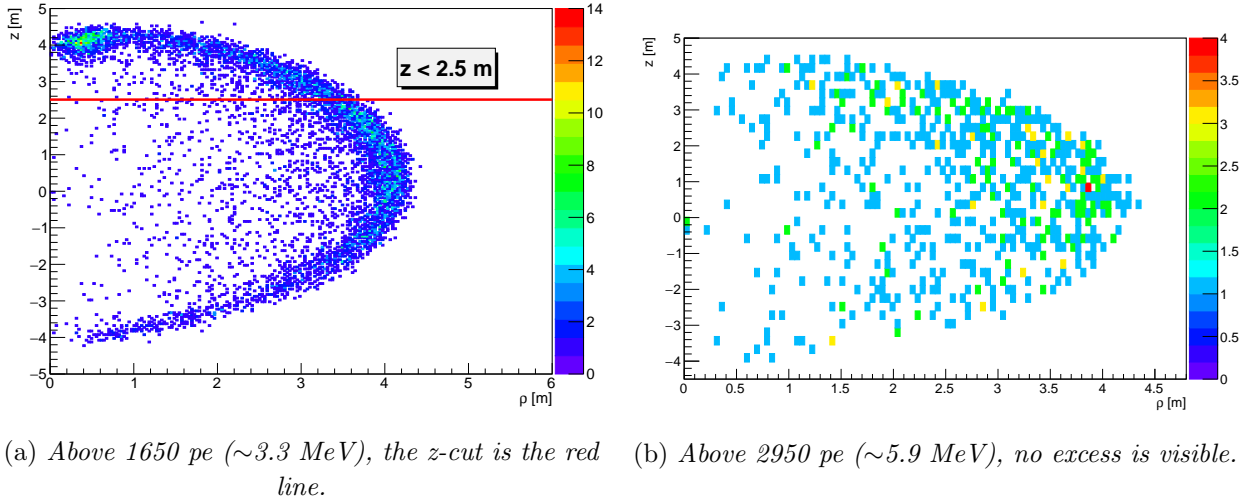
Figure 4.5: *^{8}B events distribution depending on a fix charge threshold. A clear excess is visible at the top of the vessel.*

The efficiency of this cut is estimated by measuring the part of an uniform radial distribution cut by this z-cut. This can not be done analytically as the vessel is very not symmetrical at high z. This efficiency is:

$$\epsilon_{\text{z-cut}} = 85.085\% \tag{4.2}$$

4.2 Energy calibration

4.2.1 Energy calibration in the center of the detector

In order to calibrate the detector energy response, we used an AmBe neutron source positioned at the detector center. The AmBe source emits neutrons through the reaction:

$$\ce{^9_4Be} + \alpha \Rightarrow \ce{^{12}_6C^{(*)}} + n \tag{4.3}$$

Neutrons are captured by ^{1}H and ^{12}C nuclei in the scintillator. These reactions induce γ emissions of 2.223 and 4.945 MeV respectively . To calibrate at higher energies, stainless steel was added to the source insertion system [163]. Indeed, ^{56}Fe and ^{54}Fe nuclei contained in the steel leads to additional γ at 7.631 and 9.298 MeV respectively. In 59.1% of the neutron emission, the ^{12}C nuclei emits a 4.348 MeV γ in association with a neutron. A coincidence in time ($20 < \Delta t < 1280\,\mu s$) and in space ($\Delta R < 1\,m$) is required between the 4.348 MeV γ and the one emitted from neutron capture. The space cut takes into account that the second gamma is emitted tens of centimetres away from the source position due to neutron thermalisation and diffusion. The position of the source is precisely known thanks to the CCD cameras and a LED system. Figure 4.6a shows the energy spectrum of γ emitted from the neutron captures as measured by Borexino.

(a) *Calibration from neutron capture in the center of the detector.*

(b) *Linear fit of the γ induced by neutron capture and comparison between the values given by the Monte-Carlo with experimental points (black).*
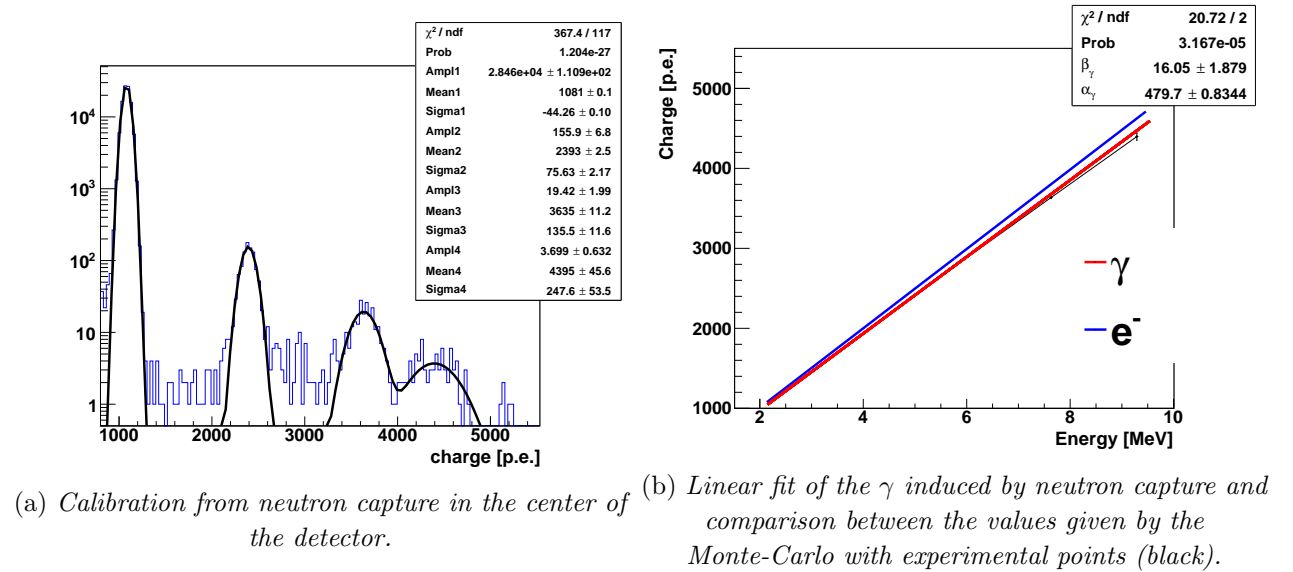
Figure 4.6: *Calibration in the center of the detector using n-capture γ on ^1H (2.223 MeV), ^{12}C (4.945 MeV), ^{56}Fe (7.631 MeV) and ^{54}Fe (9.298 MeV).*

Each of the neutron capture peaks is fitted with a Gaussian distribution, as shown in Figure 4.6a. Figure 4.6b shows the γ-equivalent energy scale at the center of the detector. The conversion from the collected number of photoelectrons to energy in MeV is given by:

$$E\,(pe) = A_\gamma E_\gamma\,(MeV) + B_\gamma \tag{4.4}$$

with $A_\gamma = 479.70 \pm 0.83$ pe/MeV and $B_\gamma = 16.05 \pm 1.88$ pe obtained from a linear fit. The deviation from the linearity is due to the quenching effect, evaluated for gammas in a factor of $Q_\gamma(2.2\,MeV) \sim 0.98$.

In order to transpose the signal of the gamma emitted by the AmBe neutron source to the electron-like expected signal, gammas and electrons were simulated in the center of the detector. Generating 3 MeV gamma, the mean charge 1464.7 ± 0.5 pe is in agreement with the light yield measured with the AmBe calibration source. Simulating electrons, the mean charge is slightly modified, as expected from quenching effect as well as from different Cerenkov emission. Those effects have been fully integrated in the Monte-Carlo leading to a correction of:

$$\text{E (pe)} = A_e \text{E}_\text{e} \text{ (MeV)} + B_e \tag{4.5}$$

with: $A_e = (496.2 \pm 0.9)$ pe/MeV and $B_e = \beta_\gamma = (16.1 \pm 1.9)$ pe. The 3 MeV threshold set for the ^{8}B analysis corresponds then to 1504.7 pe in the center of the detector.

4.2.2 Energy response in the volume

Since this analysis is performed in the whole active volume, we took into account the detector response as function of the event position. Using the AmBe source the charge response for the 2.223 MeV neutron capture peak can be mapped in the whole volume. Distance between emission and neutron capture enables a smooth mapping on the whole volume although the source was deployed only at precise locations [150]. Figure 4.7 illustrates the received charge variation depending on the reduced radius, ρ with $\rho = \sqrt{x^2 + y^2}$, and the z. The maps are built by averaging the light yield in each bin.

Using the Monte Carlo of Borexino [182], we simulated 2.223 MeV γ uniformly distributed in the volume. Figure 4.7b shows the result. The Monte Carlo is well reproducing the light yield variation when leaving the center of the detector as well as the North/South asymmetry due to PMT distribution.

(a) *AmBe data,*

(b) *Monte-Carlo of a 2.2 MeV γ in a 5 m sphere (larger than the IV),*
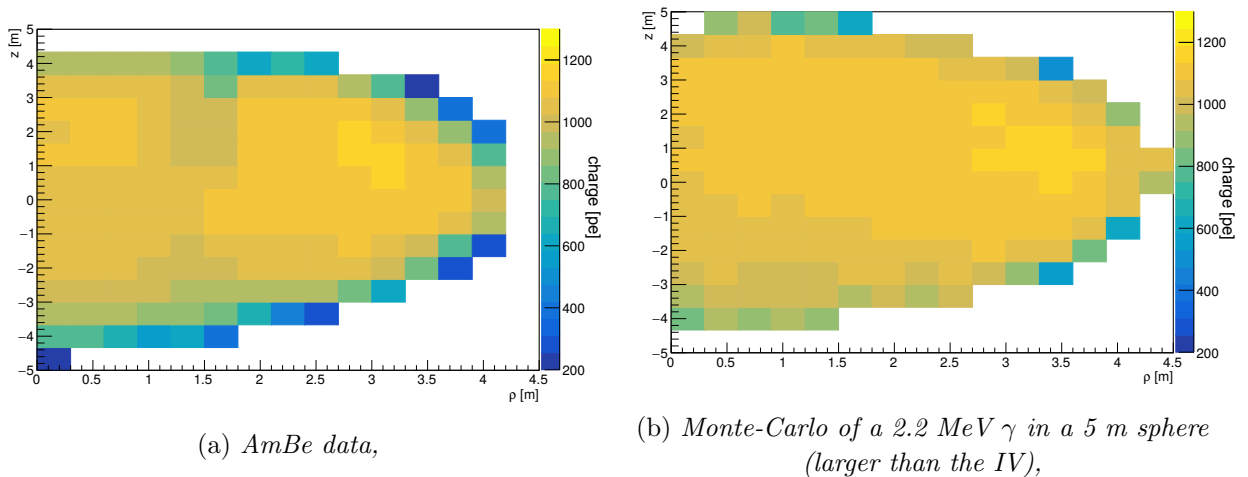
Figure 4.7: *Comparison data/MC of the charge response map for a 2.2 MeV γ in the volume.*

From figure 4.7, interpolating near bins, a map is generated showing the MC-data deviation depending on the position inside the detector. The comparison with the Monte Carlo response map shows an agreement in the light collection efficiency within 2% as displayed in figure 4.8
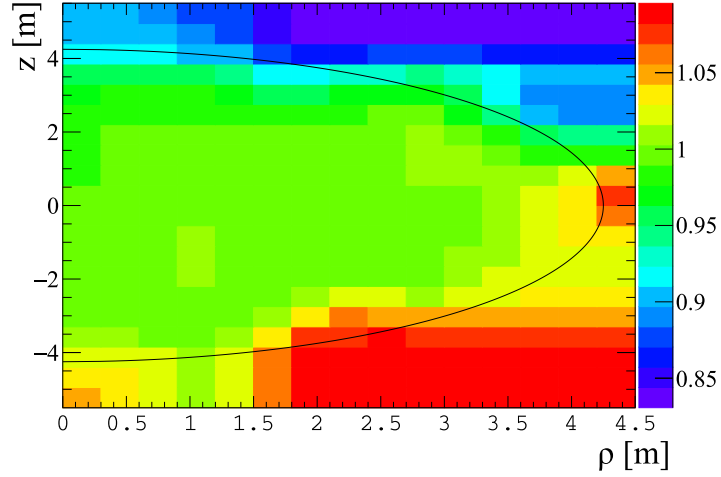
Figure 4.8: *Correction function depending on ρ and z to apply to the Monte-Carlo to reproduce the charge distribution.*

4.3 Tagged background

4.3.1 Muons events

With 4310 muons crossing the detector per day and a mean energy of 280 GeV, cosmic muons and their by-products are an important background of this analysis. Muon itself is well tagged in Borexino (more than 99.992% efficiency [144]). The Borexino trigger tags muons depending on the trigger conditions. Events detected by the OD are tagged as "trigger type 2". Even in absence of a trigger type 2, the ID can identify a muon by looking at the event pulse shape. The pulse shape is here defined as the time distribution of the detected photons. Muons are identified by looking at the mean (t_m) and peak (t_P) times of this distribution [144]. Muons are called internal if they cross the active volume, external otherwise.

The *external muon* is defined as:

- trigger type of 2

        OR

- trigger type of 1, neutrino-like event &
- More than 10 pe are deposited inside the detector &
- the Muon Trigger Board is fired or $t_P > 30$ ns or a $t_m > 100$ ns.

        OR

- event with cluster of hits.

The *internal muon* definition requires the following assessments:

- trigger type of 1, a neutrino-like event &
- Normalized charge of more than 400 pe &
- Muon Trigger Board fired or $t_P > 30$ ns or $t_m > 100$ ns;

Figure 4.9 displays the internal muons rate identification for the data set. The oscillation patterns is due to air density fluctuation, in particular with temperature. This seasonal modulation in Borexino has been reported in [183].
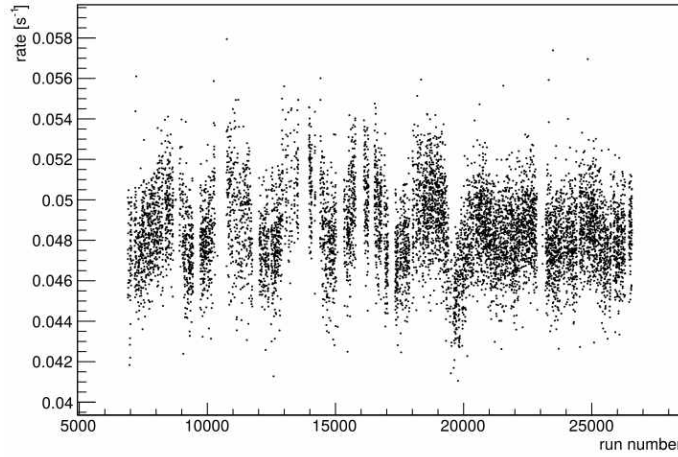
Figure 4.9: *Rate of internal muons with respect to run numbers.*

However, some muons can escape the OD detector trigger and the pulse shape discrimination. They still can be identified by the amount of energy (minimum ionizing particle about 2 MeV.cm^{-1}) they deposit in the active volume. Track and time correlation between hits enable to suppress a posteriori muon-like events. Run #21223, #22733 and #18577 were eliminated because such events were detected. Figure 4.10 shows the run #21223 after the last step of selection. Figure 4.10a shows a time distribution of neutrino candidates with an arbitrary initial time and a 1 ms binning. Assuming a ^{8}B neutrino rate of 0.25 cpd/100 t above 3 MeV, the probability to have 12 ^{8}B events in the same 1 ms window is null. Furthermore, the spatial distribution illustrated in Figure 4.10b suggests a spatial correlation that we identified as a muon track (in blue) followed by 3 cosmogenic events (in green and red).
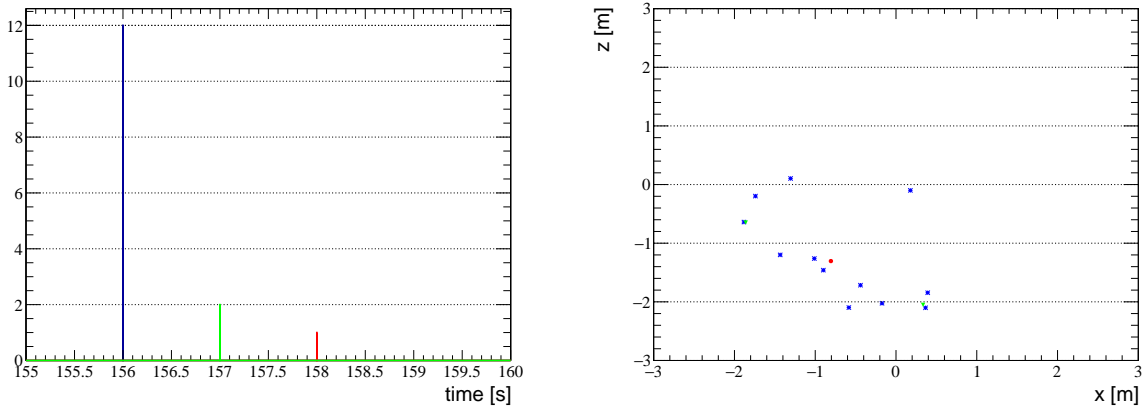
(a) *Time distribution of the events recognized as ^{8}B neutrino candidates in the step 3 selection sample.*

(b) *Spatial distribution in the (x,z) plan of these ^{8}B neutrino candidates.*

Figure 4.10: *Run #21223 shows a non-physical excess of neutrino events. Investigations lead to the identification of a non tagged muon track.*

Looking at the time distribution of these candidates, we found some correlated in time and space events. They are described in section 4.3.1. Some muons were not tagged by the OD. To get rid of

these type of events a 5 s fast coincidence veto is applied. This veto removes any selected events identified within the same 5 s time window. Having 1.27×10^{-5} Hz of selected events above 3 MeV, the accidental rate is negligible. 60 events were removed using this techniques.

We consider the residual rate due to muon alone as identical to the one measured in the previous analysis [163]:

Aside from the muon itself, muon events are tagged and identified in order to deal with induced background as well.

4.3.2 Cosmogenic neutrons

High energetic atmospheric muons colliding with nuclei of the detector can produce hadronic showers leading to free neutron emission [152]. The rate of muon producing neutrons that eventually are captured in the active detector is 67.5 day^{-1} with an average neutron multiplicity of 3.61 neutrons per muon [184]. The neutron thermalisation, $\mathcal{O}(10\text{-}100$ ns$)$, can not be distinguished from the original muon track in the IV but neutron capture can be seen as peak above the average signal value [144]. After the Muon Trigger Board (16 μs) fires, a Neutron Trigger Board is activated for 1.6 ms to look for gamma emission from neutron capture in the scintillator. 98% of the cosmogenic neutrons thermalised and are captured on hydrogen. The rate of neutron capture on ^{12}C which fall in this analysis energy window has been estimated to be 0.86 ± 0.01 cpd/100 t in the previous analysis [163].

4.3.3 Short-lived cosmogenics

An extensive study of cosmogenics production in Borexino can be found in [183] and some of the measurement done in Borexino data are displayed in Table 4.3. We consider only cosmogenic isotopes with a Q value higher than 3 MeV. Nuclei with lifetime of less than 2 s are considered as short-lived cosmogenics. Longer elements as ^{11}Be and ^{10}C are treated separately.

Isotopes	^{12}N	^{12}B	^{8}He	^{9}C	^{9}Li	^{8}B	^{6}He	^{8}Li
lifetime (s) (t_i)	0.016	0.029	0.17	0.19	0.26	1.11	1.17	1.21
Q [MeV]	17.3	13.4	10.7	16.5	13.6	18.0	3.51	16.0
Rate [cpd/100 t] (r_i)	<0.03	1.62	0.026*	0.096*	0.083	0.41	1.11	0.21
Fraction > 3 MeV (δ_i)	NA	0.886	0.898	0.965	0.932	0.938	0.009	0.875

Table 4.3: *Summary and characteristics of the short lived cosmogenics above 3 MeV. Rate are measured by the Borexino collaboration [183] (if *, the rate is extracted from KamLAND [159]).*

Among them, we group together cosmogenic isotopes with similar lifetime: ^{12}B, G1 = (^{8}He, ^{9}C, ^{9}Li) and G2 = (^{8}B, ^{6}He, ^{8}Li). ^{12}N is neglected as no contamination was observed. The lifetime of G1 and G2 are the average of the lifetimes of each radioactive element weighted by their expected rates above 3 MeV:

$$\tau_1 = \frac{\sum_{i=1}^{4}(r_i \delta_i t_i)}{\sum_{i=1}^{4}(r_i \delta_i)}, \tau_2 = \frac{\sum_{i=5}^{8}(r_i \delta_i t_i)}{\sum_{i=5}^{8}(r_i \delta_i)}$$

with r_i, δ_i, t_i defined in Table 4.3. The lifetimes are for ^{12}B, G1 and G2 are displayed in Table 4.4.

Isotopes	^{12}B	G1	G2
lifetime (s)	0.02914	0.2156	1.1428

Table 4.4: *Lifetime of the short-lived cosmogenics*

To select these events, we looked for coincidence between an internal muons and a neutrino-like event in a 6.5 s window. Figure 4.5 displays the result of the fit of the time distribution of cosmogenic events candidate with three exponentials. The time constants were fixed to the values of table 4.4. Besides, a measurement of the accidental rate for this selection was done time reversing the coincidence (asking for a muon after a cosmogenic-like event). The accidental event distribution is shown in the same plot than the cosmogenics data.

(a) *Charge between 1650 and 2950 pe,*   (b) *Charge above 2950 pe,*
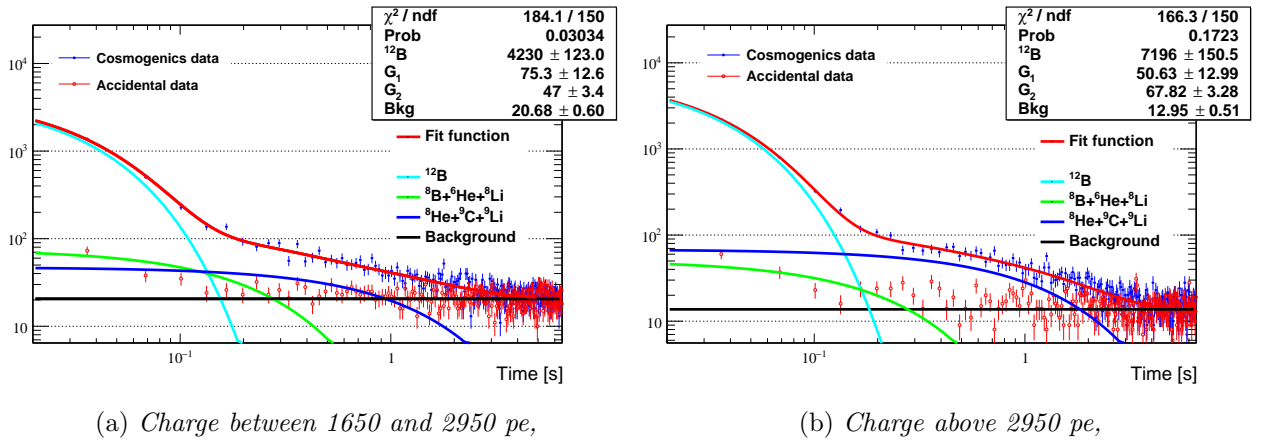
Figure 4.11: *Measuring the different cosmogenics component of the 6.5 s window after an internal muon.*

Isotopes	^{12}B	G1	G2
Expected	1.25 ± 0.03	$(1.8 \pm 0.3) \times 10^{-1}$	$(6.0 \pm 0.8) \times 10^{-1}$
2007 - 2009 [163]	1.48 ± 0.06	$(1.7 \pm 0.5) \times 10^{-1}$	$(5.1 \pm 0.7) \times 10^{-1}$
2008 - 2016	1.83 ± 0.03	$(1.5 \pm 0.2) \times 10^{-1}$	$(7.1 \pm 0.1) \times 10^{-1}$

Table 4.5: *Measured rates for a 3 MeV threshold, in cpd/100 t.*

The 6.5 s cut efficiency on ^{12}B and "G1 isotopes" is 1 while the efficiency of the temporal cut on the "G2 nuclei" is 99.66%. We estimated a residual contamination for the ^{8}B period:

$$R_{\mathrm{cosmo}}^{\mathrm{LE}} = (9.8 \pm 0.7) \times 10^{-4} \text{ cpd/100 t} \qquad R_{\mathrm{cosmo}}^{\mathrm{HE}} = (1.42 \pm 0.07) \times 10^{-3} \text{ cpd/100 t} \qquad (4.6)$$

4.3.4 ^{10}C

^{10}C (β^+, $\tau = 27.8$ s, Q = 3.6 MeV) is produced by muon-induced spallation on ^{12}C. Different processes can induced ^{10}C, most of them inducing a neutron emission.

Some of them however, called *invisible* do not emit any neutron as in ^{12}C(p; t)^{10}C or ^{12}C(π^+; π^0+d)^{10}C. Their contribution is expected to be around $\sim$1% of the total ^{10}C production [160].

In the visible channel, ^{10}C is produced in association with one or two neutrons emission from ^{12}C. To select ^{10}C events, we required a coincidence between a muon, a neutron and a ^{10}C candidate inside the fiducial volume, using the three fold coincidence (TFC). The requirements on the ^{10}C candidates are:

- trigger type to 1;
- charge above 1000 pe, ϵ_{ene};
- 0.8 m from the neutron position, ϵ_{coinc};
- 6.5 s < dt < 120 s, ϵ_τ.

with dt the time distance between the candidate and the muon. Figure 4.12 shows the ^{10}C time spectrum. The distribution is well fitted with an exponential with a time constant of 28.48 ± 1.36 s in good agreement with the theoretical value. The efficiency of the temporal selection is then ϵ_τ = 77.8 %. Using ^{10}C decay simulated spectrum, ϵ_{ene} is estimated to be 78.9%.
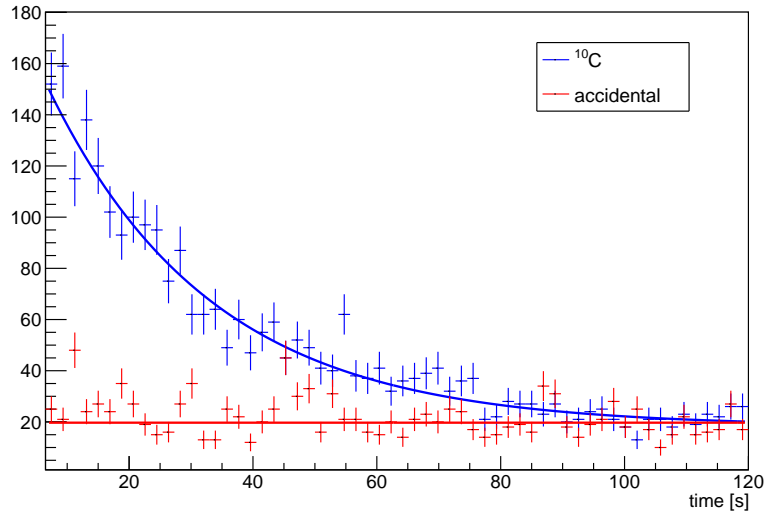
Figure 4.12: *Decay time of ^{10}C candidate.*

The spatial coincidence efficiency has been evaluated to be $\epsilon_{\text{coinc}} = (92.5^{+7.5}_{-20})$ % [184]. In a 3 m sphere, we found N_n = 629 events above 2 MeV inside the [6.5 s,120 s] window, leading to a total rate of:

$$R_{\text{vis}} = \frac{N_n}{\epsilon_\tau \epsilon_{ene} \epsilon_{coinc}} = 0.54^{+0.12}_{-0.05} \text{ cpd/100 t.} \tag{4.7}$$

in agreement with the rate measured in [184] of 0.41 ± 0.16 cpd/100 t. The total residual rate is then the sum of the ^{10}C rate above 3 MeV untagged by the spatial coincidence after the "cosmogenic cut", the invisible channel and the residual of the temporal cut:

$$R^{\text{LE}}_{^{10}\text{C}} = (6.4 \pm 1.4) \times 10^{-4} \text{ cpd/100 t} \tag{4.8}$$

4.3.5 ^{214}Bi

^{214}Bi decay can be tagged and rejected on event by event basis using time and spatial coincidence with ^{214}Po decay, as displayed in reaction 4.9. Therefore, we search for an α event few hundreds of

μs after a β decay of 3.2 MeV.

$$^{222}_{86}\text{Rn} \xrightarrow[3.82 \text{ d}]{\alpha} {}^{218}_{84}\text{Po} \xrightarrow[3.1 \text{ min}]{\alpha} {}^{214}_{82}\text{Pb} \xrightarrow[26.8 \text{ min}]{\beta^-} {}^{214}_{83}\text{Bi} \tag{4.9}$$

$$^{214}_{83}\text{Bi} \xrightarrow[19.9 \text{ min}]{\beta^- \ (3.2 \text{ MeV})} {}^{214}_{84}\text{Po} \xrightarrow[163.6 \ \mu\text{s}]{\alpha \ (7.69 \text{ MeV})} {}^{210}_{82}\text{Pb} \tag{4.10}$$
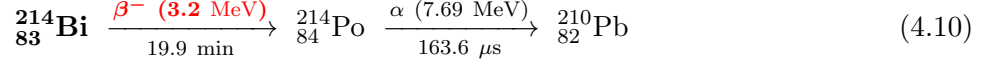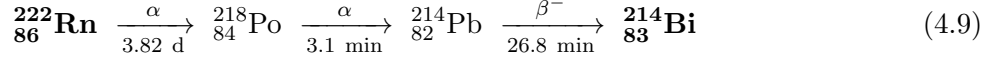
Figure 4.13a shows the energy distribution of the ^{214}Po candidates. Decaying through α (7.6 MeV) emission, the mean value as well as the width of the Gaussian are in agreement with previous measurements and prediction [146]:

$$\text{E}_\alpha = 7.69 \text{ MeV} \times Q_\alpha(7.69 \text{ MeV}) = 0.1098 \times 7.69 = 0.844 \text{ MeV} \tag{4.11}$$

which corresponds to approximately 421 pe, in good agreement with the mean value fitted in figure 4.13a.
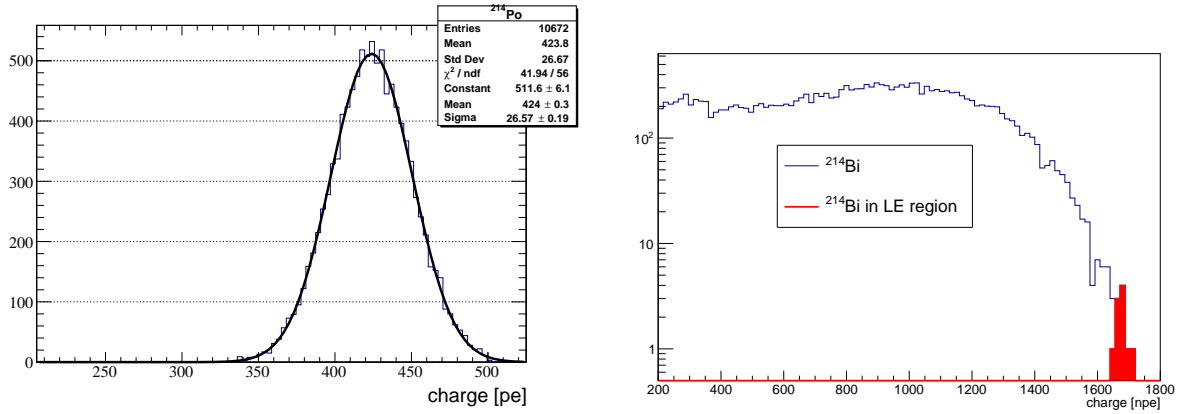
(a) ^{214}Po (α decay, $E_\alpha = 7.8$ MeV),

(b) ^{214}Bi (β decay, $Q_\beta = 3.2$ MeV),

Figure 4.13: *Charge distribution of ^{214}Bi (from MC) and ^{214}Po (from data) candidates in a 3 m sphere.*

Excesses of ^{214}Bi between the 23th of June 2010 and the 21th of September of 2011 are due to the purification campaign. Figure 4.14 shows this excess for ^{214}Bi and ^{212}Bi. They were excluded from the final data set.
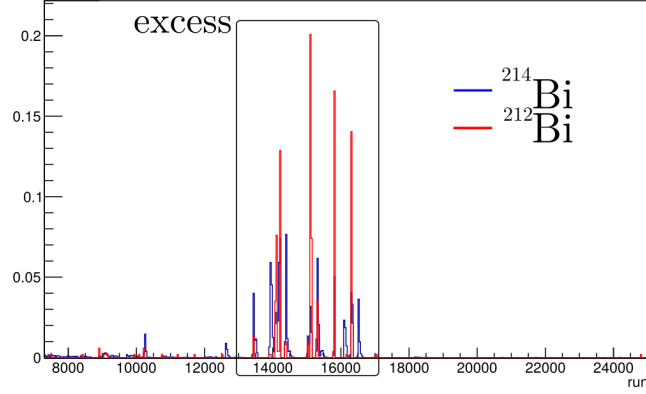
Figure 4.14: *Distribution of the events depending on the run number.*

The selection cuts applied for the BiPo identification are the following:

- ^{214}Bi decay candidate energy: E $\in$ [90,1800] pe ($\epsilon_{214_{Bi}}$);
- ^{214}Po decay candidate energy: E $\in$ [200,500] pe ($\epsilon_{214_{Po}}$);
- Time distance between ^{214}Bi and ^{214}Po between 20 μs than 1.18 ms (ϵ_{τ});
- Spatial separation between ^{214}Bi and ^{214}Po of less than 1 m (ϵ_d).

The spatial separation of the coincidence has efficiency ϵ_d =1. The time separation cut efficiency is $\epsilon_{\tau} = e^{-20/237}$ - $e^{-1.18/0.237} = 91.2\%$. The charge cuts efficiencies are estimated using charge distribution illustrated in figure 4.13b $\epsilon_{214_{Bi}} = 1$ and deriving the integral of the fitted Gaussian above 500 charge $\epsilon_{214_{Po}} = 99.95\%$ on figure 4.13a. Defining $\epsilon_{det} = \epsilon_d \times \epsilon_{214_{Po}} \times \epsilon_{214_{Bi}} \times \epsilon_{\tau}$,

$$R_{214_{Bi}} = \frac{N_{214_{Bi}}}{\epsilon_{det} \times T_{exp}} = (0.74 \pm 0.02) \text{ cpd/100 t} \tag{4.12}$$

with T_{exp} the total time exposure. The rate is estimated in 3 m to avoid any surface contamination. The estimated asymptotic value of the ^{214}Bi rate is estimated around (0.57 ± 0.05) cpd/100 ton in [44].

The residual, contaminating the ^{8}B sample, is evaluated with charge higher than 1650 pe and considering the removal of two cluster events in the same time acquisition gate (up to 16 μs). The efficiency of this cut is estimated using the whole fiducial volume $\epsilon_{cut} = 7.75 \times 10^{-4}$.

$$\text{Res}^{214_{Bi}} = R^{214_{Bi}} \times (1 - \epsilon_{det}) \times \epsilon_{cut} \tag{4.13}$$

Results of the residual contamination is compared with previous measurement in Table 4.6. The charge threshold is not the same in the two analysis.

Period	Time (d)	Res$^{214_{Bi}}$ [cpd/100 t]
2007-2009 [163]	488	$(1.1 \pm 0.4) \times 10^{-4}$
2008-2016	2064.12	$(1.3 \pm 0.1) \times 10^{-5}$

Table 4.6: *Results of the ^{214}Bi contamination above 3 MeV.*

This rate is negligible with respect to the ^{8}B signal.

4.4 Residual background

Residual background is the irreducible background using using coincidence techniques described in section 4.3. If external contamination was analytically taken into account above 3 MeV in the previous analysis, it was not the case above 5 MeV. The first section described the identification of this background (section 4.4.1), second section focus on surface contamination (section 4.4.2) and finally, spatially homogeneous contaminants are treated ^{11}Be (section 4.4.3) and ^{208}Tl (section 4.4.4).

4.4.1 External

The High Energy range (above 5 MeV) has been used as a benchmark to test our analysis in a region with no natural radioactive contamination. Quenching on the α particles ensures that no radioactive contaminant can reach 5 MeV in electron equivalent emitted light. Above 5 MeV, only atmospheric muons, short-life cosmogenics residues and ^{11}Be cosmogenic nuclei are expected. All of these contaminants coming or products of cosmic-rays must have a uniform spatial distribution. We will call this distribution "bulk" from now on.

The radial distribution of internal events is then given by equation 4.14, extracted from [148].

$$f_{\text{bulk}}(r|R, \sigma, N_1) = N_1 \frac{r}{R^3\sigma} \int_{-R}^{R} r'.e^{-\frac{(r-r')^2}{2\sigma^2}} dr' \tag{4.14}$$

with R the radius, σ the resolution assumed to be uniform and constant ($\simeq$ 10 cm), and N_1 the amplitude. These parameters are fitted using the radial distribution in a 3.5 m sphere. A comparison can be made using the Monte-Carlo and simulating bulk events. Figure 4.15 shows comparison between these two bulk distributions.

(a) *Analytical bulk modelling,*   (b) *Monte-Carlo bulk modelling,*
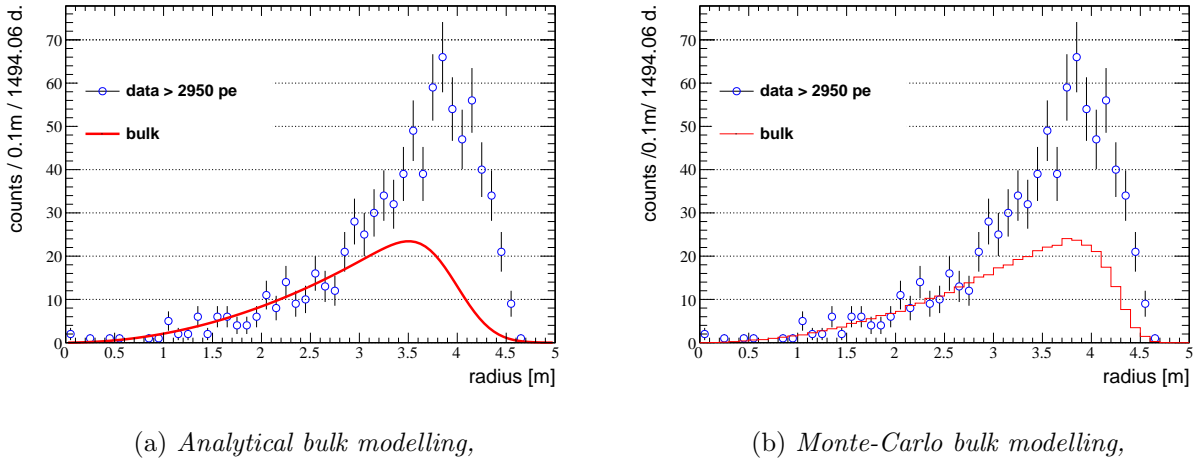
Figure 4.15: *Radial distribution of events at high energy (above 2950 pe). Analytical (left) versus MC (right) fit of the bulk contribution.*

Figure 4.15 shows that a background is not compatible with bulk events in the sample. This background is higher at large radii while the innermost part of the detector is compatible with a bulk distribution. This contamination can not come from the vessel surface as no radioactive background can produce such amount of light. Not coming from the surface of the vessel and not uniformly distributed inside the active volume, this background must come from outside the scintillator and

therefore will be called external. This contamination is still present above 8 MeV but statistics there is very low.

This background was not reported in the previous analysis [163]. However the radial cut at 3 m was removing most of this external contamination. Between 3 and 5 MeV, external contamination used to be modelled using analytical function [148] with S a Rayleigh distribution:

$$f_{\text{ext}}(r|N_2, R, \sigma, x_0) = N_2 \int_0^R (e^{\frac{x}{x_0}} - 1)S(r|R,\sigma)dx \quad , \quad S(r|R,\sigma) = \frac{r}{R^2\sigma}e^{\frac{-(r-R)^2}{2\sigma^2}} \tag{4.15}$$

with R and σ defined as in equation 4.14, N_2 being the amplitude. These functions are not reliable since the vessel is not spherical anymore.

This external component must be an energetic gamma for crossing the 2 m depth buffer. Above 5 MeV, the only source of high energy γ is neutron capture on detector materials. The most massive object close to the inner vessel is the stainless steel sphere (SSS), the water tank and extra shielding. All these materials contain iron. Neutron captures on $^{54/56}$Fe of the steel leads to γ emission above 5 MeV, in particular 9.3 and 7.6 MeV γ which are the main emission lines. Monte Carlo is then used to model any dynamical effects such as vessel deformation and energy reconstruction in the whole volume. The simulation enables us to include all the effects that can affect the radial distribution.

Figure 4.16 gives neutron radiative capture cross sections of ^{54}Fe and ^{56}Fe. They both emit γ above 5 MeV through neutron caputre, undergoing ^{54}Fe(n,γ)^{55}Fe and ^{56}Fe(n,γ)^{57}Fe reactions respectively. Furthermore, they are both strongly present in the detector and have a high relative abundance (91.72% for ^{56}Fe and 5.8% for ^{54}Fe). ^{56}Fe mainly emits 7631.18 MeV (29%) and 7645.58 MeV (25%) gammas while ^{54}Fe emits a gamma of 9.297 MeV (100 %) when absorbs a neutron. Potential candidates for neutron emission are cosmics, natural radioactivity in the environment,

(a) ^{54}Fe target

(b) ^{56}Fe target
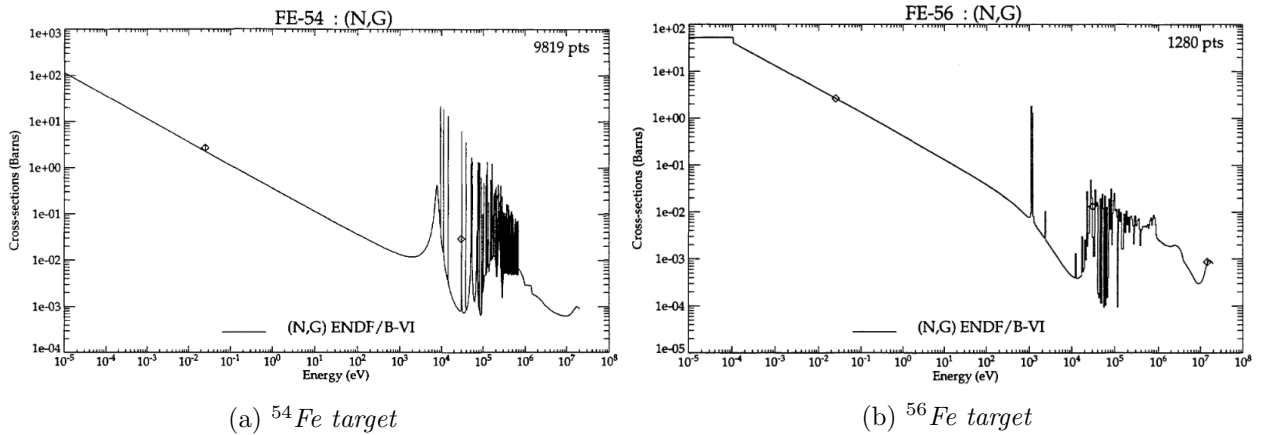
Figure 4.16: *Neutron capture cross section on iron [185].*

(α,n) reaction in the detector itself.

Cosmic-rays Atmospheric muons produce hadronic shower inside the detector. This can produce cosmogenics and free neutron. Internal muon veto (6.5 s) guarantees no neutron capture contamination from internal muons. The external muon veto (2 ms) is settle to remove free neutrons contamination coming from muons crossing the buffer. This veto removes 99.96% of the free neutron emission. Considering the rate of muon inducing free neutron emission 67.5 day^{-1} and the selection cuts, this rate is too small for being a credible candidate.

Rock walls The flux of neutrons from the rock wall in the LNGS experimental hall C has been estimated to $\phi_n^{\text{th}} = 0.24 \times 10^{-2}$ neutron.m^{-2}.s^{-1} (thermal neutrons, $E_n < 0.5$ eV) and $\phi_n^{\text{epi}} = 0.64 \times 10^{-2}$ neutron.m^{-2}.s^{-1} (epithermal neutrons, 1 eV$< E_n < 1$ MeV) [186]. The water tank shields the inner detector against neutron reducing this flux by 8 orders of magnitude before reaching the SSS [156]. The expected rate of gammas induced by neutron rock is negligible.
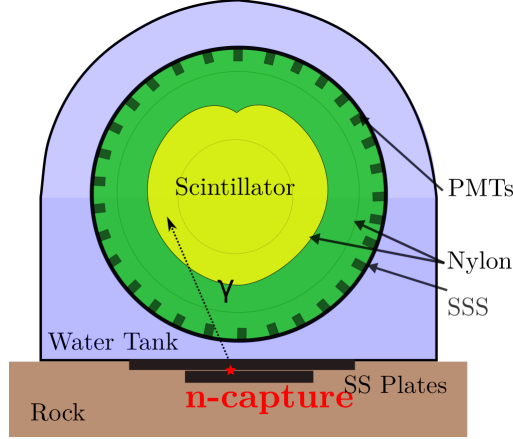
Figure 4.17: *Illustration of the n-capture process into consideration*

Below the detector, two steel plates have been added in order to compensate for the reduced water shielding. This extra shielding is composed of one 8 m×8 m×10 cm plate above a smaller 4 m×4 m×4 cm plate. Figure 4.17 gives a representation of this background emission. This extra shielding can induced high energetic γ. Estimation of this background was done using two different approaches using Monte-Carlo and analytical solution.

Analytically, we derived the γ rate from the slow and fast neutron cross section on ^{56}Fe are $\sigma_n^{\text{th}} \simeq 2.59$ barn [187] and $\sigma_n^{\text{epi}} \sim 1.44$ barn. The number of ^{56}Fe targets is $N_{56\text{Fe}} = 4.96 \times 10^{29}$ atoms per nuclei. One can expect 1.7 neutron capture per second on ^{56}Fe, leading to approximately 1.5 γ.s^{-1} above 3 MeV emitted in every direction.

With Monte Carlo, we simulated 4.0×10^7 γ of 9.3 MeV uniformly distributed inside the steel plate. Only one event was observed above 5 MeV in the detector. This leads to an efficiency of 9.73×10^{-8}. This efficiency is highly overestimated as, in reality, most of the gammas are emitted close from the rock ground. Therefore, most of the gammas are attenuated in steel before reaching the Water Tank. The conservative limit on this contamination is then $R_\gamma < 4.6$ γ.y^{-1} in the inner vessel.

Independently, a derivation was realised using analytical formulae. As the Monte-Carlo results, due to simplified hypothesis, the result must be considered as an estimation of the order of magnitude. Considering attenuation length of the neutron flux in the steel as well as γ emitted in the steel, the water and the buffer, the rate of expected γ above 5 MeV is 1.7 y^{-1} [188]. This rate is overestimated as the gamma emission point was taken to be the center of the plates, minimizing the path one gamma cross before reaching the IV.

Looking for North ($z > 0$) and South ($z < 0$) hemispheres separately, data does not rise evidences of higher external contamination in the South region. In fact, the North hemisphere shows a stronger

(a) *North hemisphere (z>0),* (b) *South hemisphere (z<0),*
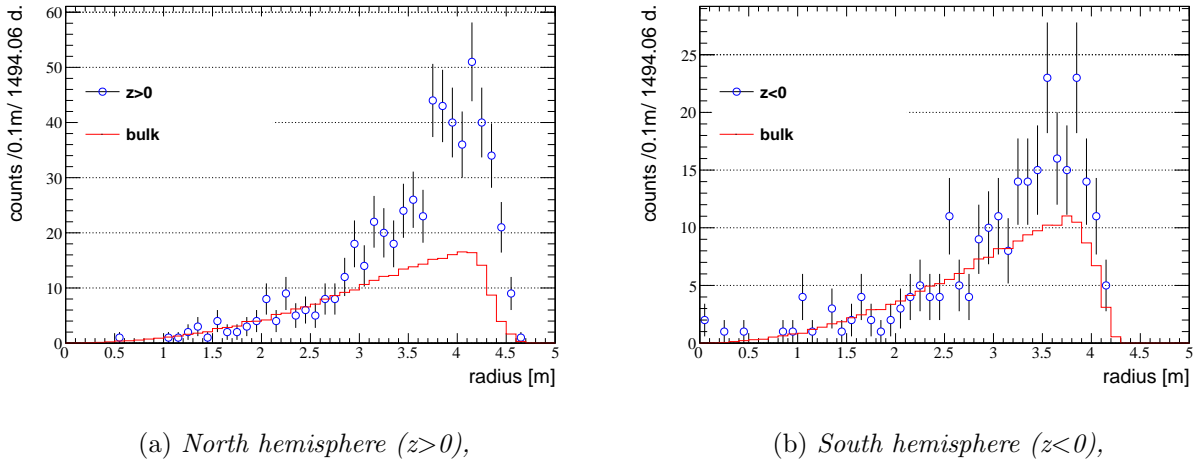
Figure 4.18: *Data distribution above 2950 pe fitted with the bulk distribution obtained from Monte-Carlo.*

external contamination. This is due to the higher mass concentrated above z=0 since the vessel deformation. The external contamination distribution confirms that the capture of neutron in the steel plate is not the source of the high energy background.

Neutron emission from detector materials Neutrons can be produced by (α,n) reactions activated by α-decays from ^{232}Th and ^{238}U decay chain. ^{232}Th and ^{238}U are present in every material. ^{232}Th and ^{238}U produce 8 and 6 α respectively along their decay chains.

Stainless steel of the SSS is the most massive component in the detector despite its contamination is low in Uranium and Thorium. PMTs are the most radioactive material inside the detector. Borexino inner detector counts 2212 8' PMTs EMI 9351 produced by Electron Tube Limited (formerly EMI). The overall radioactivity of the PMTs is mainly due to the glass covering the bialkali photo-cathode. This SCHOTT 8246 low radiation borosilicate glass has been chosen to minimize the ^{40}K contamination, high in sand used in every day glass. ^{40}K contamination is a serious source of radioactive noise in photomultiplier [189]. Unlike ^{40}K, ^{232}Th and ^{238}U contaminations have not been minimized with respect to basic glass. Table 4.7 reports on the dominant radioactive contamination for this analysis, from the extensive radiocontamination campaign done in 2002 for the Borexino experiment [149]. The secular equilibrium is assumed to be reached.

Material	^{238}U [g/g]	^{232}Th [g/g]	^{226}Ra[mBq/kg]	^{228}Th[mBq/kg]
Schott 8246 glass	$(6.6 \pm 1.9) \times 10^{-8}$	$(3.2 \pm 0.3) \times 10^{-8}$	820 ± 230	130 ± 12
Dynodes	$< 2.3 \times 10^{-8}$	$(1.1 \pm 0.4) \times 10^{-7}$	< 280	450 ± 163
AISI304L Stainless steel	$(3.7 \pm 0.7) \times 10^{-10}$	$(2.8 \pm 0.3) \times 10^{-9}$	4.6 ± 0.9	11.4 ± 1.1

Table 4.7: *Concentration of radioactive isotopes measured with HADES Ge detectors in LNGS [149].*

The total mass of the steel (AISI304L) in the SSS is 45 tons [152]. Each PMT is made of about 800 g of Schoot 8246 glass for a total mass of 1.77 tons. Finally, considering a 1 g dynode (about 0.2 cm^3 of Aluminium), and 12 dynodes per PMT, the total mass of dynode material is 26.5 kg.

Table 4.8 lists the overall Borexino contamination. The low radioactivity of the dynode makes this source negligible.

Part of the detector	^{238}U [g]	^{232}Th [g]	^{238}U [Bq]	^{232}Th [Bq]
2212 PMTs glass	$(1.2 \pm 0.3) \times 10^{-2}$	$(5.7 \pm 0.5) \times 10^{-2}$	$(1.4 \pm 0.4) \times 10^3$	$(2.3 \pm 0.2) \times 10^2$
Stainless steel sphere	$(1.7 \pm 0.3) \times 10^{-2}$	$(1.3 \pm 0.2) \times 10^{-1}$	$(2.1 \pm 0.4) \times 10^2$	$(5.3 \pm 0.6) \times 10^2$
Dynodes	$< 6.1 \times 10^{-4}$	$(2.9 \pm 1.1) \times 10^{-3}$	< 7.6	$(3.6 \pm 1.4) \times 10$

Table 4.8: *Total contamination from different detector parts.*

The (α,n) cross sections, as well as the energy spectrum of the emitted neutron vary with the contaminant and the composition of the material.

Using the University of South Dakota neutron yield data base [190], and the plug and play numeric tool [191] developed by S. Westerdale and P.D. Meyers [192] based on TALYS. This tool computes the cross section depending on the material composition, knowing the energy α spectrum. Composition of Borexino materials is:

- AISI304L : Cr (18%), Ni (10%), Mn (2%), Si (1%), C (0.02%), S (0.03%), P (0.04%) complete with Fe,

- Schott glass : SiO$_2$ (80%), B$_2$O$_3$ (13%), Al$_2$O$_3$ (5%), Na$_2$O (2%),

Table 4.9 shows the results for the intrinsic contamination of ^{232}Th and ^{238}U in the SSS and the PMT glass.

	SSS (α, n) [n/decay]	ETL low radiation glass (α, n) [n/decay]
^{238}U	^{238}U: 5.63×10^{-10} ^{226}Ra : 5.16×10^{-7}	^{238}U: 5.08×10^{-6} ^{226}Ra : 1.96×10^{-5}
^{232}Th	1.9×10^{-6}	2.62×10^{-5}

Table 4.9: *Estimation of neutron flux coming from detector materials using [192] numerical tools.*

Figure 4.19 shows expected neutron energy spectra from ^{232}Th in stainless steel and glass.

Using tables 4.8 and 4.9, table 4.10 summarized the derived neutron emission per year.

As displayed in table 4.10, the major contributor to the neutron emission is the PMT glass. Figure 4.20 illustrates one of this reaction in which a neutron emitted from the PMT gives rise to a high energy gamma toward the center.

	Estimated neutron flux [n.y^{-1}]	
	^{238}U	^{232}Th
2212 PMTs	$(1.09 \pm 0.21) \times 10^6$	$(1.89 \pm 0.16) \times 10^5$
Stainless steel sphere	$(3.41 \pm 0.66) \times 10^3$	$(3.18 \pm 0.35) \times 10^4$

Table 4.10: *Estimated neutron flux from detector part.*
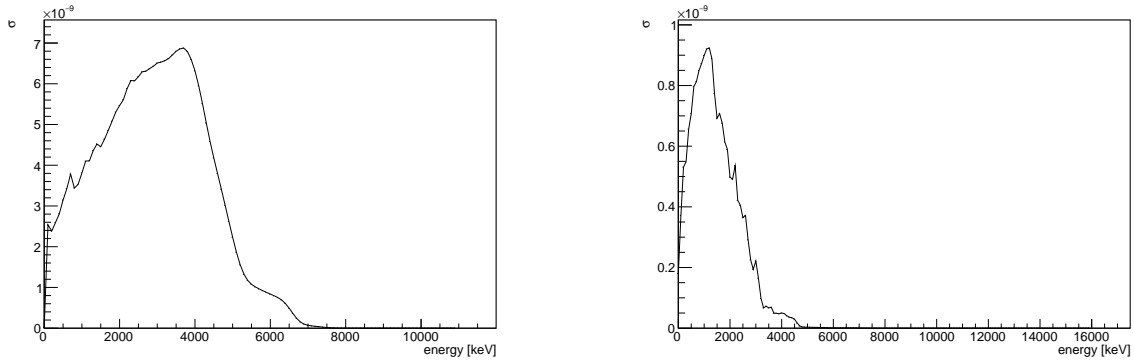
(a) *Neutron spectrum from (α,n) on glass from* ^{232}Th, (b) *Neutron spectrum from (α,n) on steel from* ^{232}Th,

Figure 4.19: *Neutron emission energy spectra by (α,n) reaction from* ^{232}Th *on different materials.*
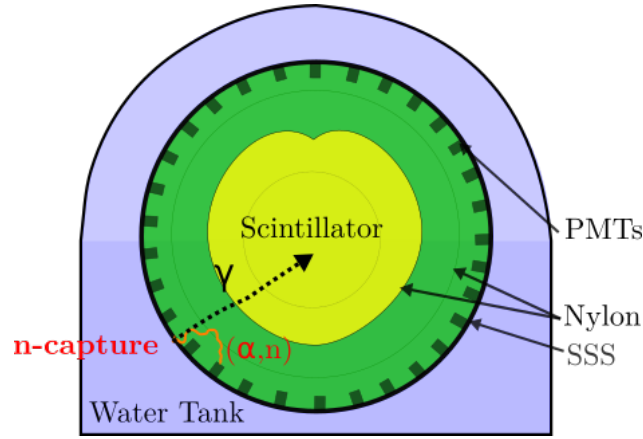
Figure 4.20: *Illustration of the n-capture process identified as a potential source of the HE external background.*

Independently of this survey, using simple analytical models and data base, we derived an order of magnitude of 0.025 n.s^{-1} coming from the PMT glass [188]. Considering the methods, this number is in good agreement with the (0.043 ± 0.011) n.s^{-1} derived from our analysis.

Besides of ^{238}U and ^{232}Th, some other glass atoms like Samarium[1] (0.1-1% glass) can be responsible of (α, n) reactions [193] and are not taken into account in this analysis.

Monte Carlo simulations were made generating neutrons from PMT glass and SSS to look at capture rate and induced γ emission. The energy spectrum of the neutron is the spectrum from ^{238}U and ^{232}Th (α,n) reactions in the PMT glass. Figure 4.21a shows the radial distribution of the neutron capture depending on the energy of the emitted γ varying the neutron source (i.e. PMT glass or SSS). The intense peak of high energy γ (E$_\gamma$ >5 MeV) is located at R ∈ [6850;6858], which is the stainless steel.

Description of the PMT in the Monte Carlo code includes glass, external structure and light cones. No strong modifications were observed adding or removing them concerning neutron capture. For computation optimisation, simulations presented are done without loading of the PMT strucutre.

---

[1] ^{147}Sm (natural abundance: 15.0%), α emission of 2.3 MeV, ^{148}Sm (n.a.: 11.2%), α emission of 2.0 MeV

(a) γ distribution neutron emission from the PMT,

(b) γ distribution from neutron emission from the SSS,
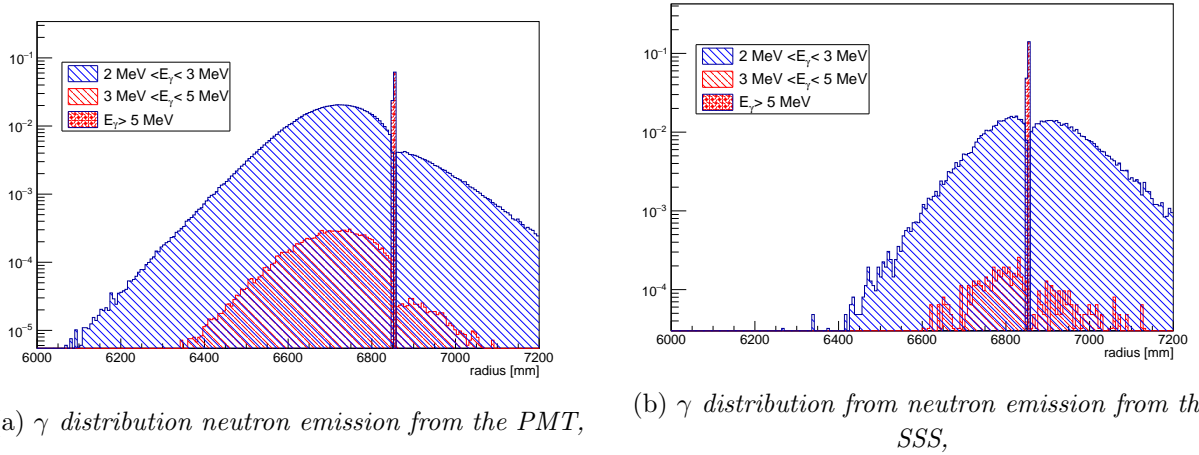
Figure 4.21: *Intensity and spatial distribution for γ emission from neutron capture. The neutrons are simulated from the ^{232}Th (α,n) emission spectra emitted by two different sources: PMT position and the SSS.*

Neutron source		ϵ_n: γ emitted per neutron		
		(2 MeV < E$_\gamma$ < 5 MeV)	(3 MeV < E$_\gamma$ < 5 MeV)	(E$_\gamma$ > 5 MeV)
PMT	^{232}Th (α,n)	(0.94 ± 0.01)	$(1.3 \pm 0.1) \times 10^{-2}$	$(4.2 \pm 0.1) \times 10^{-2}$
	^{238}U (α,n)	(0.94 ± 0.01)	$(1.2 \pm 0.2) \times 10^{-2}$	$(4.4 \pm 0.3) \times 10^{-2}$
SSS	^{232}Th (α,n)	(0.73 ± 0.01)	$(6.7 \pm 0.3) \times 10^{-3}$	$(1.9 \pm 0.1) \times 10^{-1}$
	^{238}U (α,n)	(0.73 ± 0.01)	$(7.2 \pm 0.2) \times 10^{-3}$	$(2.0 \pm 0.1) \times 10^{-1}$

Table 4.11: *γ energy range following one neutron emission. The neutron simulation is done following (α,n) energy spectra in PMT and SSS.*

I produced a map of true energy versus position of gammas above 5 MeV from the two sources and the two emitters. From this map gammas were simulated to estimate fraction of them reaching the inner vessel depositing more than 5 MeV. This fraction resulted in $\epsilon_\gamma = 4.17 \times 10^{-4}$. Combining this fraction with the rate of neutron/decay the induced background above 5 MeV is:

$$\phi_{\text{HE}} = \phi_n \times \epsilon_n \epsilon_\gamma \simeq 26 \pm 5 \text{ ev.y}^{-1} \tag{4.16}$$

This estimation was derived independently with analytical derivations [188]. In this work, neutrons are considered as thermal emitted from a point like source located in the center of one PMT, 25 cm far from the SSS. The number of emitted gamma above 5 MeV is computed by estimating the number of moderated and captured neutron on ^{56}Fe from one PMT. Taking into account the 2212 PMTs, the solid angle and the attenuation length in pseudocumene, the number of gamma above 5 MeV reaching the inner vessel can be estimated. ϵ_γ is equal to 6.86×10^{-4} to be compared with 4.17×10^{-4} obtained from the Monte Carlo method. Similarly, ϵ_n is assessed to be 1.34×10^{-2} from the analytical estimation to be compared with 4.4×10^{-2} from the Monte Carlo method.

The analytical estimation of the background is 7.3 γ.y^{-1} above 5 MeV in the detector considering only the ^{56}Fe contribution and a distance between emitted neutron and n-capture target of 25 cm. This predicted rate is 31 γ.y^{-1} if considering a source/SSS distance of 20 cm and if adding

contributions from ^{52}Cr, ^{53}Cr and ^{58}Ni.

This study can only be considered as an order of magnitude of potential contamination.

Many improvements could be done in this estimation but it would overcome the goal of this analysis which was to identify a mechanism generating high energy γ contaminating the ^{8}B analysis. A future analysis should use a specific neutronic computing software.Besides, further improvements could include:

- precise simulation of the glass (neutron capture in the ^{28}Si or the ^{10}B both high energy γ emitter),
- precise knowledge of the glass composition, in particular of α emitter (see for illustration [193]),
- precise knowledge of substructure of the detector (capture in the SSS legs?) and asymmetries (top plug?).

For now statistics is too low to have a precise picture of the energy spectrum of this external component.

4.4.2 Surface

The nylon vessel is contaminated with natural radioactive elements. The main contributor is ^{208}Tl (Q_β=5.01 MeV) coming from deposition of ^{212}Pb in the material.

Aside from this contamination, a new component was identified: diffusion of ^{220}Rn emanated from the vessel. ^{220}Rn is part of the ^{232}Th chain and is responsible for ^{212}Bi and ^{208}Tl production. The ^{208}Tl contamination is measured by counting the number of ^{212}Bi decaying into ^{212}Po using BiPo coincidence. In order to check the hypothesis of a component of ^{220}Rn diffusing from the vessel surface, the radial distribution of ^{212}Bi was carefully analysed. Figure 4.22a shows this distribution together with a bulk and a surface component. The new component appears in the plot corresponding to an emanation and diffusion of ^{212}Bi. ^{208}Tl must undergo the same behaviour. This extra part, called *diffusion*, can be selected by removing the bulk and the surface component from the ^{212}Bi spectrum.

From the Monte Carlo is extracted the response function of the detector at this radial position using the R_{true}-R_{reco} distribution. Deconvolving this function from the ^{212}Bi diffusion spectrum, figure 4.22b shows the true diffusion spectrum. Re-convolving the true diffusion spectrum with the detector response function for ^{208}Tl gives the diffusion spectrum emanating from the vessel contaminating our sample. This diffusive behaviour has already been studied [194] and observed for ^{214}Bi coming from ^{222}Rn emanation but not for ^{220}Rn.
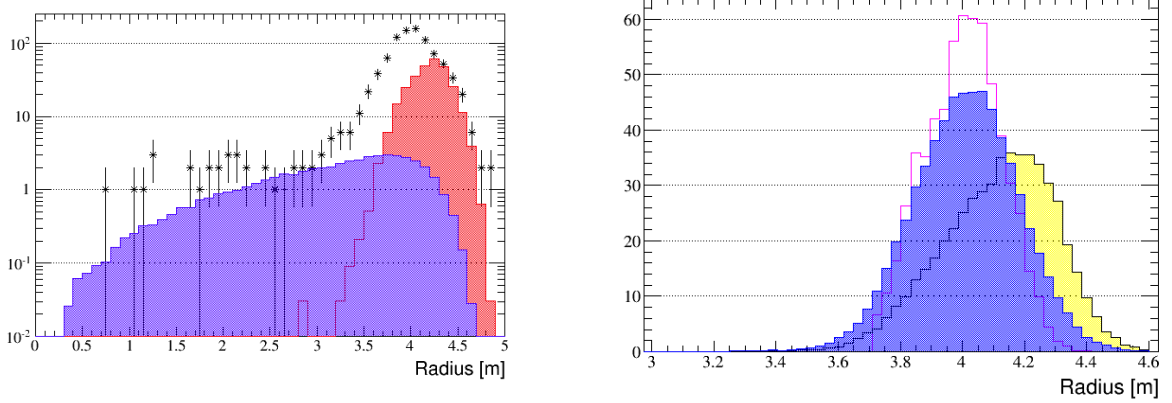
(a) *Structuration of the ^{212}Bi radial distribution data and modelling of the bulk (blue) and surface (red) components. A clear third component is visible: emanation.*

(b) *Deconvolving the data diffusion component (pink) with the detector response function, leads to the true diffusion distribution (blue) with surface distribution simulated (yellow).*

Figure 4.22: *Identification of a diffusion component to add to the surface and bulk contamination.*

4.4.3 ^{11}Be

^{11}Be is decaying through a β^- decay (Q_β = 11.5 MeV, τ = 19.94 s). The ^{11}Be long live time with respect to the other cosmogenics (see section 4.3.3), as well as its high energy makes it a dangerous contaminant. No event by event tagging is possible so it has to be subtracted statistically at the end of the analysis. The last published analysis relied on KamLAND production yield measurement Y(^{11}Be) = $(1.1 \pm 0.2) \times 10^{-7} (\mu.\text{g})^{-1}.\text{cm}^2$ [195] and estimated a residual rate of $(3.2 \pm 0.6) \times 10^{-2}$ cpd/100 t. Since then, Borexino reported a limit on the ^{11}Be yield of Y(^{11}Be)$<7.0 \times 10^{-7} (\mu.\text{g})^{-1}.\text{cm}^2$ [184]. More statistics enable us to do a more precise measurement.

The selection is using coincidence between the muon track and the ^{11}Be decay. The fiducial volume is a 3.5 m sphere, in order to avoid any accidentals. Assuming a muon crossing the detector at t_0 the following conditions are required:

- 10 s < t_{Be}-t_0 < 250 s,
- distance from the muon track of less than 2 m,
- charge of the ^{11}Be has to be higher than 3000 pe ($\sim$ 6 MeV, to avoid accidentals),
- muon charge has to be higher than 10000 pe ($\sim$ 20 MeV), to ensure a good track (MIP of 2 MeV.cm^{-1})

The accidental background is measured by reversing the time requirement (asking for a muon after a potential ^{11}Be), or by looking for a ^{11}Be event between 150 and 300 s after the muon signal and outside the cylinder of the track. The result is given in Figure 4.23. The ^{11}Be is simulated inside the vessel to get charge distribution. A 2D-fit is then realised on the time and charge distribution where ^{11}Be and background amplitudes are free parameters. The resulting fit is compatible with a null composition [196]:

$$R^{\text{HE}}_{^{11}\text{Be}} = (0^{+54.9}_{-0}) \times 10^{-4} \text{ cpd/100 t} \tag{4.17}$$

The measurement can be expanded at low energy using simulated charge spectra.

$$R^{\text{LE}}_{^{11}\text{Be}} = (0^{+36.3}_{-0}) \times 10^{-4} \text{ cpd/100 t} \tag{4.18}$$
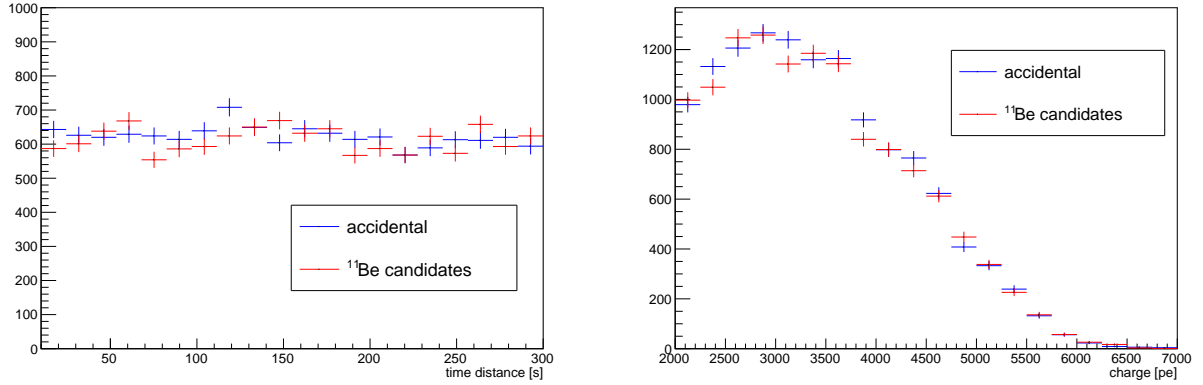
(a) *Distance in time between the muon track and the ${}^{11}Be$ candidate and accidental background.*

(b) *Charge distribution of the ${}^{11}Be$ candidate and accidental background.*

Figure 4.23: *Result of the ${}^{11}Be$ selection: comparison between accidental background and correlated events.*

The result being compatible with 0 events, the positive error will be added to the systematic of the ${}^{8}B$ rate measurement.

4.4.4 ^{208}Tl

^{208}Tl is a natural radioactive contamination belonging to the ^{232}Th chain in the ^{220}Rn segment. ^{208}Tl is produced via ^{212}Bi decay. Equation 4.19 shows the two branches of ^{212}Bi decay with their relative intensities.

$$(64.06\%)\ \ {}^{\textbf{212}}_{\textbf{83}}\textbf{Bi}\ \ \xrightarrow[\text{431 ns}]{\beta\ (2.2\ \text{MeV})}\ \ {}^{212}_{84}\text{Po}\ \ \xrightarrow[\text{0.3 }\mu\text{s}]{\alpha\ (8.78\ \text{MeV})}\ \ {}^{208}_{82}\text{Pb} \tag{4.19}$$

$$(35.94\%)\ \ {}^{\textbf{212}}_{\textbf{83}}\textbf{Bi}\ \ \xrightarrow[\text{4.47 min}]{\alpha\ (6.2\ \text{MeV})}\ \ {}^{208}_{81}\text{Tl}\ \ \xrightarrow[\text{3.05 min}]{\beta^{-}\ (5.01\ \text{MeV})}\ \ {}^{208}_{82}\text{Pb} \tag{4.20}$$
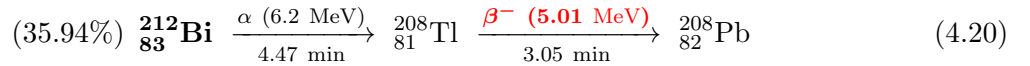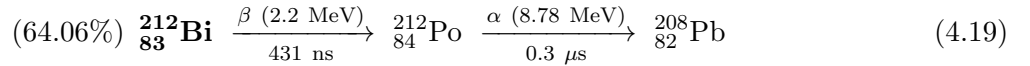
Unlike for the ^{214}Bi contamination, it is not possible to tag directly ^{208}Tl using BiTl coincidence as the decay time of ^{208}Tl is too long. The strategy is then to measure the ^{208}Tl decay rate from the competito branch (BiPo) and to subtract it statistically in the final data sample.

Figure 4.24 shows the charge distribution for ^{212}Po. From [146] the predicted energy after quenching is:

$$\text{Mean}_{\text{pred}} = E_{\alpha} \times Q_{\alpha}(E_{\alpha}) = 8.78 \times 0.1249 = 1.097\ \text{MeV} \tag{4.21}$$

which corresponds to 542 pe, in good agreement with the energy fitted in figure 4.24.
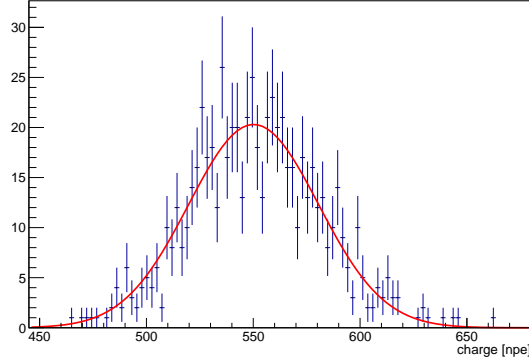
Figure 4.24: ^{212}Po energy distribution in a 3 m sphere. Gaussian parameters: Mean= 550.2 p.e. and $\sigma = 30.4$

To select the ^{212}Bi-Po candidates, we required the following criteria:

- ^{212}Bi decay candidate energy (E $\in$ [20,1200] pe), ϵ_{Bi};
- ^{212}Po decay candidate energy (E $\in$ [450,700] pe), ϵ_{Po};
- Time distance between ^{212}Bi and ^{212}Po: 0.4 μs $< \delta$t < 1.3 μs, ϵ_τ;
- Spatial separation of less than 1 m, ϵ_d.

The number of ^{208}Tl events (N$_{208Tl}$) is derived from the number of coincidences between ^{212}Bi and ^{212}Po (N$_{BiPo}$) using the relation:

$$N_{208Tl} = \left(\frac{Br_1}{Br_2}\right) \left(\frac{N_{BiPo} \times \epsilon_{Tl}}{\epsilon_\tau \times \epsilon_{\text{Bi}} \times \epsilon_{\text{Po}} \times \epsilon_d}\right) \tag{4.22}$$

where Br_i is the branching ratio of the i decay channel, ϵ_{Tl} the efficiency from the 3 MeV energy cut. The time cut efficiency is $\epsilon_\tau = e^{-\frac{0.4\mu s}{\tau_{BiPo}}} - e^{-\frac{1.3\mu s}{\tau_{BiPo}}} = 34.65\%$ and ϵ_d has been estimated to 1 [163]. Efficiencies due to charge cut can be estimated by looking at the charge distribution. Using the function fitted in Figure 4.24 and a Monte Carlo simulation, ϵ_{Bi} and ϵ_{Po} are estimated to 1. ϵ_{Tl} is measured using a simulated ^{208}Tl spectrum in the IV. We found $\epsilon_{Tl} = 90.3\%$. Using the described selection and equation 4.22, the result of ^{208}Tl residual rate can be derived. Table 4.12 summarize the results obtained.

Period	Time (d)	N$_{BiPo}$	N$_{208Tl}$	R$_{208Tl}$ [cpd/100 t]
2007-2009 [163]	488	21	29 $\pm$ 7	$(8.4 \pm 2.0) \times 10^{-2}$
2008-2016	2063.14	27	39.5 $\pm$ 7.6	$(1.9 \pm 0.4) \times 10^{-2}$

Table 4.12: Results of the ^{208}Tl contamination.

Since the purification campaign occurred in 2011, almost no event of ^{212}Bi was found inside the fiducial volume. Figure 4.25 shows the time distribution of the ^{212}Bi events inside a 3 m sphere.
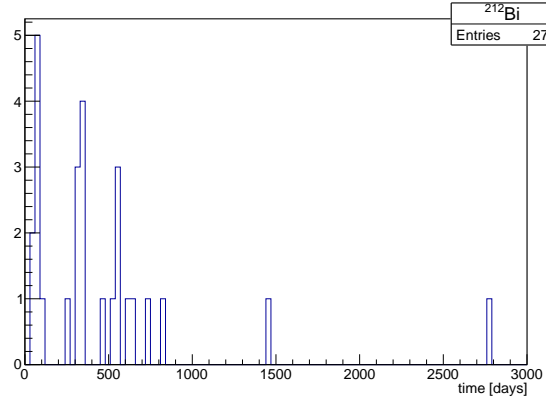
Figure 4.25: *^{212}Bi events in coincidence with a ^{212}Po in the detector.*

4.5 Radial analysis

4.5.1 Threshold determination

The deformation of the charge response depending on the radial position does not allow to translate a charge threshold in energy easily. Monte-Carlo was accurately tuned with calibration sources and allows to reproduce the charge distribution. Generating a continuous energy spectrum of electrons in the whole volume, we derive the volumic efficiency as a function of the true energy for fix charge threshold. Figure 4.26 shows the corresponding energy for two charge ranges:

- Low Energy, LE, between 1650 and 2950 pe, corresponding to event in between 3 and 6 MeV,

- High Energy, HE, above 2950 pe, corresponding to event above 6 MeV.
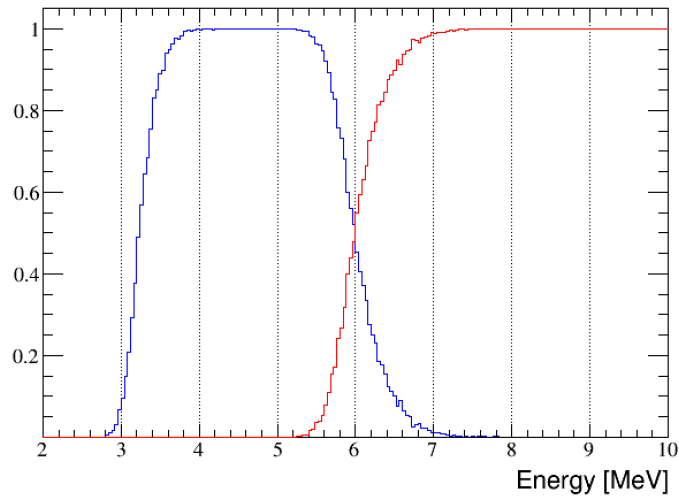
Figure 4.26: *Efficiency and corresponding energy of fix charge threshold for two zones: LE ([1650,2950]) in blue and HE (> 2950 pe) in red.*

The determination of the ^{8}B rate is then done fitting the radial distribution of the different components in these two ranges. As stated, the approach with analytical functions is not reliable

since it does not take into account instability of the nylon vessel and variation in the PMT map and detector response. Monte Carlo simulation using the official Borexino simulation,*g4bx* [182], shows very powerful reconstruction ability.

4.5.2 Time evolution of the detector

The nylon vessel shape is measured weekly by fitting the surface radioactive contamination. Figure 4.27 shows the variation of the shape along weeks for the 8 years of data considered in this study. Radius at the top of the detector is fixed to 4.25 m because of solid structure forcing the vessel to keep this length. The vessel is assumed to be symmetrical by ϕ rotation. This shape variation is modifying any radial distribution (bulk, external, surface contamination). To consider this variation, each simulation is integrating week shapes over the entire data set. Knowing the livetime of any time period, the number of events simulated with the corresponding shape is weighted by this livetime. The final radial distribution is then the sum of many different vessel shapes event reconstruction.
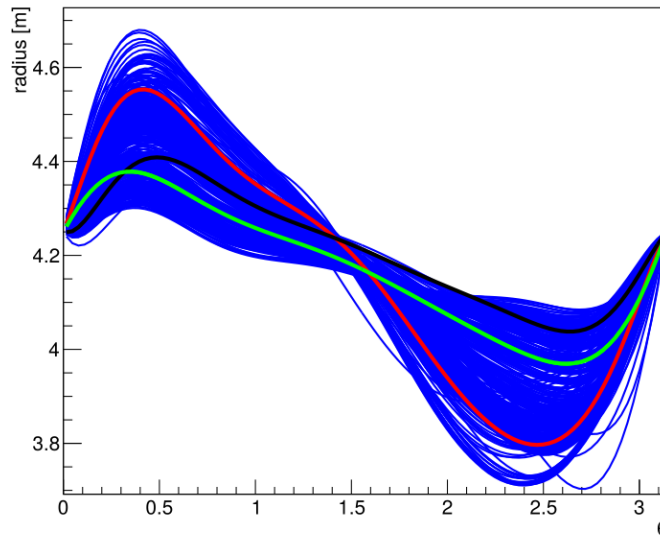
Figure 4.27: *Evolution of the shape $R(\theta)$ during 8 years of data taking. Black, Green and Red curves represent different week: respectively the 13th, Jan 2008,the 27th, May 2012 and the 15th, May 2016.*

Aside from the vessel shape evolution, the number of operating PMTs is decreasing with time. Figure 4.28 shows the time evolution. If 2212 PMTs were installed in 2002, 175 PMTs failed before taking data. Issues at the Gran Sasso laboratory in 2002-2006, PMTs remained in air operating only occasionally and the water/PC filling revealed some defects or cracks in the sealing. Since then, the failure rate is constant, around 3 PMTs per week [143].

Every charge presented in this work is always normalized with respect to 2000 working PMT, in order to be able to use the calibration and to compare 8 years of data with a perpetually evolving PMT numbers. The map of the working PMT is known. It has been observed that PMTs in the South hemisphere of the detector are deteriorating faster than in the North leading to a distortion
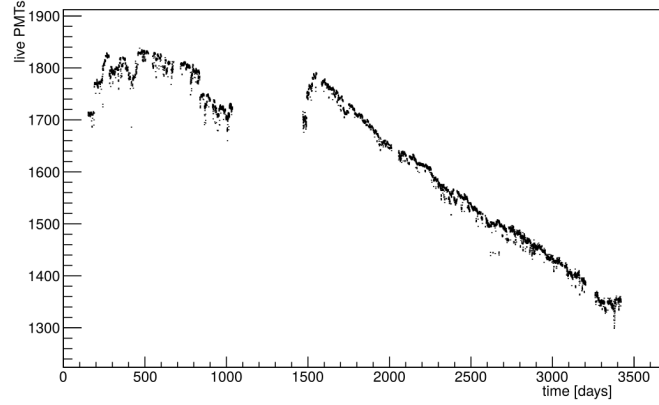
Figure 4.28: *Evolution of number of live PMTs on the selected data set.*

in the charge/energy correspondence depending on z. This effect is well reproduced by the Monte Carlo, as demonstrated in section 4.2.2.

4.5.3 Results

HE range The external background was modelled by the n-capture gammas energy and position distribution from PMT neutron emission. It is mainly composed of 7.6 MeV and 9.3 MeV gammas coming from the SSS. Figure 4.29 shows the fit of the external excess using those simulations.
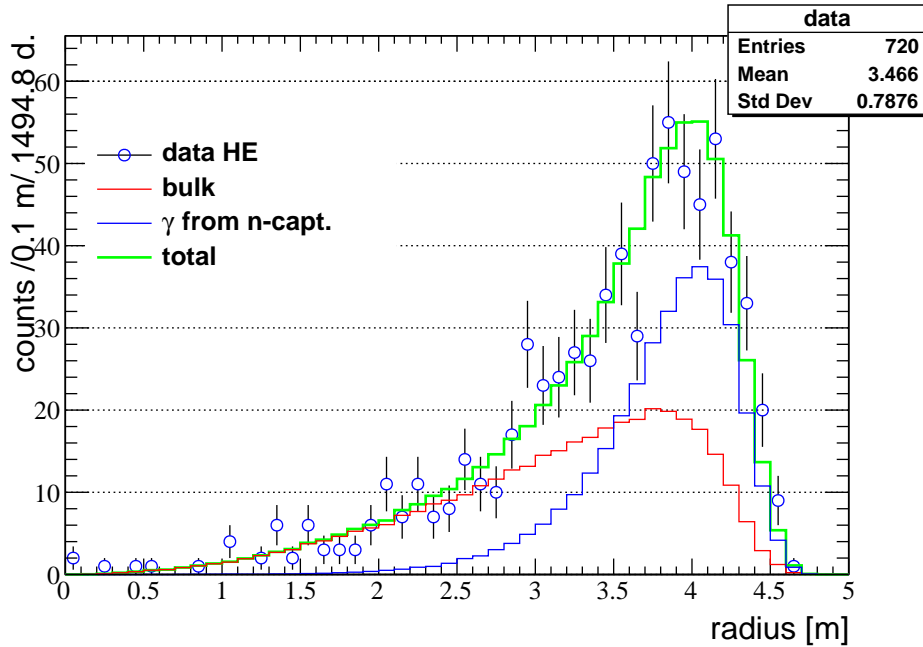
Figure 4.29: *Radial fit in the HE range. Result of the fit:* $\chi^2/NdF = 0.97$, *bulk= $(9.22 \pm 0.82) \times 10^{-2}$ cpd/100 t and external= $(8.83 \pm 0.81) \times 10^{-2}$ cpd/100 t.*

The model is in excellent agreement with the data. The expected rate was 26 ± 5 y^{-1} leading to $(2.7 \pm 0.5) \times 10^{-2}$ cpd/100 t with respect to the measured rate $(8.83 \pm 0.47) \times 10^{-2}$ cpd/100 t. The

order of magnitude is respected but more investigations are required to understand the difference.

Rate [10^{-2}cpd/100 t]	9.22 ± 0.82		
Residuals	muons	fast cosmogenics	^{11}Be
Rate [10^{-4} cpd/100 t]	(3.5 ± 0.8)	(14.2 ± 0.7)	$(0^{+54.9}_{-0.0})$

Table 4.13: *Result in the HE range.*

Table 4.13 lists the residual contaminations in the HE range. This leads to the result:

$$R^{\mathrm{HE}}_{^8\mathrm{B}} = 0.090^{+0.008}_{-0.01} \text{ cpd/100 t} \tag{4.23}$$

LE range   In the LE range, external, surface, diffusion and bulk distributions are expected. Among the bulk component, residual background must be subtracted.

The surface contamination is modelled by generating ^{208}Tl nuclei inside the nylon.

The bulk radial distribution is due to neutrino and ^{208}Tl. The ^{208}Tl distribution is slightly different from the neutrino one. Indeed, the 2.6 MeV gamma can be lost in the buffer distorting the shape at large radii. Figure 4.30 shows the two different radial distributions. Besides, having measured the ^{208}Tl contamination inside the data set, this component can be fitted in the final radial distribution with a penalty factor.
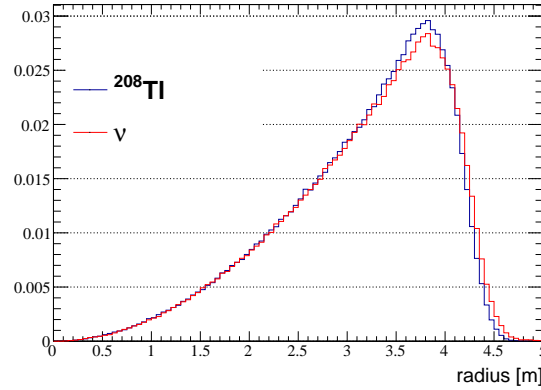
Figure 4.30: *Comparison of the internal ^{208}Tl contamination with a typical neutrino like signal.*

Beside the neutrino distribution, the final background components of the LE energy bin are external, emanation, diffusion, and surface. Measured rates and residual contaminations are listed in tables 4.14 and 4.13

Rate [cpd/100 t]	0.1361 ± 0.013				
Residuals	muons	neutrons	fast cosmogenics	^{10}C	^{11}Be
Rate [10^{-4}cpd/100 t]	(4.5 ± 0.9)	(0.9 ± 0.1)	(9.8 ± 0.7)	(6.4 ± 1.4)	$(0^{+36.3}_{-0})$

Table 4.14: *Result in the LE range.*
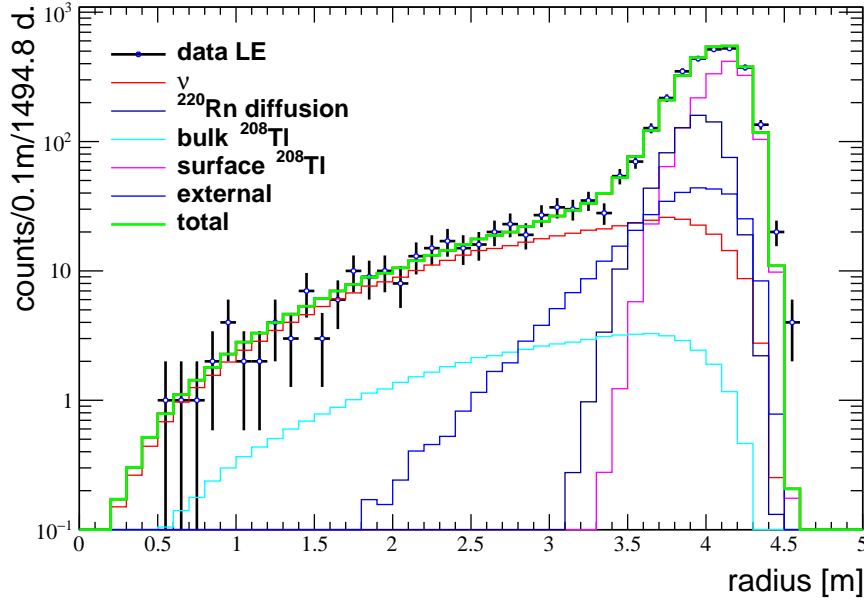
Figure 4.31: *Radial fit in the LE range.*

This leads to the final ^{8}B neutrino rate is in the LE range:

$$R_{^8\mathrm{B}}^{\mathrm{LE}} = 0.134^{+0.013}_{-0.013} \text{ cpd/100 t} \tag{4.24}$$

This result is given for illustration, definitive numbers, context and interpretations are published in [196].

Conclusion

The new analysis presented here has increased the total exposure by a factor 11, enabling to reach a total uncertainty of 8%, with respect to 19% of the previous analysis. This result has been obtained by using the entire volume of Borexino above 5 MeV. Not using fiducialisation demands to master any backgrounds in the date set. After selecting the data, a Monte Carlo method was developed to measure the dead-time induced by tagging the muons and the muon-induced backgrounds. Internal radioactive contamination identified or estimated using BiPo coincidence technique. External contamination above 5 MeV was a show stopper until its identification as coming from n-capture on the Stainless Steel Sphere. Estimation of this background coming from (α,n) reactions is in agreement with the order of magnitude of the external component. Further studies might be necessary to identify potential addition to the identified neutron sources. Identification of the emanation component between 3 and 5 MeV is an impressive achievement of this analysis as well.

Chapter 5

Cerium Antineutrino Generator

Contents

Cerium (Z=58) is classified as a lanthanide (a subfamily of the rare earth elements). Due to its oxydation numbers III and IV, it can be found in the following oxide forms, Ce_2O_3 or CeO_2 [197]. However, the Ce_2O_3 is unstable and quickly oxydates in CeO_2 in normal condition. Besides, CeO_2 is liquid above 2400 °C.

Natural Cerium is composed of 4 isotopes among which three are stables: ^{136}Ce(0.19 %), ^{138}Ce(0.25 %) and ^{140}Ce(88.48 %) and one isotope decaying via alpha emision with a very long lifetime ^{142}Ce (11.08 %) [197]. ^{144}Ce with a year-scale lifetime can not be extracted from rocks. It must be artificially produced. Cerium isotopes are major components of radioactive nuclei produced in nuclear reactors (see section 3.3.2).

5.1 Nuclear reactors: Cerium ore

In this section we will note σ_{capt}, $\sigma_{elastic}$, σ_{fiss} and σ_{tot} the cross sections for a neutron radiative capture, scattering, induced fission and total cross section respectively.

5.1.1 Induced fission and chain reactions

Nuclear plants are producing electricity mainly based upon ^{235}U and ^{239}Pu fission reactions. ^{241}Pu and ^{238}U fission reactions are playing a minor role as well. Other transuranian elements participating can be neglected. The fission process can be spontaneously or artificially activated and consists on breaking heavy (neutron rich) nuclei into smaller products. The mother nuclei having more binding energy than the fission products, the binding energy is released, usually absorbed by the system and converted into heat. As an illustration, ^{235}U fission process releases 202.8 MeV. The effective produced heat is highly depending on the capacity of the reactor to contain the energy inside the coolant. Fission energy is distributed between fission products kinetic energy ($\sim 84\%$) and γ, β, α, neutrons and $\overline{\nu_e}$ radiations [198]. Figure 5.1a shows the mass distribution of the fission products depending on the nuclei. The fission is not symmetrical: the mass of the fission products are formed of one lighter and one heavier nuclei. Figure 5.1b, shows the nuclei distribution depending

(a) *Mass distribution of the fission product for most common nuclear fuels [199].*

(b) *Mass distribution of the fission product for ^{235}U [158].*

Figure 5.1

114
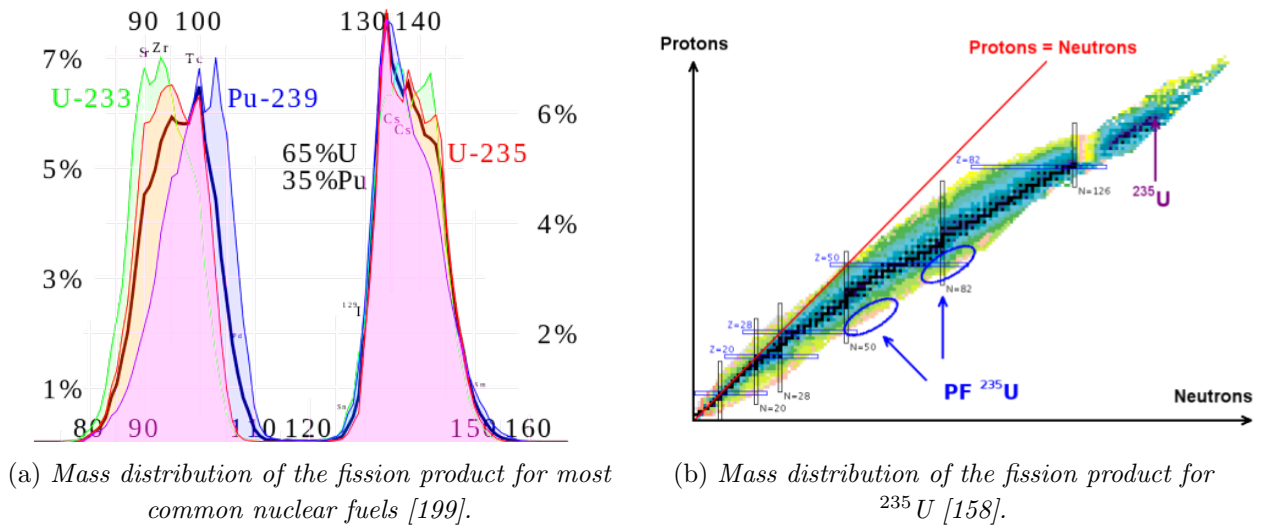
on neutron and proton composition. The fission can be induced by neutron absorption: a free neutron will be absorbed by a heavy nuclei, leading to its fission. This fission might induce neutron emission, inducing more fission [200]. The effective neutron multiplication factor, k, is the number of fission released neutrons inducing new fission. It is the key parameter to characterize any chain reaction. Neutron emission relies on two competitive processes: prompt and delayed emission. The prompt neutrons are emitted within 10^{-14}s while delayed neutron are kept by fission products for few milliseconds before being released. This process is of first importance in nuclear reactor physics. A system will be called critical if k is strictly equal to 1. A system operating in critical mode sustains the fission reactions, inducing the release of heat.

A heating system is dilating, reducing the number of target per unit of volume, loosing the criticality. The loss of the criticality cools down the core, entering in an oscillating mode. This phenomenon - together with the control rods and delayed neutron emission - helps to keep criticality. A nuclear core is then built for sticking to k=1 (being slightly sub-critical for prompt neutron emission) while a nuclear bomb is based on the realisation of the highest initial k possible. Once k is above 1, it will then fast increase with time before explosion, the initial value of k being the limitation [201].

5.1.2 Nuclear fuel

For fission to be a sustainable source of energy, the fuel has to be "easily" fissionable and naturally abundant. ^{241}Pu, ^{239}Pu, ^{233}U, ^{235}U, ^{237}U are called fissile: they are able to undergo fission after capturing a thermal neutron. Thermal neutrons refers to neutron in thermal equilibrium with the medium, meaning, at 300 K its typical energy lies below $\frac{3k_{\mathrm{B}}T}{2} \sim 40$ meV. Above Lead, only Bismuth, Thorium and Uranium have a lifetime long enough for remaining in significant quantity since Earth formation. ^{235}U is the only fissile specie which is available naturally. Natural uranium abundances are 99.29% of ^{238}U, 0.7% of ^{235}U and negligible amount of ^{234}U. Besides being abundant, uranium is easy to extract because its high solubility leads to accumulation in nowadays uranium mines. The natural abundance of ^{235}U is not high enough for considering natural water moderated reactors but it enables to think about enrichment process. This consideration drove the early development of the Uranium sector in the nuclear industry.

Fissile species can also be artificially produced through fertile material: nuclei producing fissile material under neutron irradiation. ^{232}Th and ^{238}U, for instance, are fertile material. Equations 5.1 and 5.2 described the reactions to produce fissile nuclei from thermal neutron irradiation on ^{232}Th and ^{238}U respectively [202].

$$^{232}_{90}\mathrm{Th} + n \xrightarrow{\sigma_{\mathrm{capt}}=7.4 \text{ b}} {}^{233}_{90}\mathrm{Th} \xrightarrow[22 \text{ min}]{\beta \ (1.2MeV)} {}^{233}_{91}\mathrm{Pa} \xrightarrow[27 \text{ days}]{\beta \ (0.6MeV)} {}^{233}_{92}\mathrm{U} \tag{5.1}$$

$$^{238}_{92}\mathrm{U} + n \xrightarrow{\sigma_{\mathrm{capt}}=2.7 \text{ b}} {}^{239}_{92}\mathrm{U} \xrightarrow[23 \text{ min}]{\beta \ (1.3MeV)} {}^{239}_{93}\mathrm{Np} \xrightarrow[2.4 \text{ days}]{\beta \ (0.7MeV)} {}^{239}_{94}\mathrm{Pu} \tag{5.2}$$
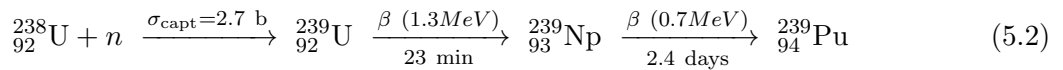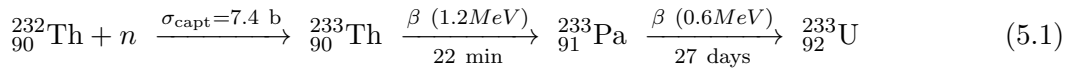
^{239}Pu, ^{233}U and ^{235}U are interesting candidates for nuclear fuel. Indeed, almost all of their thermal neutron capture leads to fission ($\sigma_{\mathrm{fiss}} \sim \sigma_{\mathrm{tot}}$) minimizing sterile capture or transuranian production and they have relatively high cross sections ($\sigma_{\mathrm{fiss}} \sim 100 - 600$ barns). Nowadays, most of the reactors are using natural or ^{235}U enriched Uranium on UO$_2$ form. Most of the commercial reactor have a fuel enriched between 3-5% of ^{235}U. Usually the fuel is contained in UO$_2$ pellets piled up in rods. The high presence of ^{238}U, leading to ^{239}Pu production, increases the probability to reach transuranians elements by neutron radiative capture. In such a mix, the heat released by

^{239}Pu is slowly dominant as it accumulates in the fuel, as shown in figure 5.2. Military fuel can be
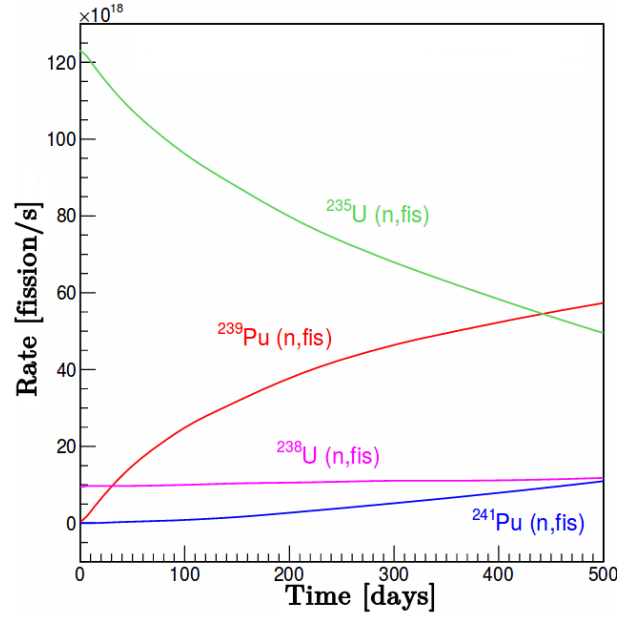
Figure 5.2: *Typical fuel evolution for a PWR commercial reactor (Chooz). Credits to [203].*

made of ^{239}Pu (from natural Uranium in thermal reactors) and pure ^{235}U. The demand during Cold War induced a lot of coherent efforts in the ^{235}U extraction/enrichment at the industrial scale.

5.1.3 Nuclear reactors

Nuclear reactor is a technological solution to keep k_{eff} very close to unity, leading to sustainable chain reactions. Two possibilities can be exploited: using fission fast neutrons or thermalising them to increase capture cross section. In the first option (fast neutron reactors), σ_{fiss} being low, chain reaction demands to increase neutron density in the core. The second option exploits moderators (thermal reactor) to increase σ_{fiss}. Reactors geometry, technology and fuel are strongly depending on purpose:

- commercial: power generation, grid-connected, usually less than 4% ^{235}U enriched, large;

- research: intense neutron source for irradiation or fundamental research, study of reactor physics, low power, highly enriched;

- military: nuclear weapon material generation, natural uranium, medium power, graphite or heavy water.

Moderators

A moderator is a material combining a low σ_{capt} and a high $\sigma_{elastic}$. Furthermore the lighter is the moderator, the most momentum can be transferred during elastic collision of the neutrons. The most common moderators used are light water (H_2O), heavy water (D_2O) and graphite (carbon crystal) [204]. Fuel rod gains are generally built in Zirconium because of its low interaction rate with neutrons. At the opposite, the control rods are composed of high neutron absorber such as cadmium, halfnium or boron in order to stop the chain reactions.

Commercial reactors

Most of the commercial reactors in the world are using thermal neutron and low enriched ^{235}U (3-5%). The most common used technology is the Pressurized Water Reactor (PWR, REP in France and VVER in Russia). Water is used for neutron moderation, cooling and heat transfer, fuel rods are immersed in light water. Usually two water loops are used: the primary circuit, under high pressure and the second circuit at atmospheric pressure for stream production. The steam is then used for spinning turbines and generating electricity. The water of the first circuit, in contact with the core, reachs 325 °C. It is though necessary to pressurize it around 150 bar for keeping it liquid: hence the name Pressurized Water Reactor.

Other reactor designs use different moderators or coolant. They are called BWR, GCR, PHWR, LWGR and FBR refering to Boiling Water, Gaz Cooled, Pressurized Heavy Water, LightWater Graphite, and Fast Breeder reactors respectively [204].

Research reactors

Each of the research reactors has almost its own unique design, depending on the building period and purpose. One of the characteristics is that fuel is usually highly enriched uranium fuel (from 20% to 95%). In order to increase the ratio of ^{235}U over extracted Uranium, different methods are used. All isotopic separation methods needs individual atoms behaviour demanding a gaseous phase: uranium hexafluoride (UF_6). First, mass spectrometer technique were used in 1944 to differentiate the curvature after uranium beam acceleration (California University Cyclotron: Calutron). Then resins separated isotopes by their migration velocity (chromatography). Those two methods were too energy consuming. Finally nowadays, two techniques were industrially developed: gaseous diffusion and centrifugation [205]. The first one is the most used and is based on differentiating thermal velocity depending on particle mass ($v_{\text{th}} \propto \sqrt{k_B T/m}$): for the same temperature, the ^{235}U average velocity will be higher than ^{238}U, leading to more contacts with the wall of a box. Compressing the UF_6 in porous material during several cycles will enrich the gas in ^{235}U. The most competitive process is enrichment by gaseous centrifugation. The heaviest element being more concentrated fare from the rotating axis, the lighter ^{235}U is collected near the center. Multiplying cycle process enables to enrich Uranium at any requested levels.

5.1.4 Rare earth production

Fission of ^{239}Pu and ^{235}U induces production of many isotopes as illustrated in figure 5.1a. Some have a long lifetime or are stable and will be part of nuclear waste. Rare earth are relatively abundant products of nuclear waste. Table 5.1 gives the cumulative fission yield of the most abundant Cerium isotopes from ^{239}Pu and ^{235}U.

From Table 5.1, taking into account lifetime and yield of Cerium isotopes, the only expected background after Cerium selection will be ^{140}Ce and ^{142}Ce. Calling $\zeta_{^{144}\text{Ce}}$ the ratio of ^{144}Ce among Cerium stable isotopes, $\zeta_{^{144}\text{Ce}}$ is 31% for a pure ^{235}U and 27% for a pure ^{239}Pu. It means that extracting the source from a power reactor or from a research reactor modifies a priori ^{144}Ce specific activity. Besides, the Spent Nuclear Fuel (SNF) can be extracted from a research reactor core faster than from a commercial reactor because of the lower decay heat. With a lifetime of 411 days, this cooling delay of few years is not negligible. A lot of rare earth are produced as well in SNF

| Isotopes | $T_{1/2}$ | thermal Cumulative Fission Yield | |
		^{235}U	^{239}Pu
^{136}Ce	stable	8.1×10^{-12}	-
^{138}Ce	stable	7.0×10^{-11}	1.8×10^{-7}
^{139}Ce	137.6 d.	1.2×10^{-11}	4.2×10^{-9}
^{140}Ce	stable	0.063	0.053
^{141}Ce	32.5 d.	0.059	0.052
^{142}Ce	$> 5 \times 10^{16}$ y.	0.059	0.050
^{143}Ce	33 h.	0.060	0.045
^{144}Ce	284.9 d.	0.055	0.038
^{145}Ce	3.01 min.	0.040	0.030
^{146}Ce	13.5 min.	0.030	0.024
^{147}Ce	56.4 s.	0.019	0.019
^{148}Ce	56 s.	0.016	0.010
^{149}Ce	5.3 s	7.8×10^{-3}	6.0×10^{-3}
^{150}Ce	4.0 s.	4.0×10^{-3}	2.8×10^{-3}
^{151}Ce	1.7 s.	1.0×10^{-3}	6.4×10^{-4}
^{152}Ce	1.4 s.	2.1×10^{-4}	1.2×10^{-4}

Table 5.1: *Fission yield from ^{235}U, ^{239}Pu and ^{238}U, the 3 main components of nuclear core fuel. Extracted from [206], [207].*

by fission reactions. A complex separation process is needed to extract ^{144}Ce from this hazardous environment.

5.2 Specifications

A tendering process assessed that PA MAYAK is the only installation in the world able to produce such quantity of ^{144}Ce. The contract for the production of the CeANG source between CEA and *Federal State Unified Enterprise Production Association Mayak* (PA MAYAK) has been signed in December 2016. This contract lists the specifications demanded for the production of a cerium antineutrino generator for neutrino physics i.e. very low background experiment.

The source must be between 3.7 and 5.55 PBq (100-150 kCi) (see section 3.3.2) at delivery time in St Petersbourg. Technical issues arise from such an active material, especially heat generation. The maximum temperature of the external stainless steel capsule has been settled to 500 °C and the maximum pressure inside the capsule must not exceed 6 atmospheres.

The source has to be in a classical form of CeO_2 powder. This powder will have a density in between 2.5 and 5 g.cm^{-3}. Indeed, a less dense powder would have a lower heat conductivity and heat evacuation limited. If the liquefaction temperature of Cerium is not an issue (2400 °C), the gas pressure in the volume in contact with the powder is strongly increasing with temperature. To ensure keeping this density range a press will be used to compact the extracted powder at the encapsulation time. Beside, Copper radiators were added to facilitate heat evacuation.

The purity of the source is one of the main issue of the CeSOX experiment. Extracted from

wasted reactor fuel and concentrated in a nuclear facility, the high level of radio-purity is a major challenge. The issue is to avoid any bias in the calorimetric estimation on which rely the measured oscillation spectrum as well as long term storage. All of those points are developed in further sections (see in particular 7.3). The requirements on the source purity at delivery time are:

- heat released by all the controllable contaminants shall be 10^{-3} lower than heat released by ^{144}Ce+^{144}Pr,
- activity of contaminants emitting γ above 1 MeV shall be 10^{-3} lower than the activity of ^{144}Ce-^{144}Pr ,
- activity of ^{244}Cm+^{243}Cm shall be 5×10^{-3} lower than the activity of ^{144}Ce-^{144}Pr ,
- activity of ^{241}Am+^{238}Pu shall be 10^{-5} lower than the activity of ^{144}Ce-^{144}Pr .

Extracting such a radio-pure and very active source from a spent nuclear fuel is a major technological challenge.

5.3 CeO$_2$ production

5.3.1 CeANG selected seed material

PA MAYAK is located in the Tcheliabinsk oblast, at the feet of the Oural chain. The construction of the military nuclear complex begin in 1945 in order to produce ^{239}Pu for nuclear warhead in the Cold War context. If the ^{239}Pu production has been officially stopped, the complex is now specialized in SNF reprocessing for realisation of the so called "closed nuclear fuel cycle". Part of nuclear waste are treated for production of medical radioisotopes [199, 208].

Kola nuclear plant

At the origin of the negotiation between CEA and Production Association MAYAK, the fuel was decided to be coming from Kola reactors. Located in the Mourmansk oblast, this nuclear plant is composed of 4 VVER-440 MWe reactors (Pressured Water type). These commercial reactors are fed with stationary reloading mode in three-, four-, five- and six-years fuel cycle. Considering the spent Fuel Assembly (FA) is important because the specific activity of ^{144}Ce is depending on Pu/U ratio and batch history (end of irradiation, time of the cycle, position of the rod inside the detector, cooling time). The shortest is the fuel cycle, the highest specific activity of ^{144}Ce is and the cleanest is the sample [209]. PA MAYAK agreed on delivering fresh SNF Fuel assemblies (1-1.5 y instead of the usual 3 y. minimum of cooling time) to increase ^{144}Ce specific activity. As illustration, the 2$^{\text{nd}}$ batch discussed with PA MAYAK would have been constituted of 29 FA for 2.9 tons containing 8.5 kg of Cerium and 192 g of ^{144}Ce for a specific activity of 2.7 TBq per gram of Cerium [210, 211, 212, 213].

Research reactors

In 2015, due to difficulty in reach the desired activity, and time delay on the contract signature, PA MAYAK suggests to use research reactor SNF [214]. According to public knowledge [199], two running reactors might be still working on site: Rsulan, 1000 MWth using light water and Ljudmila (LF-2), 1000 MWth using heavy water. For now, we assume the fuel to be 95% enriched in ^{235}U but we have no knowledge on the composition, age and batch used for the source extraction. Activity of ^{144}Ce per gram of Cerium should be higher, enabling PA MAYAK to concentrate 5.5

PBq of ^{144}Ce while respecting the contractual density range for the CeO_2 (for thermal and pressure preoccupations).

5.3.2 Cerium extraction and online analytical control

Figure 5.3 gives an overview of the first step of purification, from the fuel assembly to the PUREX raffinate. Following paragraphs will complete this overview.
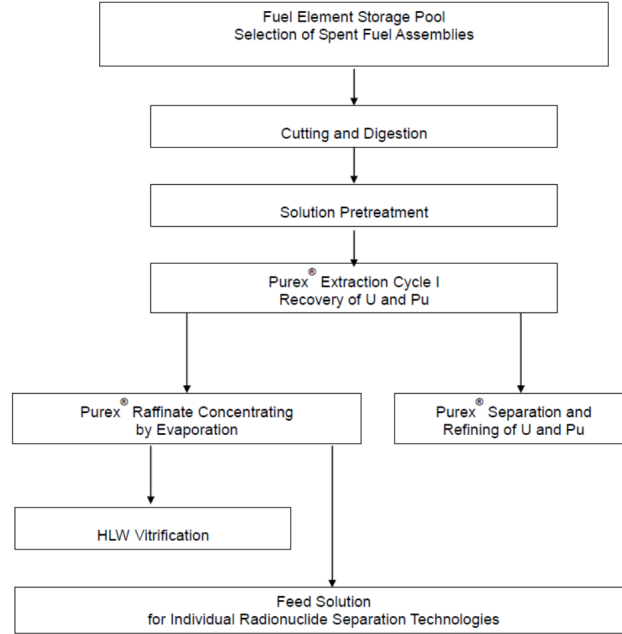
Figure 5.3: *Schematic overview of the purification processes. Credits to [210].*

Cutting and cleaning

From the reactor core, the wasted fuel is then transport to a post-reactor water pool storage. After cooling time the SNF Fuel Assemblies are transported to the Radiochemical Plant RT-1, Ozersk, Chelyabinsk region, Russia. The end pieces of Fuel Assemblies are separated but UO_2 pellets are not extracted from the fuel rods. The girdle and the UO_2 are both cut into small pieces using hydromechanical processes. The mixture is then dissolved into nitric acid. The not pellet elements are flocculated using high-molecular organic agent. The solution is then filtered and cleaned from flocculated agent. This first step is primordial as those contaminations from fuel assembly could affect the PUREX process.

PUREX process

Plutonium and Uranium Refining by EXtraction, PUREX, is a procedure used to extract Uranium and Plutonium from fission products and minor actinides. An organic solvent (tributyl phosphate and hydrocarbon) is added to the mixture, extracting part of the Uranium and Plutonium [215].

Many cycles are necessary to extract them efficiently. The leftovers are acid nitric with high concentration in fission product. Some commercial reprocessing facility are extracting Uranium and Plutonium in order to reuse ^{238}U, ^{235}U and ^{239}Pu in fuel (standard fuel or mixed oxide fuel -MOX- for burning ^{239}Pu). On 290.000 t of discharged fuel, 30% have been reprocessed so far[216]. After getting rid of Uranium and Plutonium, the leftover is converted into stable oxide form for storage. Usually, PUREX process is applied on light-water reactor fuel typically after more than 5 years cooling period. The PUREX process used by PA MAYAK is therefore optimized and slightly modified with respect to the worldwide used techniques.

The PUREX raffinate - i.e. the acid nitric solution containing the fission product- is transported to an other radiochemical plant through a 1.5 km pipeline in order to be concentrated by acid nitric evaporation. In PA MAYAK, like in all the other reprocessing facility, the PUREX raffinate is usually directed to vitrification unit for disposal of high radioactive waste in form of phosphate glasses [210]. However, in some case, the facility can pump the PUREX raffinate to extract ^{137}Cs, ^{90}Sr, rare earth (REE) and trans-plutonium (TPE) elements for scientific, medical or industrial applications.

Rare Earth Extraction
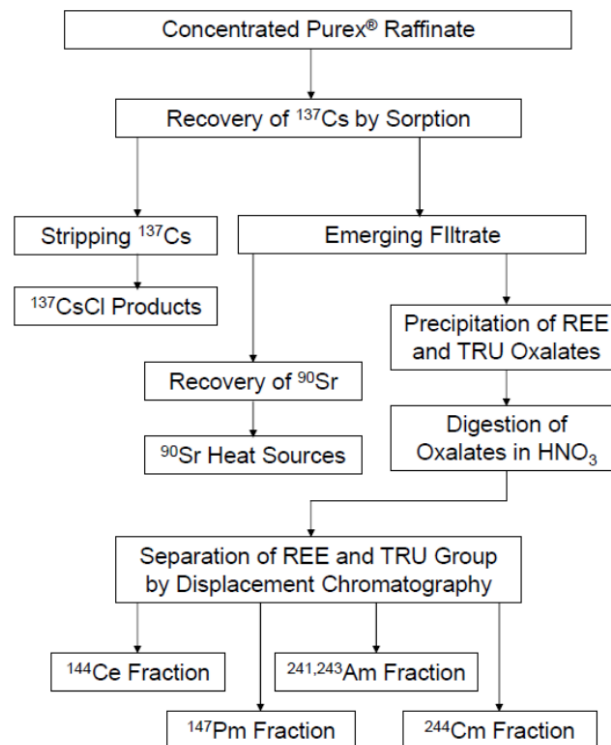
Figure 5.4: *Cycle from PUREX raffinate to Cerium extraction. Credits to [210].*

Figure 5.4 gives an overview of the different processes used in order to get Cerium extracted from the PUREX raffinate. It is important to notice that in most of the rare earth extraction processes, Cerium is an impurity to get rid off because of its high concentration in the ore after the

Element	La	Ce	Pr	Nd	Pm	Sm	Eu	Am	Cm	Fe	Cr	HNO$_3$
Concentration g.L^{-1}	4	9.95	4	15.8	0.6	2.8	0.2	0.027	0.009	0.2	0.02	76
Activity Ci.L^{-1}	-	1790	-	-	625	-	6	-	-	-	-	-

Table 5.2: *Composition of REE and TPE concentrate after oxalate precipitation and digestion. Extracted from [210].*

first selection [217].

At this stage, the raffinate is a thick liquid that can be assimilate as a pulp. Dilution in water is needed in order to get a liquid, easier to handle. Some metal ions like Fe, Ni or Cr and impurities (namely ^{137}Cs and ^{90}Sr) are still contaminating the sample. To get rid of them, oxalate acid ($C_2O_4^{2-}$) is used. Oxalate ions are easily fixing metallic ion with a valency of three or more (REE and TPE). Figure 5.5a shows the form of the molecule while figure 5.5b displays the formation of Cerium oxalate ($Ce_2(C_2O_4)_3$) from precipitation of Cerium with oxalate acid. Using precipitation

(a) *Oxalate acid ($C_2O_4^{2-}$),*

(b) *Cerium oxalate ($Ce_2(C_2O_4)_3$),*
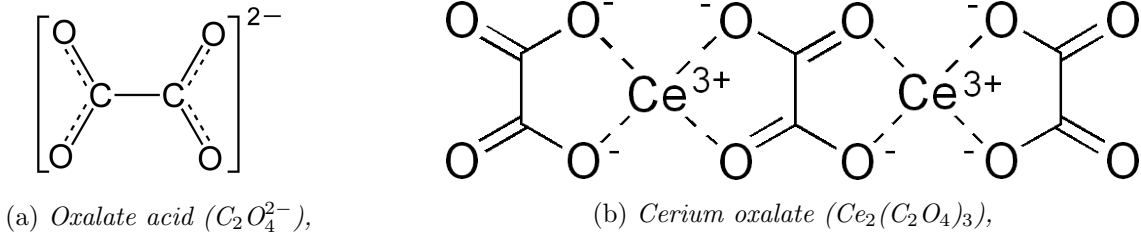
Figure 5.5: *Selection of the REE and TPE using oxalate precipitation.*

of REE and TPE, the solution is filtered. The extracted substrate is then dissolved using nitric acid. This step is usually done twice, giving its name: double oxalate precipitation. Table 5.2 list the composition of REE and TPE after double oxalate precipitation and dissolution [210]. This composition is given for illustration, the fuel used for CeANG extraction is not a commercial SNF, the concentration of Cerium and other REE and TPE radioactive isotopes might be higher at this stage. From the reception of the SNF from the reactor fuel pool to the end of the rare earth extraction, the duration of the treatment is between 3 and 8 months [218].

Displacement Complexing Chromatography

Displacement Chromatography is based on binding affinity competition. The stationary phase (also called matrix) binding sites are first occupied by a carrier. This matrix is chosen for its differentiating binding affinity depending on compound of the solution one wants to separate. With respect to other chromatography, displacement chromatography has sharp-edged separation bands between compounds while elution chromatography have Gaussian-like separation bands.Separation operation can be divided in three: loading, displacement and regeneration [219], represented in figure 5.6b.

The first step is the loading. The separation column is first filled with a carrier occupying the stationary phase. Adding the solution at the head of the column and passing through the matrix, the higher-affinity compounds of the analyte first displace the carrier. The higher the affinity is, the less compounds are able to move through the column. With this principle, the downstream flow,

gravity driven, slowly separates compound of the analyte. This leads to sharpe-edged separation bands. Indeed, if any element of one higher band is moving downward a lower band region, it will easily displace element of this band from stationary phase and thus moving slower until elements of its own band catch it up. First elements reaching the bottom of the column will be the mobile phase with no affinity with the matrix. The column size is chosen to let the process reaches completion. The separation bands are called a "displacement train".

Second step is the displacement. The operator adds a displacer (or eluent) at the head of the column. This displacer has a higher affinity with the matrix than any compound of the solute. Therefore, this solution pushes downward the highest band of the displacement train. This first band will act as a displacer for the second contiguous band, pushing it downward as well. Few by few, the train begins to move downward. Each compound of the solution can then be recuperated at the bottom of the column with each individual zone having a uniform concentration of the band element.

Finally, the regeneration is the step in which the displacer, now occupying the whole column is removed to come back to the initial state with a matrix filled with a carrier. This step can be difficult as the displacer has been chosen for its high compatibility with the matrix. Increasing or decreasing the pH of the column liquid can be a solution to modify the affinity of the displacer and to wash out the matrix.

(a) *From left to right: 1/matrix and carrier, 2/loading, 3/elements with higher affinity are retained by the stationary phase.*
Credits to [199].

(b) *Illustration of rare-Earth concentration as a function of the volume of eluent added to the column, from [220]*
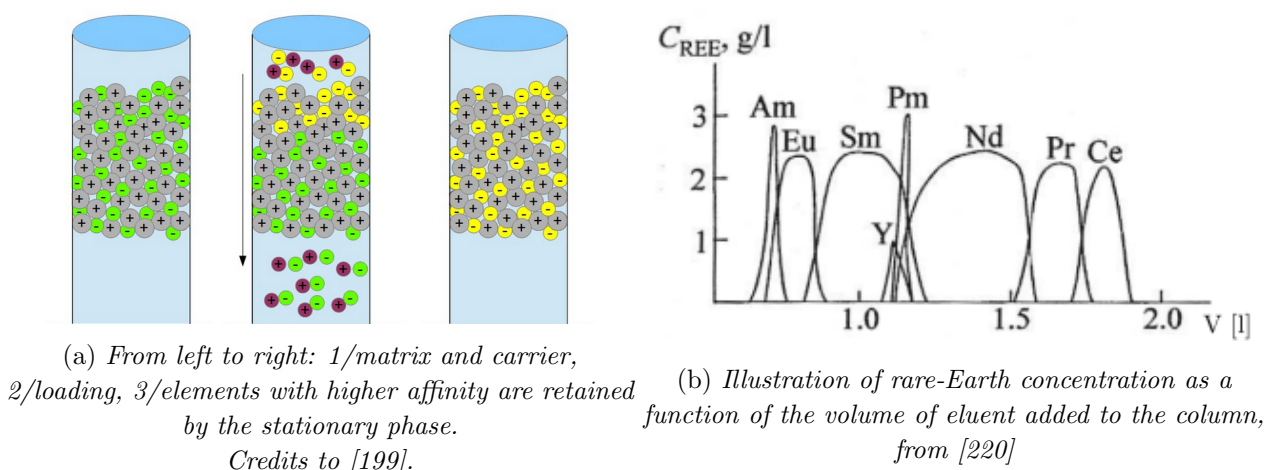
Figure 5.6: *Complexing Displacement Chromatography illustrations*

In a Complexing Displacement Chromatography, ionic exchange are used as affinity. This technique is common in Rare Earth extraction as it is sensible to the proton number.

Mayak facilities and specificity The Mayak chromatography installation is employing a ionic resin as a stationary phase mixed with a counter-ions solution for mobile phase. The pH is optimized for maximizing the binding affinity of the element one wants to select [221]. The installation is composed of eight columns connected in line with decreasing cross section (from KV-I: 502.9 cm^2 to KV-8: 2.0 cm^2). Schematically, each column is two time larger than its forerunner. Figure 5.7 illustrates the process. Each column is filled with solid sulfonic cation resin KUx8 (Dowex-50 type) for the stationary phase in very acid pH. The retain capacity of the stationary phase is about 85 g of rare earth for one resin litre. Once the raffinate has crossed the columns, separation is done using eluent 20 g of DTPA (diethylenetriaminepentaacetic acid) per litre of solution in neutral pH [218] as

a displacer. The resin volume of the first column is 125 L, including the efficiency, the first column can sorb 9 kg of rare earth material in which $\sim$ 2 kg is Cerium.
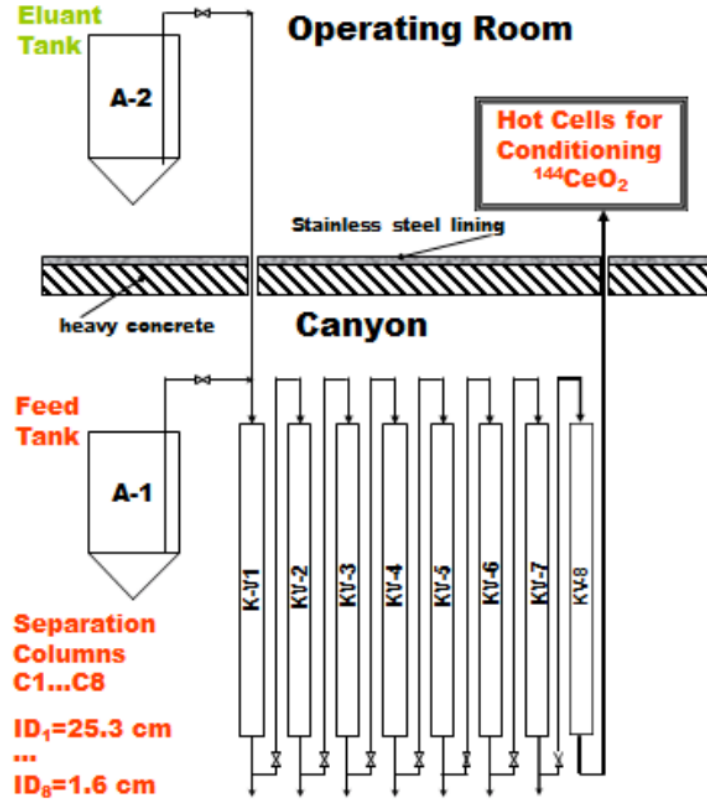
Figure 5.7: *Chromatography columns facility for rare earth extraction. Credits to [210].*

The eluant, coming out of the chromatography columns is recycle and reuse for further REE.

A complete cycle, meaning extraction one by one of Eu, Sm, Pm, Y Nd, Ce and washing is about 16 days. Similar extraction was succeed of [147]Pm in gram amounts [222, 220]. The number of cycles as well as further details on the expected contamination of radioisotopes and the enrichment of [144]Ce with respect to Cerium is highly depending on the SNF used.

The chromatography of the Radiochemical plant of Mayak is unique and is one of the most critical point of the CeANG production. If extracting Rare Earth is an everyday process, techniques used for radioactive material treatment have to be adapted to a very hazardous environment, modifying chemical binding, resin purity and resistivity as well as operator access.

Online monitoring

An optical spectrometer (AVANTES Fiber-optic) is used in order to identify individual rare earth and to monitor the displacement chromatography. A contamination from close mass would decrease the specific activity of the extracted liquid. The spectrometer identifies rare earth element by looking for absorption band in UV, visible and IR frequency (200-1100 nm) [223, 224] using fibre-optic spectrometers to avoid radiation issue.

5.3.3 Manufacturing of the CeO$_2$ compound

400 L/cycle of Cerium solution ($\simeq$ 5 g.L^{-1}) are leaving the chromatography facility. The ^{144}Ce activity is only depending on the mass fraction of ^{144}Ce over Cerium isotopes. Assuming the Cerium specific activity of the two selected batch from Kola, 2.7 TBq/g, a 5.4 PBq source is available. Batch from highly enriched fuel might have an higher Cerium specific activity. Some liquid samples will be extracted at this stage. The solution is then transformed in Cerium oxalate Ce$_2$(C$_2$O$_4$)$_3$ and the precipitate is extracted of the solution using paper filters. This filtration enables to get rid of 95% of the liquid volume. Those aggregate are then calcined in order to produce Cerium oxide (CeO$_2$) by heating the solution up to 120 °C for 1 hours then 700 °C for an extra 2 hours. Researches and developments were made by PA MAYAK in order to optimize this method, especially due to the specific needs of the CeSOX experiment [210, 225]. Batch with pure and impure Cerium solution were used to check for density and oxidation. This process is lasting about 3 days. The extracted powder is then compressed in hot cell. At this step, any delays is critical as it would decrease the specific activity of the source.

5.3.4 Characterisation of Cerium compound

Sampling of the Cerium compound will be done at the end of the displacement chromatography. Solution of Cerium of few kBq will be made out of the samples and each of them are passing through mass, γ and α spectrometers for characterization and certification. CEA asked to obtain some representative samples as well for cross measurements. ICP-MS, γ and α spectrometers have been installed or prepared in parallel in Saclay for this cross measurements. This is developed in chapter 7.

α spectroscopy

The PA MAYAK α spectrometer is a semiconductor detector (SEA-13P) [226]. Method of measurement allows to measure α contamination from 3.5 to 9 MeV. The result described below focus on detection limit as no α contamination is expected. Four distinct areas have been defined in the energy spectrum. Table 5.3 gives the sensibility for each areas.

Area	Range [MeV]	Targets	DL [Bq/Bq]
I	[3.2 ; 5.3]	^{148}Gd, ^{209}Po, ^{227}Ac, ^{235}Np, ^{208}Po, ^{242m}Am, ^{232}U	0.5×10^{-5}
II	$\sim$ 5.4	^{241}Am/^{238}Pu overlapped with: ^{228}Ra	0.5×10^{-5}
III	$\sim$ 5.8	^{244}Cm/^{243}Cm overlapped with: ^{236}Pu	$1. \times 10^{-5}$
IV	[5.8 ; 6.6]	^{249}Cf, ^{250}Cf, ^{252}Cf, ^{248}Cf, ^{254}Es, ^{252}Es	0.1×10^{-5}

Table 5.3: *Summary of the expected sensibility from α spectroscopy. DL is the limit of detection given in Bq of the contaminant per Bq of ^{144}Ce. From [226].*

γ spectroscopy

The PA MAYAK γ spectroscopy is done using an HPGe detector [226] with relative efficiency from 25% to 40%. The energy spectrum is defined between 50 keV to 2700 keV. In order to eliminate β from ^{144}Ce-^{144}Pr , a fine Aluminium layer is settled between the sample and the detector [226]. Table 5.4 lists the sensibility of each radio-element as given by PA MAYAK [211].

Isotopes	γ line [MeV]	DL [Bq/Bq]
^{60}Co	1.173 1.332	6×10^{-5}
^{22}Na	1.2745	6×10^{-5}
^{54}Mn	0.8348	1×10^{-4}
^{65}Zn	1.1155	2×10^{-4}
^{137}Cs	0.6616	3×10^{-4}
^{154}Eu	1.2740	2×10^{-4}
^{152}Eu	1.4080	3×10^{-4}

Table 5.4: *Summary of the expected sensibility from γ spectroscopy. DL is the limit of detection given in Bq of the contaminant per Bq of ^{144}Ce.*

Mass spectroscopy

The mass spectrometer used by PA MAYAK is an inductively coupled plasma mass spectrometer (ICP-MS): PerkinElmer NexION 300 and/or OPTIMA 8300 Perkin Elmer [226].

Activity measurement

The activity is measured by PA MAYAK using calorimetric measurement. The calorimeter is made of two identical copper cans with resistance thermometers in their bottom parts connected by a balanced bridge [226]. Those cans are the same than the one presents in the CeANG capsule. The capsule contained 3 cans as described in section 5.4.The bridge circuit is balanced when temperatures of the sample and reference cans are equal. Heat flow is determined from direct measurement of voltage at the heater of the reference can. It is the Wheatstone bridge principle, equilibrating two resistances with a potentiometer. An example of such detector is given in [227]. When the reference can is in thermal equilibrium with the sample can, calibration curved are used for temperature estimation. The heat flow measurement ranges are from 170 to 800 W.

Assuming that the conversion factor between power released and activity for ^{144}Ce-^{144}Pr source is 216 W.PBq^{-1}, the Radiochemical plant calorimeter will convert calorimetric measurement to activity. The error on the heat being 3.5 % the activity is measured with a 7% error. Besides, the calorimeter can not measure an activity above 3.7 PBq. This gives an upper value for the specific activity but is not crucial as we expect 6.5 PBq at a source maximal value during production (< 2 full cans).

Figure 5.8 gives an idea of the time expected for each production process.

5.4 Special Form of Radioactive Material Capsule

The extracted powder is compressed in Copper cans which are encased in a capsule. This capsule has a radioactive material container must fulfil specification. The capsule's certifications are PA MAYAK contractual obligations.

5.4.1 CeSOX Specifications

The spectifications of the capsule can be summarized as the following:
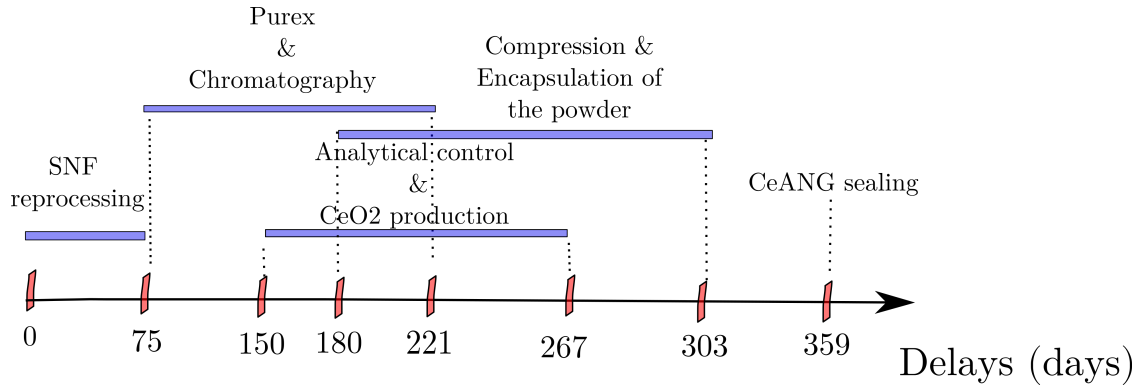
Figure 5.8: *Schematic overview of the expected planning from SNF reprocessing to sealing of the Ce0$_2$ powder in the can.*

- CeANG radioactive material source must be enclosed in a bi-capsular cylinder made of corrosion and heat resistant steel,
- temperature of the external stainless steel capsule must not exceed 500 °C,
- pressure inside the capsule, at any time, must not exceed 6 atmosphere ($\sim$ 6.08 bar).

Aside, CeANG has to meet requirements from special form of radioactive substance according to "Regulations for Safe Transport of Radioactive Material" [228], the ISO 9978 [229] and ISO 2919 [230] demanded by the Autorité de Sureté Nucléaire (ASN - the French Nuclear Safety Authority). The CeANG will be delivered with a quality certificate assessing those specifications.

5.4.2 Geometry

Figure 5.9 displays the layout of the source pellets inside the copper cans. Three copper cans are piled up inside the capsule. The capsule is made of two stainless steel cylinders. The copper cans, storing the Cerium oxide, play the role of radiators to avoid any thermal issue. The number of radioactive Cerium oxyde pellets are unknown for the moment. It will be depending on the specific activity reached by the CeANG production.
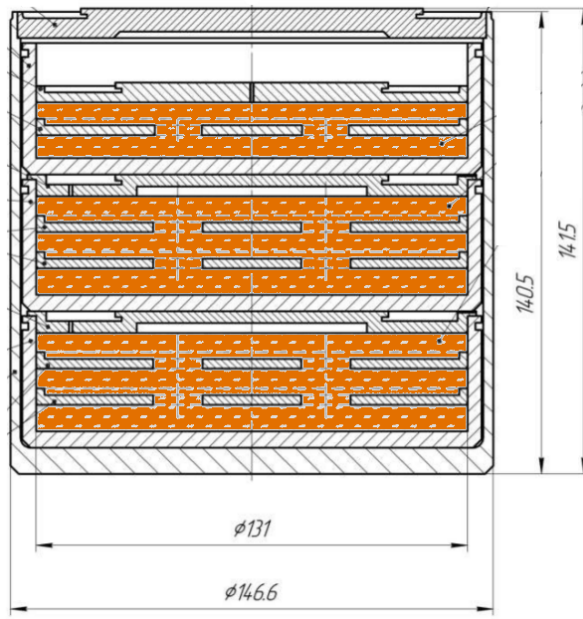
(a) *Industrial map. In orange is where the CeO$_2$ is located, all the other hachered material being copper and distance given in mm. The free space is occupied by air.*
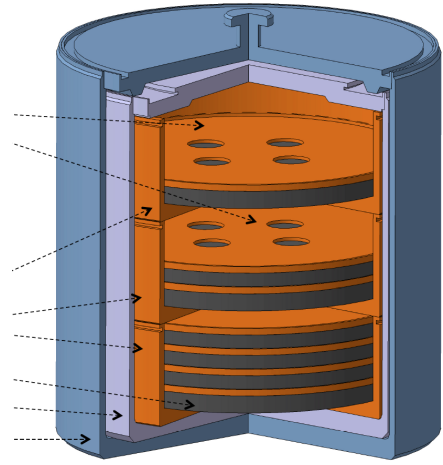
(b) *Simulation of the encapsulation of the CeANG with a different soruce powder distribution. Credits to:*

Figure 5.9: *Geometry of the can.*

5.4.3 Special Form Radioactive Material certification

The Special Form Radioactive Material (SFRM) certification [228] is needed for international transport of radioactive source and is made for minimizing leakage and deformation during the transport. To obtain the certification tests have to be done in capsule similar to the final one ("dummy" capsule). For those tests, a Cerium powder is mixed with trace of ^{90}Sr/Y and inserted in a dummy capsule.

Heat, leak, and percussion tests described below were realised on April, 2017 in the PA MAYAK installation. The immersion tests are done in hot distilled water. The ISO standards [230, 229] described below are precising how the tests have to be realised. The immersion leak test has to be done before and after each constraints applied to the capsule. It consists in measuring ^{90}Sr/Y β-activity in the entire volume of distilled water. The tests are the following:

1. Impact test: dropping the capsule from a height of 9.52m,
2. Percussion test: strinking the capsule by a 1.5 kg bar free dropped from a height of 1 m,
3. Heat test: exposing the capsule to 800-820 °C for 11 minutes .

5.4.4 ISO 9978 and 2919 certifications

The ISO 2919 and ISO 9978 norms are demanded by the Autorité de Sureté Nucléaire (ASN - the French Nuclear Safety Authority) as the standards in Radiation Protection and Sealed Radioactive sources.

The ISO 2919 [230] is defining tests and certification depending on the working environment of the sealed source. The considered situation is the CeANG inserted inside the Tungsten shield under

Borexino for the SOX experiment duration. The temperature is stable and monitored, no vibration, external pressure or puncture are possible. One can identify the certifications needed depending on the external environment the source will be in contact with [230]. PA MAYAK notifies that Integrity Rating of the CeANG source to be established according to ISO 2919:2012(E) is ISO/12/E31111, with 12 for the year of approval of the standard used and E ranking the source activity. The CeANG can be identified as: (31111) because if the inner part of the tungsten shield might reached 80 °C, no external pressure, impacts, vibration or puncture are possible under Borexino.

The ISO 9978:1992 [229] is defining leaking test for the working environment. It describes the condition of the immersion of the capsule to respect. The dummy capsule, in which ^{90}Sr has been deposited, is completely immersed in pure water. The liquid is then heat to 50 °C for at least 4 h. The capsule is then removed and the liquid activity has to be lower than 0.2 kBq for the entire volume.

The SFM certification is more restrictive than the ISO9978/ISO2919. Consequently, SFM tests are enough to assess the certifications.

5.5 High Density Tungsten Alloy Shielding

^{144}Pr is a very strong gamma emitter (2.185 MeV, 0.694%). Therefore the source must be shielded for radio-protection. The high-density tungsten alloy shield (HDTAS) will provide such biological shielding and background suppression during the data taking period in SOX. Prior to inserting the CeANG in the HDTAS, the latter will be placed inside the calorimeter to measure its thermal properties. The shield is also an important piece concerning safety and integrity of the source in case of accident during integration or transport.

5.5.1 Specifications

Biological protection

A prime requirement is that the biological protection must shield gamma rays to satisfy the dose limits imposed by the IAEA safety rules for radioactive source transportation and handling, as well as the safety rules imposed by the Italian authorities.

The legal radioactive limit for nuclear package transport on road according to [231] is 10 mSv.h^{-1} at 3 m from the container and the occupational dose for public worker is 1 mSv.y^{-1}.

Achieving such an attenuation factor while minimizing the size of the biological protection make then necessary to use very high-density materials. Iron ($\sim$ 7.8 g.cm^{-3}), stainless steel ($\sim$ 8.1 g.cm^{-3}), lead ($\sim$ 11.3 g.cm^{-3}) are not dense enough for compromising gamma attenuation and compactness for SOX tunnel. Tungsten can be used in radiation shielding (industrial production facilities). Tungsten with a density between 18.0 g.cm^{-3} and 18.5 g.cm^{-3} must be used.

In order to guarantee the needed level of attenuation along any direction, the density must be homogeneous at the level of $\pm$ 0.2 g.cm^{-3} over the full HDTAS volume. The overall density of each shielding part should be checked and certified to be compatible with the above mentioned specification, using Archimedes' weighting method.

Corrosion

As mentioned in the previous section, the shielding will be inserted into a calorimetric device prior to the start of the experiment, in order to precisely assess the source activity. During the calorimetric measurement, the shielding material will be in contact with pure water circulating in a closed loop up to 80 °C for one week or two. Any significant corrosion of the shielding would then change the water heat capacity and spoil the measurement. Therefore, the tungsten alloy must resist corrosion with a limit set to a corrosion rate levels smaller than 0.1 mm/y for month-scale exposure time.

Contamination

The CeANG will be inserted with an articulated arm into the HDTAS, placed underneath a hot cell. Any cleaning of the HDTAS outer surface should then be done to prevent any contamination by radioactive dust particles. The roughness of the surface has been specified accordingly to this functionality. Threaded holes should be closed by plugs to avoid introducing any active dust. Aside from the dust, natural tungsten can contain radionuclide such as ^{40}K, ^{238}U, ^{235}U, ^{232}Th. Ensuring low concentration levels of such radionuclide is of great importance in low background environment like the LNGS. The sample of the powder material did not show any strong contamination of the tungsten.

5.5.2 Background suppression

Most of the β and α are not going out of the CeO_2 powder and the rest is unable to cross the source capsule itself. Oppositely, neutron and γ are escaping the capsule and enter the shield. Studies were done in order to constrain the impact on Borexino measurement and the associated background [173]. The study was done using Tripoli-4 for both neutron and gamma background estimation. Tripoli-4 is a more efficient library for neutron transport and highly attenuating media. This study is relevant for obtaining an order of magnitude. A 50 % error can be considered as a systematics due to propagation with such enormous attenuation factor (10^{20}).

Gammas

As stated, among the ^{144}Ce-^{144}Pr gammas emitted, the only preoccupying γ potentially leaving the shield is the 2.185 MeV ^{144}Pr line emitted with 0.694 % intensity. Figure 5.10a displays the Tripoli-4 geometry considered for this analysis and Figure 5.10b the deposited energy spectrum by one 2.185 MeV γ coming from the CeANG. The result is giving 1 MeV deposition in the target volume with a probability of 6×10^{-17} per initial γ. Assuming a 5.5 PBq ^{144}Ce source and no fiducial cut in the scintillator, 198 ev.days^{-1} γ are expected between 1 and 2.2 MeV (below the ^{8}B threshold). For the SOX program, those γ can mimic IBD coincidence leading to an induced IBD-like signal of 3.8×10^{-4} ev.days^{-1} [173]. This is negligible with respect to the ~ 80 ev.days^{-1} expected signal at the delivery time.
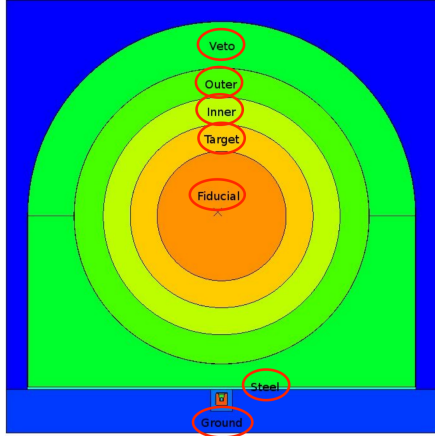
(a) *Tripoli-4 geometry used,*
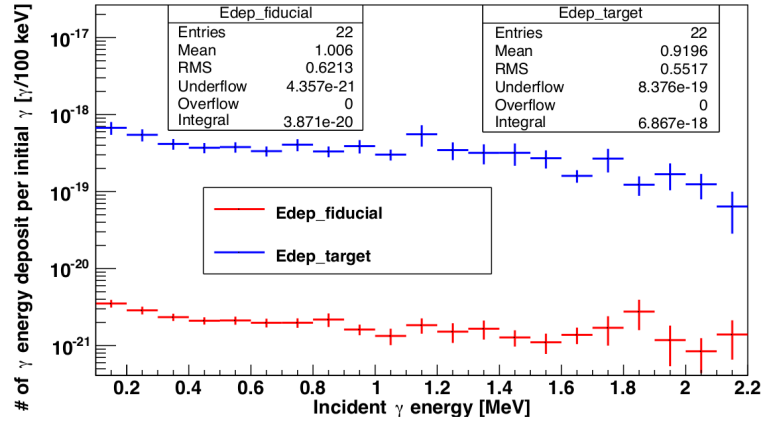
(b) *Energy spectrum and efficiency of one 2.2 MeV γ coming from the CeANG under Borexino to the target (R<4.2m) and the fiducial volume (R<3 m),*

Figure 5.10: *Simulation of source induced background in Borexino considering the HDTAS from [173].*

Neutrons

No neutron emitter is expected in a pure ^{144}Ce-^{144}Pr material. However, as detailed above, many potential contaminations have to be taken into account due to the nuclear waste purification process. Taking into account Spent Nuclear Fuel composition, Curium and Americium are the most probable neutron contaminant. Among Curium and Americium isotopes, ^{244}Cm ($T_{1/2}$= 18.1 y.) and ^{241}Am ($T_{1/2}$= 432.2 y.) are the most dangerous nuclei.

Assuming a 5.5 PBq source, and the worst possible scenario, 8×10^4 n.s^{-1} are expected coming from ^{244}Cm. Similarly, the neutron flux derived from the limit contamination in ^{241}Am is 5×10^2 n.s^{-1}.

As for the γ emission spectrum, the neutron transport was simulated through the capsule, the tungsten shield, the stainless steel plates under Borexino and the whole detector. Two different neutron induced backgrounds have to be studied: the fast neutron depositing energy by proton recoil inside the scintillating liquid and the γ emitted by n-capture in detector material.

Fast neutrons background have been studied and an upper limit of 10^{-12} neutrons reaching the target volume has been estimated [173]. Considering that the neutron would have to deposit more than 1 MeV visible energy, and knowing the high quenching of the proton, this background is completely negligible.

γ induced by n-capture is a more interesting background. The neutrons would leave the shield almost intact ($\sim 60\%$ only are captured by the shielding [173]). A capture on hydrogen or carbon would then lead to a 2.2 or 4.9 MeV. Water tank and buffer are good candidate for such a process. Assuming a 5.5 PBq ^{144}Ce source and not fiducial cut in the scintillating liquid the expected n-induced γ signal is around 3.7×10^2 ev.days^{-1} in the whole energy range. IBD-like signal would be around 3.6×10^{-2} ev.days^{-1} to compare with ~ 80 ev.days^{-1} expected signal at the delivery time [173].

5.5.3 Safety issues

A study was ordered for radiological exposition estimation to CEA specialized laboratory in Saclay. The shield attenuation of γ has been estimated around 2.8 $\times 10^{-7}$. The dose has been calculated for a 5.5 PBq source at delivery time: 120 μSv.h^{-1} at contact with the shield and 7 μSv.h^{-1} at 1 m. It means that assuming a worker should not stay in touch with the shield for more than 7 h (considering activity hot spots) or 142 h around the source. The HDTAS is respecting the safety regulation condition of transport and working conditions under radiation. Special care will be taken in hall C, during the deployment for this specific risk.

At 5.5 PBq, the source is heating the shield around 180 °C (assuming a thermal equilibrium with the hall C air around 10 °C) [232]. Special care would be taken for the manipulation of a hot object and the evacuation of the heat when immerging the source in the water cooled calorimeter.

The laboratory of Gran Sasso is imposing a limit on any neutron source to: 10^5 n.s^{-1}. This limit is well respected (conservative hypothesis leads to 8.1×10^4 n.s^{-1}) thanks to the extra limits fixed on those two neutron emitters.

5.5.4 Design

The shield is one of the most massive tungsten one-piece manufactured in the world (2.3 t.). To minimize sealing, the design has been simplified to 3 different parts: the bulk (2.1 t) will contain the source, the plugg to close after deposition of the source and the flange above the plug for fixation and loading purpose. The form of the plug has been designed to avoid any straight interspace between the source and the exterior of the shield. Figure 5.11 displays the design of the shield and more precise description can be found in Appendice C.
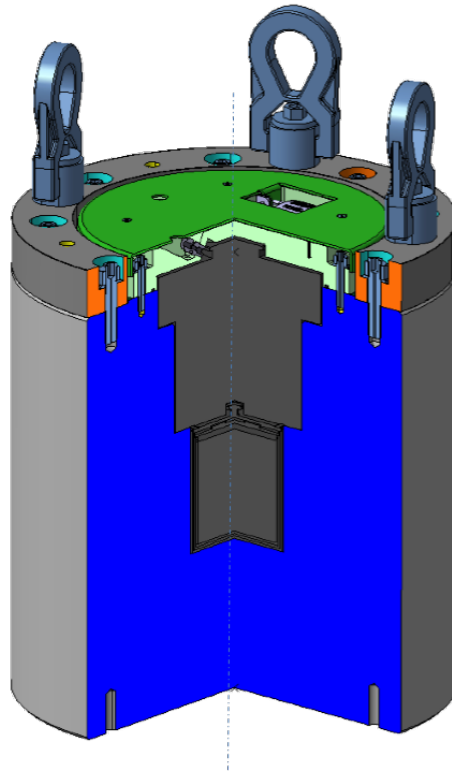
Figure 5.11: *Schematics of the shield. Tungsten is in blue. Credits to:*

5.5.5   Manufacturing

The shield was manufactered by Xiamen Tungsten Corporation (XTC) factory in Xiamen, China mainly on March, 2016. Final tests and delivery happened late 2016. The chosen material is HWNF50 (95 % W,3.5 % Ni, 1.5% Fe) mainly from density and hardness considerations. Several tests and measurements have been realised by XTC in presence of CEA experts:

- precise geometry measurement using Computerized Measuring Machine devices,
- density measurement using Archimede technics gives: 18.14 g.cm^{-3} for the shielding, 18.23 g.cm^{-3} and 18.06 g.cm^{-3} for the two plugs.
- random extraction of 9 sampling for density variation, all in between 17.8 and 18.2 g.cm^{-3}.
- porosity was measured using ultrasonic analysis with a Scanning Electron Microscope: no pore bigger than 3 mm was detected.
- corrosion was tested by immersing sample in pure water for 3 weeks: the corrosion rate is lower than 0.1 mm.y^{-1}.
- tightness and brittleness tests were correct.

5.6   Transport

After a tendering process, the chosen transporter is Areva TN. The contract with Areva TN included the transport of the Tungsten shield from CEA Cadarache to France and the source transport from St Petersburg harbor to Gran Sasso.

5.6.1 A challenge on the road

A main reasons chosing the ^{144}Ce-^{144}Pr pair was Q_β of ^{144}Pr and ^{144}Ce long lifetime enabling separated production and experimental locations. During the CeLAND project, a preliminary study of the source transportation gives possible options for transportation of 144Ce antineutrino generator from PA Mayak(Ozersk, Russia) to Kamioka mine (Japan):

A/ By air from Koltsovo airport to one of airport in Japan, and then by truck from an airport to Kamioka mine (about 5 days in total),

B/ By train to one of the Eastern ports in Vladivostok, Russia, then by ship to one of harbor in Japan crossing Japan sea, and then by truck from an harbor to Kamioka mine ($\sim$ 20 d.),

C/ By train to St. Petersburg port in Russia ($\sim$ 12 d.), then by ship to one of harbor in Japan one of three routes: around Africa and Australia ($\sim$ 60 d.); via Atlantic ocean and Panama Canal ($\sim$ 55 d.) or via the Northern Sea Route ($\sim$ 30 d.); and then by truck from an harbor to Kamioka mine.

Accordingly to IAEA rules, for transportation of radioactive source by air transport there is a severe constraint of total activity of 0.6 PBq (16.2 kCi) per transport package (containment). Assuming a 100 kCi source, one would need at least 7 individual sources with their own transport contained and then a merging apparatus in Japan. This was not a credible transport option. The only solution was to use ships. However, no container was licensed to circulate between Russia and Japan. This experience is pertinent for any international high activity source transportation.

The transportation greatly simplified with Borexino. Areva TN is accustomed to transfer radioactive material between Russia and France. Le Havre is one of the few harbour authorized to transfer class 7 radioactive material. For this reason as well as safety authorisation reasons, the container travel is divided in 2 independent routes:

- From St Petersburg, Russia to CEA Saclay, France,
- From CEA Saclay, France to LNGS Gran Sasso, Italy.

Figure 5.12 shows the path chosen by the company for moving the source from Saint-Petersburg to Gran Sasso, by ship until Le Havre (5-6 days) then by truck to Gran Sasso through Saclay (14 days on the road, more if hosted in Saclay). The transfer of the source shielded from PA MAYAK to St Petersburg (train? truck?) is PA MAYAK responsibility and "delivery time" always refers to the time the source reaches St Petersburg.

Figure 5.12: *Chosen path from the Oural to Abruzzo. In blue is the part of the source trip which is PA MAYAK's responsability, in red is the part being AREVA TNI's responsability.*

5.6.2 Transport container: TN-MTR

The TN-MTR is the cask chosen to transport the source after an invitation to tender. Material Testing Reactor (MTR) container was developped to transport from research reactor spent nuclear fuel, usually highly enriched Uranium, for reprocessing. Countries with reprocessing plant (France, United Kingdom, Russia and Japon) are reprocessing fuels from other nuclear countries. Licensed by Areva TN (ex TRANSNUCLEAIRE) in Russia, in Italy and in France, respecting specifications for transport package [228] and for dose rate evolution [233]. The characteritics of the package are described in [234, 235]. The cask is a cylinder of 2.08 m height for 2.08 m diameter. The cavity is an inner cylinder of height 1.08 m and diamater 0.96 m. It weights 21 tons empty and can reach 23.4 tons once loaded. The inner cavity is composed of stainless steel while a thick γ Lead shield composed the external layer. Figure 5.13 illustrates the TN-MTR cask geometry.

Heat transfer was carefully managed inside the TN-MTR and the heat production can not exceed 8 kW (around 1.5 kW expected for the CeANG).
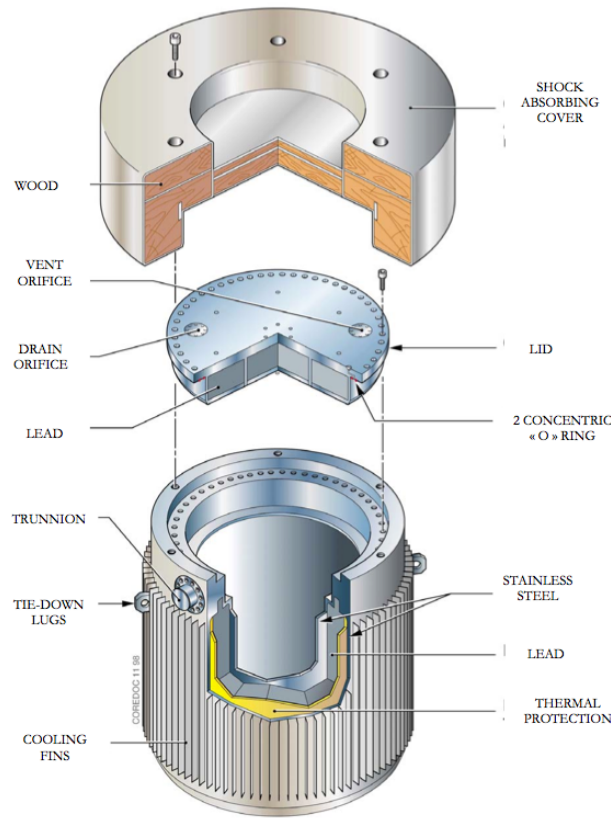
Figure 5.13: *TN-MTR schematics.*

5.7 Disposal and long term storage issues

Being property of the CEA, the French safety authority is demanding to have a clear view of the future of the source. French regulation imposed that radioactive sealed material disposal is responsibility of the radioactive material manufacturer [236].

However, international legislation is not as constraining as domestic law. The collaboration first plan is still to send back the CeANG to P.A. Mayak, and a long term storage in France is considered in case the transfer back to Russia would not be possible.

5.7.1 Plan A: disposal in Russia

The disposal of the CeANG in Russia is subject to an other contract than the CeANG production one. It is running from 3 months after delivery to 2020 depending on logistic issues. The transport from Gran Sasso to St Petersburg harbour is CEA responsibility. The TNMTR is planned to be send back. Situation of the HDTAS is more complicated as it will depend on the long term storage solution adopted by the Russian administration.

5.7.2 Plan B: disposal in France

In case the first option would not be possible, the storage has to be considered from the French available installation point of view.

French authority and the Radioactive waste management agency

The French legislation is detailing classification depending on period and activity of the source composition [237]. The French national radioactive waste management agency (ANDRA) is in charge of managing radioactive waste. The different options given by ANDRA[1] are:

- Low-level long-lived waste in shallow disposal (15-200 m underground). Metal baskets put into concrete containers, sealed with cement.
- Low and intermediate level short-lived waste in Andra CSFMA waste disposal facility, Aube district. Metal or concrete containers embedded in concrete.
- Intermediate and High level long-lived waste in 500-m deep disposal (CIGEO - not built yet). The final form has not been commissioned yet. For now stored in production site (Marcoule (CEA), Cadarache (CEA) and La Hague (Areva)).

Figure 5.14 is illustrating these categories as well as the corresponding storage technique in France. It is considered here to have a clean ^{144}Ce source, more complicated scenario involving long live time contaminant are being taken into consideration in the last chapter of the present manuscript.
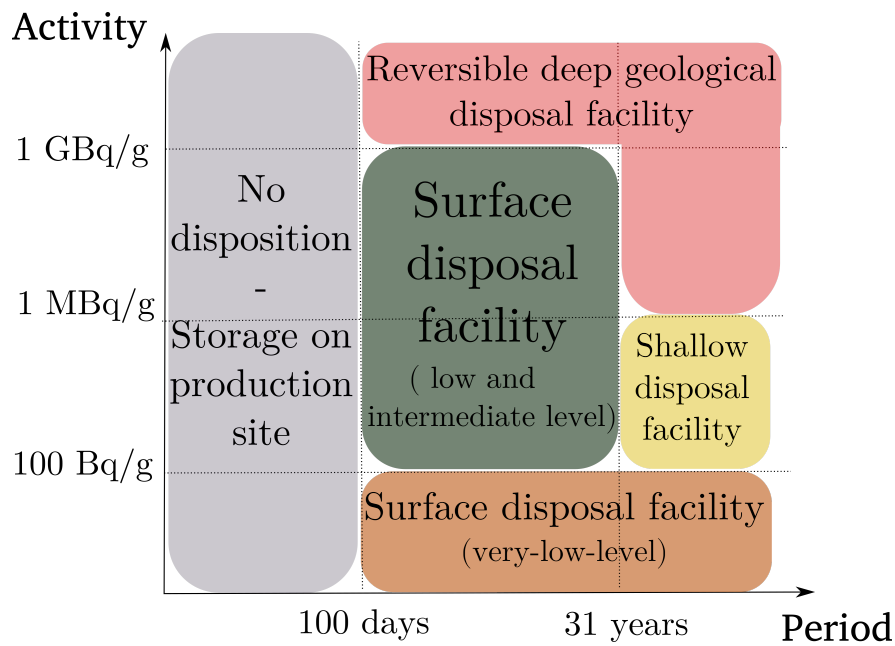
Figure 5.14: *Classification of radioactive material for storage as defined in law [237].*

With a period of 25 mins, ^{144}Pr is at secular equilibrium with ^{144}Ce from chromatographic separation already. If we assume a 5.5 PBq ^{144}Ce source at delivery (conservative hypothesis), and a 625 cm^3 volume for the $\sim$ 2.5 g.cm^{-3} CeO$_2$ powder, we have a classical exponential decay as display in figure5.15. It means that 10 years of temporary is necessary to reach the 1 GBq.g^{-1} limit imposed by legislation. For this purpose, sites were researched in CEA installations. After this delay, heat is not an issue anymore. Not knowing precisely the source composition on long-lived isotopes would require to plan for the most conservative long-term storage: deep geological disposal in France.

---

[1] https://www.andra.fr/international/pages/en/menu21/waste-management/waste-classification-1605.html
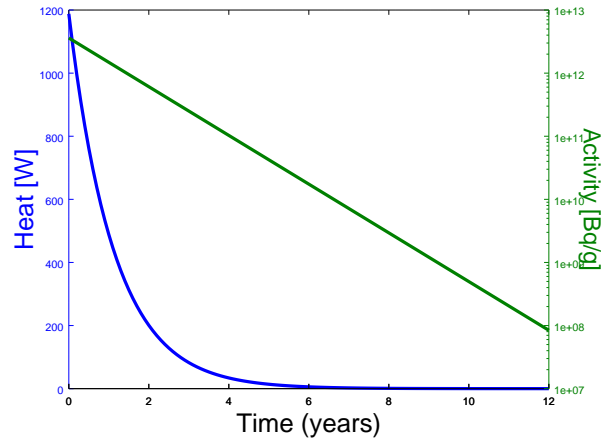
Figure 5.15: *Evolution of the heat released and the massic activity of the* ^{144}Ce *source.*

Deep geological disposal option

For a deep geological disposal in France, the only long term installation is CIGEO (Industrial Center for Geological Disposal). Due to public protestations, the construction of this site has been postponed. A typical cask for disposal can contains 870 L and less than 3 tons (cask plus waste). The HDTAS weighting 1996 kg, it seems unrealistic to keep it. The CHICADE installation might be used for transferring the CeANG source from the Tungsten biological shield to a Lead shield of same dimension, reducing the total mass from 1996 kg to 1360 kg. Indeed, keeping the same 19 cm width of Lead, the dose can be estimated to 0.92 mSv/h at contact with the shield and 0.03 mSv/h at 1 meter.

Chapter 6

γ spectroscopy: HPGe calibration and full simulation

Contents

This chapter describes the HPGe detector located at the laboratory Dario Motta, at CEA-Saclay. The simulation and the analysis tools have been developed for realising the γ spectroscopy on the ^{144}Ce-^{144}Pr SOX source samples. The goal of this work is to provide all the necessary tools to promptly search for gamma radio-impurities in the final cerium antineutrino generator samples.

The first section describes the experimental apparatus (6.1), the second focus on calibration and characterisation of the detector (6.2) while the third one details the Monte-Carlo developed (6.3), and finally result of the detector modelling (6.4).

6.1 Apparatus

Germanium detectors are semiconductor sensors: a particle passing through the crystal gives energy to electrons of Germanium atoms, rising them from the valence to the conduction band. The crystal is built up as a p-n junction functioning in reversed-bias mode with electrodes imposing high electric field. The reverse-biased diode enables to increase impact ionization and avalanche multiplication of electron/hole pairs between the electrodes [238]. Consequently, electron-hole pairs migrate toward the electrodes. The induced current is then measured by the acquisition chain. Germanium detectors have a better energy resolution than silicon detector but they have to be cooled down, hence the use of liquid nitrogen in our set-up.

6.1.1 Experimental set-up

The detector is located underground at the CEA Saclay, in an old cyclotron hall. The rooms have been decommissioned and do not contain specific radioactive activity anymore. The laboratory overburden is equivalent to 15 mwe in all directions, providing a good shielding against the cosmic showers and reducing the atmospheric muon rate by 66% [239]. Muons, saturating the detector, induced a negligible dead time. However, hadrons and gammas from muon showers are inducing a continuous background, feeding the 511 keV peak from e$^+$ annihilation in background measurements.

The detector itself is a 132.65 cm^3 ORTEC p-type coaxial high purity germanium crystal. It is a cylinder of 58.8 mm diameter and 58 mm height. Precise description is shown in figure D.1 in Appendix D. Grown up industrially from a seed and doped, the cylinder is then polished and dug with a cylindrical hole of 9.4 mm diameter and 45 mm depth. This hole, called the cold finger, is used for charge migration purpose and cooling, using respectively an electrode and a pure Copper pin. Lithium ions diffusion is performed on ~ 700 μm of the external surface of the crystal. Later on, Boron ions are implanted on the 0.3 μm surface of the cold finger crystal surface. Lithium and Boron form the n and the p contacts of the diode respectively. When doped, some area at the periphery of the crystal gets passivated producing dead layers. They are not part of the active volume and are specific to each detector. Furthermore, those areas get extended when the crystal is at ambient temperature for a long time (typically more than a month) because of diffusion process inside the semiconductor[240]. Our detector, bought in 1997, has been unused and warm for years.

The crystal is surrounded by many layers and kept under vacuum for thermal insulation. Aluminium encapsulation is used (low Z), to allow X-ray and low-energy γ's from samples penetrating the detector. A precise description is in Appendix D.1. Unlike in other experiment, the detector has never been opened neither x-rayed, enabling only tuning from simulation and external calibration.
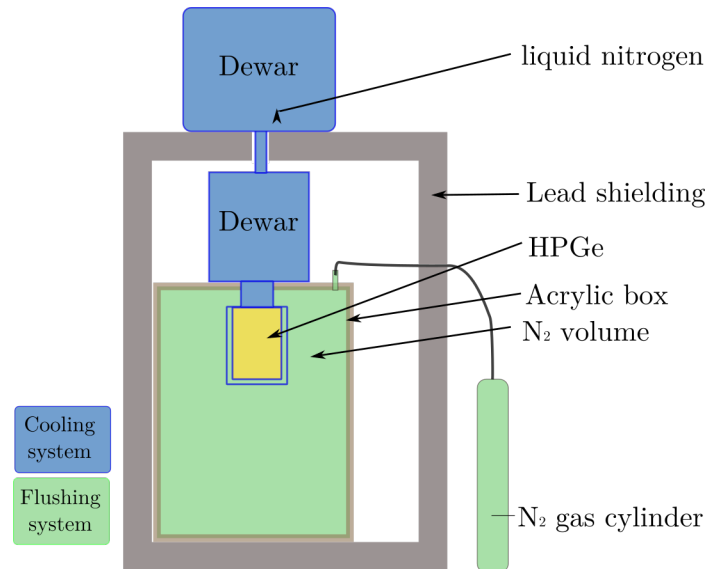
Figure 6.1: *Schematic of the experimental set-up*

The HPGe is cooled down using liquid nitrogen (~ 77 K). The thermal connection to the liquid nitrogen is realised through a Copper contact pin and a cooling rod stabilizer for vibration absorption. Nitrogen is pour in an external dewar when the refilling is done. This external dewar is connected to a smaller dewar located inside the lead shield as represented in figure 6.1. The HPGe is inside an acrylic box filled with pure gaseous nitrogen to avoid close contact between radon from the air and the crystal. The acrylic box is therefore maintained at a slight overpressure. This box stands in a lead bricks shielding external radioactivity. This lead shield is not airtight. Figure 6.1 represents schematically the present structure of the detector.

6.1.2 Radioactive sources

Three different sets of data have been used for calibration purpose depending on the experimental set-up:

- ^{144}Ce sample sent by PA MAYAK.
- ^{137}Cs,^{60}Co and ^{22}Na calibration sources with $\sim$1 MeV γ's,
- ^{241}Am calibration source,

With ten full absorption peaks in the whole (50 keV-3 MeV) spectrum, the ^{144}Ce sample sent by PA MAYAK is the most powerful calibration tool. The high energy γ calibration sources can be used to tune the detector geometry using the Compton continuum and full-deposited peak of low-energy gammas.

Two experimental configurations are defined: "TOP" and "BOT". Figure 6.2 illustrates these two set-up in the ^{144}Ce case. TOP defines the option where the source is settled over seven Petri dishes while the BOT defines the situation where the source is directly deposited at the bottom of the acrylic box.
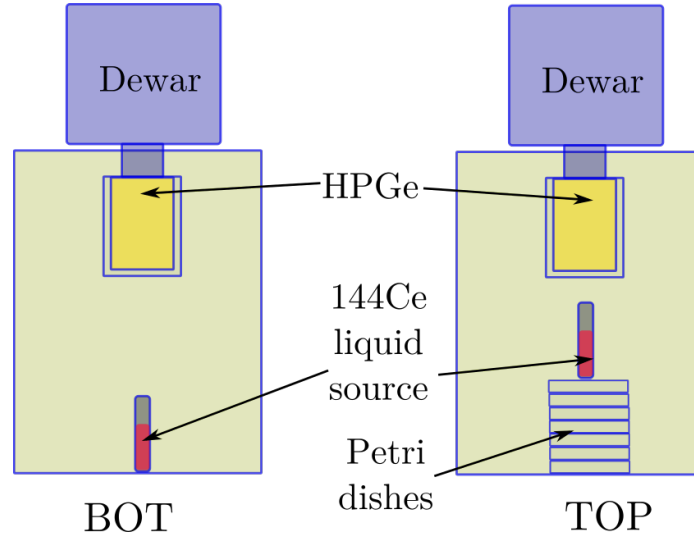
Figure 6.2: *The two experimental situations: BOT without Petri dishes and TOP with a source over seven Petri dishes.*

Solid angle of each source position was estimated using Monte Carlo simulations and sending geantinos [1]. Therefore, the solid-angle estimation does not take into account Compton interactions. Solid angles are of 1.04% and 5.24% for BOT and TOP configurations respectively.

6.1.2.1 ^{144}Ce sample

Three ^{144}Ce liquid samples were sent by PA MAYAK after a pilot production of few kCi of ^{144}Ce. Sample is constituted of liquid Cerium oxide diluted in nitric acid. The mass of each sample is 23.5 g. It is worth noting that these samples are not fully representative since the production facility has been modified during the R&D carried out between CEA and PA MAYAK. Analysis realised in CEA revealed a strong presence (2.67×10^{-9} g/g) of mass number 90. Chemical separation ensured that this contamination was ^{90}Zr coming from fuel girdle. With such strong contamination, the sample was probably not processed through chromatographic separation. However, these samples constitute a typical ^{144}Ce source and were used for calibration of source characterisation tools in CEA, as the HPGe described in this chapter. Representative ^{144}Ce samples will be delivered to CEA at fall 2017 directly extracted from the CeANG production process as described in section 5.3.4. The ^{144}Ce activity measurement of the three received samples was certified to be 60 kBq with a 11% precision the 10th, September, 2014. This measure was checked by the LNHB using γ spectroscopy to be 58.9(25) kBq on the 1st, October, 2014. We use only one sample for the HPGe measurements, the two other being dispatched between β spectroscopy measurements, ^{144}Ce/^{144}Pr separation tests and mass spectroscopy.

The experimental parameters on which our ^{144}Ce sample was used are displayed in table 6.1 in particular the position of the source, the activity at the measurement time and the exposition time. Table 6.2 shows the most intense γ emitted by ^{144}Ce-^{144}Pr source.

---

[1] A geantino is a virtual particle internally defined in Geant4 which has the particularity to pass through volume without interacting.

Situation	A_{theo} [kBq]	T [s] ([days])	Date
TOP	29.9 ± 3.3	256932 (3.0)	23rd, March 2015
BOT	60.0 ± 6.6	595807 (6.9)	30th, Sept. 2014

Table 6.1: ^{144}Ce sample experimental parameters.

^{144}Ce	Energy [keV]	53.4	80.1	100.0	133.5		
	Intensity [%]	0.10	1.36	0.04	11.09		
^{144}Pr	Energy [keV]	675.0	696.5	814.1	864.5	1388.0	1489.16	2185.7
	Intensity [%]	0.003	1.34	0.003	0.002	0.007	0.28	0.69

Table 6.2: Most intense γ lines from a ^{144}Ce-^{144}Pr source [158].

6.1.2.2 High energy γ sources

As for the ^{144}Ce case, we defined two experimental configurations: TOP and BOT. Table 6.3 describes the calibration realised with ^{60}Co, ^{137}Cs and ^{22}Na, their activity (A_{th}) at the time of the measurement (Date) and the exposition time (T). Table 6.4 lists the γ lines and their efficiency. No errors were given by the CEA source authority concerning measurements of the activity.

Sources	Sit.	A_{th} [Bq]	T[s] ([days])	Date
^{60}Co	TOP	1382	245207 (2.8)	17th, Mar. 15
^{60}Co	BOT	1453	362490 (4.2)	17th, Apr. 15
^{137}Cs	TOP	4227	505676 (5.9)	14th, Sep. 15
^{137}Cs	BOT	4276	35467 (0.4)	18th, Ma. 15
^{22}Na	TOP	786	353884 (4.1)	14th, Sep.. 15
^{22}Na	BOT	955	64355 (0.7)	20th, Mar. 15

Table 6.3: Experimental parameters.

Source	E. [keV]	Intensity (%)
^{60}Co	1332.4	99.98
	1173.2	99.85
	826.10	0.0076
	347.14	0.0075
	2158.57	0.00120
^{137}Cs	661.7	85.10
	283.5	$5.8 \; 10^{-4}$
^{22}Na	511.0	180.8
	1274.5	99.94

Table 6.4: γ lines from the calibration sources.

From table 6.4, the calibration sources have a simple γ emission scheme which enables us to use their Compton shape on wide energy range. These sources will be used mostly in order to tune the Monte-Carlo simulation.

The sources used are the same used in the Nucifer experiment([241]). The geometry was optimized for deployment inside the scintillating liquid tank [201]. The three high energy γ sources ^{60}Co,^{22}Na and ^{137}Cs have the same geometry displayed in figure 6.3.

(b) *Calibration source*
geometry when closed [201]

(a) *Inner capsule [201]*

(c) *Simulated capsule source geometry.*
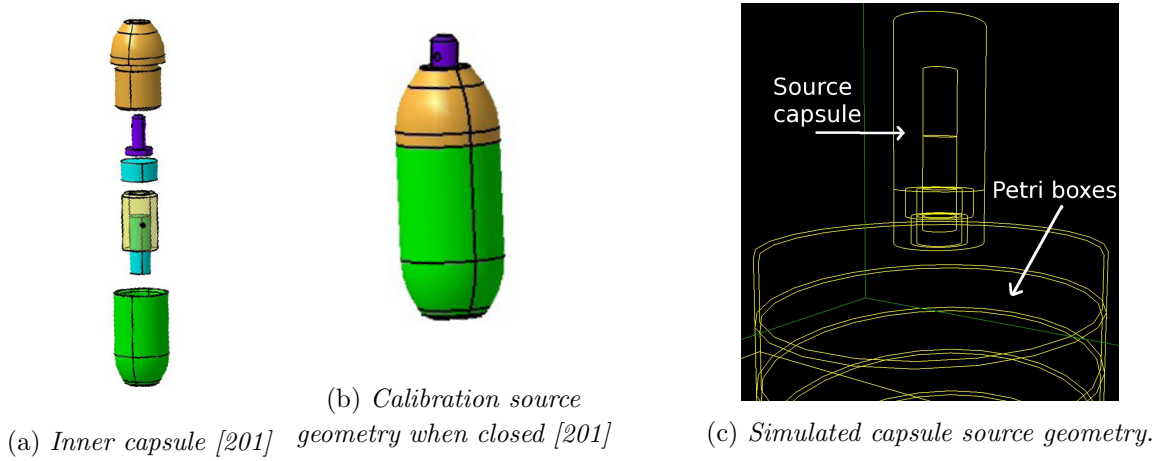
Figure 6.3: *Description of the capsule source geometry for ^{60}Co, ^{22}Na and ^{137}Cs.*

6.1.2.3 ^{241}Am source

We used a 458 kBq ^{241}Am calibration source. ^{241}Am decays through α emission to ^{237}Np ($Q_\alpha =$ 5.64 MeV, $T_{1/2}$=432.6 y) [242]. The source was made in CEA by pouring a liquid drop between two slices of glass held by an acrylic structure. The long half-life of ^{237}Np implies it has not reached secular equilibrium. The activity of the source can be considered as constant and only due to ^{241}Am decay. The important γ lines are listed in table 6.5.

The goal of using an americium source with low energy γ's is to tune the detector inner geometry more precisely by scanning additional positions. Five positions were explored around the detector, TOP and BOT as previously stated with additional "ASIDE", "FAR_ASIDE" and TOP+ represented in Figure 6.4. ASIDE and FAR_ASIDE are interesting because they are breaking the axial symmetry of the crystal, enabling us to compare detector response depending on the operating side. The high activity of the source induced dead-time and pileup if too close from the crystal. Covering the source would not be an appreciable compromise because of the low X-ray and γ loss and the loss in energy resolution. Increasing the solid angle was the only solution even if it implies to average the potential asymmetry of the dead layers.

(a) *The ASIDE position.*

(b) *The TOP+ position.*

(c) *The FAR_ASIDE position*
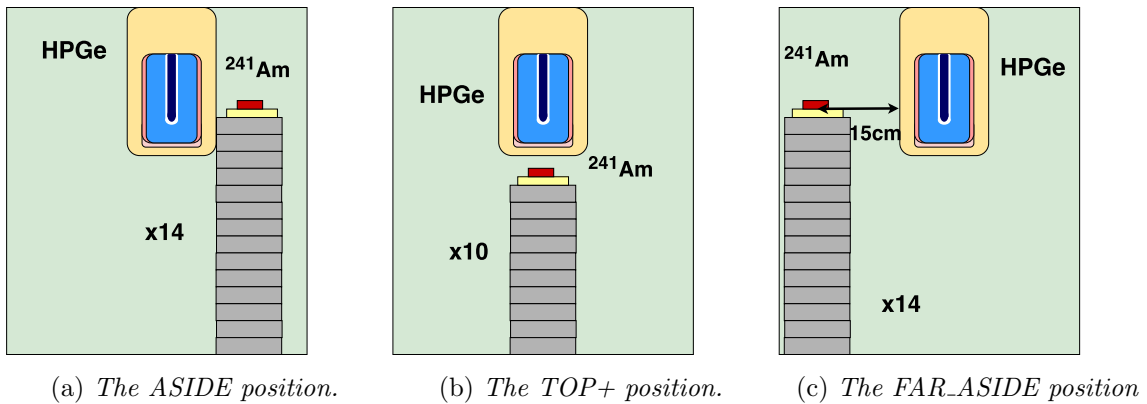
Figure 6.4: *Schematics of the three extra positions used only for the ^{241}Am calibration source.*

The americium source has been simulated as an hollow acrylic cylinder of 2.5 cm external

Energy [keV]	59.5	26.3	33.2	43.4	99.0	103.0
Intensity [%]	35.9	2.40	0.126	0.073	0.0203	0.0195

Table 6.5: γ lines from ^{241}Am calibration source [243].

diameter, 1.5 cm internal diameter and 3 mm height standing on a 4.2 cm diameter cylinder of foam. The inner part of the acrylic cylinder is a 3 mm width glass of 1.5 cm diameter. The γ's are uniformly generated in a small cylinder centred inside this glass material picturing the dry drop deposit.

6.1.3 Acquisition chain

The electronic acquisition is handled by a DSPEC jr 2.0 from Ortec. In the card, the signal is processed analogically using a trapezoidal shaping analysis. The rising time for a coaxial germanium is between 200 and 700 ns. The trapezoidal interpolation used has a typically 6 μs plateau in order to get a stable value for the maximal tension. The delivered signal is the integrated charge and the file format is an ASCII file representing the charge histogram for the exposure time. The plateau integration is leading to an acquisition rate limited at $\sim$10 kHz. The bandwidth is 10^5 cps, thus it is not the limiting factor.

Dead-time induced by cosmic-rays is negligible. However pile-up induced dead-time can be an issue. When the acquisition card detects a pile-up, the whole event is rejected. The limit activity before getting 10% of dead-time is about 220×I kBq and 44×I kBq with I the intensity of the γ line in BOT and TOP situation respectively. The acquisition chain delivers live time and real time, estimating the dead-time. ORTEC assesses 3% accuracy on the live time. It has been checked with independent method for the ^{144}Ce, see section 6.2.3.

6.1.4 Monte Carlo approach

A Monte Carlo code using the Geant4.10 library is used in order to simulate the HPGe and its near environment. The Monte Carlo output is written as a binary file event by event, enabling user to stop at any point the simulation without corrupting the file. An extra routine using Root 5 (compatible with Root 6) read the binary file and fill a TTree in an output root file. The size of the binary file is tunable using option in the input file (*.mac). The time of simulation varies from 10^{-5} s/events to ms/events in optical photons production and propagation. The simulation uses a cut value of 0.1 mm for the physical processes path and the extended Livermore package for electromagnetic interaction. Indeed, literature states slight differences in the Compton effect simulation depending on the electromagnetic library picked [244].
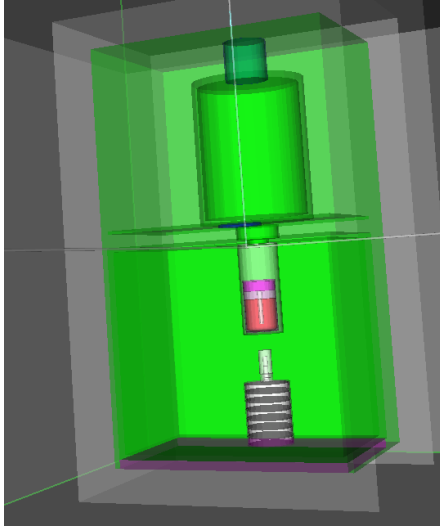
(a) *The lead box surrounding the detector and a calibration source standing on 7 Petri dishes.*
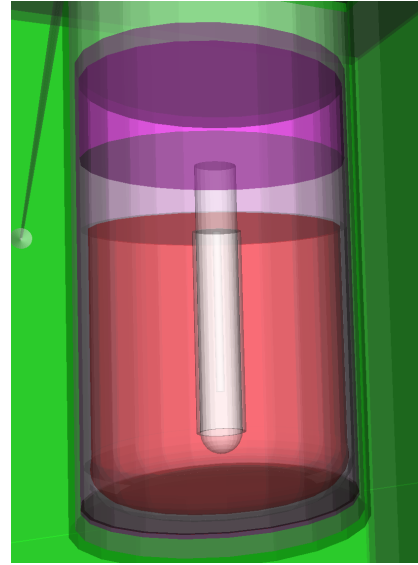
(b) *A zoom in the detector itself: active zone in red (the germanium crystal), copper above the crystal in purple, copper in the cold finger in white and vacuum in grey.*

Figure 6.5: *Simulation geometry.*

The code developed is modular containing different detector geometries , different source geometry and most of the relevant parameters can be tuned from the input file.

6.2 Characterisation of the detector

Simulations are key elements for testing the geometry of the detector, extracting the efficiency from one specific sample to a complete different geometry and measure the level of contamination.

The acquisition card integrates the signal and stores it in a global histogram. A measurement is then made of 12684 values, and therefore no digital pulse shape analysis can be achieved neither event-by-event analysis.

6.2.1 Energy calibration

Semiconductor detectors are in a first approximation linear in energy between 50 keV and 2.5 MeV with a small offset [245]. The calibration can be done using background or external sources. In background based calibration, five peaks coming from the ^{228}Ac and ^{208}Tl were identified and integrated (^{238}U and ^{232}Th chains).
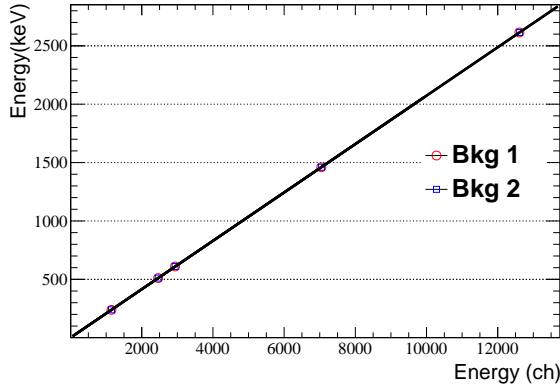
(a) *Comparison between two background measurements. The fitted function are:* $E_1[keV] = 0.20726 \times E[ch] + 0.96$ & $E_2[keV] = 0.20713 \times E[ch] + 0.96$ *respectively,*
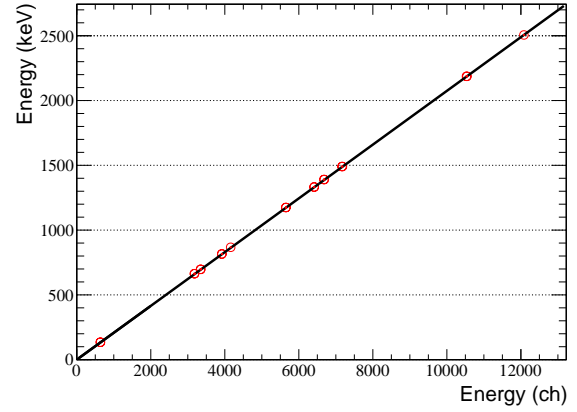
(b) *Calibration using external sources. Fitted function is* $E[keV] = 0.20743 \times E[ch] + 0.25$

Figure 6.6: *Linear energy calibration.*

Figure 6.6a compares two different measurements. These variations lead to less than 1 keV shift at 1 MeV. Fine calibration has to be done after each measurement in order to reduce this effect. This might be an issue for a complete automation of the system.

6.2.2 Resolution

The resolution is an important parameter of the HPGe characterisation as it sets limits on the ability to separate two γ lines close to each other. The resolution R, the standard deviation σ and the full width at half maximum, Ξ_{tot}, of a semiconductor detector are defined as:

$$R = \frac{\Xi_{tot}}{E} = \frac{2\sqrt{ln(2)}\sigma}{E} \tag{6.1}$$

It can be decomposed as [145]:

$$\Xi_{tot} = \sqrt{\Xi_{stat}^2 + \Xi_{eff}^2 + \Xi_{elec}^2} \tag{6.2}$$

Ξ_{stat} takes into account the statistical fluctuation of the number of charge carriers. Ξ_{eff} represents the variation in the charge collection efficiency. Ξ_{elec} is the electronic noise of the acquisition chain. Those components of the resolution can be disentangle using their variation with energy [246]:

$$\Xi_{elec}^2 \propto E^2 \tag{6.3}$$

$$\Xi_{stat}^2 = (2\sqrt{ln(2)})^2 F\delta \times E \tag{6.4}$$

$$\Xi_{eff} \propto cstt \tag{6.5}$$

with Ξ_{eff} not depending on the energy, F, the Fano factor, to be determined and δ the energy needed to create a e$^-$/hole pair. δ is 2.96 eV in Germanium at 77 K [247]. To determine the Fano factor, all the available γ lines were used but ^{22}Na 511 keV peak to avoid Doppler broadening effect (see section 6.3.1.1). The Fano factor is not depending on source position, thus TOP and BOT positions

147

were both added. The peaks were fitted with a Gaussian distribution after background subtraction. FWHM (Ξ_{tot}) is extracted using equation 6.1.

In order to extract the Fano factor Ξ_{tot} is fitted with:

$$\Xi_{tot} = \sqrt{p_0^2 + p_1^2 E + p_2^2 E^2} \tag{6.6}$$

from which the Fano factor is determined easily:

$$F = \frac{p_1^2}{4 ln(2)\delta} \tag{6.7}$$

Figure 6.7 shows the FWHM as a function of the energy and the function Ξ_{tot} fitted. The Fano
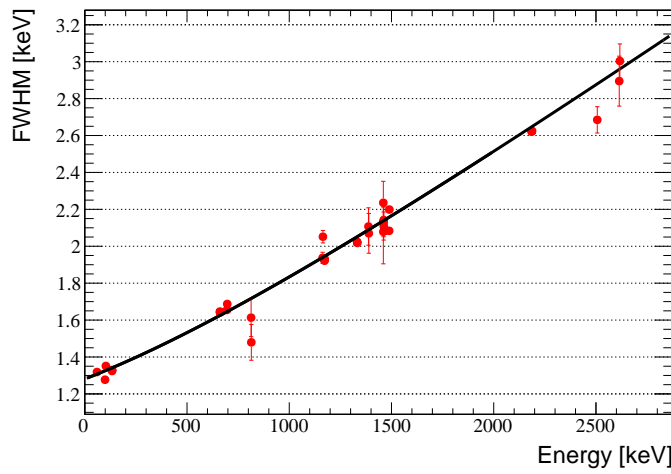
Figure 6.7: *Fit of the FWHM depending on the energy.*
Following eq. 6.6, $p_0 = 1.281$, $p_1 = 3.323 \times 10^{-2}$ and $p_2 = 7.86 \times 10^{-4}$.

factor in our HPGe has been measured to be $F = 0.135 \pm 0.022$ for a theoretical estimated value at 0.13 in Germanium [248].

6.2.3 Dead-time

We define the ratio R as:

$$R = \int r(E)dE = \int \left(\frac{N(E)}{A_{theo} \times \tau \times \Omega} \right) dE \tag{6.8}$$

with N(E) the integral of the spectrum over the peak at E, Ω the solid angle of the geometry and τ the time of exposure of the measurement. The ratio $r(E)$ represents the proportion of observed events with respect to the total expected events. If there is no dead time in the detector, R must not depend on the source activity. To modulate the activity of the source we compared BOT and TOP, having a different solid angle.

Table 6.6 displays the relative distance of the ratio R depending on the TOP or BOT situation using the ^{144}Ce-^{144}Pr sample and the ^{241}Am calibration source. It is clear that pile-up and induced dead-time are occurring more often in the ^{241}Am measurements since this source has a much

Source	Ratio top	Ratio bot	Relative distance
^{144}Ce-^{144}Pr	9.12×10^{-2}	9.17×10^{-2}	5.4×10^{-3}
^{241}Am	2.040×10^{-2}	2.280×10^{-2}	0.10520

Table 6.6: *Integrated ratios R over the entire spectrum range for the ^{144}Ce-^{144}Pr sample and the ^{241}Am calibration source.*

higher activity. We see here the limit of the acquisition gate of the HPGe and no relevant activity measurement could be perform without taking it into account.

The times measured by the acquisition chain are displayed in Tables 6.7a and 6.7b . The

Situation	Real Time (s)	Live Time (s)	Corrected dead time (%)
TOP	258379	256932	0.56
BOT	597284	595807	0.25

(a) ^{144}Ce-^{144}Pr *sample.*

Situation	Real Time (s)	Live Time (s)	Corrected dead time (%)
BOT	9491	9444	0.50
TOP	11923	11674	2.09
TOP++	1237	1139	7.92
FAR ASIDE	79715	79255	0.58
ASIDE	154088	150778	2.15

(b) ^{241}Am *calibration source*

Table 6.7: *Time measurements from the DSPEC*

dead-time for the high energy gamma sources was negligible.

6.2.4 Experimental efficiency

The efficiency is determined using only the full-energy peaks. Considering a γ line E_γ with a branching ratio of $\mathcal{B}_R$, the efficiency is the ratio of the observed number of E_γ over the expected signal from this line ($\tau \times \mathcal{B}_R \times A$). The efficiency can be divided as:

$$\epsilon_{tot}(E) = \epsilon_{geo}(E) \times \epsilon_{detector}$$

with ϵ_{tot} the efficiency found experimentally and ϵ_{geo} the efficiency from the simulation including solid angle and probability to escape after Compton interaction inside the crystal. The determination of $\epsilon_{detector}$ will take into account collection efficiency and is considered as a scale factor.

Using the ^{144}Ce-^{144}Pr γ lines, one can determine the efficiency for TOP and BOT. The two experimental efficiencies are shown respectively in the figures 6.8a and 6.8b.

(a) *The TOP position,*
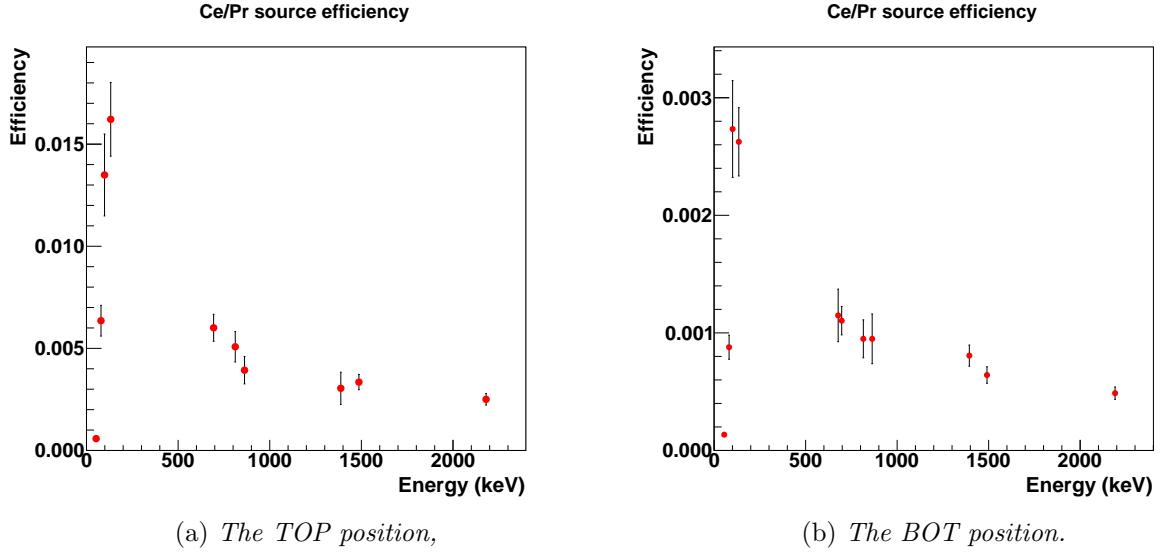
(b) *The BOT position.*

Figure 6.8: *Experimental efficiencies measured for each position.*

The factor 5 between the TOP and the BOT efficiency is in agreement with the solid angle estimation.

6.2.5 Background
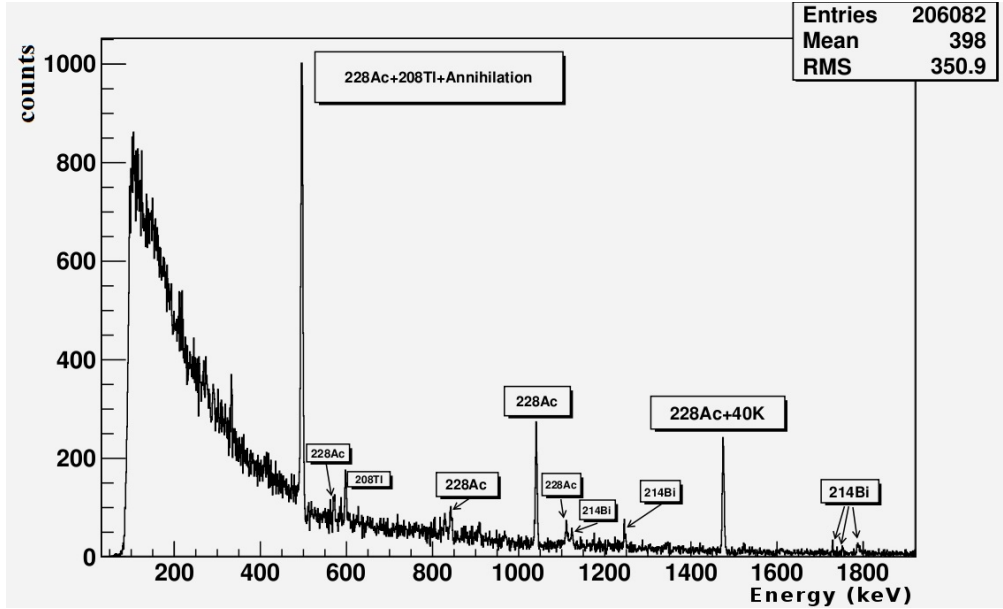
Figure 6.9: *Identification of the background peaks.*

The background is constituted of the natural background: ^{238}U, ^{232}Th and ^{40}K. Radon is carried with air while ^{40}K is mostly human contamination by contact with surrounding material. We observed a fluctuating radon rate inside the airtight acrylic box due to decaying radon. A gaseous nitrogen flushing system was installed to wash out this contamination. The flushing system reduces the total background by a factor 5, from 5 Hz to 1 Hz. With a 200 mL/min flux, the 22.4 litres

acrylic box is flushed more than 10 times on a day, the box is then considered as radon free. Although the acrylic box is under higher pressure than the laboratory, it does not stop radon decay between acrylic box and the lead box, leading to a irreducible background. This background should be more or less constant as the Lead box is not airtight. Aside from natural contamination, MeV γ's can excite surrounding nuclei. The HPGe detected X-rays mostly coming from the Lead of the shielding and correlated with the presence of a radioactive source inside the Lead box. Figure 6.9 shows a typical background spectrum measured in laboratory.

6.3 Monte Carlo simulation

The simulation aims at reproduce the full energy peak as well as the Compton shape. For this purpose, the environment of the detector has been fully integrated inside the Monte-Carlo. Although drawings of the detector and its surrounding environment exist (as in figure D.3 in Appendix), several parameters remain unknown at the requested precision. Furthermore, free parameters of the HPGe geometry must be determined. In order to avoid distortion while determining those parameters, instead of converting the data from charge to energy, the Monte Carlo simulation itself is converted in charge. Data being stored as histogram this enable us to compare data/MC without binning issue.

Graphics in the following section present comparison of Monte-Carlo simulation (red) and data (black) of the deposited energy. Residuals are plotted as: $\frac{\text{data}-\text{simulation}}{\text{data}}$.

6.3.1 Environment analysis

6.3.1.1 The backscattering effect

The Compton interaction undergoes a maximal transferred electron energy effect called Compton edge and corresponding to a full backscatter of the incident γ. The energy of the Compton edge is given by the formula:

$$E_{Ce} = \frac{E_\gamma}{1 + \frac{m_e c^2}{2E_\gamma}} \tag{6.9}$$

Inversely, when a γ endures a full backscatter interaction within material of the environment, the γ might enter the detector to deposit the residual part of its momentum, E_{bs}. Therefore, in addition to the Compton edge, the detector will see an other peak called backscattering peak (E_{bs}):

$$E_{bs} = E_\gamma - E_{Ce} = E_\gamma \frac{m_e c^2}{m_e c^2 + 2E_\gamma} \tag{6.10}$$

Unlike the Compton edge, the backscattering peak is highly dependent of the near environment of the detector as it assumes a first interaction outside the detector. It is an ideal cross-check for environment simulation. Typical value of E_{bs} is around 200 keV. This energy range can not be neglected for contaminant research and must be calibrated. Considering the ^{137}Cs calibration source, the backscatter peak is clearly visible in the simulation and in the data as shown in figure 6.11. However a discrepancy is also visible between model and data. Figure 6.10 shows main areas of backscatter event production from the simulation: the acrylic box, the shelf of the plastic box and the source capsule. The Petri dishes were simulated as well but their effect is negligible.
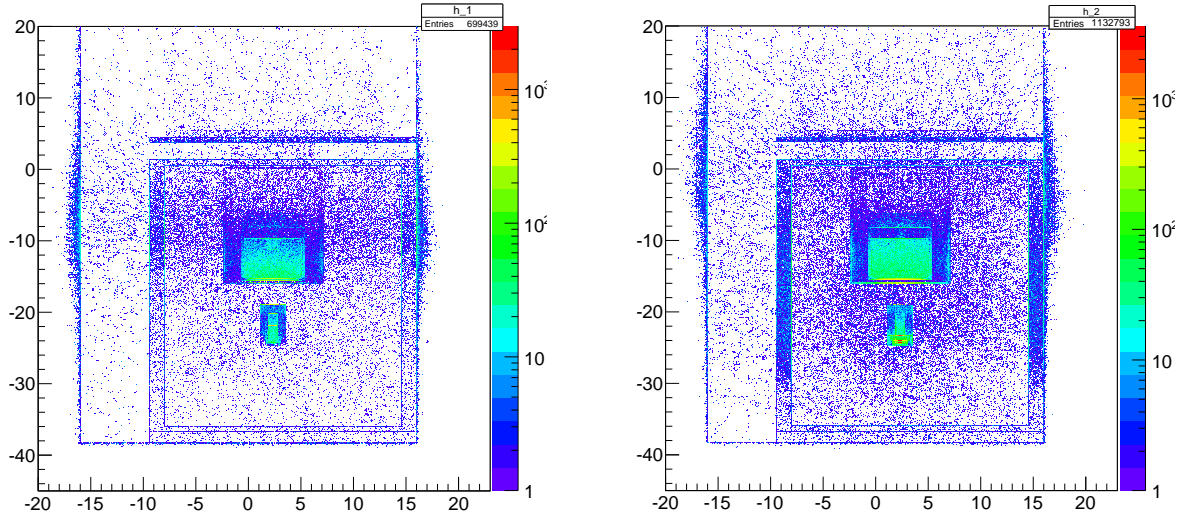
(a) *Energy deposited in the germanium higher than $E_{backscattering}$*

(b) *Energy deposited in the germanium equal to $E_{backscattering}$*

Figure 6.10: *Simulation of energy deposition in the all environment. On the left focusing on events depositing in the HPGe more than the backscattering and on the right backscattering events.*

Figure 6.10 shows the importance of mismodelling of the material around the sensitive target. The width of the acrylic box as well as the capsule itself are major production places of the backscatter peak. Figure 6.11 illustrates the impact on the Monte-Carlo simulation of varying the acrylic box width. Simulations are normalized with respect to the full absorption peak. The simulation enables to precisely determine the geometrical parameters as the acrylic box width.
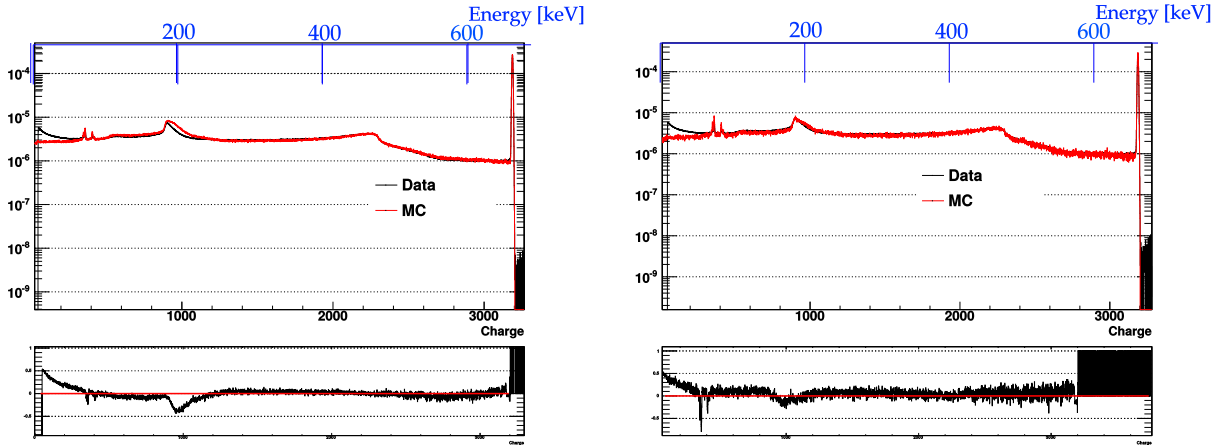
(a) *Simulation with a 12 mm width acrylic box*

(b) *Simulation with a 8 mm width acrylic box*
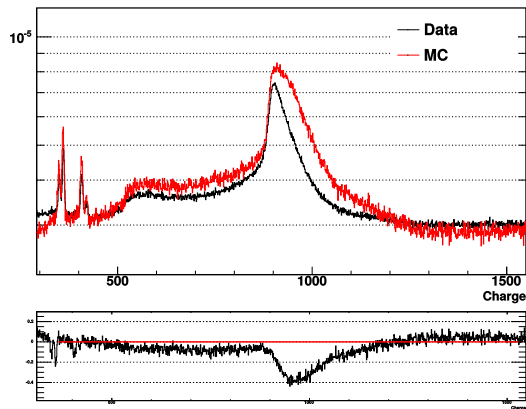
(c) *Zoom in of 6.11a*
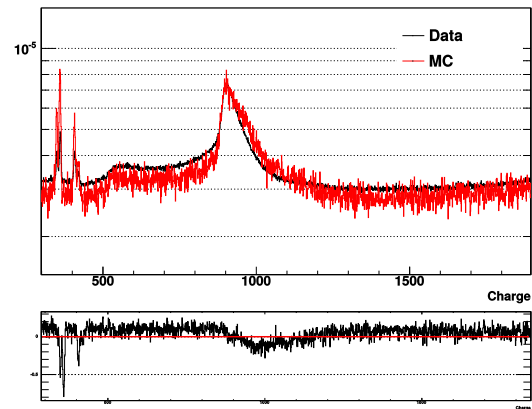
(d) *Zoom in of 6.11b*

Figure 6.11: ^{137}Cs *spectra highlighting the effect of the environment on the result at low energy.*

6.3.2 The detector simulation

6.3.2.1 The "smoothing" effect

Tests showed the effect of realistic object, especially the "smooth" angle of the crystal and the cold finger. Smooth angles were finally implemented for the cold finger cylinder, the Germanium crystal hollow for inserting cold finger, the Germanium crystal edges and the dead layers. Figure 6.12 shows a comparison of the simulated geometry depending on the implemented form and Geant4 object.
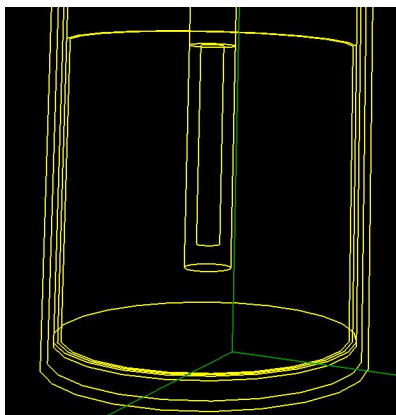
(a) *Sharp geometry*
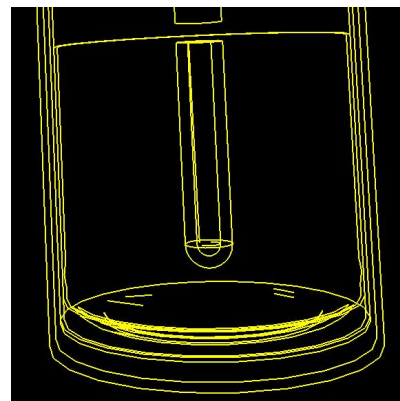
(b) *Rounded geometry*

Figure 6.12: *3D visualisation of the detector using view3dscene.*

Figure 6.13 shows for the entire spectrum and for Compton shape only, the effect of those rounded angle on the data/MC agreement.

The residue shows a better agreement between Monte Carlo and data when geometrical object inside the detector are smoothed. The two spectrum are normalized with respect to the total spectrum. Compton edge and low energy region are sensible to this modification.

(a) *Using sharp geometric objects*   (b) *Using more physical smooth curves*
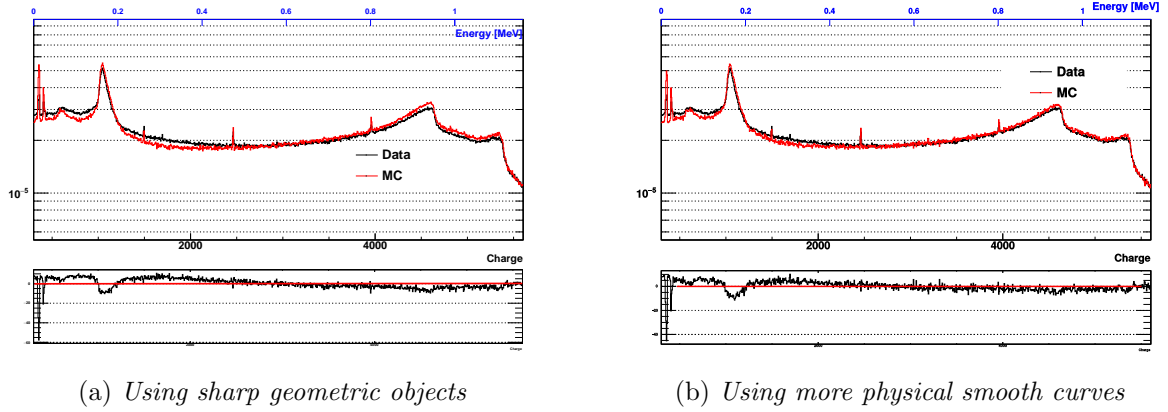
Figure 6.13: *Effect of round geometrical objects for the ^{60}Co calibration source in the TOP configuration.*

6.3.2.2 The cold finger

The cold finger is an other item relatively important. It is not described by the ORTEC documentation. It cannot be fully in contact with the crystal to avoid vibration propagation from the outside. The contact between cold finger and crystal are then done by thermal bridges like Copper pins. The ratios of radius and height were fixed to: $R_{\text{Cold finger}} = 0.7.R_{\text{Hole}}$ and $H_{\text{Cold finger}} = 0.8.H_{\text{Hole}}$. The smooth bottom of the cold finger ensures that no contact was simulated with the crystal.

6.3.2.3 The dead layers

Finally, the last items to be implemented are the dead-layers of the detector. In the Monte-Carlo, two free dead-layers were simulated: one concerning the core of the germanium cylinder called lateral dead-layers and the other at the bottom of the detector called top dead-layer. Figure 6.14 sketches the simulation of the HPGe. The main effect of the dead-layer except for decreasing the total active volume, is on low energy γ's (E_γ <100 keV). Literature shows example of tuning dead-layer as a global efficiency loss [249]. Here we consider for now only the Compton shape as we normalized the simulation to the full absorption peak.
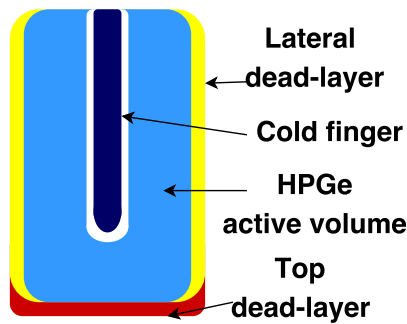
Figure 6.14: *Schematic of crystal with the to-be-tuned parameters: lateral and top dead layers, radius and height of the cold-finger.*

To test this energy range, we used X-rays from the Lead as well as low-energy Compton shape. A lower limit on the lateral dead-layer was estimated around 0.7 mm which is the value given by ORTEC. Analysis of the low energy ^{144}Ce-^{144}Pr spectrum shows as well a lower intensity of low energy γ's with respect to the entire spectrum hence bottom dead layer lower limit around 1 mm. Finally, the ^{241}Am source was used. Figure 6.15 showed the 60 keV backscattering peak for different (δ_{top},$\delta_{lateral}$) values. Because of dead-time consideration, we used the ^{241}Am calibration source in the "TOP _ASIDE" position (as described in 6.4c).
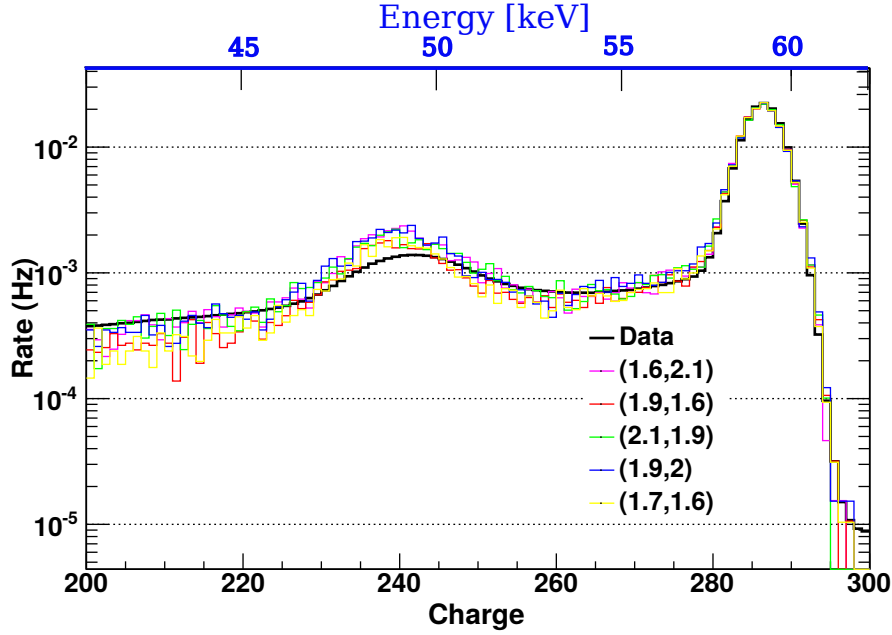
Figure 6.15: *Comparison of the 60 keV backscattering peak fit for different (δ_{top},$\delta_{lateral}$) values.*

Unfortunately the ^{241}Am calibration wasn't successful enough and we therefore had to look for other complementary methods to assess the dead layers.

6.3.3   Detector efficiency

Aside from the Compton shape, the efficiency is an other observable that can be fitted with the Monte Carlo. The determination of the efficiency is done using the full energy peak and is consequently independent from the Compton shape. In order to do that, the ^{144}Ce-^{144}Pr sample was used because of the several intense γ's from ^{144}Ce and ^{144}Pr. The experimental curve is displayed in Section 6.2.4.

Dead layers are absorbing the low energy γ's, roughly below 200 keV, as well as X-rays. This inert part of the detector reduces the total active volume, deforming the global spectrum and the efficiency. In order to consider a set of data as undistinguishable, a routine transformed the tree from the simulation to an histogram similar to the experimental raw data and the determination of the efficiency was done with the same technique for data and Monte Carlo.

To compare data and Monte Carlo for sets of dead-layer values, we extracted a χ^2 as described

in equation 6.11.

$$\chi^2 = \sum_{\text{peaks}} \left(\frac{\text{data} - \text{MC}}{\sigma_{\text{data}}}\right)^2 \qquad (6.11)$$

Searching for the minimal χ^2, χ^2_{min}, we defined $\Delta\chi^2$ as $\Delta\chi^2 = \chi^2 - \chi^2_{\text{min}}$.

Figure 6.16 represents the variation of $\Delta\chi^2$ depending on both top and lateral dead layer.
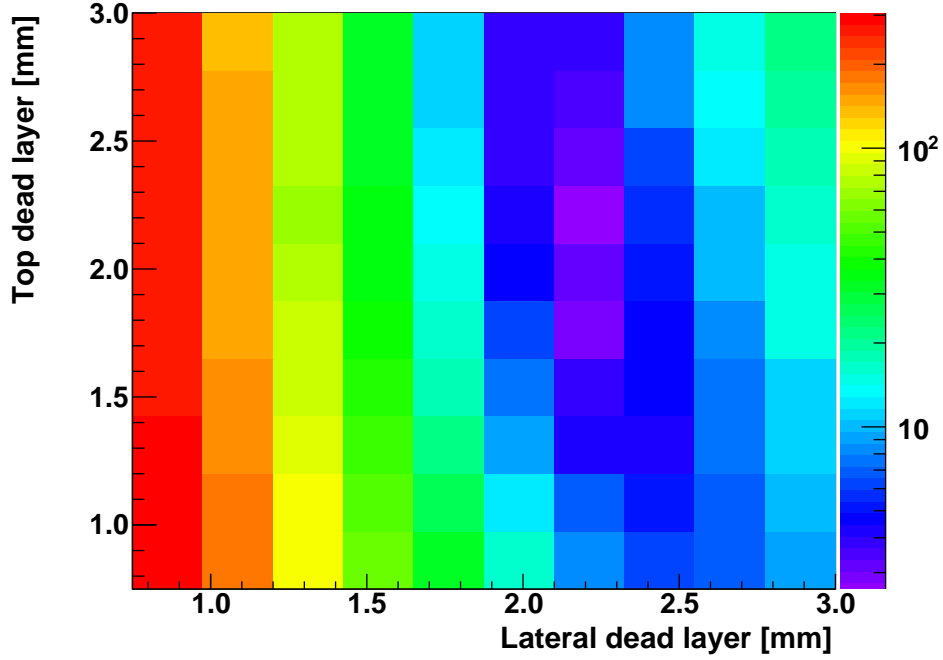
Figure 6.16: *The $\Delta\chi^2$ variation as function of the dead layers.*

Each point of the graph of Figure 6.16 is averaged over the $\epsilon_{\text{detector}}$ - the simulation normalization factor -, varying from 0.8 to 0.95. One can constrain the dead layers with 95% insurance between:

$$1 \text{ mm} \leq \delta_{\text{top}} \leq 3 \text{ mm} \ \& \ 2 \text{ mm} \leq \delta_{\text{lateral}} \leq 2.75 \text{ mm}.$$

Following the map, we fixed both dead-layers to 2.1 mm (χ^2_{min})

6.3.4 Results and limitations of the Monte Carlo

6.3.4.1 Results

The global agreement between data and Monte Carlo simulation is good as shown in figures 6.17, 6.18 and 6.19 show for ^{60}Co, ^{137}Cs and ^{22}Na calibration sources respectively.

(a) *BOT configuration*

(b) *TOP configuration*
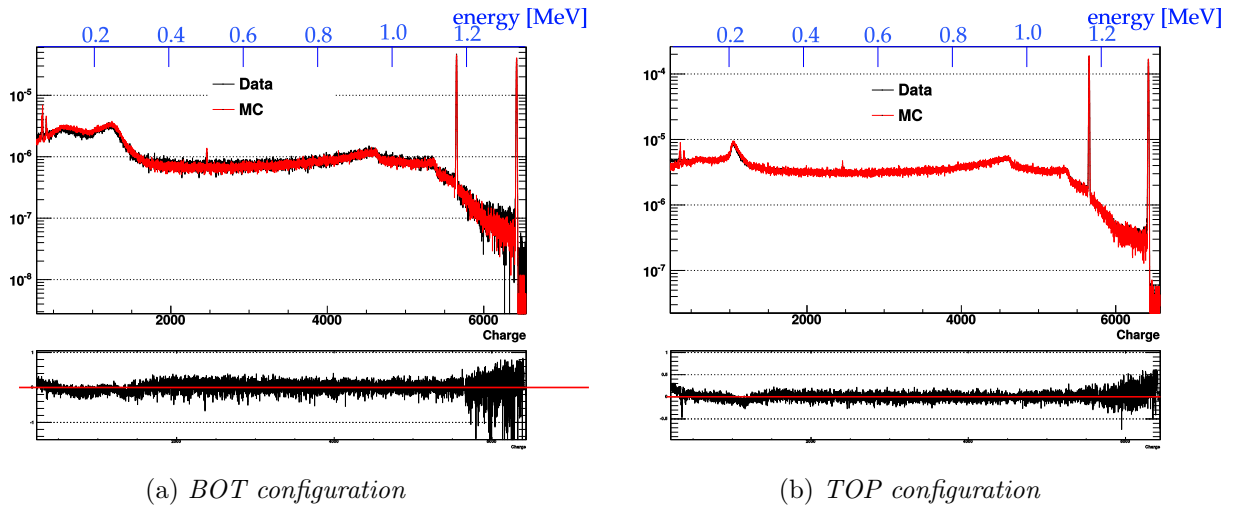
Figure 6.17: *Comparison MC/data for the ^{60}Co source.*

(a) *"Bot" situation*

(b) *"Top" situation*
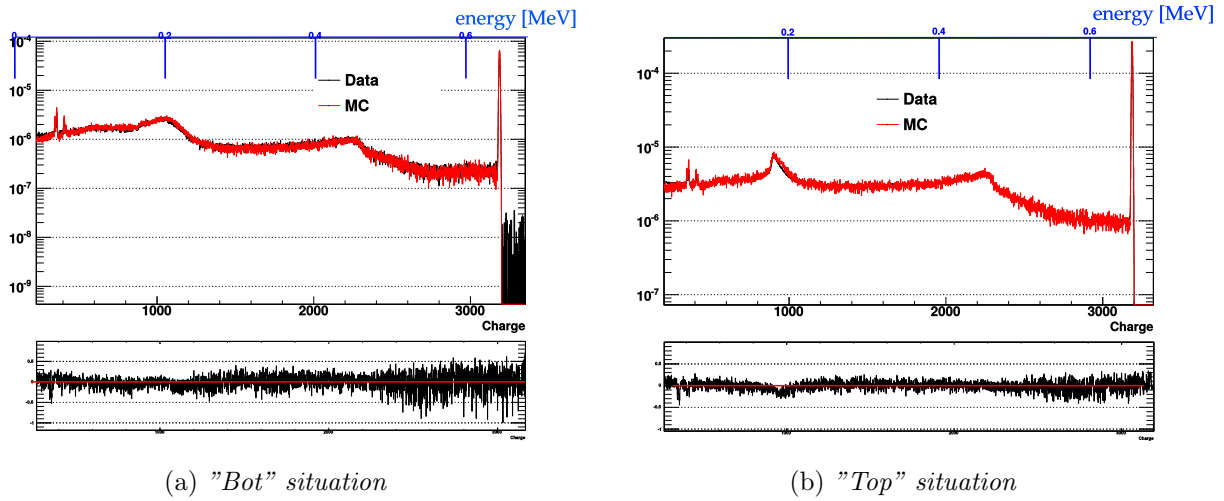
Figure 6.18: *Comparison MC/data for the ^{137}Cs source.*

(a) *"Bot" situation*

(b) *"Top" situation*
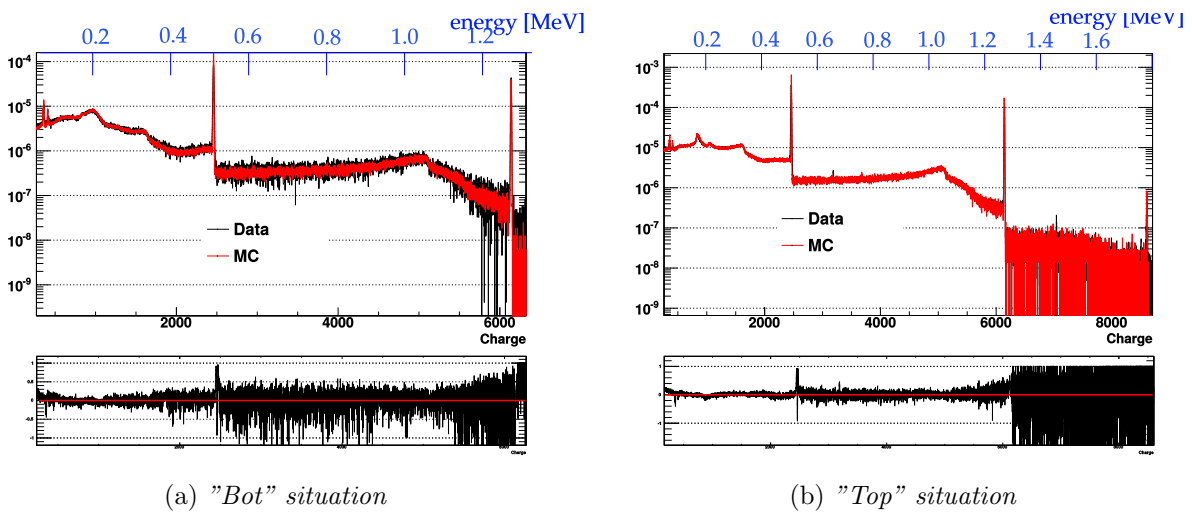
Figure 6.19: *Comparison MC/data for the ^{22}Na source. The 511 keV peak is not well fitted as explained in the following section.*

6.3.4.2 Limitations

The Doppler broadening effect The Doppler broadening effect is a well known spread in the e^-/e^+ annihilation peak [250]. It has become a relatively new domain of spectroscopy: Positron Annihilation Spectroscopy (PAS) used in atomic physics [251], with applications in many fields [252, 253, 254]. When the e^+ is emitted from the ^{22}Na source it forms a positronium with an e^- from a specific shell of the atom of the target. The different shells implies different Doppler shapes hence a global broadening [251].
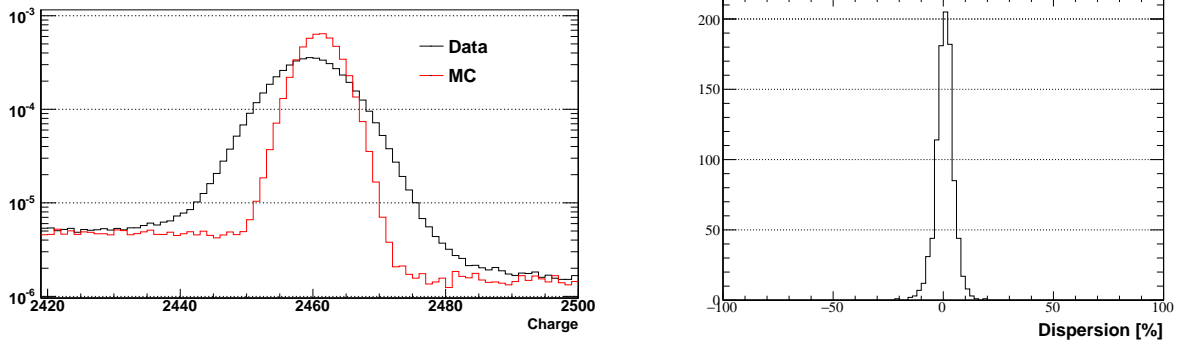
(a) *The Doppler broadening effect is not correctly simulated in the ^{22}Na calibration source γ spectrum.*

(b) *Distribution of the residue for the ^{60}Co source in the BOT situation.*

Figure 6.20: *Illustration of simulation limitations.*

Dispersion The agreement between data and simulation has been evaluated with a ^{60}Co source. Figure 6.20b displays the dispersion of the simulation with respect to the data. The mean value is 0 because the simulation is normalized with respect to the data. The symmetrical shape of the gaussian is showing the robustness of the simulation: no spectral distortion is found in the overall spectrum. As the simulation has been fitted on calibration sources including ^{60}Co. The sigma of this distribution is 3.7%. Section 6.4 is comparing the data/MC agreement for a new *gamma* emitter and a more complex spectrum.

6.4 Results on the ^{144}Ce sample

Figure 6.21 shows the sample spectrum in the BOT position before background subtraction. The two 2.614 MeV ^{208}Tl peaks are in perfect agreement. However, if one wants to use highly binned spectra, background must be adjusted before subtraction due to slight modification of the energy/channel conversion. This is problematic as we want no modification of the binning width except by integer factor. To solve the problem, the analysis of contamination inside the sample is done in reduced energy window in which background can be adjusted.
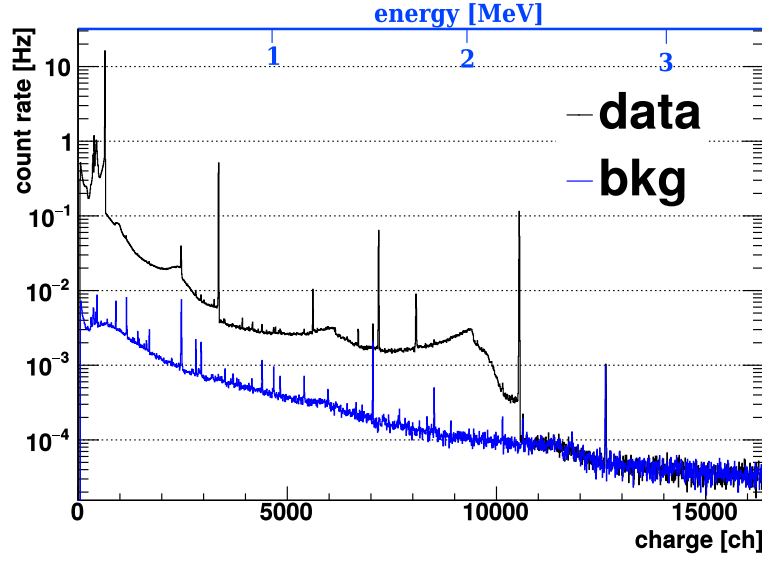
Figure 6.21: *^{144}Ce-^{144}Pr spectrum together with associated background.*

Efficiency Figure 6.22 shows the agreement between experimental and simulated efficiency for the ^{144}Ce-^{144}Pr sample. The result was obtained for $(\delta_{top},\delta_{lateral})$=(2.1 mm,2.1 mm) and $\epsilon_{detector}$ = 0.88.
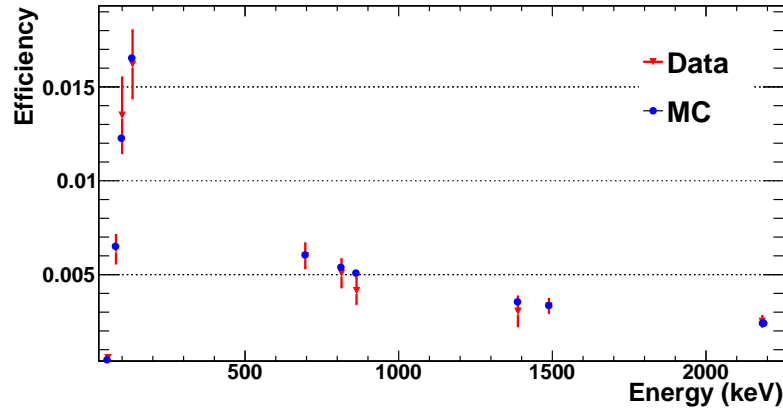
Figure 6.22: *Comparison data and Monte Carlo for a $(\delta_{top},\delta_{lateral})$=(2.1mm,2.1mm) and a normalization factor of 88%.*

Data and Monte Carlo full absorption peak were integrated in an automatic way. The main uncertainty to the experimental efficiency determination is coming from the activity measurement of the sample.

Shape Finally, figure 6.21 shows the shape comparison data/MC. The whole spectrum is fitted with the same normalisation but was divided in two ranges to highlight the relatively good agreement between data and MC at high energy. The low energy shapes highlight a discrepancy. Below 50 keV data are affected by multiple distorsions and are therefore not used. Between 50 keV and 130 keV simulated shape does not match data either. The full absorption peak of ^{144}Ce (133.5 keV) as well

159

as Pb X-rays (88 keV) and ^{144}Ce (80.1 keV) are well reproduced but not the 133.5 keV Compton shape.
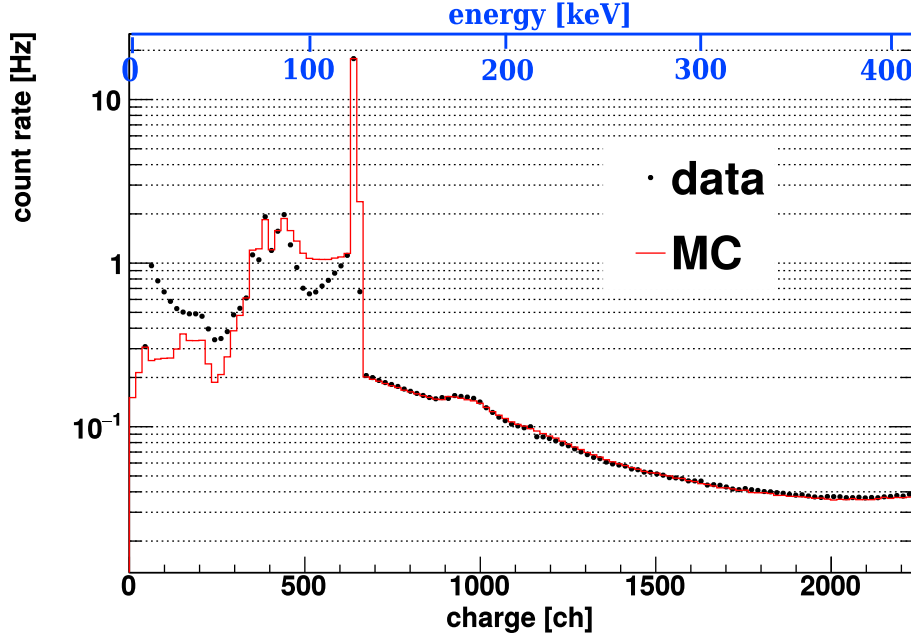
(a) *At low energy,*
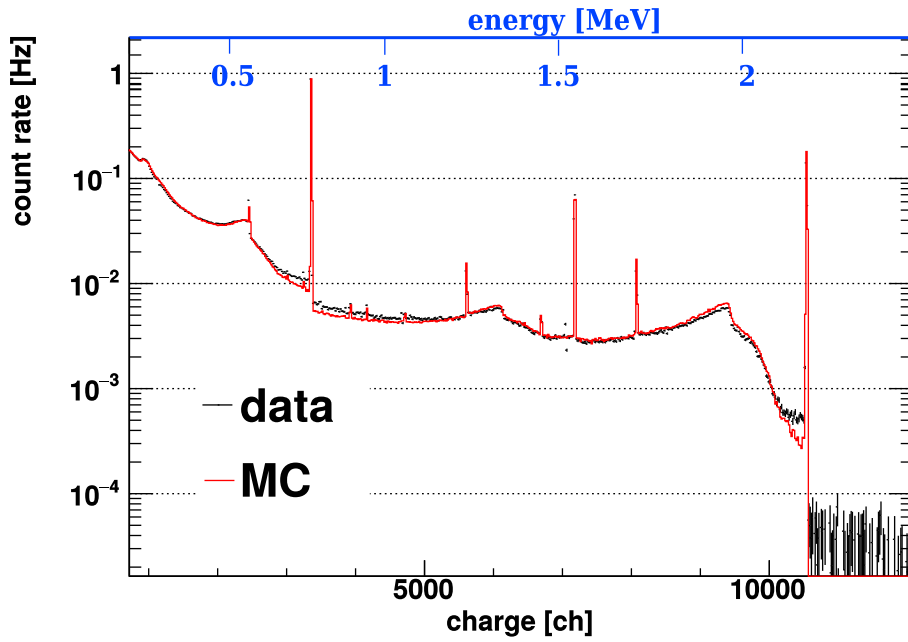
(b) *At high energy*

Figure 6.23: *Comparison data/MC for the ^{144}Ce-^{144}Pr spectrum in the BOT situation. While the high energy (>150 keV) agreement is good, a high discrepancy appears at low energy. Simulation is normalized with respect to the data: only shape comparison.*

To quantify this agreement, figure 6.24 shows the shape agreement between data and simulation

between 150 keV and 500 keV. The region 500 keV-520 keV is not fitted well due to the Doppler broadening effect. Deviation is constrained to 3-5% in each bin. Anticipating the next chapter, the error bars include the systematic uncertainty on the efficiency determination (see section 7.2). Figure 6.25 shows the deviation in a broader energy window (from 1.1 MeV to 2.1 MeV).
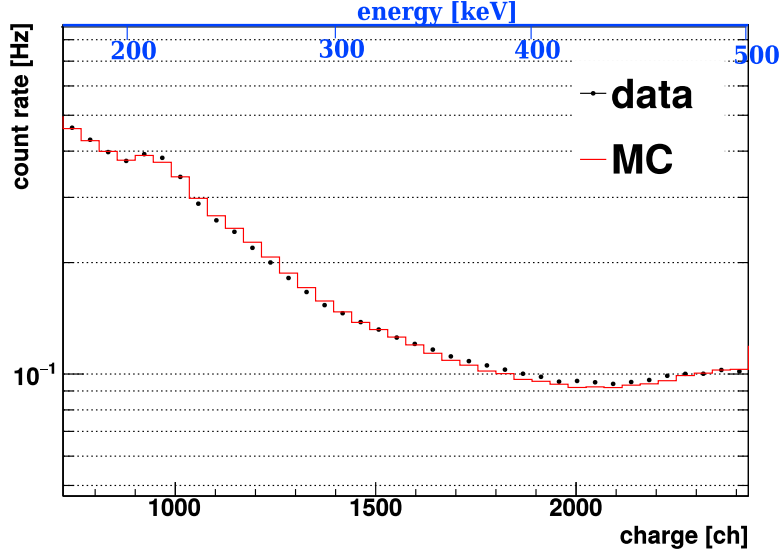
(a) *Comparison data/MC,*
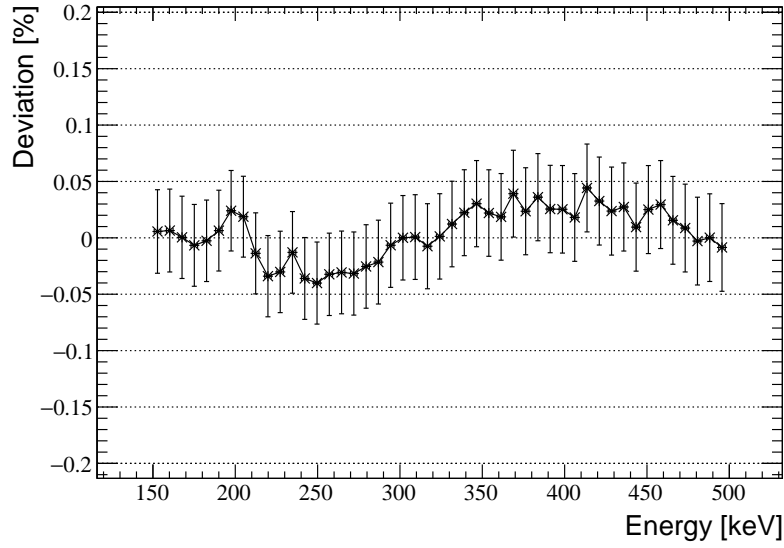
(b) *Deviation from the data,*

Figure 6.24: *Comparison of data/MC in a typical region of interest: 150 keV - 500 keV.*
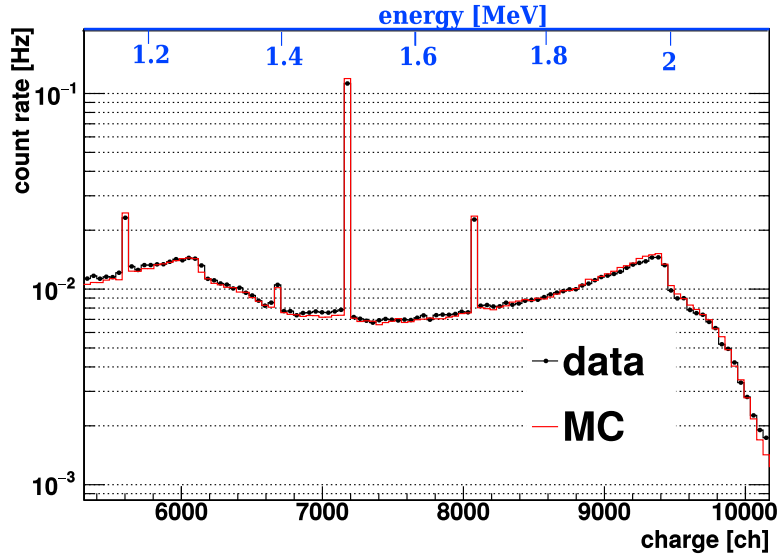
(a) *Comparison data/MC,*
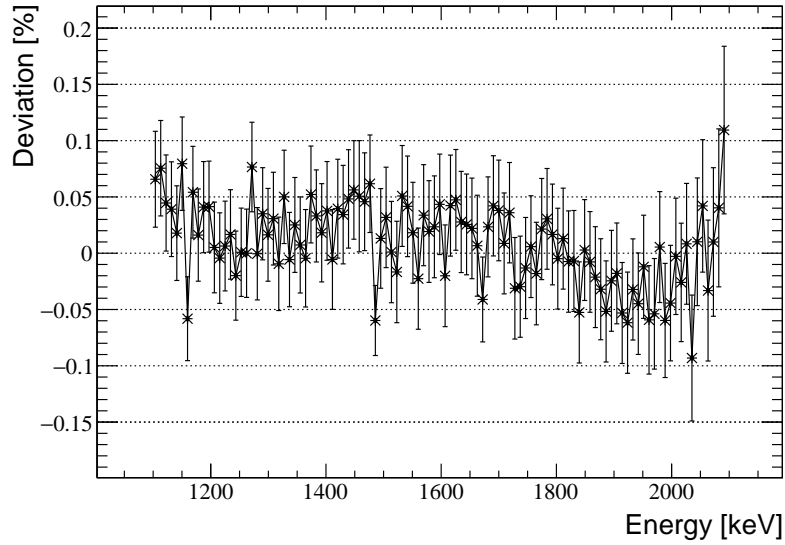
(b) *Deviation from the data,*

Figure 6.25: *Comparison of data/MC in an extended region of interest: 1100 keV-2100 keV.*

6.4.1 Conclusion

The HPGe characterisation and calibration aimed at being ready to analyse SOX ^{144}Ce samples that will be delivered during the course of the ^{144}Ce production. They will be sampled after the chromatographic separation and present in a liquid form. Thanks to calibration sources as well as a non representative sample sent by PA MAYAK, the detector and its near environment are well reproduced in the simulation. ^{144}Ce is a strong background which must be understood to estimate radio-purity from γ spectroscopy. Full energy peak and Compton shape area are well enough reproduced to be exploited in order to constrain contamination inside the source.

Chapter 7

Characterisation of the Cerium source

Contents

As we have seen in section 3.2.3, the Borexino detector has reached a very high level in material radio-purity and background comprehension, consequently observing for the first time neutrino rate from the Sun [41] as well as from Earth [172]. Deformed vessel and energy reconstruction at high radii for $\overline{\nu}_e$ signal are very challenging, but the most unknown parameter for the SOX experiment remains the ^{144}Ce source itself as discussed in section 3.3. Previous neutrino source experiments used irradiating material [168, 116, 117] in which radio-purity can be constrained with a precise knowledge of material inserted in the core. Extracting the source from spent nuclear fuel, potential contaminations are legion. The characterisation of the SOX ^{144}Ce source is a two sided coin: knowing pure ^{144}Ce and ^{144}Pr β shapes, and knowing what is not ^{144}Ce-^{144}Pr in the SOX source itself.

A first section 7.1 describes the potential source contaminants and lists their characteristics. The next section 7.2 describes the constraints derived from γ spectroscopy as well as the method employed. Other spectroscopy techniques are discussed as well in section 7.3. Finally, the ^{144}Ce β spectrometer is described, calibration and first result are reported in section 7.4.

7.1 Potential radio-impurities

An exhaustive list of potential contaminants was established for the SOX experiment. Considered nuclei have half-life between 0.5 and 1000 years. More unstable nuclei would be reduced at the level of the traces at the time of the delivery while long-lived isotopes can not have a dangerous activity for the experiment. The spent nuclear fuel used to produce the source being poorly known, no constraints was set on the pertinence of potential contaminants, from fission products to chemical contamination during transfer. No secular equilibrium can be assumed in the radioactive chains due to the complicated purification process.

Tables 7.1, 7.3 and 7.4 are displaying the potential radioactive contaminants inside the ^{144}Ce source. This list is important for assessing the level of radio-impurity reached in the source production, playing a role in the activity measurement (biased by any unknown heat source in the capsule), the safety rules and the long term storage issues. Table 7.2 details the same characteristics for ^{144}Ce and ^{144}Pr for illustration. Those tables explicit the half-life ($T_{1/2}$), the specific activity, the averaged heat released per decay in keV and the fission yields when relevant. Radioactive elements from the same chain are studied separately except if they have reached secular equilibrium at delivery time. We assumed a delay of 1.5 years between the end of the irradiation inside the reactor core and the delivery at Saint Petersburg harbour.

Element	Decay	$T_{1/2}$ [y]	A_{spe} [Bq.g^{-1}]	Heat/decay [keV]
^{3}H	β^-	12.32	3.58e+14	5.7
^{22}Na	β^+	2.6027	2.31e+14	2393.0
^{32}Si	β^-	153	2.70e+12	69.6
^{39}Ar	β^-	269	2.73e+12	218.8
^{42}Ar	β^-	32.9	2.23e+13	233.0
^{44}Ti-^{44}Sc	EC&EC	59.1	5.09e+12	595.8
^{49}V	EC	0.903	2.99e+14	2.7
^{54}Mn	EC	0.855	2.87e+14	3.0
^{55}Fe	EC	2.744	8.76e+13	3.0
^{57}Co	EC	0.744	3.12e+14	110.0
^{60}Co	β^-	5.27	4.18e+13	2599.0
^{63}Ni	β^-	101.2	2.07e+12	17.4
^{65}Zn	EC	0.669	3.05e+14	564.7
^{68}Ge-^{68}Ga	2 EC	0.741	2.63e+14	784.3

Table 7.1: *Characteristics of the contaminants: light elements*

Element	$T_{1/2}$ [y]	A_{spe} [Bq.g^{-1}]	Heat/decay [keV]	Heat [W.g^{-1}]
^{144}Ce-^{144}Pr	0.78	1.18e+14	1290-1332	24.4-25.2

Table 7.2: *Characteristics of ^{144}Ce-^{144}Pr.*

Element	Decay	$T_{1/2}$ [y]	A_{spe} [Bq.g^{-1}]	Heat/decay [keV]	Pf ^{235}U [Bq/Bq]	Pf ^{239}Pu [Bq/Bq]
^{85}Kr	β^-	10.739	1.45e+13	253.0	2.70e-03	1.30e-03
^{90}Sr-^{90}Y	2 β^-	28.79	5.11e+12	1130.0	5.90e-02	2.10e-02
^{91}Nb	EC	680	2.14e+11	13.8	2.72e-14	2.07e-13
^{93m}Nb	IT	16.12	8.82e+12	28.1	6.07e-02	3.70e-02
^{106}Ru-^{106}Rh	2 β^-	1.023	1.22e+14	3215.0	4.02e-03	4.28e-02
^{101}Rh	EC	3.3	3.97e+13	309.0	3.27e-16	4.38e-14
^{102}Rh	EC	0.567	2.29e+14	507.0	1.55e-09	9.17e-12
^{102m}Rh-^{102}Ru	EC	3.742	3.47e+13	2162.0	8.60e-10	5.09e-12
^{108m}Ag	EC	438	2.80e+11	1613.0	4.30e-12	1.31e-09
^{110m}Ag	β^-	0.684	1.76e+14	2860.0	1.78e-09	2.68e-07
^{109}Cd	EC	1.263	9.61e+13	106.3	1.00e-14	6.56e-12
^{113m}Cd	β^-	14.1	8.30e+12	185.4	2.60e-06	1.05e-05
^{119m}Sn	IT	0.802	1.39e+14	83.5	5.10e-07	2.04e-06
^{121m}Sn	IT, β^-	43.9	2.49e+12	33.1	7.10e-06	2.62e-05
^{125}Sb	β^-	2.75856	3.84e+13	519.3	2.93e-04	1.11e-03
^{134}Cs	β^-	2.0652	4.78e+13	1716.0	1.27e-07	9.89e-06
^{137}Cs	β^-	30.08	3.21e+12	811.2	6.20e-02	6.72e-02
^{133}Ba	EC	10.551	9.43e+12	445.2	5.00e-13	1.80e-11
^{143}Pm	EC	0.726	1.27e+14	319.6		
^{144}Pm	EC	1	9.19e+13	1574.0	1.23e-16	1.30e-14
^{145}Pm	EC	17.7	5.15e+12	39.7		2.70e-12
^{146}Pm	EC, β^-	5.53	1.64e+13	764.6		2.03e-10
^{147}Pm	β^-	2.6234	3.43e+13	61.9	2.10e-02	2.04e-02
^{145}Sm	EC	0.931	9.80e+13	88.7		
^{151}Sm	β^-	90	9.73e+11	19.6		7.70e-03
^{150}Eu	EC	36.9	2.39e+12	1530.0		2.50e-12
^{152}Eu	EC, β^-	13.517	6.44e+12	1218.0		4.60e-09
^{154}Eu	β^-	8.601	9.99e+12	1464.0		9.20e-07
^{155}Eu	β^-	4.753	1.80e+13	116.0		1.65e-03
^{157}Tb	EC	71	1.19e+12	8.0		1.30e-10
^{158}Tb	EC, β^-	180	4.65e+11	896.4		1.84e-09
^{171}Tm	β^-	1.92	4.03e+13	24.8		1.88e-09

Table 7.3: *Characteristics of the contaminants: fission products*

Element	Decay	$T_{1/2}$ [y]	A_{spe} [Bq·g^{-1}]	Heat/decay [keV]
^{148}Gd	α	71.1	1.26e+12	3182.0
^{153}Gd	EC	0.658	1.31e+14	141.3
^{173}Lu	EC	1.37	5.58e+13	220.8
^{174}Lu	EC	3.31	2.30e+13	95.4
^{172}Hf-^{172}Lu	2 EC	1.87	4.11e+13	2195.0
^{179}Ta	EC	1.82	4.06e+13	30.7
^{178m}Hf	IT	31	2.40e+12	2446.0
^{194}Os-^{194}Ir	2 β^-	6	1.14e+13	902.4
^{192}mIr	IT	241	2.86e+11	157.0
^{193}Pt	EC	50	1.37e+12	5.2
^{195}Au	EC	0.509	1.33e+14	121.4
^{194}Hg-^{194}Au	2 EC	444	1.54e+11	1068.0
^{204}Tl	β^-	3.783	1.71e+13	236.9
^{210}Pb$\rightarrow^{206}$Pb	$2\beta^- + \alpha$	22.2	2.84e+12	5834.0
^{207}Bi	EC	31.55	2.03e+12	1642.0
^{208}Po	α	2.898	2.19e+13	5215.0
^{209}Po	α	102	6.21e+11	4979.0
^{228}Ra$\rightarrow^{208}$Pb	$5\alpha+4\beta^-$	5.75	1.01e+13	33757.0
^{227}Ac$\rightarrow^{207}$Pb	$5\alpha+3\beta^-$	21.772	2.68e+12	34295.0
^{228}Th$\rightarrow^{208}$Pb	$5\alpha+2\beta^-$	1.9116	3.03e+13	33380.0
^{232}U$\rightarrow^{208}$Pb	$6\alpha+2\beta^-$	68.9	8.27e+11	38794.0
^{235}Np	EC	1.084	5.19e+13	3.0
^{236}Pu-^{232}U	α	2.858	1.96e+13	5867.0
^{238}Pu$\rightarrow^{230}$Th	2α	87.7	6.34e+11	10452.0
^{239}Pu	α	24110	2.30e+09	5245.0
^{240}Pu	α	6564	8.39e+09	5256.0
^{241}Pu-^{241}Am	β^-	14.29	3.84e+12	5.2
^{241}Am	α	432.6	1.27e+11	5636.0
^{242m}Am-^{234}U	$2\alpha+1\beta^-$	141	3.72e+11	12460.0
^{243}Cm $\rightarrow^{235}$U	2α	29.1	1.87e+12	11414.0
^{244}Cm	α	18.1	2.99e+12	5902.0
^{248}Bk-^{244}Am	$\alpha+\beta^-$	10	5.33e+12	5000.0
^{249}Bk-^{249}Cf	β^-	0.903	5.88e+13	32.4
^{248}Cf	α	0.913	5.84e+13	6361.0
^{249}Cf	α	351	1.51e+11	6295.0
^{250}Cf	α	13.08	4.04e+12	6128.0
^{252}Cf	α	2.645	1.98e+13	6217.0
^{252}Es	α, EC	1.291	4.06e+13	5178.0
^{254}Es-^{250}Bk	$\alpha+\beta^-$	0.755	6.90e+13	7782.0

Table 7.4: *Characteristics of the contaminants: actinides, lanthanides*

Constraints on potential contamination are described in chapter 5. Depending on the final delivery activity and the ^{144}Ce-^{144}Pr mean energy, the source will emit between 800-1200 W. Tables 7.5 and 7.6 are giving activities of the contaminant at delivery time and 10 years after assuming that each contaminant is releasing 10^{-3} W/W(^{144}Ce+^{144}Pr) and a source of 5.5 PBq (initial activity at the delivery in Saint Petersburg). It is the most conservative scenario as the contract limits the heat released by all of the "detectable" contaminants. Indeed, during the agreement it was discussed that putting constraints on every contaminants would penalize any extra research effort made by PA MAYAK to recognize exotic contaminants if not reaching the sensitivity.

Contaminant	A_{th} [Bq/Bq]	A_{th} @10 y. [Bq/Bq]	Heat [W.g^{-1}]	Contaminant	A_{th} [Bq/Bq]	A_{th} @10 y. [Bq/Bq]	Heat [W.g^{-1}]
^{3}H	2.37e-1	976.3	0.326	^{148}Gd	4.24e-4	2.780	0.641
^{22}Na	5.63e-4	0.2841	88.6	^{153}Gd	9.54e-3	0.0018	2.98
^{32}Si	1.94e-2	134.0	3.01e-2	^{157}Tb	1.70e-1	1112	1.51e-3
^{39}Ar	6.16e-3	43.43	9.58e-2	^{158}Tb	1.50e-3	10.47	6.68e-2
^{42}Ar	5.79 e-3	33.90	0.834	^{171}Tm	5.44e-2	10.65	0.160
^{44}Ti-^{44}Sc	2.26 e-3	14.56	0.486	^{173}Lu	6.11e-3	0.280	1.97
^{49}V	4.99e-1	1.680	0.129	^{174}Lu	1.41e-2	12.59	0.351
^{54}Mn	4.49e-1	0.9797	0.138	^{172}Hf-^{172}Lu	6.14e-4	0.1091	14.5
^{55}Fe	4.49e-1	259.9	4.21e-2	^{179}Ta	4.39e-2	7.041	0.200
^{57}Co	1.23 e-2	0.0080	5.50	^{178m}Hf	5.51e-4	3.188	0.940
^{60}Co	5.19e-4	1.007	17.4	^{194}Os-^{194}Ir	1.49e-3	3.404	1.64e-6
^{63}Ni	7.75e-2	523.3	5.78e-3	^{192}mIr	8.59 e-3	60.35	7.19e-3
^{65}Zn	2.39e-3	0.0005	27.6	^{193}Pt	2.58e-1	1623	1.15e-3
^{68}Ge-^{68}Ga	1.72e-3	0.0011	33.0	^{195}Au	1.11e-2	0.0001	2.59
^{85}Kr	5.33e-3	20.21	0.587	^{194}Hg-^{194}Au	1.26e-3	8.989	2.63e-02
^{90}Sr-^{90}Y	1.19e-3	6.783	0.925	^{204}Tl	5.69e-3	6.588	0.651
^{91}Nb	9.74e-2	697.4	4.74e-4	^{210}Pb→^{206}Pb	2.31e-4	1.223	2.65
^{93m}Nb	4.79e-2	225.4	3.98e-2	^{207}Bi	8.21e-4	4.767	0.533
^{106}Ru-^{106}Rh	4.19e-4	0.0035	62.9	^{208}Po	2.58e-4	0.1710	18.3
^{101}Rh	4.36 e-3	3.863	1.96	^{209}Po	2.71e-4	1.830	0.495
^{102}Rh	2.66e-3	0.0001	18.6	^{228}Ra→^{208}Pb	4.0e-5	0.0865	54.6
^{102m}Rh-^{102}Ru	6.23e-4	0.7075	12.0	^{227}Ac→^{207}Pb	3.9e-5	0.2068	14.7
^{108m}Ag	8.36e-4	5.950	7.23e-2	^{228}Th→^{208}Pb	4.0e-5	0.0078	162
^{110m}Ag	4.71e-4	0.0001	80.6	^{232}U→^{208}Pb	3.5e-5	0.2273	5.14
^{109}Cd	1.27e-2	0.3794	1.64	^{235}Np	4.44e-1	5.369	2.52e-2
^{113m}Cd	7.27e-3	32.17	0.247	^{236}Pu-^{232}U	2.30e-4	0.1470	18.4

Table 7.5: *Constraints on contaminants from the heat specification [1/2]*

Contaminant	A_{th} [Bq/Bq]	A_{th} @10 y. [Bq/Bq]	Heat [W.g^{-1}]
^{119m}Sn	1.61e-2	0.0206	1.86
^{121m}Sn	4.07e-2	251.34	1.32e-2
^{125}Sb	2.60e-3	1.522	3.19
^{134}Cs	7.86e-4	0.1981	13.1
^{137}Cs	1.66e-3	9.547	0.417
^{133}Ba	3.03e-3	11.36	0.672
^{143}Pm	4.22e-3	0.0022	6.53
^{144}Pm	8.56e-4	0.0060	23.2
^{145}Pm	3.40e-2	166.0	3.28e-2
^{146}Pm	1.76 e-3	3.641	2.01
^{147}Pm	2.18e-2	11.21	0.340
^{145}Sm	1.52e-2	0.0642	1.39
^{151}Sm	6.87e-2	459.9	3.06e-3
^{150}Eu	8.81e-4	5.282	0.586
^{152}Eu	1.11 e-3	4.794	1.26
^{154}Eu	9.21e-4	2.975	2.34
^{155}Eu	1.16e-2	19.55	0.334

Contaminant	A_{th} [Bq/Bq]	A_{th} @10 y. [Bq/Bq]	Heat [W.g^{-1}]
^{238}Pu$\rightarrow^{230}$Th	1.29e-4	0.8620	1.06
^{239}Pu	2.57e-4	1.859	1.93e-3
^{240}Pu	2.56e-4	1.853	7.07e-3
^{241}Pu-^{241}Am	2.58e-1	1148	3.22e-3
^{241}Am	2.39e-4	1.703	0.115
^{242m}Am-^{234}U	1.08e-4	0.7450	0.743
^{243}Cm $\rightarrow^{235}$U	1.18e-4	0.6732	3.42
^{244}Cm	2.28e-4	1.127	2.83
^{248}Bk-^{244}Am	2.70e-4	0.9751	4.27
^{249}Bk-^{249}Cf	4.16e-2	0.1396	0.305
^{248}Cf	2.12e-4	0.0008	59.5
^{249}Cf	2.14e-4	1.519	0.153
^{250}Cf	2.20e-4	0.9367	3.97
^{252}Cf	2.17e-4	0.1141	19.8
^{252}Es	2.60e-4	0.0088	33.7
^{254}Es-^{250}Bk	1.73e-4	0.0001	86.0

Table 7.6: *Constraints on contaminants from the heat specification [2/2]*

7.2 γ spectroscopy

The HPGe calibration and simulation is described in chapter 6. The following section describes the γ spectroscopy results and methods to constrain contamination inside a ^{144}Ce-^{144}Pr source. For this sensitivity study we used a 60 kBq sample of ^{144}Ce sent by PA MAYAK and we assume the same experimental protocol for the future source: one week or more of data taking for a 60 kBq ^{144}Ce activity representative sample.

7.2.1 Limits of detection

Considering a binned γ spectrum N with N_i, value of the bin i. The signal we aim at measuring is a contamination inside a ^{144}Ce γ spectrum considered as a background. The ^{144}Ce activity is dominant in any range of energy over any potential contaminant. Therefore, unlike most of radio-purity experiments, N will always be high with respect to our signal. The detection method being a counting measurement, the statistical fluctuation of detected N_i around true $\overline{N}_i$ is Poissonian. N_i being high in every bin i, the statistical error can be considered as Gaussian. Considering a 95% confidence interval decision ($\alpha=\beta=5\%$), the detection threshold (DT) and the detection limit (DL) are defined as in the following [255]:

$$DT = K_{1-\alpha}\sigma_B = 1.645\sqrt{N} \tag{7.1}$$

The detection limit (DL) is then:

$$DL = (K_{1-\beta})^2 + 2K_{1-\alpha}\sigma_B = 1.645^2 + 3.29\sqrt{N} \tag{7.2}$$

They represent the classical opposition between the so-called H$_0$ and H$_1$ hypothesis as illustrated in figure 7.1. In one hand (H$_0$), DT defines what is the threshold to observe a given proportion
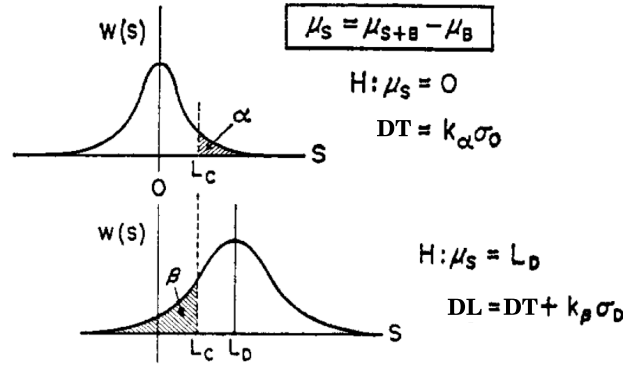
Figure 7.1: *Illustration of the difference between detection threshold (DT) and the detection limit (DL) [255].*

(5%) of events wrongly identified as signal events. In an other hand, the detection limit (H_1) is assuming a signal, what is the limit to identify as background a given proportion (5%) of signal.

Finally, the Minimum Detectable Activity (MDA), in Bq.g^{-1} will be defined as:

$$MDA = \frac{DL}{\Delta t \times \epsilon \times \mathfrak{B}_R \times m} \tag{7.3}$$

with Δt the time of exposure, ϵ the global efficiency (solid angle and detector efficiency), $\mathfrak{B}_R$ the branching ratio of the γ line and m the mass of the sample.

DT is used for qualitative determination. Detection limit (DL) and the Minimum Detectable Activity (MDA) are for quantitative determination of contamination/signal events in a counting detector [255]. These threshold are not depending on the knowledge of the expected signal shape. MDA is used in ultra low radio-contamination detection (Edelweiss [256]).

7.2.2 Experimental efficiency

In order to convert a limit of detection in count per second to an activity in Bq or Bq/g, the HPGe efficiency has to be determined. Efficiency is defined as the ratio of full energy peak deposited in the crystal over the all number of emitted γ. It depends on the size, the form and type of the detector as well as the energy [145].

Two experimental apparatus were defined for the calibration campaign: TOP and BOT (section 6.2.4). The BOT position is the one analysed to avoid any dead time effect. The efficiency of a p-type HPGe coaxial detector can be described using the function of equation 7.4 extracted from [257]. Other empirical formulae are described in [258, 259].

$$f(x) = \sum_{i=0}^{N} (a_i \times (ln(x))^i) \tag{7.4}$$

Figure 7.2 shows the result of fitting the efficiency with N=6. The error on the experimental points is dominated by the uncertainty on the sample activity (58.9 kBq $\pm$ 4.2%). The systematics associated with the fit of the efficiency is on the order of 3% on any activity measurement. It is the dominant error at low energy where the statistical error is low.
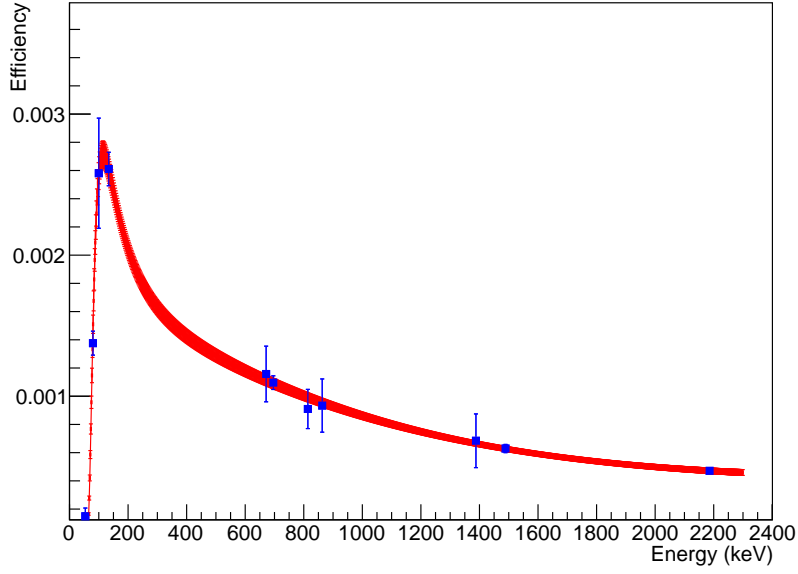
Figure 7.2: *The experimental efficiency in the BOT situation for the $^{144}Ce/Pr$ source. In blue, the experimental points, in black the fitted function and in red, the error associated with the evaluation of the fitting function.*

7.2.3 Monte Carlo method

Using the simulation of the detector, every contaminants has been simulated. A contaminant (^{Z}N) is added to the ^{144}Ce spectrum with a ratio α. Knowing N_i the measured spectrum and B_i the background corresponding, the measured spectrum after background subtraction will be written (s_i=N_i-B_i). The simulated ^{144}Ce spectrum and the simulated contaminant ^{Z}N are noted MC_i^{144Ce} and MC_i^{zN} respectively.

The idea is then to fit $\alpha MC_i^{ZN} + \beta MC_i^{144Ce}$ with respect to s_i using a likelihood ($\mathcal{L}(s_i|\alpha,\beta)$) minimization. The contamination is always low with respect to the source activity, therefore β is close to 1. The profile likelihood method allows us to let freely vary β while fixing the α value: $\mathcal{L}(s_i|\alpha,\beta) \rightarrow \mathcal{L}(s_i|\alpha)$. Furthermore, as the statistical distribution of s_i follows a Gaussian law, maximizing the likelihood is the same as minimizing $\chi^2(\alpha)$.

The $\chi^2(\alpha)$ is derived between bins $i_{\min}$ and $i_{\max}$, the extreme bins of the selected energy range.

$$\chi^2(\alpha) = \sum_{i_{\min}}^{i_{\max}} \left(\frac{s_i - \alpha MC_i^{ZN} - \beta MC_i^{144Ce}}{\sqrt{\sigma_{s_i}^2 + \sigma_{\epsilon_i}^2}} \right)^2 \tag{7.5}$$

with σ_{s_i} the statistical error and σ_{ϵ_i} the systematic associated with the efficiency of the bin i. The χ^2 distribution is used to determine the minimum contamination to be compared with the MDA. To determine the χ^2 distribution for all the contaminants, the protocol is the following:

1. List the potential γ contaminants and define the best energy range detection window;

2. Determine the χ^2 (as in 7.5) for the two situations: [^{144}Ce/Pr] and α[^{Z}N]+β[^{144}Ce/Pr];

3. Study the evolution of $\chi^2(\alpha)$ and measure the smaller $\alpha_{\lim}$ as: $\Delta\chi^2 = \chi^2(\alpha_{\lim}) - \chi^2(0) > 9$ [1];

4. Measure the integral of a ^{Z}N full energy peak in the energy range considered corrected from the efficiency and the branching ratio;

5. Determination of the sensitivity to contaminant: $R_{ZN} = \frac{\mathcal{A}_{ZN}}{\mathcal{A}_{144Ce}}$;

Figure 7.3 shows the $\Delta\chi^2$ evolution with and without the add of the systematic on efficiency determination.
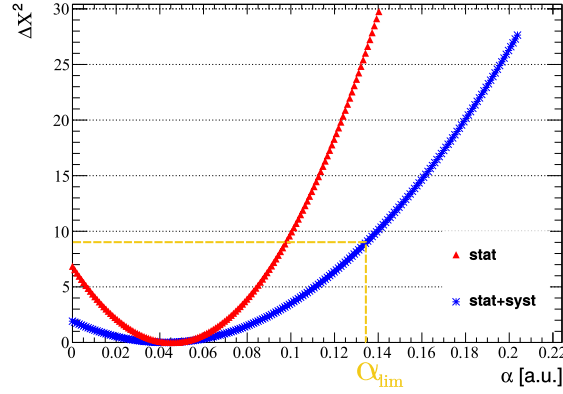
Figure 7.3: *Evolution of the $\Delta\chi^2$ depending on α with and without the systematic on the efficiency for ^{106}Rh contamination.*

7.2.4 Illustration of the method

^{60}Co detection limit determination is described as an illustration. Global results for every contaminants are given in section 7.2.5.1.

^{60}Co decays emitting mainly 1173 keV (99.85%) and 1332 keV (99.98%) gammas. Table 7.7 presents the χ^2 value obtained for different energy range choices ($i_{\min}$, $i_{\max}$). One can see the significative amelioration if both lines are included in the energy window. The 1173 keV peak can not be used alone as a clear and independent tag of ^{60}Co because of the strong presence of ^{144}Pr at 1163 keV (double escape peak of the 2185 keV line).

---

[1] $\Delta\chi^2 > 9 \iff$ reject the null hypothesis at 99.73% for one free parameter (here α). From [81].

$i_{\min}$[keV]	$i_{\max}$[keV]	χ^2 (0)	$\chi^2(0)$/NdL	α_{lim}		$R_{^{60}Co}$[Bq/Bq]	
				$\beta = 1$	β free	$\beta = 1$	β free
1200	1360	41.0961	0.483483	0.01504	0.01476	2.32×10^{-5}	2.28×10^{-5}
1200	1500	550.184	3.43865	0.01992	0.0174	3.0×10^{-5}	2.64×10^{-5}
1100	1360	116.332	0.836924	0.01276	0.01272	1.95×10^{-5}	1.94×10^{-5}
1000	1450	225.077	0.933927	0.01328	0.01308	2.02×10^{-5}	1.99×10^{-5}
1000	1400	215.789	1.00836	0.01328	0.01304	2.02×10^{-5}	1.98×10^{-5}
1000	1300	180.767	1.12979	0.01756	0.01684	2.56×10^{-5}	2.67×10^{-5}
1000	1500	750.95	2.80205	0.02088	0.01664	3.16×10^{-5}	2.52×10^{-5}

Table 7.7: *Analysis parameters and controls depending on the energy window selected and β.*

Coloured lines in table 7.7 are the most reliable energy window. A strong variation of the α_{lim} is observed when only one ^{60}Co γ line is included.

(a) $[i_{min};i_{min}]$=[1000;1300]

(b) $[i_{min};i_{min}]$=[1000;1400]
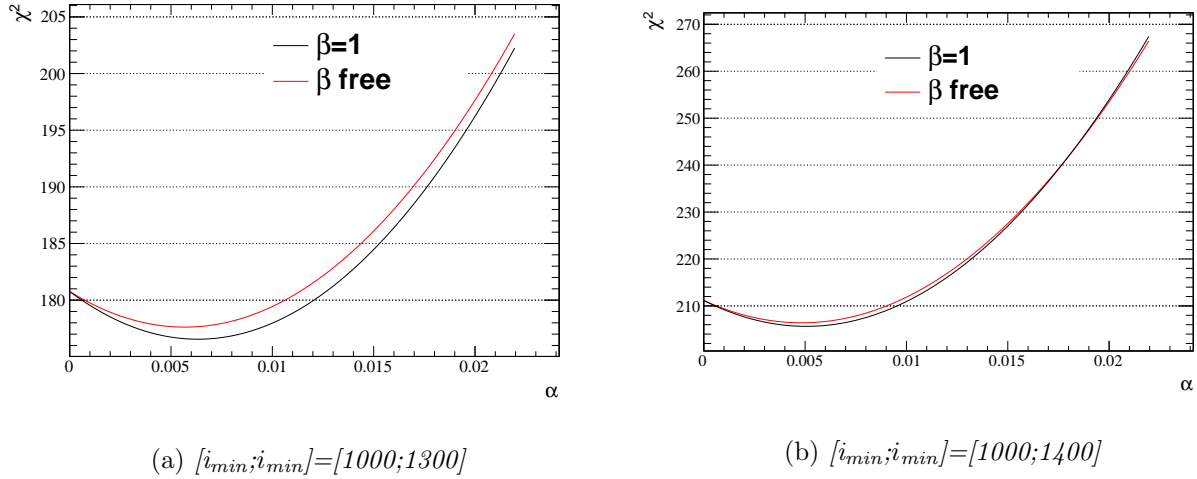
Figure 7.4: $\chi^2(\alpha)$ *evolution for ^{60}Co contamination in a ^{144}Ce depending on β model and energy window*

Scanning α values, the simulated spectrum ($\alpha MC^{ZN} + \beta MC^{144\text{Ce}}$) is normalized with respect to the data spectrum if β is free. Table 7.7 compares results with/without this free parameter. If $\beta = 1$ seems a more conservative hypothesis (α_{lim} is systematically higher) it is specific to this example. β freely varying around 1, leads to a smoother $\chi^2(\alpha)$ as illustrated in figure 7.4. β is systematically free on the global analysis.

Figure 7.4 shows the evolution of $\chi^2(\alpha)$. One can notice that the minimum of the distribution is not χ^2 (0). However, as the goal of this analysis is to discriminate the H1 hypothesis from H0, $\Delta\chi^2$ is defined as $\Delta\chi^2 = \chi^2(\alpha) - \chi^2(0)$ and not $\Delta\chi^2 = \chi^2(\alpha) - \chi^2_{\min}$.

Finally, figure 7.5 compares γ spectra before and after adding ^{60}Co contamination. On the right picture, the spectrum shows the amount of contaminant (α_{lim}) from which a contamination can be measured with 99% confidence.
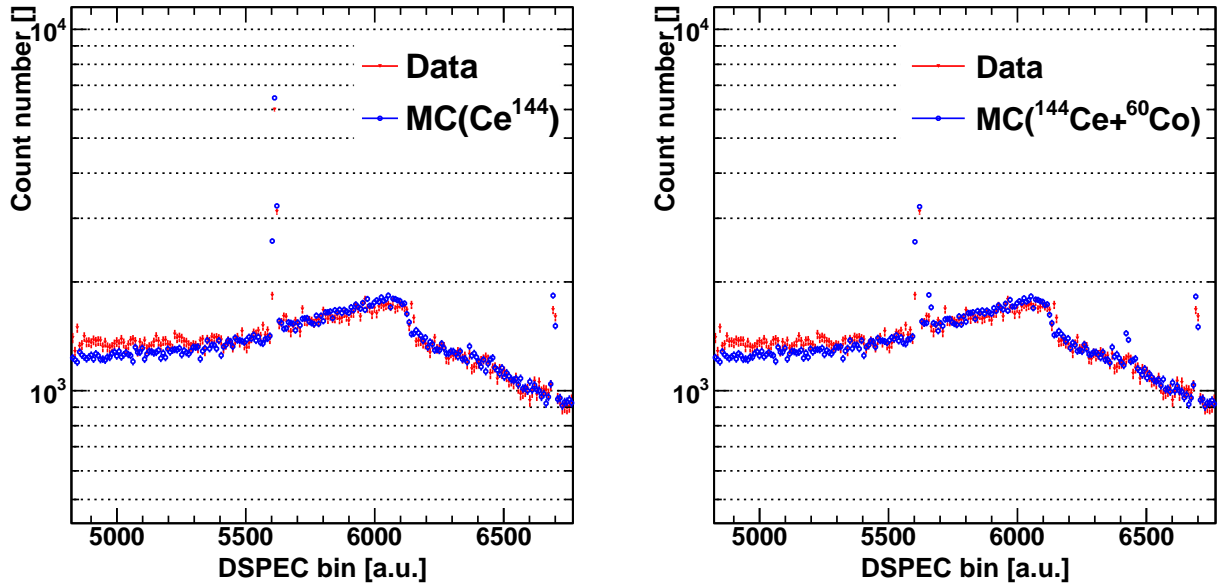
Figure 7.5: *Comparison of γ spectra with (right) and without (left) adding ^{60}Co as contaminant. On the right picture, the amount of contamination added to the ^{144}Ce background spectrum is exactly α_{lim}.*

To conclude this example, this method is highly competitive with the contractual specification. Indeed, the limit activity certified by P.A.Mayak is derived to be 8.8×10^{-4} Bq/Bq. We are able to certify an absence of contamination below 2.0×10^{-5} Bq/Bq.

7.2.5 Comparison for a measured contamination

The ^{137}Cs contamination measurement was needed for safety purpose. The contamination has been measured independently from the Monte Carlo method and can be used for comparison. ^{137}Cs is decaying to ^{137}Ba (β^-, Q_β=1.18 MeV) emitting mainly a 661.7 keV γ (85.1%).

Analytical estimation

The first method estimates ^{137}Cs contamination using analytical fit. The region of interest has been defined as [568 keV;681 keV]. The selected region must be large enough to increase statistics but must avoid intense ^{144}Ce-^{144}Pr lines (here the ^{144}Pr 696 keV line). Other peaks present in the energy window are well identified so they can be fitted, constraining the direct environment of the ^{137}Cs peak. Figure 7.6a is showing the identified spectrum before background subtraction.

The fitting function is the sum of a second order polynomial and five Gaussian distributions. Figure 7.6b shows the ^{144}Ce-^{144}Pr spectrum after background subtraction. The same fit was realised before and after background subtraction. If ^{208}Tl peak, produced by ^{220}Rn (τ=55 s) decay chain, is successfully removed after background subtraction, ^{214}Bi is still visible. Coming from ^{222}Rn (τ=3.2 d), it is an evidence that the residual ^{222}Rn rate has evolved inside the acrylic box between data and background. This might be due to trapped radon at the inner surface or a variation of

(a) *Before background subtraction,*   (b) *After background subtraction,*
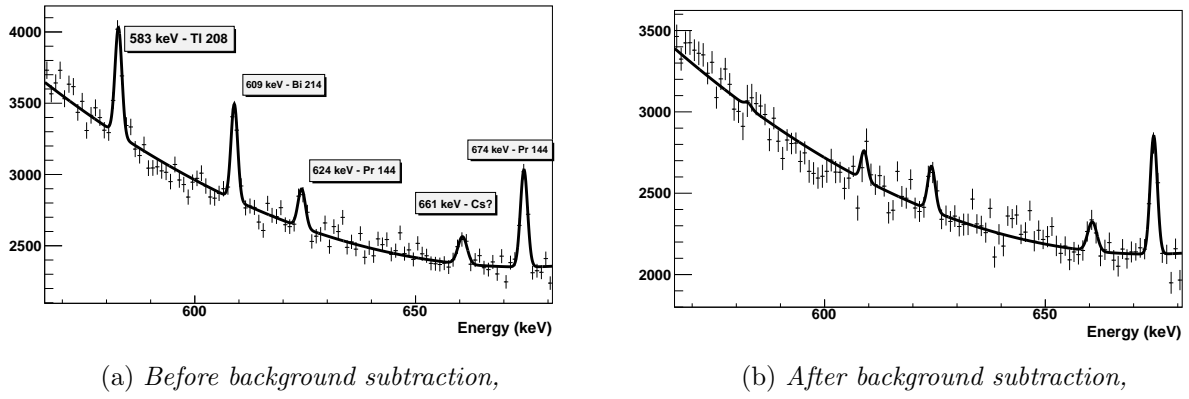
Figure 7.6: ^{144}Ce-^{144}Pr γ *spectrum in the region of interest before and after background subtraction.*

the flushing system.

In order to check the consistency of the fitted ^{137}Cs peak, its resolution and mean energy was compared with respect to neighbours true γ fit functions. Figure 7.7 shows the linearity of the energy scale and the resolution variations for the five Gaussian distribution in order to check the consistency of the ^{137}Cs fitted peak.

(a) *Comparison of the fitted peak energy scale*   (b) *Resolution of the 5 fitted peaks,*
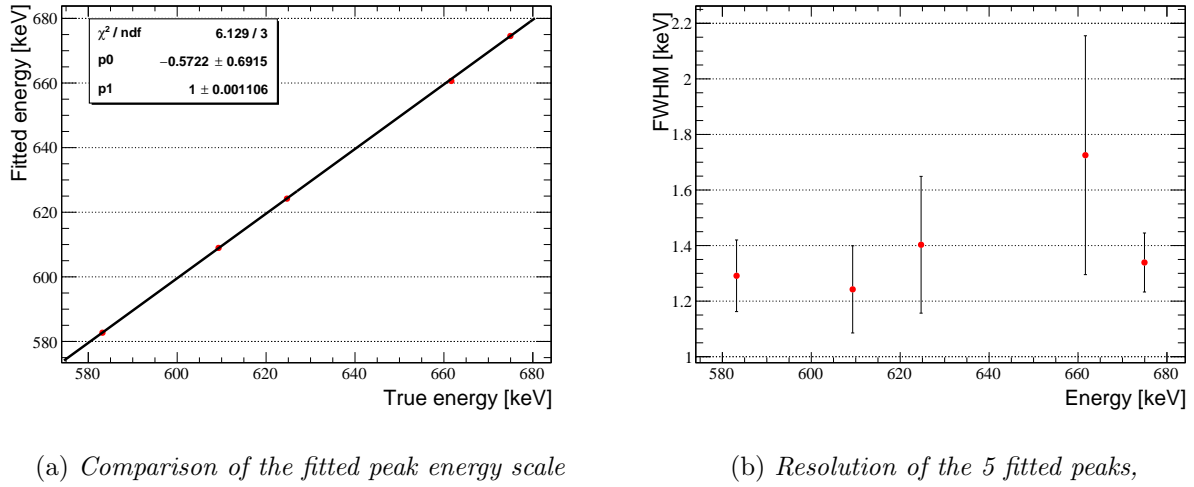
Figure 7.7: *Linearity of the energy scale and resolution.*

The measured activity is then: $A_{Cs} = 1.28 \times 10^{-5} \pm 0.27 \times 10^{-5}\ A_{Ce}$.

Monte-Carlo estimation

Using the Monte-Carlo, figure 7.8 shows a comparison between data and a simulated spectrum in which ^{137}Cs has been added. The best fit at 2σ is $A_{Cs} = 1.5 \times 10^{-5}\ A_{Ce}$, in good agreement with the analytical method. The power of the Monte Carlo method is the generalisation of this study to any potential contaminant in any energy range of the ^{144}Ce spectrum. A limit on the contamination can be derived using the Monte-Carlo from the Compton shape and not only from the full absorption peak.
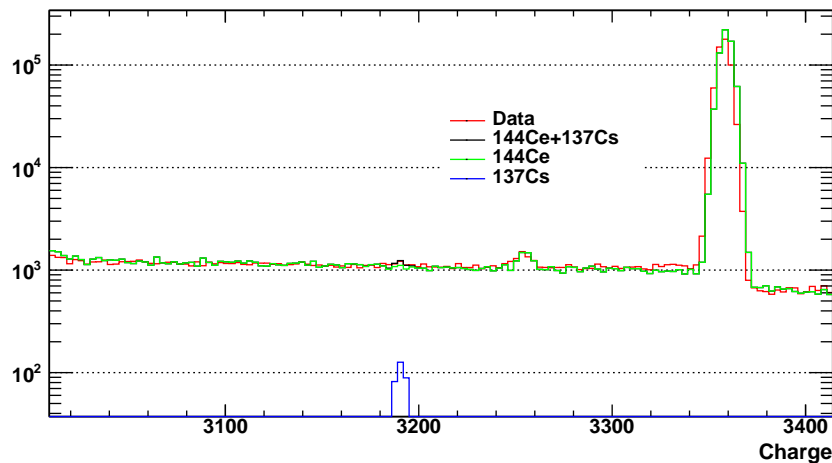
Figure 7.8: *Fitting the experimental data with $^{137}Cs + ^{144}Ce + ^{144}Pr$ simulated spectrum.*

7.2.5.1 Results

Result of the sensitivity of the HPGe to contaminants is displayed in table 7.8,7.9 and 7.10 (see annexe E for intermediate results). Limit on activity are given for any γ emitter and in yellow if a presence was measured. Value given by PA MAYAK are given for fruitful comparison.

7.3 Other spectroscopy for contaminants hunting

7.3.1 α spectroscopy

Alpha spectroscopy has been investigated in CEA, Saclay. Grid Ionization Chamber and Passivated Implemented Planar Silicon detectors can be used.

Grid Ionization Chamber Fraction of the sample is poured ($250\mu L$) and evaporated under radiant warmer. The gas circulate into an ionisation chamber. Two electrodes generate a constant electric field in which any α particle induces ionisation of the gas. Ions and electrons migrate toward cathode and anode respectively but with different time constant (collection time is $\sim 10^3$ lower for electrons than for ions). Electronic signal is preferred over ionic one to avoid distortion in charge collection. Finally, a Frisch–Grid is settled between the gas and the anode with a fix potential, acting as an electrostatic shield. Charge is not depending on interaction point inside the gas but only on the number of induced electrons, proportional to the α energy and the gas pressure. Resolution of such technique is 60 keV for an efficiency of $\sim$50%. Samples were analysed using this technique, rmeasuring a residual contamination of 7.6×10^{-6} Bq/Bq in ^{244}Cm

Passivated Implemented Planar Silicon Measurement could be done with a Passivated Implemented Planar Silicon (PIPS) under vacuum. If resolution of PIPS is about 15 keV, enabling more α discrimination, the low efficiency of this technique, around few percents, makes it not competitive for determining low level of contamination.

7.3.2 Mass spectroscopy

A powerful tool to identify elements of any solution is mass spectrometer. This techniques is complementary of the α and γ spectroscopy as it does not measure any radiations. One of the main difficulty is to precisely settle a limit on a radioactive contamination from a mass measurement. An illustration of isobaric degeneracy is given for the test sample analysed in 2015 at CEA.

The Argon itself has firstly been ionized by inductive coupling with free electrons oscillating in a 27 MHz magnetic field. A drop of the solution is first nebulized in order to transform the liquid into an aerosol. From desolvation to vaporization, the sample is traversing the spray chamber and entering the quartz torch box using a peristaltic pump. It is dried, dissociated, atomized and ionized by contact with the Argon plasma ($\sim 10^4$ K). After the plasma coupling, the sample ions are first driven into a vacuum chamber through a sampling cone (~ 1 mm hole, reducing the size of the sample without introducing bias). Secondly, they pass through a skimmer cone (~ 0.4 mm for vacuum installation purpose). To eliminate photons/neutral particles emitted by the plasma, ions are curved to an off axis tube. The ions are finally accelerated by a high voltage electrostatic field. The quadrupole selectively filters and transmits ions subject to their mass. Figure 7.9 illustrates this process. The signal is then proportional to the concentration of the element in the sample [260].
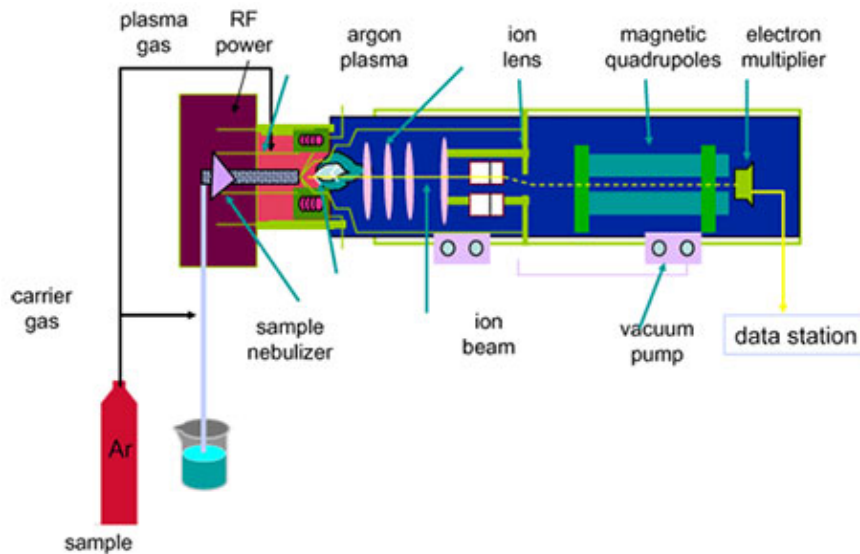
Figure 7.9: *Illustration of the ICP-MS functioning principles [261].*

The required sample volume for the analysis is 5 ml. ICP-MS detection limits for the elements without isobaric overlaps is 1 ng.L^{-1}. The solution must be diluted with a factor 10^6 for radio-protection purposes of material, meaning the effective limit on source contamination is on the order of 1 mg.L^{-1}. Using ICP-MS, the SOX collaboration must be able to measure the specific activity of ^{144}Ce over Cerium content and power separation of the chromatography columns used in Mayak which are useful informations to constrain even more potential contaminants.

7.3.3 Results

Contaminant	A_{th} [Bq/Bq]	A_{th} @10 y. [Bq/Bq]	Sensibility (Spectroscopy) [Bq/Bq]	Mayak [226] [Bq/Bq]
^{3}H	2.37×10^{-1}	976.3		
^{22}Na	5.63×10^{-4}	0.2841	5.1×10^{-5} (γ)	$6.\times10^{-5}$ (γ)
^{32}Si	1.94×10^{-2}	134.0		
^{39}Ar	6.16×10^{-3}	43.43		
^{42}Ar	5.79×10^{-3}	33.90		
^{44}Ti-^{44}Sc	2.26×10^{-3}	14.56	4.2×10^{-2} (γ)	
^{49}V	4.99×10^{-1}	1.680		
^{54}Mn	4.49×10^{-1}	0.9797	1.4×10^{-5} (γ)	$1.\times10^{-4}$ (γ)
^{55}Fe	4.49×10^{-1}	259.9		
^{57}Co	1.23×10^{-2}	0.0080		
^{60}Co	5.19×10^{-4}	1.007	1.9×10^{-5} (γ)	$6.\times10^{-5}$ (γ)
^{63}Ni	7.75×10^{-2}	523.3		
^{65}Zn	2.39×10^{-3}	0.0005		$2.\times10^{-4}$ (γ)
^{68}Ge-^{68}Ga	1.72×10^{-3}	0.0011	3.2×10^{-4} (γ)	
^{85}Kr	5.33×10^{-3}	20.21		
^{90}Sr-^{90}Y	1.19×10^{-3}	6.783		
^{91}Nb	9.74×10^{-2}	697.4		
^{93m}Nb	4.79×10^{-2}	225.4		
^{106}Ru-^{106}Rh	4.19×10^{-4}	0.0035	2.5×10^{-4} (γ)	
^{101}Rh	4.36×10^{-3}	3.863	4.5×10^{-4} (γ)	
^{102}Rh	2.66×10^{-3}	0.0001	1.1×10^{-4} (γ)	
^{102m}Rh-^{102}Ru	6.23×10^{-4}	0.7075		
^{108m}Ag	8.36×10^{-4}	5.950		
^{110m}Ag	4.71×10^{-4}	0.0001		
^{109}Cd	1.27×10^{-2}	0.3794		
^{113m}Cd	7.27×10^{-3}	32.17		
^{119m}Sn	1.61×10^{-2}	0.0206		
^{121m}Sn	4.07×10^{-2}	251.34		
^{125}Sb	2.60×10^{-3}	1.522	7.6×10^{-5} (γ)	
^{134}Cs	7.86×10^{-4}	0.1981	9.6×10^{-6} (γ)	
^{137}Cs	1.66×10^{-3}	9.547	3.9×10^{-5} ($\boxed{1.5\times10^{-5}}$)(γ)	$3.\times10^{-4}$ (γ)
^{133}Ba	3.03×10^{-3}	11.36	6.0×10^{-5} (γ)	
^{143}Pm	4.22×10^{-3}	0.0022	3.0×10^{-5} (γ)	
^{144}Pm	8.56×10^{-4}	0.0060	2.1×10^{-5} (γ)	
^{145}Pm	3.40×10^{-2}	166.0		
^{146}Pm	1.76×10^{-3}	3.641	4.8×10^{-5} (γ)	
^{147}Pm	2.18×10^{-2}	11.21		
^{145}Sm	1.52×10^{-2}	0.0642		

Table 7.8: *Results [1/3]. Highlighted figures are measured contamination and not limits. ^{137}Cs measured contamination is $\sim 2\sigma$, the limit is given for a 3σ measurement.*

Contaminant	A_{th} [Bq/Bq]	A_{th} @10 y. [Bq/Bq]	Sensibility (Spectroscopy) [Bq/Bq]	Mayak [226] [Bq/Bq]
^{151}Sm	$6.87{\times}10^{-2}$	459.9		
^{150}Eu	$8.81{\times}10^{-4}$	5.282	$2.9{\times}10^{-5}(\gamma)$	
^{152}Eu	$1.11{\times}10^{-3}$	4.794	$5.3{\times}10^{-5}(\gamma)$	$3{\times}10^{-4}\ (\gamma)$
^{154}Eu	$9.21{\times}10^{-4}$	2.975	$4.9{\times}10^{-5}\ (\gamma)$	$2{\times}10^{-4}\ (\gamma)$
^{155}Eu	$1.16{\times}10^{-2}$	19.55	$0.433(\gamma)$	
^{148}Gd	$4.24{\times}10^{-4}$	2.780		$1{\times}10^{-6}\ (\alpha)$
^{153}Gd	$9.54{\times}10^{-3}$	0.0018	$0.212(\gamma)$	
^{157}Tb	$1.70{\times}10^{-1}$	1112		
^{158}Tb	$1.50{\times}10^{-3}$	10.47	$2.1{\times}10^{-5}(\gamma)$	
^{171}Tm	$5.44{\times}10^{-2}$	10.65		
^{173}Lu	$6.11{\times}10^{-3}$	0.280	$2.1{\times}10^{-4}(\gamma)$	
^{174}Lu	$1.41{\times}10^{-2}$	12.59	$1.8{\times}10^{-4}(\gamma)$	
^{172}Hf-^{172}Lu	$6.14{\times}10^{-4}$	0.1091	$2.0{\times}10^{-5}(\gamma)$	
^{179}Ta	$4.39{\times}10^{-2}$	7.041		
^{178m}Hf	$5.51{\times}10^{-4}$	3.188	$1.6{\times}10^{-5}(\gamma)$	
^{194}Os-^{194}Ir	$1.49{\times}10^{-3}$	3.404	$5.2{\times}10^{-5}(\gamma)$	
^{192m}Ir	$8.59{\times}10^{-3}$	60.35	$9.2{\times}10^{-3}(\gamma)$	
^{193}Pt	$2.58{\times}10^{-1}$	1623		
^{195}Au	$1.11{\times}10^{-2}$	0.0001	$6.4{\times}10^{-1}(\gamma)$	
^{194}Hg-^{194}Au	$1.26{\times}10^{-3}$	8.989	$5.2{\times}10^{-5}(\gamma)$	
^{204}Tl	$5.69{\times}10^{-3}$	6.588		
^{210}Pb$\rightarrow^{206}$Pb	$2.31{\times}10^{-4}$	1.223		
^{207}Bi	$8.21{\times}10^{-4}$	4.767	$1.9{\times}10^{-5}(\gamma)$	
^{208}Po	$2.58{\times}10^{-4}$	0.1710		$1{\times}10^{-6}\ (\alpha)$
^{209}Po	$2.71{\times}10^{-4}$	1.830	$1.1{\times}10^{-3}(\gamma)$	$1{\times}10^{-6}\ (\alpha)$
^{228}Ra$\rightarrow^{208}$Pb	$4.0{\times}10^{-5}$	0.0865	$2.7{\times}10^{-5}(\gamma)$	
^{227}Ac$\rightarrow^{207}$Pb	$3.9{\times}10^{-5}$	0.2068		
^{228}Th$\rightarrow^{208}$Pb	$4.0{\times}10^{-5}$	0.0078	$1.4{\times}10^{-4}(\gamma)$	
^{232}U$\rightarrow^{208}$Pb	$3.5{\times}10^{-5}$	0.2273		$1{\times}10^{-6}\ (\alpha)$
^{235}Np	$4.44{\times}10^{-1}$	5.369		$1{\times}10^{-6}\ (\alpha)$
^{236}Pu-^{232}U	$2.30{\times}10^{-4}$	0.1470		
^{238}Pu$\rightarrow^{230}$Th	$1.29{\times}10^{-4}$	0.8620	$(2.0\pm1.6){\times}10^{-6}\ (\alpha)$	$0.5{\times}10^{-5}(\alpha)$
^{239}Pu	$2.57{\times}10^{-4}$	1.859		
^{240}Pu	$2.56{\times}10^{-4}$	1.853		
^{241}Pu-^{241}Am	$2.58{\times}10^{-1}$	1148		
^{241}Am	$2.39{\times}10^{-4}$	1.703	$(2.0\pm1.6){\times}10^{-6}\ (\alpha)$	$5{\times}10^{-6}(\alpha)$

Table 7.9: *Results [2/3]. Highlighted figures are measured contamination and not limits.*

Contaminant	A_{th} [Bq/Bq]	A_{th} @10 y. [Bq/Bq]	Sensibility (Spectroscopy) [Bq/Bq]	Mayak [226] [Bq/Bq]
^{242m}Am-^{234}U	1.08×10^{-4}	0.7450		1×10^{-6} (α)
^{243}Cm $\to^{235}$U	1.18×10^{-4}	0.6732	$(7.7\pm3.2)\times10^{-6}$ (α)/2.8×10^{-4} (γ)	$1.\times10^{-5}$(α)
^{244}Cm	2.28×10^{-4}	1.127	$(7.7\pm3.2)\times10^{-6}$ (α)	$1.\times10^{-5}$(α)
^{248}Bk-^{244}Am	2.70×10^{-4}	0.9751	1.3×10^{-5}(γ)	
^{249}Bk-^{249}Cf	4.16×10^{-2}	0.1396		
^{248}Cf	2.12×10^{-4}	0.0008		1×10^{-6} (α)
^{249}Cf	2.14×10^{-4}	1.519	6.6×10^{-5}(γ)	1×10^{-6} (α)
^{250}Cf	2.20×10^{-4}	0.9367		1×10^{-6} (α)
^{252}Cf	2.17×10^{-4}	0.1141		1×10^{-6} (α)
^{252}Es	2.60×10^{-4}	0.0088		1×10^{-6} (α)
^{254}Es-^{250}Bk	1.73×10^{-4}	0.0001	2.0×10^{-4}(γ)	1×10^{-6} (α)

Table 7.10: *Results [3/3]. Highlighted figures are measured contamination and not limits.*

7.3.4 Conclusion

Representative samples of the source should be received in September/October 2017. The number of samples is not known neither if they will all be representative of the same batch or if some will have particularities. Each of them will undergo γ, α and mass spectroscopies to constrain impurities. Depending on the numbers of sample, mixing measurement might be a good idea. New measurements could be done at regular interval with γ spectroscopy for checking any new impurities arising from the decreasing ^{144}Ce-^{144}Pr. They would be very useful for disposal issue, looking for residual after experiment.

7.4 β spectroscopy

The need of measuring precisely the ^{144}Ce and ^{144}Pr β spectrum shapes has already been discussed in section 3.3.3. This section described the experimental apparatus, calibration and simulation developed at Saclay/APC in order to realise this measurement.

7.4.1 Experimental apparatus

The detector is constituted of cylindrical plastic scintillator of 2.1 cm diameter and 4.2 cm height. Light is measured by two R6231-100 Hamamatsu PMTs facing each other. This disposition enables to use coincidence to trigger scintillation light with respect to PMT dark noise. A reflective cylindrical shell is closely surrounding the plastic. The inner surface of this cylinder is tapped with teflon film to enhance reflection and to optimize light collection. The detector is encased in a wooden rectangular box for external light insulation. Box walls are covered with plastic tarpaulin (in pink in figure 7.10) and a black sheet cover the whole installation to avoid any light penetration. Lead bricks shields the box against external backgrounds. Figure 7.10 is showing pictures of the installation.

The PMT glass is a 46 mm diameter super bialkali photocathode with a maximum 35% quantum efficiency at 320 nm. The scintillator is a Eljen EJ204 plastic scintillator chosen for its wavelength

Figure 7.10: *Photos of the experimental set-up: the rails on which PMTs are fixed, the cylindrical scintillating plastic surrounded by reflective tape and the electronic rack.*

of maximum emission at 408 nm, its light yield (1.04×10^4 photons per MeV electron) and its high light attenuation length (1.6 m). Figure 7.11 is displaying the spectral response of the PMT together with the scintillation light wavelength distribution.
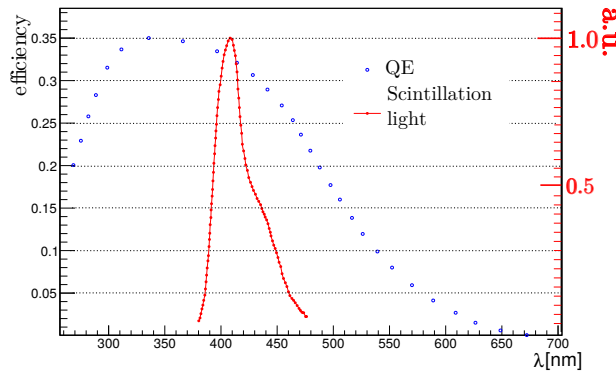
Figure 7.11: *Spectrum of the EJ200 scintillation light (red curve) and super bialkali photocathode quantum efficiency (blue dots).*

The shape and the size of the plastic was designed to fit the size of the PMT glass, to minimize light attenuation and to enable measurements without moving the set-up. At first, we cut the cylinder in two identical parts, digging a small hole in the middle of one face to settle sources, finally sticking them back together. We soon realised that this technique induced different light collection depending on the direction of the electron due to bad light transmission in the middle of the scintillator, despite the use of light coupling. Furthermore, the repeatability of the measurements was questionable as the two half scintillators would have been decoupled from the PMTs, opened, cleaned and finally closed again between each measurement. To avoid this effect, an inner cavity

is dug in which a drop of liquid source could be deposited. For now only water-based liquids were tested but adding scintillator to increase photon statistics is under investigation. The cavity is a 24 mm depth and 2 mm diameter cylinder as illustrated in figure 7.12. The cavity is thin to avoid energy loss in the liquid, especially low energy electrons which are of first importance for our measurement. Finally the PMTs are coupled with the scintillator using optical grease.
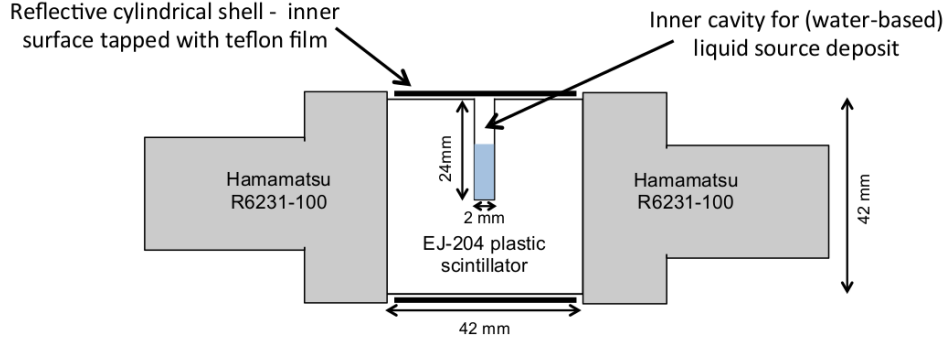

Figure 7.12: *Schematics of the final experimental set-up.*

The acquisition chain is constituted of NIM modules powered by VMN crates on a rack displayed in figure 7.10. The photomultiplier tubes are supplied using High Voltage CAEN NDT1470. The output signal is first divided in two identical channels using a linear Fan-In/Fan-out CAEN N625 (FIFO). One channel of each PMT is then directed toward a constant fraction discriminator CAEN N842. The discriminator is sending a pulse when the input signal reaches a fixed ratio of the peak intensity. A Lecroy 622 coincidence module is then responsible of the time coincidence between the two discriminator outputs. If both PMTs are fired in coincidence, they are integrated by a charge-to-digital converter (ADC) CAEN V792 using the second output of the FIFO and a delay module.

In parallel, a gate generator sends random triggers, at 1 Hz frequency, to measure the electronic pedestal. Improving the modules and the connectors, the pedestal width was reduced by a factor two during the calibration campaign. Figure 7.13 is schematically illustrating the acquisition chain.
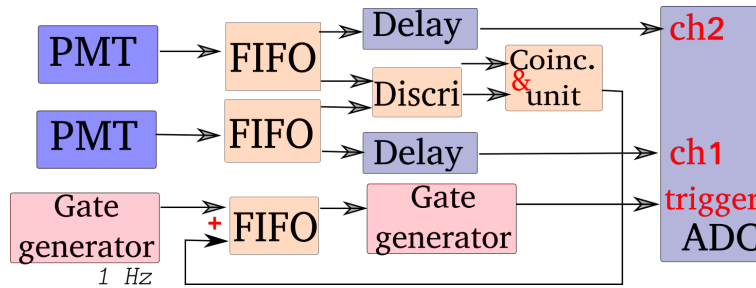

Figure 7.13: *Illustration of the acquisition chain.*

7.4.2 Photomultipliers characterisation

In order to obtain the gain of the PMTs, single photoelectron response (SPE) is measured. To do so, a blue LED pulsing at kHz frequencies, a set of filters and an external fast amplifier were

used, varying the PMT voltage. Figure 7.14 is showing the fit of the SPE and the pedestal using a phenomenological model described in [201]. The multi-PE peak is constrained to be a multiple of the SPE mean.

(a) *PMT n° 1 at 1450 V,* (b) *PMT n° 2 at 1445 V,*
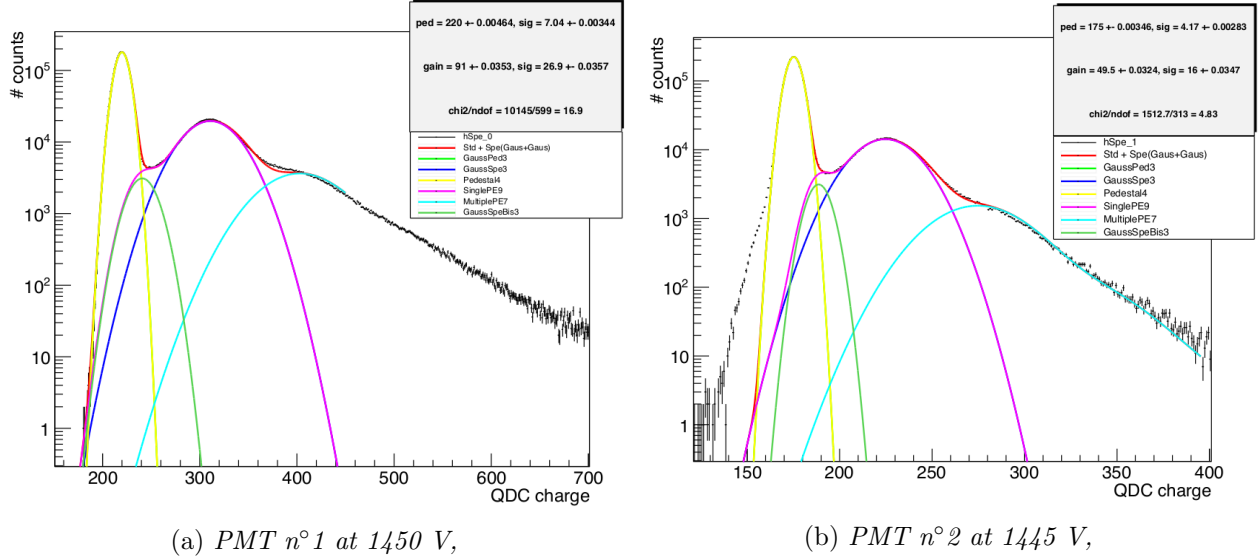
Figure 7.14: *SPE and pedestal fitted for the two PMTs.*

Result of the PMT voltage scanning, displayed in figure 7.15, is then giving the evolution of the gain with respect to high voltage power supply depending on the PMT. Three PMTs were tested and PMT_1 was dismissed due to bad performance. High voltage will then be systematically adapted to adjust the gain of one tube with respect to the other.
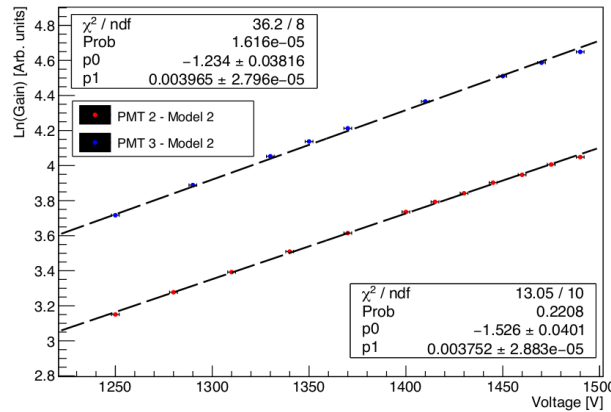
Figure 7.15: *PMT gain evolution depending on the voltage [262].*

7.4.3 Simulation

The detector was fully simulated using Geant4 libraries. The scintillating property of the plastic was implemented including the absorption length, the refractive index, and the scintillation yield. Optical photons are then propagated through the plastic toward the cathodes where the quantum

efficiency is implemented. Any photon reaching the cathode is assumed to be killed immediately and the number of received photons is considered as the number of photoelectrons. Reflective surfaces were added around the scintillator assuming a 90% of efficiency for the teflon tape. The optical contact at two edges of the cylinder between scintillator and PMT glass was assumed to be of 75%. The light yield emission in the plastic is 1.04×10^4 pe/MeV, the gain is extracted from PMT characterisation and the light collection efficiency including reflection and PMT non ideal quantum efficiency, is tuned using calibration sources. The effective light yield (LY_e) simulated is found to be around 1000 pe per deposited MeV.

7.4.4 Calibration

The LNHB provides us with β and monoenergetic electron emitter calibration sources. A drop of each source is deposited inside the scintillator well. ^{90}Sr, ^{36}Cl and ^{207}Bi were used so far. An additional campaign is being organized in autumn 2017. Table 7.11 lists the source features.

Source	Decay	E_{e^-}[keV] ($\mathcal{B}_R$ [%])	E_γ[MeV] ($\mathcal{B}_R$ [%])
^{90}Sr	β^-	Q_β= 546(100)	-
^{90}Y	β^-	Q_β=2280 (99.99),519.4 (0.01)	2186 (1.4×10^{-6})
^{36}Cl	β^-, EC	Q_β=709.5 (98.1), Q_{e^+}=120.1 (1.9)	511 (3.8)
^{207}Bi	EC	975 (7.1), 1048 (1.8), 481 (1.5)	569 (97.8), 1064 (74.5), 1770 (6.9)

Table 7.11: *Calibration sources characteristics*

As a first preliminary MC/data comparison, ^{207}Bi, ^{36}Cl and ^{90}Sr were simulated in a water solution. The comparison is shown in figure 7.16, figure 7.17 and figure 7.18. If the agreement seems relatively correct for ^{207}Bi and ^{90}Sr, it is not the case for ^{36}Cl. Theoretical spectra of each source would be an interesting input to test the database used by Geant4 and to disentangle β shape effect from detector tuning. The ^{207}Bi can be used as a tuning source for the Monte Carlo because it does not decay through β decay.
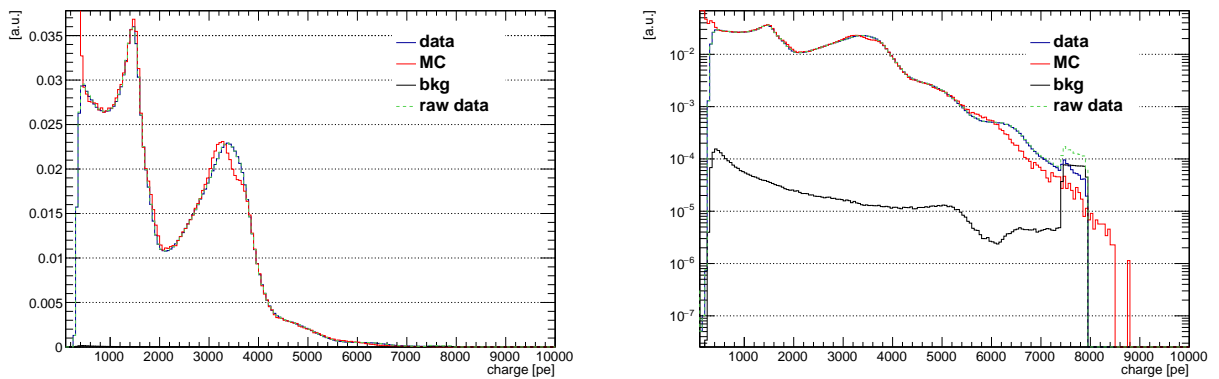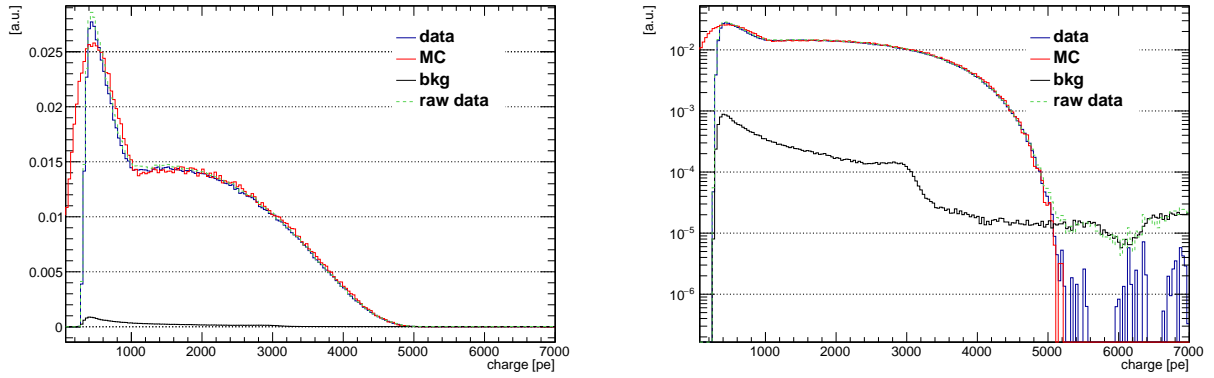

Figure 7.16: *Comparison of the simulation with data for the ^{207}Bi.*

185

Figure 7.17: *Comparison of the simulation with data for the* ^{90}Sr.
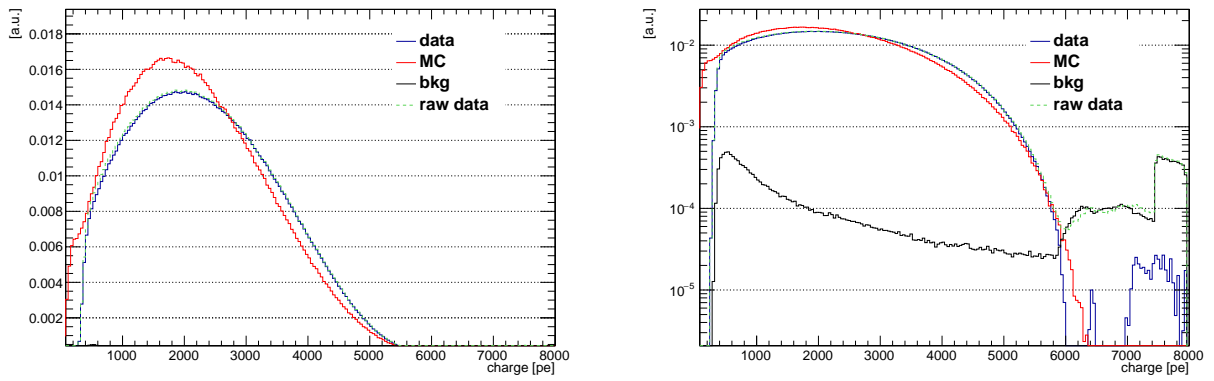
Figure 7.18: *Comparison of the simulation with data for the* ^{36}Cl.

7.4.5 ^{144}Ce/^{144}Pr separation

The β spectrum installation is located inside the Laboratoire National Henri Becquerel (LNHB), at the CEA Saclay. One of the challenge of the SOX experiment is indeed the precise knowledge of the ^{144}Pr low energy beta spectrum. In this range ^{144}Ce β spectrum lies as well.

A chemical separation of Cerium and Praseodymium can be performed in LNHB can be done using a resin column or a liquid-liquid extractor (HDEHP). While a solution of ^{144}Ce (III,IV) and ^{144}Pr (III) is poured into a resin, only cation with an oxidation number of IV are bounded to the resin. ^{144}Pr and part of ^{144}Ce are therefore washed out. Three columns are connected in line, between each of them a gamma spectrometer can measure the concentration in ^{144}Ce. If the concentration in ^{144}Ce is estimated to be sufficiently low before reaching the next column, it is not used, to fasten the separation. The resin can then be washed regularly with water based solution to extract ^{144}Pr produced by the decay of ^{144}Ce trapped in the resin. The liquid-liquid power extraction is less predictable. It might be used instead of chromatography if any chemical instability is observed with the water-based resin washer or if we want to try using scintillating liquid instead of water to pour in the β spectrometer. LNHB estimates that the separation power ^{144}Pr/^{144}Ce using resin column separation is around a factor 100. One uncertainty rises from the

ignorance of the real composition of the samples sent. In particular, all Cerium isotopes might be trapped in the resin as well as any isotope with the same oxidation number [263].

The measurement must be done quickly after the separation because of the short ^{144}Pr lifetime, hence the necessity to host the detector nearby.

Conclusion

The Borexino detector celebrated this year its 10 years anniversary of data taking. It has done an amazing work at measuring solar neutrino fluxes and spectra. The global fit analysis of phase-II recently published [264], confirmed the phase-I results. ^{7}Be rate measurement is now measured with a 2.7% precision, opening the way to dismiss solar models using neutrino signal. ^{8}B rate measurement is among the best specie to test solar metallicity models. Its strategic spectrum, covering the matter as well as the vacuum area of the MSW transition, enables its measurement to be a test for exotic oscillation models.

The analysis presented here aimed at improving the previous measurement of ^{8}B above 3 MeV in Borexino [163]. To do so, we increase the total exposure by a factor 11, enabling to reach a total uncertainty of 8%, with respect to 19% of the previous analysis. This result has been obtained by using the entire scintillating volume of Borexino above 5 MeV. Not using fiducialisation demands to master any background present in our sample as well as having a good description of the detector evolution close to its border. I participated to the selection of the data and the estimation of residual contamination after background identification as well as dead-time measurement. I worked on the external background identification and estimated as well as simulated components of the final radial fits at high energy. The external background component was identified as being high energy γ produced by n-capture. The main source of neutron is (α,n) reactions located in the glass of the PMTs. This identification as well as the emanation component at low energy were necessary to include the whole scintillator volume in the final exposure. Leak events observation however leads to cut the active volume at z higher than 2.5 m in the low energy region. This improvement of the ^{8}B will help to constrain non standard neutrino interaction as well as solar model using the MSW transition shape [196]. The observation of the CNO neutrino signal would be the last missing piece of the long solar neutrino hunt with Borexino.

Future of Borexino is now the SOX experiment, testing the sterile hypothesis by bringing a 3.7-5.5 PBq ^{144}Ce source below the detector. The SOX experiment is the only "on-going" experiment testing the light sterile hypothesis using a radioactive source. In order to map the detector response at high radius, Borexino will undergo calibration campaign in 2018. The Borexino detector has been studied for 10 years now and has shown is ability at detecting rare $\overline{\nu_e}$ flux with almost no background [172]. In parallel, samples will arrive in Saclay for characterising the ^{144}Ce source. A key of this experiment dwells on the understanding of the Cerium Antineutrino Generator. A precise description of its extraction from spent nuclear fuel has been given in the present work. The rate analysis relies on calorimetric measurement of the source activity and specific detectors are now ready to dissect representative samples sent by PA MAYAK. An HPGe detector has been calibrated and entirely simulated, showing result precise enough to constrain γ contaminant in the

source. This precise spectroscopy will also help to determine the best long term storage solution for the ^{144}Ce source. α and mass spectroscopy are also ready for a multi detector approach to derivate final measurement on the source composition. Finally, measuring the ^{144}Ce and ^{144}Pr β spectrum will be the challenge of the next months.

SOX should release results at the end of next year, in the same time than some short baseline experiments using nuclear reactor. ^{235}U $\overline{\nu_e}$ spectrum being a hot topic of discussion nowadays, it will enable a "no reactor" evaluation of very short baseline oscillation and finally adress the Reactor Antineutrino Anomaly.

Bibliography

[1] M. Sklodowska Curie. Comptes rendus de l'académie des sciences, t., 1898.

[2] Marie Curie. Conférence nobel, 1911. `http://musee.curie.fr/media/files/conference-nobel-1911_0.pdf`.

[3] E. Rutherford. Uranium radiation and the electrical conduction produced by it. *Philosophical Magazine*, 47(109), 1899.

[4] Nobel committee, editor. *Nobel lectures*, chapter Chemistry 1901-1921. Elsevier Publishing Company, 1966.

[5] P. Villard. Comptes rendus de l'académie des sciences, t., April 1900.

[6] J. Chadwich. Intensitätsverteilung im magnetischen spectrum der β-strahlen von radium b + c. *Verhandl. Dtsch. Phys. Ges.*, 16:383, 1914.

[7] N. Bohr. On the constitution of atoms and molecules. *Philosophical Magazine*, 26(151), 1913.

[8] E. Rutherford. The connexion between the β and γ ray spectra. *Philosophical Magazine S.6*, 28(165):305–319, 1914.

[9] N. Bohr, H. A. Kramers, and J. C. Slater. The quantum theory of radiation. *Philosophical Magazine*, 47:159–175, 1924.

[10] C. D. Ellis and W. A. Wooster. The continuous spectrum of β-rays. *Nature*, 119:563–567, 1927.

[11] L. Meitner and W. Orthmann. Über eine absolute bestimmung der energie der primären ß-strahlen von radium e. *Zeitschrift für Phys.*, 60:143 – 155, 1930.

[12] K. S. Krane. *Introductory Nuclear Physics*. John Wiley & Sons, 1988. Beta Decay, p.277.

[13] G. Gamow and E. Teller. Selection rules for the β-disintegration. *Phys. Rev.*, 49:895–899, Jun 1936.

[14] Carlo Giunti and Chung W. Kim. *Fundamentals of Neutrino Physics and Astrophysics*. Oxford University Press, 2007.

[15] H. Bethe and R. Peierls. The neutrino. *Nature*, 133:532–532, 1934.

[16] H. R. Crane. An attempt to observe the absorption of neutrinos. *Phys. Rev.*, 55:501–502, Mar 1939.

[17] F. Reines. The neutrino: from poltergeist to particle. Nobel lecture, 1995.

[18] F. Reines. Neutrinos to 1960 - personal recollections. *Journal de Physique*, Colloque C8, Tome 43(supplément au n°12):237–260, 1982.

[19] CERN. Ghosts in the machine, 2016. `http://cerncourier.com/cws/article/cern/65501`.

[20] Frederick Reines and Clyde Cowan. The Neutrino. *Nature*, 178(4531):446–449, 1956.

[21] T. D. Lee and C. N. Yang. Question of parity conservation in weak interactions. *Phys. Rev.*, 104:254–258, Oct 1956.

[22] R. P. Feynman and M. Gell-Mann. Theory of the fermi interaction. *Phys. Rev.*, 109:193–198, Jan 1958.

[23] M. Goldhaber, L. Grodzins, and A. W. Sunyar. Helicity of neutrinos. *Phys. Rev.*, 109:1015–1017, Feb 1958.

[24] P. M. Watkins. Discovery of the w and 2 bosons. *Contemporary Physics*, 27(4):291–324, 1986.

[25] Melvin Schwartz. Nobel laureate lecture, 1988.

[26] G. Danby, J-M. Gaillard, K. Goulianos, L. M. Lederman, N. Mistry, et al. Observation of high-energy neutrino reactions and the existence of two kinds of neutrinos. *Phys. Rev. Lett.*, 9:36–44, Jul 1962.

[27] K. Kodama, N. Ushida, C. Andreopoulos, N. Saoulidou, G. Tzanakos, et al. Observation of tau neutrino interactions. *Physics Letters B*, 504(3):218 – 224, 2001.

[28] The ALEPH, DELPHI, L3, OPAL, SLD Collaborations and the LEP Electroweak Working Group, The SLD Electroweak and Heavy Flavour Groups. Precision electroweak measurements on the z resonance. *Physics Reports*, 427(5–6):257 – 454, 2006.

[29] A. S. Eddington. *The Internal Constitution of the Stars*. Cambridge University Press, 1926.

[30] W. A. Fowler. Completion of the Proton-Proton Reaction Chain and the Possibility of Energetic Neutrino Emission by Hot Stars. *Astrophysical Journal*, 127:551, May 1958.

[31] H. A. Bethe. Energy production in stars. *Phys. Rev.*, 55:434–456, Mar 1939.

[32] John N. Bahcall, M. H. Pinsonneault, and Sarbani Basu. Solar models: Current epoch and time dependences, neutrinos, and helioseismological properties. *Astrophys. J.*, 555:990–1012, 2001. `https://arxiv.org/abs/astro-ph/0010346`.

[33] Antoine Kouchner. Lectures on neutrino physics: Experiments, 2013–2014. Master NPAC.

[34] J. N. Bahcall and M. Cribier. The standard solar model. In *Inside The Sun*. Kluwer Academic Publishers, 1990.

[35] John N. Bahcall and M. H. Pinsonneault. What do we (not) know theoretically about solar neutrino fluxes? *Phys. Rev. Lett.*, 92:121301, Mar 2004.

[36] John N. Bahcall, Aldo M. Serenelli, and Sarbani Basu. New solar opacities, abundances, helioseismology, and neutrino fluxes. *The Astrophysical Journal Letters*, 621(1):L85, 2005.

[37] M. Asplund, N. Grevesse, A. J. Sauval, and P. Scott. The Chemical Composition of the Sun. *Annual Review of Astronomy and Astrophysics*, 47:481–522, September 2009.

[38] N. Grevesse and A.J. Sauval. Standard solar composition. *Space Science Reviews*, 85(1):161–174, 1998.

[39] M. Asplund, N. Grevesse, and A. J. Sauval. The Solar Chemical Composition. In T. G. Barnes, III and F. N. Bash, editors, *Cosmic Abundances as Records of Stellar Evolution and Nucleosynthesis*, volume 336 of *Astronomical Society of the Pacific Conference Series*, page 25. September 2005.

[40] Núria Vinyoles, Aldo M. Serenelli, Francesco L. Villante, Sarbani Basu, Johannes Bergström, et al. A new generation of standard solar models. *The Astrophysical Journal*, 835(2):202, 2017.

[41] BOREXINO Collaboration, G. Bellini, J. Benziger, D. Bick, G. Bonfini, et al. Neutrinos from the primary proton-proton fusion process in the Sun. *Nature*, 512:383–386, August 2014.

[42] J. N. Bahcall. Solar models: An historical overview. *Nuclear Physics B - Proceedings Supplements*, 118:77–86, 2003.

[43] John N. Bahcall. The luminosity constraint on solar neutrino fluxes. *Phys. Rev. C*, 65:025801, Jan 2002.

[44] G. Bellini, J. Benziger, D. Bick, G. Bonfini, D. Bravo, et al. Final results of borexino phase-i on low-energy solar neutrino spectroscopy. *Phys. Rev. D*, 89:112007, 2014.

[45] Raymond Davis. Attempt to detect the antineutrinos from a nuclear reactor by the $cl^{37}(\overline{\nu}, e^-)a^{37}$ reaction. *Phys. Rev.*, 97:766–769, Feb 1955.

[46] John N. Bahcall. Solar neutrinos. i. theoretical. *Phys. Rev. Lett.*, 12:300–302, Mar 1964.

[47] Raymond Davis. Solar neutrinos. ii. experimental. *Phys. Rev. Lett.*, 12:303–305, Mar 1964.

[48] Raymond Davis, Don S. Harmer, and Kenneth C. Hoffman. Search for neutrinos from the sun. *Phys. Rev. Lett.*, 20:1205–1209, May 1968.

[49] Bruce T Cleveland, Timothy Daily, Jr. Raymond Davis, James R Distel, Kenneth Lande, et al. Measurement of the Solar Electron Neutrino Flux with the Homestake Chlorine Detector. *The Astrophysical Journal*, 496(1):505, 1998.

[50] J. N. Abdurashitov, V. N. Gavrin, V. V. Gorbachev, P. P. Gurkina, T. V. Ibragimova, et al. Measurement of the solar neutrino capture rate with gallium metal. iii. results for the 2002-2007 data-taking period. *Phys. Rev. C*, 80:015807, Jul 2009.

[51] M Altmann, M Balata, P Belli, E Bellotti, R Bernabei, et al. Complete results for five years of {GNO} solar neutrino observations. *Physics Letters B*, 616(3–4):174–190, 2005. https://arxiv.org/abs/hep-ex/0504037.

[52] M. Koshiba. Observational neutrino astrophysics. *Physics Reports*, 220(5):229 – 381, 1992.

[53] M. Koshiba. Proton decay experiment and neutrinos from supernova (Kamiokande-2). In *ESA Special Publication*, volume 283 of *ESA Special Publication*. 1988.

[54] K. Hirata, T. Kajita, M. Koshiba, M. Nakahata, Y. Oyama, et al. Observation of a neutrino burst from the supernova sn1987a. *Phys. Rev. Lett.*, 58:1490–1493, Apr 1987.

[55] K. S. Hirata, T. Kajita, T. Kifune, K. Kihara, M. Nakahata, et al. Observation of ^{8}B solar neutrinos in the kamiokande-ii detector. *Phys. Rev. Lett.*, 63:16–19, Jul 1989.

[56] Y. Fukuda, T. Hayakawa, K. Inoue, K. Ishihara, H. Ishino, et al. Solar neutrino data covering solar cycle 22. *Phys. Rev. Lett.*, 77:1683–1686, 1996.

[57] J. Hosaka, K. Ishihara, J. Kameda, Y. Koshio, A. Minamino, et al. Solar neutrino measurements in super-kamiokande-i. *Phys. Rev. D*, 73:112001, Jun 2006.

[58] J. P. Cravens, K. Abe, T. Iida, K. Ishihara, J. Kameda, et al. Solar neutrino measurements in super-kamiokande-ii. *Phys. Rev. D*, 78:032002, Aug 2008.

[59] K. Abe, Y. Hayato, T. Iida, M. Ikeda, C. Ishihara, et al. Solar neutrino results in super-kamiokande-iii. *Phys. Rev. D*, 83:052010, Mar 2011.

[60] K. Abe, Y. Haga, Y. Hayato, M. Ikeda, K. Iyogi, et al. Solar neutrino measurements in super-kamiokande-iv. *Phys. Rev. D*, 94:052010, Sep 2016.

[61] S. Fukuda, Y. Fukuda, T. Hayakawa, E. Ichihara, M. Ishitsuka, et al. The super-kamiokande detector. *Nuclear Instruments and Methods in Physics Research Section A: Accelerators, Spectrometers, Detectors and Associated Equipment*, 501(2–3):418 – 462, 2003.

[62] Y. Fukuda, T. Hayakawa, E. Ichihara, K. Inoue, K. Ishihara, et al. Measurements of the solar neutrino flux from super-kamiokande's first 300 days. *Phys. Rev. Lett.*, 81:1158–1162, Aug 1998.

[63] B. Aharmim, S. N. Ahmed, A. E. Anthony, N. Barros, E. W. Beier, et al. Combined analysis of all three phases of solar neutrino data from the sudbury neutrino observatory. *Phys. Rev. C*, 88:025501, Aug 2013.

[64] J Boger, R.L Hahn, J.K Rowley, A.L Carter, B Hollebone, et al. The sudbury neutrino observatory. *Nuclear Instruments and Methods in Physics Research Section A: Accelerators, Spectrometers, Detectors and Associated Equipment*, 449(1–2):172 – 207, 2000.

[65] Q. R. Ahmad, R. C. Allen, T. C. Andersen, J. D.Anglin, J. C. Barton, et al. Direct evidence for neutrino flavor transformation from neutral-current interactions in the sudbury neutrino observatory. *Phys. Rev. Lett.*, 89:011301, Jun 2002.

[66] S. N. Ahmed, others, A. E. Anthony, E. W. Beier, A. Bellerive, et al. Measurement of the total active ^{8}B solar neutrino flux at the sudbury neutrino observatory with enhanced neutral current sensitivity. *Phys. Rev. Lett.*, 92:181301, 2004.

[67] Q. R. Ahmad, R. C. Allen, T. C. Andersen, J. D. Anglin, G. Bühler, et al. Measurement of the rate of $\nu_e + d \rightarrow p + p + e^-$ interactions produced by ^8b solar neutrinos at the sudbury neutrino observatory. *Phys. Rev. Lett.*, 87:071301, Jul 2001.

[68] J N Bahcall. Solar models and solar neutrinos. *Physica Scripta*, 2005(T121):46, 2005.

[69] Takaaki KAJITA. Atmospheric neutrinos and discovery of neutrino oscillations. *Proceedings of the Japan Academy, Series B*, 86(4):303–321, 2010.

[70] C.V. Achar, M.G.K. Menon, V.S. Narasimham, P.V.Ramana Murthy, B.V. Sreekantan, et al. Detection of muons produced by cosmic ray neutrinos deep underground. *Physics Letters*, 18(2):196 – 199, 1965.

[71] F. Reines. Iv. high energy neutrinos underground: Status of the case-wits-irvine experiment and future prospect. *Proceedings of the Royal Society of London A: Mathematical, Physical and Engineering Sciences*, 301(1465):125–135, 1967.

[72] K.S. Hirata, T. Kajita, M. Koshiba, M. Nakahata, S. Ohara, et al. Experimental study of the atmospheric neutrino flux. *Physics Letters B*, 205(2):416 – 420, 1988.

[73] D. Casper, R. Becker-Szendy, C. B. Bratton, D. R. Cady, R. Claus, et al. Measurement of atmospheric neutrino composition with the imb-3 detector. *Phys. Rev. Lett.*, 66:2561–2564, May 1991.

[74] Ch. Berger, M. Fröhlich, H. Mönch, R. Nisius, F. Raupach, et al. Study of atmospheric neutrino interactions with the fréjus detector. *Physics Letters B*, 227(3):489 – 494, 1989.

[75] M. Aglietta, G. Badino, G. Bologna, C. Castagnoli, A. Castellina, et al. Experimental study of upward stopping muons in nusex. *EPL (Europhysics Letters)*, 15(5):559, 1991.

[76] Makoto Kobayashi and Toshihide Maskawa. Cp-violation in the renormalizable theory of weak interaction. *Progress of Theoretical Physics*, 49(2):652, 1973.

[77] Y. Fukuda, T. Hayakawa, K. Inoue, T. Ishida, S. Joukou, et al. Atmospheric vve ratio in the multi-gev energy range. *Physics Letters B*, 335(2):237 – 245, 1994.

[78] Y. Fukuda, T. Hayakawa, E. Ichihara, K. Inoue, K. Ishihara, et al. Evidence for oscillation of atmospheric neutrinos. *Phys. Rev. Lett.*, 81:1562–1567, Aug 1998.

[79] Nobel Committee. The nobel prize in physics 2015 - advanced information. *Nobel Media AB 2014*, 2014. `http://www.nobelprize.org/nobel_prizes/physics/laureates/2015/advanced.html`.

[80] M. H. Ahn, E. Aliu, S. Andringa, S. Aoki, Y. Aoyama, et al. Measurement of neutrino oscillation by the k2k experiment. *Phys. Rev. D*, 74:072003, Oct 2006.

[81] C. Patrignani and Particle Data Group. Review of particle physics. *Chinese Physics C*, 40(10):100001, 2016.

[82] P. Adamson, I. Anghel, A. Aurisano, G. Barr, M. Bishai, et al. Combined analysis of ν_μ disappearance and $\nu_\mu \rightarrow \nu_e$ appearance in minos using accelerator and atmospheric neutrinos. *Phys. Rev. Lett.*, 112:191801, 2014.

[83] M. Apollonio, A. Baldini, C. Bemporad, E. Caffau, F. Cei, et al. Search for neutrino oscillations on a long base-line at the CHOOZ nuclear power station. *The European Physical Journal C - Particles and Fields*, 27(3):331–374, 2003.

[84] Y. Abe, C. Aberle, T. Akiri, J. C. dos Anjos, F. Ardellier, et al. Indication of Reactor $\overline{\nu}_e$ Disappearance in the Double Chooz Experiment. *Phys. Rev. Lett.*, 108:131801, Mar 2012.

[85] F. P. An, J. Z. Bai, A. B. Balantekin, H. R. Band, D. Beavis, et al. Observation of Electron-Antineutrino Disappearance at Daya Bay. *Phys. Rev. Lett.*, 108:171803, 2012.

[86] J. K. Ahn, S. Chebotaryov, J. H. Choi, S. Choi, W. Choi, et al. Observation of Reactor Electron Antineutrinos Disappearance in the RENO Experiment. *Phys. Rev. Lett.*, 108:191802, May 2012.

[87] Y. Abe, C. Aberle, T. Akiri, J. C. dos Anjos, F. Ardellier, et al. Indication of reactor $\overline{\nu}_e$ disappearance in the double chooz experiment. *Phys. Rev. Lett.*, 108:131801, 2012.

[88] F. P. An, A. B. Balantekin, H. R. Band, M. Bishai, S. Blyth, et al. Improved measurement of the reactor antineutrino flux and spectrum at Daya Bay. *Chinese Physics C*, 41(1):013002, 2017.

[89] David Colling. Advanced particle physics, 2012/2013. Lecture given at Imperial College of London.

[90] David Griffiths. *Introduction to Elementary Particles*. Wiley-VCH, second edition, 2008.

[91] C. S. Wu, E. Ambler, R. W. Hayward, D. D. Hoppes, and R. P. Hudson. Experimental test of parity conservation in beta decay. *Phys. Rev.*, 105:1413–1415, Feb 1957.

[92] S. Lavignac. Physique des neutrinos. *Ecole de Gif 2016: La physique souterraine*, 2016.

[93] D.I. Scully. *Neutrino Induced Coherent Pion Production*. Ph.D. thesis, University of Warwick (UK), 2013. `http://danielscully.co.uk/thesis/index.html`.

[94] COHERENT Collaboration. The coherent experiment at the spallation neutron source. *ArXiv*, 2015. `https://arxiv.org/abs/1509.08702v2`.

[95] Joseph A. Formaggio, E. Figueroa-Feliciano, and A. J. Anderson. Sterile neutrinos, coherent scattering, and oscillometry measurements with low-temperature bolometers. *Phys. Rev. D*, 85:013009, 2012.

[96] D. Akimov, J. B. Albert, P. An, C. Awe, P. S. Barbeau, et al. Observation of coherent elastic neutrino-nucleus scattering. *Science*, 2017.

[97] The Ultimate Neutrino group. `http://cupp.oulu.fi/neutrino/nd-cross.html`.

[98] M. Fukugita and T. Yanagida. *Physics of Neutrinos and Applications to Astrophysics*. Springer, 2003.

[99] F. Englert and R. Brout. Broken symmetry and the mass of gauge vector mesons. *Physical Review Letters*, 13(13):321–323, 1964.

[100] P.W. Higgs. Broken symmetries, massless particles and gauge fields. *Physics Letters*, 12(2):132–133, 1964.

[101] G. Aad, T. Abajyan, B. Abbott, J. Abdallah, S. Abdel Khalek, et al. Observation of a new particle in the search for the standard model higgs boson with the {ATLAS} detector at the {LHC}. *Physics Letters B*, 716(1):1 – 29, 2012.

[102] S. Chatrchyan, V. Khachatryan, A.M. Sirunyan, A. Tumasyan, W. Adam, et al. Observation of a new boson at a mass of 125 gev with the {CMS} experiment at the {LHC}. *Physics Letters B*, 716(1):30 – 61, 2012.

[103] Ettore Majorana. Teoria simmetrica dell'elettrone e del positrone. *Il Nuovo Cimento (1924-1942)*, 14(4):171, 1937.

[104] Ivan Esteban, M. C. Gonzalez-Garcia, Michele Maltoni, Ivan Martinez-Soler, and Thomas Schwetz. Updated fit to three neutrino mixing: exploring the accelerator-reactor complementarity. *Journal of High Energy Physics*, 2017(1):87, 2017.

[105] V. N. Aseev, A. I. Belesev, A. I. Berlev, E. V. Geraskin, A. A. Golubev, et al. Upper limit on the electron antineutrino mass from the troitsk experiment. *Phys. Rev. D*, 84:112003, 2011.

[106] C. Kraus, B. Bornschein, L. Bornschein, J. Bonn, B. Flatt, et al. Final results from phase ii of the mainz neutrino mass searchin tritium β decay. *The European Physical Journal C - Particles and Fields*, 40(4):447–468, 2005.

[107] C. Weinheimer. Katrin, a next generation tritium β decay experiment in search for the absolute neutrino mass scale. *Progress in Particle and Nuclear Physics*, 48(1):141 – 150, 2002.

[108] Project8 Collaboration, Ali Ashtari Esfahani, David M Asner, Sebastian Böser, Raphael Cervantes, et al. Determining the neutrino mass with cyclotron radiation emission spectroscopy—project 8. *Journal of Physics G: Nuclear and Particle Physics*, 44(5):054004, 2017.

[109] Project8 Collaboration, D. M. Asner, R. F. Bradley, L. de Viveiros, P. J. Doe, et al. Single-electron detection and spectroscopy via relativistic cyclotron radiation. *Phys. Rev. Lett.*, 114, 2015.

[110] Planck Collaboration, Ade, P. A. R., Aghanim, N., Arnaud, M., Ashdown, M., et al. Planck 2015 results - xiii. cosmological parameters. *A&A*, 594:A13, 2016.

[111] Nathalie Palanque-Delabrouille, Christophe Yèche, Julien Baur, Christophe Magneville, Graziano Rossi, et al. Neutrino masses and cosmology with lyman-alpha forest power spectrum. *Journal of Cosmology and Astroparticle Physics*, 2015(11):011, 2015.

[112] L. Wolfenstein. Neutrino oscillations in matter. *Phys. Rev. D*, 17:2369–2374, 1978.

[113] K. Eguchi, S. Enomoto, K. Furuno, J. Goldman, H. Hanada, et al. First results from kamland: Evidence for reactor antineutrino disappearance. *Phys. Rev. Lett.*, 90:021802, 2003.

[114] John N. Bahcall and Carlos Peña-Garay. A road map to solar neutrino fluxes, neutrino oscillation parameters, and tests for new physics. *Journal of High Energy Physics*, 2003(11):004, 2003.

[115] G. Bellini, J. Benziger, D. Bick, S. Bonetti, G. Bonfini, et al. First evidence of *pep* solar neutrinos by direct detection in borexino. *Phys. Rev. Lett.*, 108:051302, Feb 2012.

[116] Gallex Collaboration, W Hampel, G Heusser, J Kiko, T Kirsten, et al. Final results of the 51cr neutrino source experiments in {GALLEX}. *Physics Letters B*, 420(1–2):114 – 126, 1998.

[117] SAGE Collaboration, J. N. Abdurashitov, V. N. Gavrin, S. V. Girin, V. V. Gorbachev, et al. Measurement of the response of a ga solar neutrino experiment to neutrinos from a ^{37}Ar source. *Phys. Rev. C*, 73:045805, 2006.

[118] John N. Bahcall. Gallium solar neutrino experiments: Absorption cross sections, neutrino spectra, and predicted event rates. *Phys. Rev. C*, 56:3391–3409, 1997.

[119] Gallex Collaboration, F. Kaether, W. Hampel, G. Heusser, J. Kiko, et al. Reanalysis of the gallex solar neutrino flux and source experiments. *Physics Letters B*, 685(1):47 – 54, 2010.

[120] C Athanassopoulos, L.B Auerbach, D Bauer, R.D Bolton, R.L Burman, et al. The liquid scintillator neutrino detector and lampf neutrino source. *Nuclear Instruments and Methods in Physics Research Section A: Accelerators, Spectrometers, Detectors and Associated Equipment*, 388(1):149 – 172, 1997.

[121] C. Athanassopoulos, L. B. Auerbach, D. A. Bauer, R. D. Bolton, B. Boyd, et al. Candidate events in a search for $\overline{\nu}_{\mu} \rightarrow \overline{\nu}_{e}$ oscillations. *Phys. Rev. Lett.*, 75:2650–2653, 1995.

[122] R. Adhikari, M. Agostini, N. Anh Ky, T. Araki, M. Archidiacono, et al. A white paper on kev sterile neutrino dark matter. *Journal of Cosmology and Astroparticle Physics*, 2017(01):025, 2017.

[123] A. A. Aguilar-Arevalo, B. C. Brown, L. Bugel, G. Cheng, E. D. Church, et al. Improved search for $\overline{\nu}_{\mu} \rightarrow \overline{\nu}_{e}$ oscillations in the miniboone experiment. *Phys. Rev. Lett.*, 110:161801, 2013.

[124] Th. A. Mueller, D. Lhuillier, M. Fallot, A. Letourneau, S. Cormon, et al. Improved predictions of reactor antineutrino spectra. *Phys. Rev. C*, 83:054615, 2011.

[125] K. Schreckenbach, G. Colvin, W. Gelletly, and F. Von Feilitzsch. Determination of the antineutrino spectrum from ^{235}U thermal neutron fission products up to 9.5 MeV. *Physics Letters B*, 160:325–330, 1985.

[126] A. A. Hahn, K. Schreckenbach, W. Gelletly, F. von Feilitzsch, G. Colvin, et al. Antineutrino spectra from ^{241}Pu and ^{239}Pu thermal neutron fission products. *Physics Letters B*, 218:365–368, 1989.

[127] G. Mention, M. Fechner, Th. Lasserre, Th. A. Mueller, D. Lhuillier, et al. Reactor antineutrino anomaly. *Phys. Rev. D*, 83:073006, 2011.

[128] Patrick Huber. Determination of antineutrino spectra from nuclear reactors. *Phys. Rev. C*, 84:024617, Aug 2011.

[129] F. P. An, A. B. Balantekin, H. R. Band, M. Bishai, S. Blyth, et al. Evolution of the Reactor Antineutrino Flux and Spectrum at Daya Bay. *ArXiv e-prints*, 2017.

[130] Victor Hélaine. Sterile neutrino search at the ILL nuclear reactor: the STEREO experiment. In *Prospects in Neutrino Physics (NuPhys2015) London, UK, December 16-18, 2015*. 2016.

[131] A. P. Serebrov et al. Neutrino-4 experiment on search for sterile neutrino with multi-section model of detector, 2016. Https://arxiv.org/pdf/1605.05909.pdf.

[132] Yamiel Abreu. Solid: An innovative anti-neutrino detector for searching oscillations at the sck-cen br2 reactor. *Nuclear Instruments and Methods in Physics Research Section A: Accelerators, Spectrometers, Detectors and Associated Equipment*, 845:467 – 470, 2017. Proceedings of the Vienna Conference on Instrumentation 2016.

[133] J. Ashenfelter, A. B. Balantekin, H. R. Band, G. Barclay, C. D. Bass, et al. The prospect physics program. *Journal of Physics G: Nuclear and Particle Physics*, 43(11):113001, 2016.

[134] Y. J. Ko, B. R. Kim, J. Y. Kim, B. Y. Han, C. H. Jang, et al. Sterile neutrino search at the neos experiment. *Phys. Rev. Lett.*, 118:121802, 2017.

[135] Y. Abe, S. Appel, T. Abrahão, H. Almazan, C. Alt, et al. Measurement of θ_{13} in double chooz using neutron captures on hydrogen with novel background rejection techniques. *Journal of High Energy Physics*, 2016(1):163, Jan 2016.

[136] J. H. Choi, W. Q. Choi, Y. Choi, H. I. Jang, J. S. Jang, et al. Observation of energy and baseline dependent reactor antineutrino disappearance in the reno experiment. *Phys. Rev. Lett.*, 116:211801, May 2016.

[137] Mikhail Danilov for the DANSS Collaboration. Search for sterile neutrinos at the danss experiment, 2017. Talk given at the EPS-HEP Conference, Venice.

[138] I. Alekseev, V. Belov, V. Brudanin, M. Danilov, V. Egorov, et al. Danss: Detector of the reactor antineutrino based on solid scintillator, 2016. `https://arxiv.org/pdf/1606.02896.pdf`.

[139] Vladislav Barinov, Vladimir Gavrin, Dmitry Gorbunov, and Tatiana Ibragimova. Best sensitivity to o(1) ev sterile neutrino. *Phys. Rev. D*, 93:073002, Apr 2016.

[140] Marc Korzeczek. ev & kev sterile neutrino studies with katrin, 2016. *Master thesis*, `https://www.katrin.kit.edu/publikationen/MKorz-MA-eV-keV%20sterile%20Neutrinos.pdf`.

[141] G Alimonti, C Arpesella, H Back, M Balata, T Beau, et al. Science and technology of borexino: a real-time detector for low energy solar neutrinos. *Astroparticle Physics*, 16(3):205 – 234, 2002.

[142] Olivier Dadoun. *Mesure des neutrinos de réacteurs nucléaires dans l'expérience Borexino*. Ph.D. thesis, Université Paris-Diderot, 2003.

[143] G. Alimonti, C. Arpesella, H. Back, M. Balata, D. Bartolomei, et al. The borexino detector at the laboratori nazionali del gran sasso. *Nuclear Instruments and Methods in Physics Research Section A: Accelerators, Spectrometers, Detectors and Associated Equipment*, 600(3):568 – 593, 2009.

[144] G Bellini, J Benziger, D Bick, S Bonetti, M Buizza Avanzini, et al. Muon and cosmogenic neutron detection in borexino. *Journal of Instrumentation*, 6(05):P05005, 2011.

[145] Glenn F. Knoll. *Radiation Detection and Measurement*. John Wiley and Sons, third edition, 1999. Scintillator: p.219-227, HPGe: p.417 & 449-453, Cerenkov: p.712-713.

[146] R. Saldanha. Precision Measurement of the ^{7}Be Solar Neutrino Interaction Rate in Borexino. *PhD-thesis*, page 92, 2012.

[147] Kevin B. McCarty. *The Borexino Nylon Film and the Third Counting Test Facility*. Ph.D. thesis, Princeton University, 2006.

[148] D. Franco. *The Borexino Experiment: Test of the Purification Systems and Data Analysis in the Counting Test Facility*. Ph.D. thesis, Universita' degli studi di Milano, 2005. P. 100.

[149] C. Arpesella et al. Measurements of extremely low radioactivity levels in *BOREXINO*. *Astroparticle Physics*, 18:1 – 25, 2002.

[150] H Back, G Bellini, J Benziger, D Bick, G Bonfini, et al. Borexino calibrations: hardware, methods, and results. *Journal of Instrumentation*, 7(10):P10018, 2012.

[151] IAEA, Conference on Nuclear Electronics V. II. *A new linear method of discrimination between elementary particles in scintillation counters*, 1962. `http://www.iaea.org/inis/collection/NCLCollectionStore/_Public/43/116/43116625.pdf?r=1`.

[152] D. Manuzio. *Towards the detection of subMeV solar neutrinos in Borexino: data reconstruction and analysis tools*. Ph.D. thesis, Universitá degli studi di Genova, 2004. P. 79.

[153] K.B. McCarty. *TThe Borexino Nylon Film and the Third Counting Test Facility*. Ph.D. thesis, Princeton University, 2006. P. 213.

[154] Steven E. Hardy. *Measuring the ^{7}Be Neutrino Flux From the Sun: Calibration of the Borexino Solar Neutrino Detector*. Ph.D. thesis, Virginia Polytechnic Institute and State University, 2010.

[155] J.N. Bahcall. *Neutrino Astrophysics*. Cambridge University Press, 1989.

[156] A.C. Re. Solar-ν: Expected interaction rates and survival probabilities in borexino. Technical report, INFN, Milano, 2017.

[157] A.C. Re. *The Borexino impact in the global analysis of neutrino data*. Ph.D. thesis, Universita' degli studi di Milano, 2012.

[158] M.B. Chadwick, M. Herman, P. Obložinský, M.E. Dunn, Y. Danon, et al. ENDF/B-VII.1 nuclear data for science and technology: Cross sections, covariances, fission product yields and decay data. *Nuclear Data Sheets*, 112(12):2887–2996, 2011.

[159] S. Abe, S. Enomoto, K. Furuno, Y. Gando, H. Ikeda, et al. Production of radioactive isotopes through cosmic muon spallation in kamland. *Phys. Rev. C*, 81:025807, 2010.

[160] J. Quirin Meindl. *Reconstruction and Measurement of Cosmogenic Signals in the Neutrino Experiment Borexino*. Ph.D. thesis, Technische Universität München, 2013.

[161] D.-M. Mei and A. Hime. Muon-induced background study for underground laboratories. *Phys. Rev. D*, 73:053004, 2006.

[162] G. Bellini, J. Benziger, D. Bick, S. Bonetti, G. Bonfini, et al. Precision measurement of the ^{7}Be solar neutrino interaction rate in borexino. *Phys. Rev. Lett.*, 107:141302, 2011.

[163] G. Bellini et al. Measurement of the solar ^{8}B neutrino rate with a liquid scintillator target and 3 MeV energy threshold in the Borexino detector. *Phys. Rev.*, D82:033006, 2010.

[164] D. Franco, G. Consolati, and D. Trezzi. Positronium signature in organic liquid scintillators for neutrino experiments. *Phys. Rev. C*, 83:015504, 2011.

[165] S. Gariazzo, C. Giunti, M. Laveder, and Y. F. Li. Updated Global 3+1 Analysis of Short-BaseLine Neutrino Oscillations. *ArXiv e-prints*, mar 2017.

[166] G. Bellini, D. Bick, G. Bonfini, D. Bravo, B. Caccianiga, et al. Sox: Short distance neutrino oscillations with borexino. *Journal of High Energy Physics*, 2013(8):38, Aug 2013.

[167] A. Gando, Y. Gando, S. Hayashida, H. Ikeda, K. Inoue, et al. CeLAND: search for a 4th light neutrino state with a 3 PBq 144Ce-144Pr electron antineutrino generator in KamLAND. *ArXiv e-prints*, 2013.

[168] M Cribier, L Gosset, P Lamare, J.C Languillat, P Perrin, et al. Production of a 62 pbq 51cr low energy neutrino source for gallex. *Nuclear Instruments and Methods in Physics Research Section A: Accelerators, Spectrometers, Detectors and Associated Equipment*, 378(1):233 – 250, 1996.

[169] Michel Cribier, Maximilien Fechner, Thierry Lasserre, Alain Letourneau, David Lhuillier, et al. Proposed Search for a Fourth Neutrino with a PBq Antineutrino Source. *Phys. Rev. Lett.*, 107:201801, 2011.

[170] W.C. Haxton. ^{37}Ar as a calibration soure for solar neutrino detectors. *Physical Review C*, 38, 1988.

[171] David Bravo Berguño. *Precision Background Stability And Response Calibration in Borexino*. Ph.D. thesis, Virginia Polytechnic Institute, 2016.

[172] M. Agostini, S. Appel, G. Bellini, J. Benziger, D. Bick, et al. Spectroscopy of geoneutrinos from 2056 days of borexino data. *Phys. Rev. D*, 92:031101, 2015.

[173] J. Gaffiot, T. Lasserre, G. Mention, M. Vivier, M. Cribier, et al. Experimental parameters for a Cerium 144 based intense electron antineutrino generator experiment at very short baselines. *Physical Review D - Particles, Fields, Gravitation and Cosmology*, 91(7):1–21, 2015.

[174] Matthieu Vivier. Beta spectrometry sensitivity to the shape of the ^{144}Ce-^{144}Pr spectrum. Borexino Collaboration meeting, July 2015.

[175] Mathieu Durero. Beta spectrum modeling for the celand experiment antineutrino source. Technical report, KTH, School of Engineering Sciences (SCI), Physics, 2013. `http://www.diva-portal.org/smash/get/diva2:657172/FULLTEXT01.pdf`.

[176] H. Behrens and J. Jänecke. *Numerical Tables for Beta-Decay and Electron Capture*. Springer-Verlag Berlin Heidelberg, 1969.

[177] G.K Schenter and P. Vogel. A simple approximation of the fermi function in nuclear beta decay. *Nuclear Science and engineering*, 83:393–395, 1983.

[178] Konrad Altenmüller, Matteo Agostini, Birgit Neumair, and Stefan Schönert. ^{144}Ce-^{144}Pr spectral measurements and impact on sox. Technical report, Technische Universität München, 2015. SOX db 72-v1.

[179] Birgit Neumair. Updated sensitivity plots, June 2016. Borexino General Meeting - hosted by LNGS.

[180] Konrad Altenmüller and Lea DiNoto. Analysis of the power measurements with the Munich-Genoa Calorimeter, February 2016. Borexino General Meeting.

[181] L. Papp, M. Agostini, K. Altenmüller, S. Appel, A. Caminata, et al. A high precision calorimeter for the sox experiment. *Nuclear Instruments and Methods in Physics Research Section A: Accelerators, Spectrometers, Detectors and Associated Equipment*, 824:699 – 700, 2016.

[182] M. Agostini, K. Altenmuller, S. Appel, V. Atroshchenko, Z. Bagdasarian, et al. The Monte Carlo simulation of the Borexino detector. *ArXiv e-prints*, 2017.

[183] G. Bellini et al. Cosmic-muon flux and annual modulation in Borexino at 3800 m water-equivalent depth. *Journal of Cosmology and Astroparticle Physics*, 05:015, 2012.

[184] G. Bellini, J. Benziger, D. Bick, G. Bonfini, D. Bravo, et al. Cosmogenic backgrounds in borexino at 3800 m water-equivalent depth. *Journal of Cosmology and Astroparticle Physics*, 2013(08):049, 2013.

[185] J. Kopecky, J.C Sublet, J.A. Simpson, R.A. Forrest, and D. Nierop. *Atlas of Neutron Capture Cross Sections*. International Nuclear Data Committee, International Atomic Energy Agency, 1997. `http://www.iaea.org/inis/collection/NCLCollectionStore/_Public/28/060/28060364.pdf`.

[186] H. Wulandari, J. Jochum, W. Rau, and F. von Feilitzsch. Neutron flux at the gran sasso underground laboratory revisited. *Astroparticle Physics*, 22:313 – 322, 2004.

[187] INTERNATIONAL ATOMIC ENERGY AGENCY. *Database of Prompt Gamma Rays from Slow Neutron Capture for Elemental Analysis*. INTERNATIONAL ATOMIC ENERGY AGENCY, Vienna, 2007.

[188] M. Cribier. Neutrons and high energy gammas in borexino. Technical report, APC, Paris, 2017.

[189] Hamamatsu. *Photomultiplier tubes, Basics and Applications*. Hamamatsu Photonics K.K., third (3a) edition, 2007.

[190] `http://neutronyield.usd.edu/`.

[191] `https://github.com/shawest/neucbot`.

[192] S. Westerdale and P. D. Meyers. Radiogenic Neutron Yield Calculations for Low-Background Experiments. *Nucl. Instrum. Meth. A*, 2017.

[193] D.-M. Mei, C. Zhang, and A. Hime. Evaluation of (α,n) induced neutrons as a background for dark matter experiments. *Nuclear Instruments and Methods in Physics Research Section A: Accelerators, Spectrometers, Detectors and Associated Equipment*, 606(3):651 – 660, 2009.

[194] L. Cadonati. Note on background due to ^{222}Rn emanation from the inner vessel nylon film in borexino. Technical report, Princeton University, 2001. Internal Notes of the Borexino Collaboration.

[195] S. Abe et al. Production of radioactive isotopes through cosmic muon spallation in KamLAND. *Phys. Rev. C*, 81:025807, Feb 2010.

[196] M. Agostini, K. Altenmuller, S. Appel, V. Atroshchenko, Z. Bagdasarian, et al. Improved measurement of ^{8}B solar neutrinos with 1.5 kt.y of Borexino exposure. *arXiv*, Sept 2017. https://arxiv.org/pdf/1709.00756.pdf.

[197] C. Colle and C. Mourlon. Fiche radionucléide: Cérium 144 et son environnement. Technical report, Institut de Radioprotection et de Sûreté Nucléaire (IRSN), 2003.

[198] V. I. Kopeikin, L. A. Mikaelyan, and V. V. Sinev. Reactor as a source of antineutrinos: Thermal fission energy. *Physics of Atomic Nuclei*, 67(10):1892–1899, 2004.

[199] Wikimedia foundation. Wikipedia. http://en.wikipedia.org.

[200] H. Von Halban, F. Joliot, and L. Kowarski. Liberation of neutrons in the nuclear explosion of uranium and number of neutrons liberated in the nuclear fission of uranium. *Nature*, 143:470 & 680, Mar 18, 1939.

[201] J. Gaffiot. *Étude des neutrinos de réacteur : mise en place et caractérisation du détecteur Nucifer*. Ph.D. thesis, Université Paris-Sud, 2012.

[202] S.F. Mughabghab. Thermal neutron capture cross sections resonance integrals and g-factors. Technical report, IAEA-INDC(NDS), 2003. http://www.iaea.org/inis/collection/NCLCollectionStore/{_}Public/34/020/34020739.pdf.

[203] Thomas Mueller. *Expérience Double Chooz: simulation des spectres antineutrinos issus de réacteurs*. Ph.D. thesis, Université Paris-Sud XI, Orsay, 2010. P. 57.

[204] IAEA Power Reactor Information System. Nuclear power reactors in the world. Vienna, 2016. http://www-pub.iaea.org/MTCD/Publications/PDF/RDS_2-36_web.pdf.

[205] United States Nuclear Regulatory Commission. Uranium enrichment. *Backgrounder - Office of Public Affairs*, 2017. https://www.nrc.gov/docs/ML0313/ML031330159.pdf.

[206] J Laurec, A Adam, T De Bruyne, E Bauge, T Granier, et al. Fission Product Yields of 233U, 235U, 238U and 239Pu in Fields of Thermal Neutrons, Fission Neutrons and 14.7-MeV Neutrons. *Nuclear Data Sheets*, 111(12):2965–2980, 2010.

[207] M B Chadwick, M Herman, P Obložinský, M E Dunn, Y Danon, et al. ENDF/B-VII.1 Nuclear Data for Science and Technology: Cross Sections, Covariances, Fission Product Yields and Decay Data. *Nuclear Data Sheets*, 112(12):2887–2996, 2011.

[208] IAEA - Division of Nuclear Fuel Cycle and Waste Technology. The nuclear fuel cycle, 2011. `https://www.iaea.org/sites/default/files/nfc0811.pdf`.

[209] A.S. Gerasimov, V.N. Kornoukhov, I.S. Sal'dikov, and G.V. Tokhomirov. Production of high specific activity ^{144}Ce for artificial sources of antineutrinos. *Atomic Energy*, 116(1), 2014.

[210] Internal Report n°1. The feasibility of producing a 75 kCi ^{144}Ce antineutrino source as well a preliminary study of the source transportation. Technical report, PA MAYAK, December 2013.

[211] Internal Report n°2. Methods and Equipment to be used to assess ^{144}Ce activity and impurities in the CeANG sources. Technical report, PA MAYAK, March 2014.

[212] Internal Report n°3. Second batch of "fresh" Spent Fuel and feasibility of the CeANG production with activity > 100 kCi, Final design of CeANG Capsule, and Transportation scheme of CeANG from PA Mayak to St Petersburg. Technical report, PA MAYAK, September 2014.

[213] Vasily Kornoukhov. Private communication.

[214] Internal Report n°6. Ceang features and sfrm capsule. Technical report, PA MAYAK, November 2015.

[215] E. R. Irish. Description of purex plant process. Technical report, United States atomic Energy Commission, 1959. `https://digital.library.unt.edu/ark:/67531/metadc100576/m2/1/high_res_d/metadc100576.pdf`.

[216] World Nuclear Association. Processing of used nuclear fuel. 2016.

[217] C. K. Gupta and N. Krishnamurthy. *Extractive Metallurgy of Rare Earths*. CRC Press LLC, 2005.

[218] Internal Report n°0. Description of the method for production of 100 kBq ^{144}Ce samples at PA MAYAK and method to transporting to CEA. Technical report, PA MAYAK, March 2013.

[219] Huba Kalász. Displacement chromatography. *Journal of Chromatographic Science*, 41, July 2003.

[220] V.M. Gelis, G.B. Maslova, and E.A. Chuveleva. Isolation of gram amounts of ^{147}Pm. ii. preparation of high-quality promethium by displacement complexing chromatography. *Radiochemistry*, 40(1):59–63, 1998.

[221] E. A. Kozlitin, G. B. Maslova, and N. I. Polyakova. Recovery and Purification of ^{89}Sr, ^{140}Ba,^{91}Y,^{141}Ce and ^{144}Ce. I. Conditions of Separation of Radionuclides by Elution Chromatography. *Radiochemistry*, 38(5):413–416, 1996. Translated from Radiokhimiya.

[222] V.M. Gelis and G.B Maslova. Isolation of gram amounts of ^{147}Pm. i. calculation of optimal chromatographic separation parameters. *Radiochemistry*, 40(1):55–58, 1998.

[223] A. P. Sandréa. Etude et détermination microspectrographique d'absorption des minéraux de terres rares. *Bulletin de la Société Française de Minéralogie et Cristallographie*, 76:294–299, 1953.

[224] J. W. Adams. The visible region absorption spectra of rare-earth minerals. *The American Mineralogist*, 50:356–366, 1965. `http://rruff.info/doclib/am/vol50/AM50_356.pdf`.

[225] Internal Report n°5. Update on the CeANG production process: assessment of ^{144}Ce activity and impurity content. Technical report, PA MAYAK, Juin 2015.

[226] Internal Report n°7. Details about Analytical controls of the whole process of CeANG fabrication. Summary of the CeANG expected features: mass (activity) of ^{144}Ce, density, temperature, pressure, expected impurities, ISO classifications. A short summary of the production process. Technical report, PA MAYAK, December 2016.

[227] T. P. Donohoue, C. P. Oertel, W. H. Tyree, and J. L. Valdez. Radionuclide calorimeter system. United States Patent 5067820, 1991.

[228] IAEA Safety Standards. *Regulations for the Safe Transport of Radioactive Material*, ssr-6 edition, 2012. `http://www-pub.iaea.org/MTCD/publications/PDF/Pub1570_web.pdf`.

[229] International Standard Organization. *ISO 9978: Radioprotection — Sources radioactives scellées — Méthodes d'essai d'étanchéité*, 1992. `https://www.iso.org/obp/ui/#iso:std:iso:9978:ed-1:v1:en`.

[230] International Standard Organization. *ISO2919: Radiation protection - Sealed radioactive sources - General requirements and classification*, second edition, 1999. `https://www.nrc.gov/docs/ML0036/ML003686268.pdf`.

[231] IAEA Safety Standards. *Radiation Protection Programmes for the Transport of Radioactive Material*, 2007. `http://www-pub.iaea.org/MTCD/publications/PDF/pub1269_web.pdf`.

[232] R. Musenich and S. Farinon. 2d steady state and transient analysis of cesox source. Report, INFN, 2017.

[233] ICRP. 1990 recommendations of the international commission on radiological protection. *Annals of the ICRP*, 1991.

[234] International topical meeting on research reactor fuel management, organized by the European Nuclear Society. *Spent Fuel transportation with the TN-MTR packaging*, 2000. `http://www.iaea.org/inis/collection/NCLCollectionStore/_Public/32/027/32027411.pdf`.

[235] The 1998 International Reduced Enrichment for Test Reactor Conference. *MTR Transport expericences of transnucleaire in South America and status of the new TN-MTR Packaging*, 1998. `http://www.rertr.anl.gov/Fuels98/SpentFuel/OKonirsch.pdf`.

[236] Code de la santé publique. Article R1333-52. Décret n°2015-231 du 27 février 2015 relatif à la gestion des sources radioactives scellées usagées, 2015. `https://www.legifrance.gouv.fr/affichCodeArticle.do?cidTexte=LEGITEXT000006072665&idArticle=LEGIARTI000006910123&dateTexte=&categorieLien=cid`.

[237] Code de l'environnement. Décret n°2013-1304 du 27 décembre 2013 pris pour application de l'article l. 542-1-2. `https://www.legifrance.gouv.fr/affichTexte.do?cidTexte=JORFTEXT000028409031&categorieLien=cid`.

[238] ORTEC company. Review of the physics of semiconductor detectors. `https://www.ortec-online.com/-/media/ametekortec/catalog%20files/detectors.pdf?la=en`.

[239] M.A. Hofman. *Liquid Scintillators and Liquefied Rare Gases for Particle Detectors, Background-Determination in Double Chooz and Scintillation Properties of Liquid Argon*. Ph.D. thesis, Technische Universitat Munchen, 2012.

[240] Ngo Quang Huy. The influence of dead layer thickness increase on efficiency decrease for a coaxial {HPGe} p-type detector. *Nuclear Instruments and Methods in Physics Research Section A: Accelerators, Spectrometers, Detectors and Associated Equipment*, 621(1–3):390 – 394, 2010.

[241] G. Boireau, L. Bouvet, A. P. Collin, G. Coulloux, M. Cribier, et al. Online monitoring of the osiris reactor with the nucifer neutrino detector. *Phys. Rev. D*, 93:112006, 2016.

[242] LNE LNHB/CEA. Table de Raduionucléides - $-^{241}_{95}$Am$_{146}$. `http://www.nucleide.org/DDEP_WG/Nuclides/Am-241_tables.pdf`.

[243] S. Ramavataram and C.L. Dunford. Nuclear Science References Coding Manual. *Report BNL-NCS-51800, Rev. 08/96*, Rev. 08/96, 1996.

[244] G. Soti, F. Wauters, M. Breitenfeldt, P. Finlay, I. S. Kraev, et al. Performance of Geant4 in simulating semiconductor particle detector response in the energy range below 1 MeV. *Nuclear Instruments and Methods in Physics Research Section A: Accelerators, Spectrometers, Detectors and Associated Equipment*, A728:11–22, 2013.

[245] M.F. dos Santos et al. Energy linearity of high-purity germanium detectors in the region of the ge k-absorption edge: experimental results. *Applied Radiation and Isotopes*, 53:739 – 743, 2000.

[246] L. Calligaris, A. Massironi, and L. Presotto. Gamma spectroscopy - academic year 2006/2007, 2007. `http://virgilio.mib.infn.it/labdida/lib/exe/fetch.php?id=laboratorio_di_fisica_delle_particelle&media=relazionelaboratoriogamma.pdf`.

[247] C. Kittel. *Introduction to Solid State Physics*. John Wiley and Sons, 6th edition, 1986.

[248] R. C. Alig, S. Bloom, and C. W. Struck. Scattering by ionization and phonon emission in semiconductors. *Phys. Rev. B*, 22:5565–5582, Dec 1980.

[249] E. Chham and F. et al. Pinero Garcia. Monte carlo analysis of the influence of germanium dead-layer thickness on the hpge gamma detector experimental efficiency measured by use of extended sources. *Applied Radiation and Isotopes*, 95:30 –35, 2015.

[250] I.K. Mackenzie, H. Bird, and J. Boulter. A source of well-defined annihilation gamma-rays. *Nuclear Instruments and Methods*, 47:176–178, 1967.

[251] E. do Nascimento et al. Doppler broadening of positron annihilation radiation: fitting the coincidence spectrum. *Nuclear Instruments and Methods in Physics Research Section A: Accelerators, Spectrometers, Detectors and Associated Equipment*, 538:723–730, 2005.

[252] L. Torrisi et al. Doppler-broadening of positron annihilation in a biological environment. *Q J Nucl Med.*, 41(1):18–24, 1997.

[253] R.S. Brusa et al. Doppler-broadening measurements of positron annihilation with high-momentum electrons in pure elements. *Nuclear Instruments and Methods in Physics Research B*, 194:519–531, 2002.

[254] E. Kamiyamaa et al. Doppler broadening spectroscopy of positron annihilation near ge and si (001) single crystal surfaces. *ECS Solid State Lett.*, 2:89–90, 2013.

[255] L. A. Currie. Limits for qualitative detection and quantitative determination. *Application to radiochemistry*, 40 (3):586–593, 1968.

[256] M-Y De Jesus. Experimental technics for dark matter research. *Ecole de Gif 2016*, 2016.

[257] L.P. Geraldo and D.L. Smith. Covariance analysis and fitting of germanium gamma-ray detector efficiency calibration data. *Nuclear Instruments and Methods in Physics Research Section A*, 290:499–508, 1990.

[258] Z. Kis, B. Fazekas, J. Östör, Zs. Révay, T. Belgya, et al. Comparison of efficiency functions for ge gamma-ray detectors in a wide energy range. *Nuclear Instruments and Methods in Physics Research Section A: Accelerators, Spectrometers, Detectors and Associated Equipment*, 418(2–3):374 – 386, 1998.

[259] C. Coceva, A. Brusegan, and C. van der Vorst. Gamma intensity standard from thermal neutron capture in 35cl. *Nuclear Instruments and Methods in Physics Research Section A: Accelerators, Spectrometers, Detectors and Associated Equipment*, 378(3):511 – 514, 1996.

[260] Agilent Technologies, Inc. *Agilent 7500 Inductively Coupled Plasma Mass Spectrometry: Course Number H8974A ChemStation Revision 01.XX NT*, 2001. `homepage.ntu.edu.tw/~yhhwang/file/0905_4.pdf` .

[261] Merck enterprise. `http://www.merckmillipore.com/FR/fr/water-purification/learning-centers/applications/inorganic-analysis/icp-ms/_e2b.qB.s7QAAAFAniQQWTtN,nav?ReferrerURL=https%3A%2F%2Fwww.google.fr%2F`.

[262] M. Vivier, on behalf of the Saclay/APC group. Beta spectrometry sensitivity to the shape of the ^{144}Ce-^{144}Pr spectrum. Borexino Collaboration meeting, June 2016.

[263] Private communications with P. Cassette (LNHB) and V. Lourenço (LNHB), September 2014.

[264] M. Agostini, K. Altenmuller, S. Appel, V. Atroshchenko, Z. Bagdasarian, et al. First Simultaneous Precision Spectroscopy of pp, ^{7}Be, and pep Solar Neutrinos with Borexino Phase-II. *arXiv*, July 2017. `https://arxiv.org/abs/1707.09279`.

[265] Geant4 Collaboration. *Geant4 User's Guide for Application Developers*, version geant4.10.3 edition, 2016. P.97, `http://geant4.web.cern.ch/geant4/UserDocumentation/UsersGuides/ForApplicationDeveloper/fo/BookForAppliDev.pdf`.

Appendix A
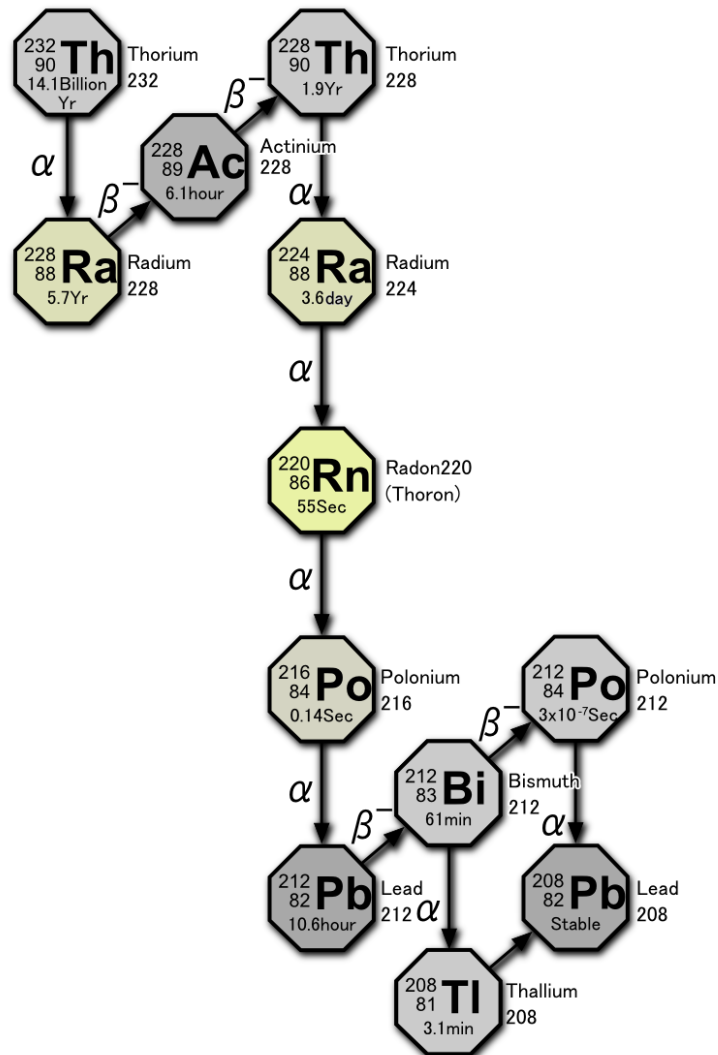
Natural radioactivity decay chains
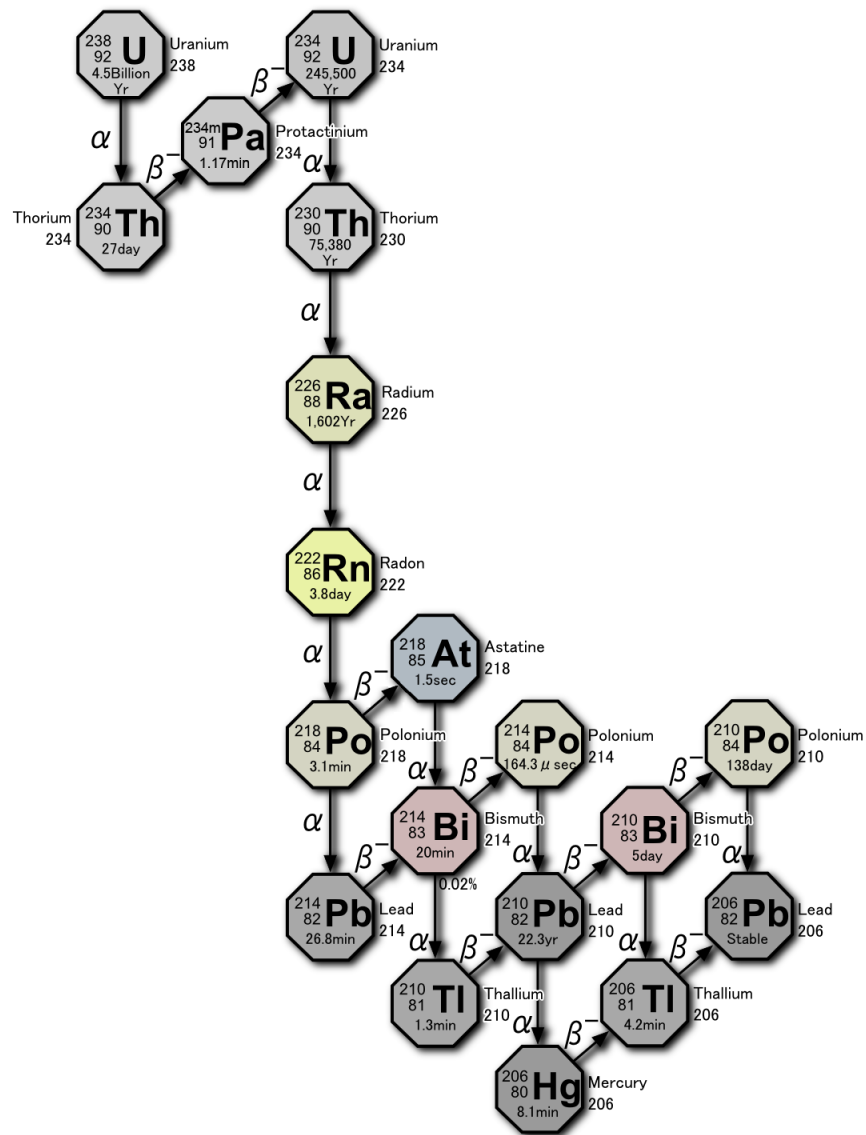

Figure A.1: ^{232}*Th decay chain [199].*

Figure A.2: ^{238}U decay chain [199].

Appendix B

^{8}B ν_e measurement

B.1 Run lists

Excluded dsts	Reasons
2009_Jan_25	excluded from the pp analysis
2009_Feb_01	excluded from the pp analysis
2009_Jun_21	excluded from the pp analysis
2009_Jun_28	excluded from the pp analysis
2009_Jul_05	excluded from the pp analysis
2009_Jul_12	excluded from the pp analysis
2009_Jul_19	excluded from the pp analysis
2010_Jan_31	excluded from the pp analysis
2010_Feb_07	excluded from the pp analysis
2014_Aug_31	"retriggering problem"
2014_Sep_07	"retriggering problem"
2016_Apr_17	

Table B.1: *List of dsts excluded from the analysis. Two of them have been excluded at the beginning of September 2014 because of problems on the trigger crate ("retriggering problem").*

Excluded runs	Reasons	Corresponding dsts
#10853	unphysical excess	%2009_Aug_09
#13412 → #13461	WE periods	%2010_Jun_13
#13728 → #13963	WE periods	2010_Jul_11,2010_Jul_18, 2010_Jul_25
#14084 → #14191	WE periods	%2010_Aug_29, 2010_Sep_05,%2010_Sep_12
#14210 → #14402	WE periods	%2010_Sep_19,2010_Sep_26
#15029 → #15084	WE periods	%2011_Jan_13
#15091 → #15328	WE periods	%2011_Jan_30,2011_Feb_06,2011_Feb_13
#15791 → #16102	WE periods	% 2011_May_08,2011_May_15,2011_May_22 2011_May_29,2011_Jun_05
#16296 → #16517	WE periods	%2011_Jul_17,2011_Jul_24 2011_Jul_31,2011_Aug_07
#21223	muon trace not tagged	%2013_Oct_20

Table B.2: *List of runs excluded from the analysis. Most of them belong to the water extraction periods.% meaning that only a part of the dst has been removed.*

B.2   Analytical distribution

A radial distribution of events inside the vessel can be described with the convolution of the detector resolution and a volumic distribution [148, 153]. Assuming the resolution (σ) is constant in the whole volume, f(x,y,z) being the probability density function associated with this resolution, V the whole volume and N the total number of event, R(X) is the distribution of internal events:

$$R(X) = \frac{N}{V} \int_V f(X,Y)dY \tag{B.1}$$

$$\text{with } f(X,Y) = \frac{e^{-\frac{(X-Y)^2}{2\sigma^2}}}{(2\pi\sigma^2)^{3/2}} \tag{B.2}$$

Leading to:

$$R(X) = \frac{N}{V(2\pi\sigma^2)^{3/2}} \int_V e^{-\frac{\|X\|^2 + \|Y\|^2 - 2\|X\|\|Y\|cos(X.Y)}{2\sigma^2}} dY$$

Transforming in spherical coordinate:

$$R(r) = \frac{N}{V(2\pi\sigma^2)^{3/2}} \int_0^{2\pi} \int_0^R \int_0^\pi e^{-\frac{r^2 + \tilde{r}^2 - 2r\tilde{r}cos(\theta)}{2\sigma^2}} \tilde{r}^2 sin(\theta) d\theta d\tilde{r} d\phi$$

$$R(r) = \frac{N2\pi}{V(2\pi\sigma^2)^{3/2}} \int_0^R \tilde{r}^2 e^{-\frac{r^2 + \tilde{r}^2}{2\sigma^2}} \int_0^\pi e^{\frac{r\tilde{r}cos(\theta)}{\sigma^2}} sin(\theta) d\theta d\tilde{r}$$

Defining $\alpha = cos(\theta)$, we have $d\alpha = sin(\theta)d\theta$ hence:

$$\int_0^\pi e^{\frac{r\tilde{r}cos(\theta)}{\sigma^2}} sin(\theta)d\theta = \int_1^{-1} e^{\frac{r\tilde{r}\alpha}{\sigma^2}} d\alpha = \left[\frac{\sigma^2}{r\tilde{r}} e^{\frac{r\tilde{r}\alpha}{\sigma^2}}\right]_1^{-1}$$

Hence:

$$R(r) = \frac{N2\pi\sigma^2}{V(2\pi\sigma^2)^{3/2}r} \int_0^R \tilde{r}e^{-\frac{r^2+\tilde{r}^2}{2\sigma^2}} \left(e^{\frac{r\tilde{r}}{\sigma^2}} - e^{\frac{-r\tilde{r}}{\sigma^2}}\right) d\tilde{r}$$

$$R(r) = \frac{3N}{4\pi R^3 r\sqrt{2\pi}\sigma} \int_0^R \tilde{r} \left(e^{-\frac{(r-\tilde{r})^2}{2\sigma^2}} - e^{-\frac{(r+\tilde{r})^2}{2\sigma^2}} \right) d\tilde{r}$$

The integrated function being even, and $\tilde{r} = (-r) \Rightarrow \tilde{r}d\tilde{r} = (-r)d(-r) = rdr$ one can write:

$$\int_0^R \tilde{r} \left(e^{-\frac{(r-\tilde{r})^2}{2\sigma^2}} - e^{-\frac{(r+\tilde{r})^2}{2\sigma^2}} \right) d\tilde{r} = \int_0^R \tilde{r}e^{-\frac{(r-\tilde{r})^2}{2\sigma^2}} d\tilde{r} + \int_R^0 \tilde{r}e^{-\frac{(r+\tilde{r})^2}{2\sigma^2}} d\tilde{r} = \int_{-R}^R \tilde{r}e^{-\frac{(r-\tilde{r})^2}{2\sigma^2}} d\tilde{r}$$

Finally leading to:

$$R(r) = \frac{3N}{4\pi R^3 r\sqrt{2\pi}\sigma} \int_{-R}^R \tilde{r}e^{-\frac{(r-\tilde{r})^2}{2\sigma^2}} d\tilde{r} \tag{B.3}$$

which will be called a "bulk" distribution. The number of visible reconstructed events is then [148]:

$$V(r|R,\sigma,N_1) = R(r) \int_\Omega d\Omega = 4\pi r^2 \times R(r) \tag{B.4}$$

Combining equations B.3 and B.4:

$$V(r|R,\sigma,N_1) = N_1 \frac{r}{R^3\sigma} \int_{-R}^R r.e^{-\frac{(r-r')^2}{2\sigma^2}} dr \tag{B.5}$$

with N_1, σ and R, fitted parameters of the radial distribution.

B.3   Surface position generator

The vessel is defined in the Borexino Monte Carlo, using a G4GenericPolycone [265]. In this geometry, the shape is generated with an axis of rotation. A set of 2D coordinates, (z,R), is first given, drawing a 2D profile. This profile is then propagated in 3D by a simple rotation over the axis.

From the simulation we extracted N coordinates, (R_i, z_i). The R_i and z_i distribution are plotted in figure B.1a. In order to have an uniform distribution in 3D, we want to simulate uniform points in 2D before applying the rotation following ϕ. To do so, we consider the incrementation of the R(z) function: $L_i = \sqrt{(Z_i - Z_{i-1})^2 + (R_i - R_{i-1})^2)}$. The cumulative is then only $f_j = \frac{\sum_i^j L_i}{\sum_i^N L_i}$ built by adding at each step the surface added to the polycone. Then the cumulative function is transformed in the θ space where the function is monotonous. By generating random theta following this cumulative, we ensure that the position generated are uniformly distributed in the surface. Then the conversion between theta and (R,z) is automatic using figure B.1b. In *g4bx*, the 125μm-width nylon vessel is enclosed in two G4GenericPolycone representing the inner and the outer vessel surfaces so we add a spread considering this width.
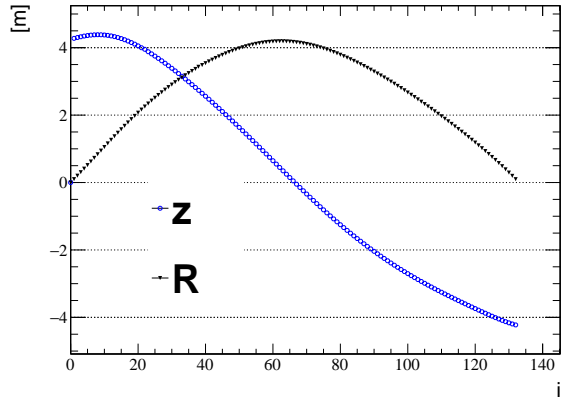
(a) *The R(z) fonction describing one vessel shape in blue and the cumulative in black.*
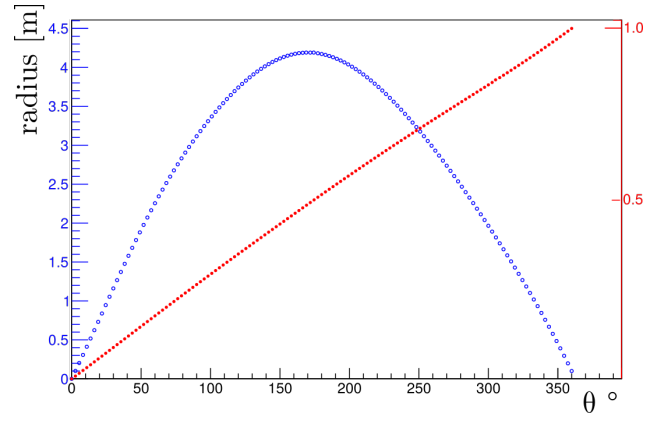
(b) *The R(z) fonction describing one vessel shape in blue and the cumulative in black.*

Appendix C

CeANG production

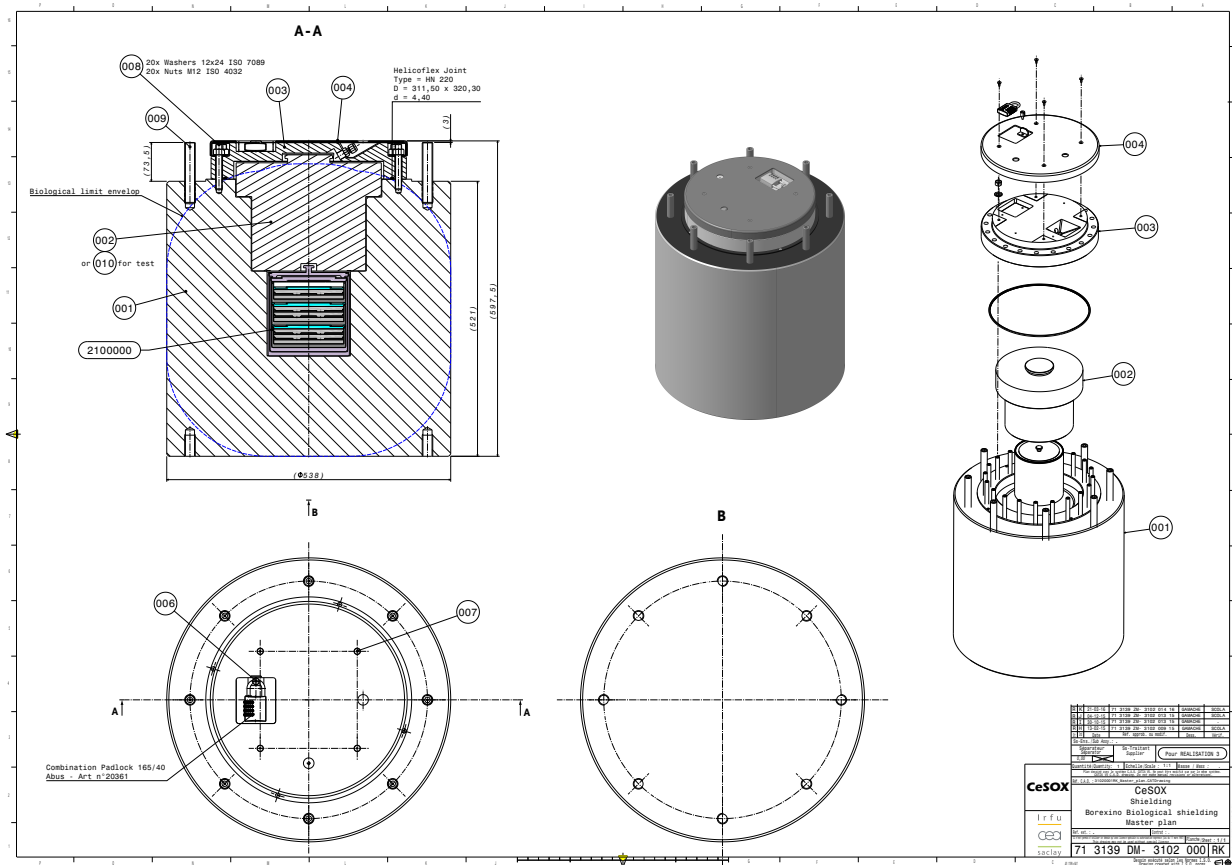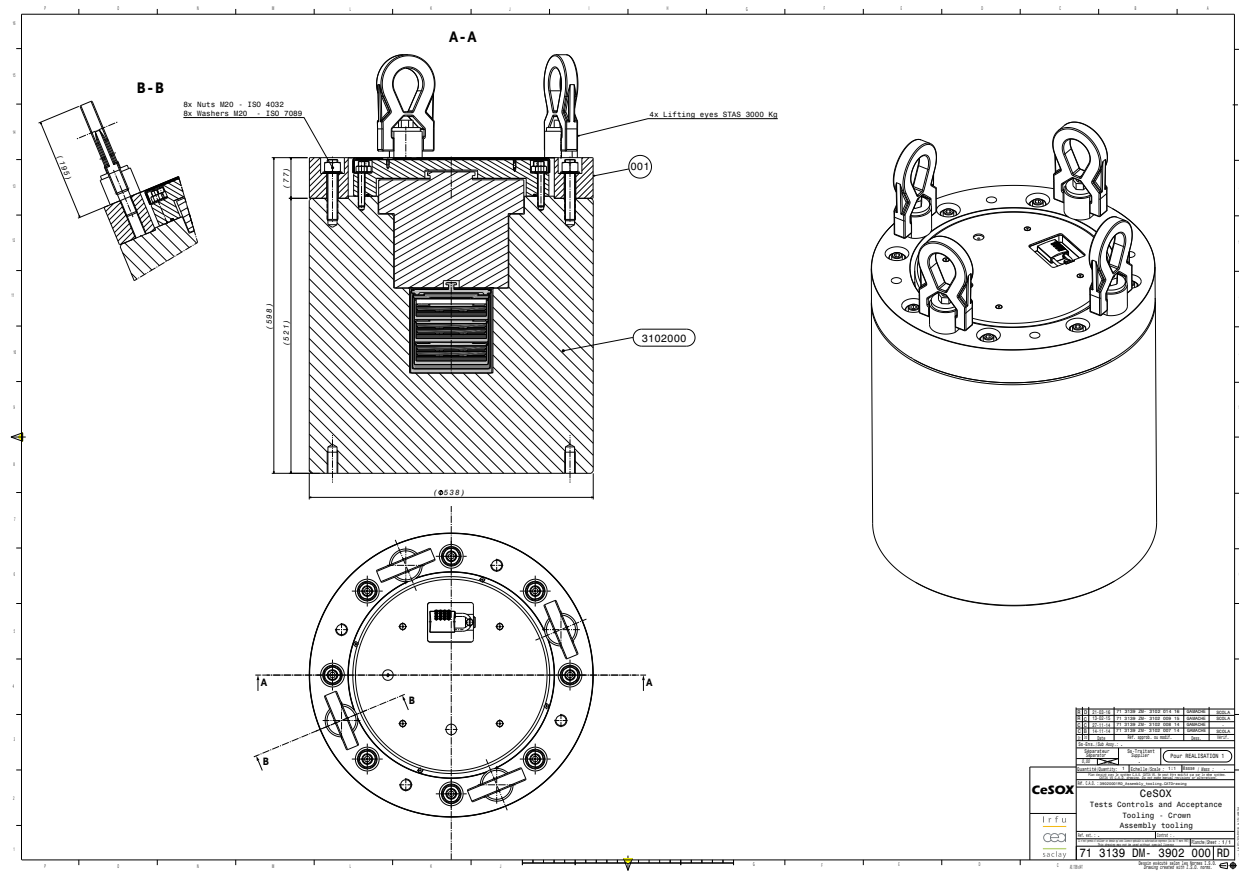## High Density Tungsten Shield

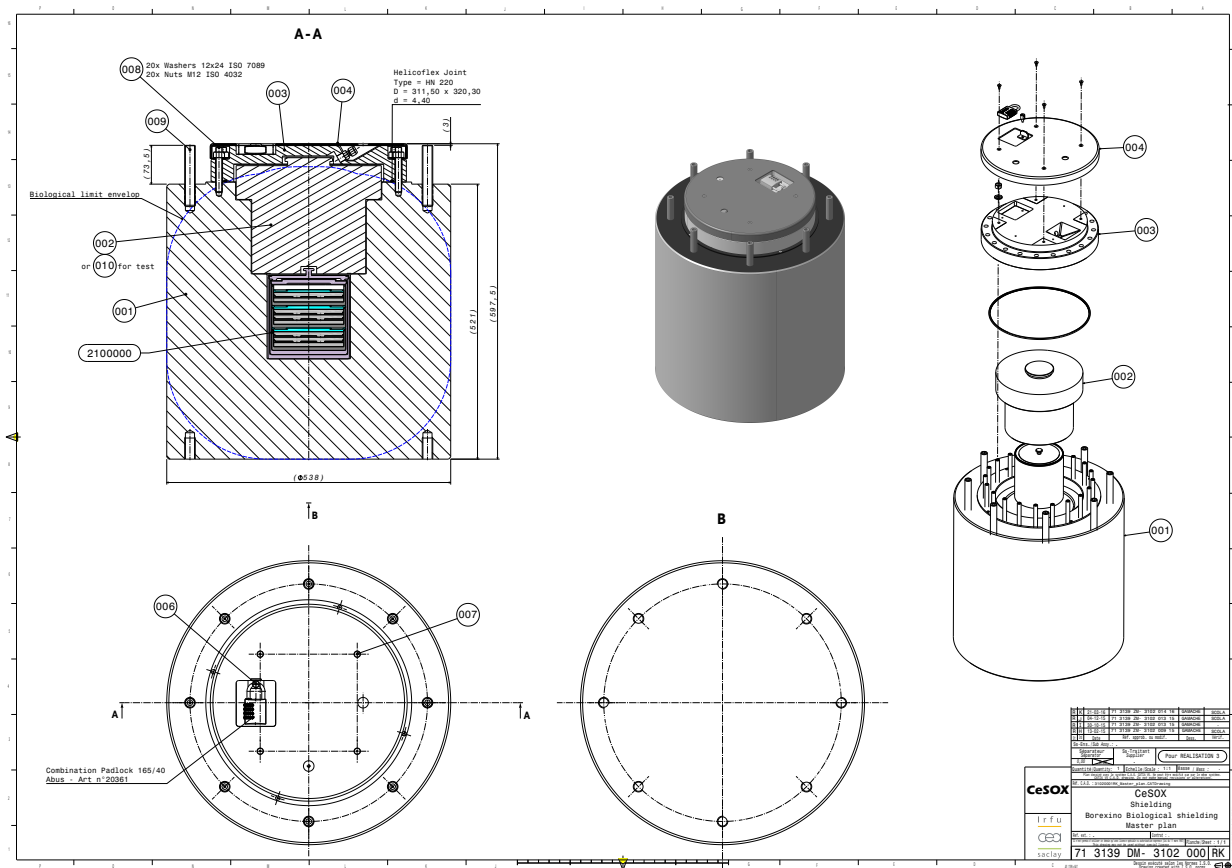
Figure C.1: *Industrial map*

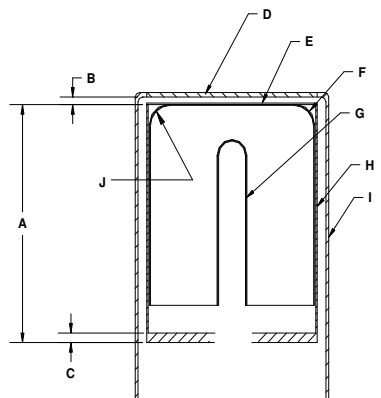Figure C.2: *Geometry of the HDTAS.*

Figure C.3: *Industrial map*

Appendix D

HPGe Calibration

GERMANIUM DETECTOR DIAGRAM

SERIAL NUMBER 37-P21207B

COMPANY PRIVATE

BASIC DETECTOR DIMENSIONS	
DETECTOR DIAMETER	58.8 mm
DETECTOR LENGTH	58 mm
DETECTOR END RADIUS (J)	8 mm, NOMINAL
HOLE DIAMETER	9.4 mm
HOLE DEPTH	45 mm
HOLE BOTTOM RADIUS	HOLE DIAMETER / 2, NOMINAL

MISCELLANEOUS DETECTOR ASSEMBLY DIMENSIONS AND MATERIALS			
IDENTIFIER	DIMENSION	DESCRIPTION	MATERIAL(S)
A	94 mm	MOUNT CUP, LENGTH	ALUMINUM
B	3 mm	END CAP TO CRYSTAL GAP	N.A.
C	3.2 mm	MOUNT CUP BASE	ALUMINUM
D	1.3 mm	END CAP WINDOW	ALUMINUM
E	0.03/0.03 mm/mm	INSULATOR/SHIELD	MYLAR/ALUMINIZED MYLAR
F	700 microns	OUTSIDE CONTACT LAYER	Ge with Li ions
G	0.3 microns	HOLE CONTACT LAYER	Ge with B ions
H	0.76 mm	MOUNT CUP WALL	ALUMINUM
I	1.3 mm	END CAP WALL	ALUMINUM

ORTEC
801 S. ILLINOIS AVE.
OAK RIDGE TN 37831

Figure D.1: *Scheme of the HPGe detector as given by ORTEC.*

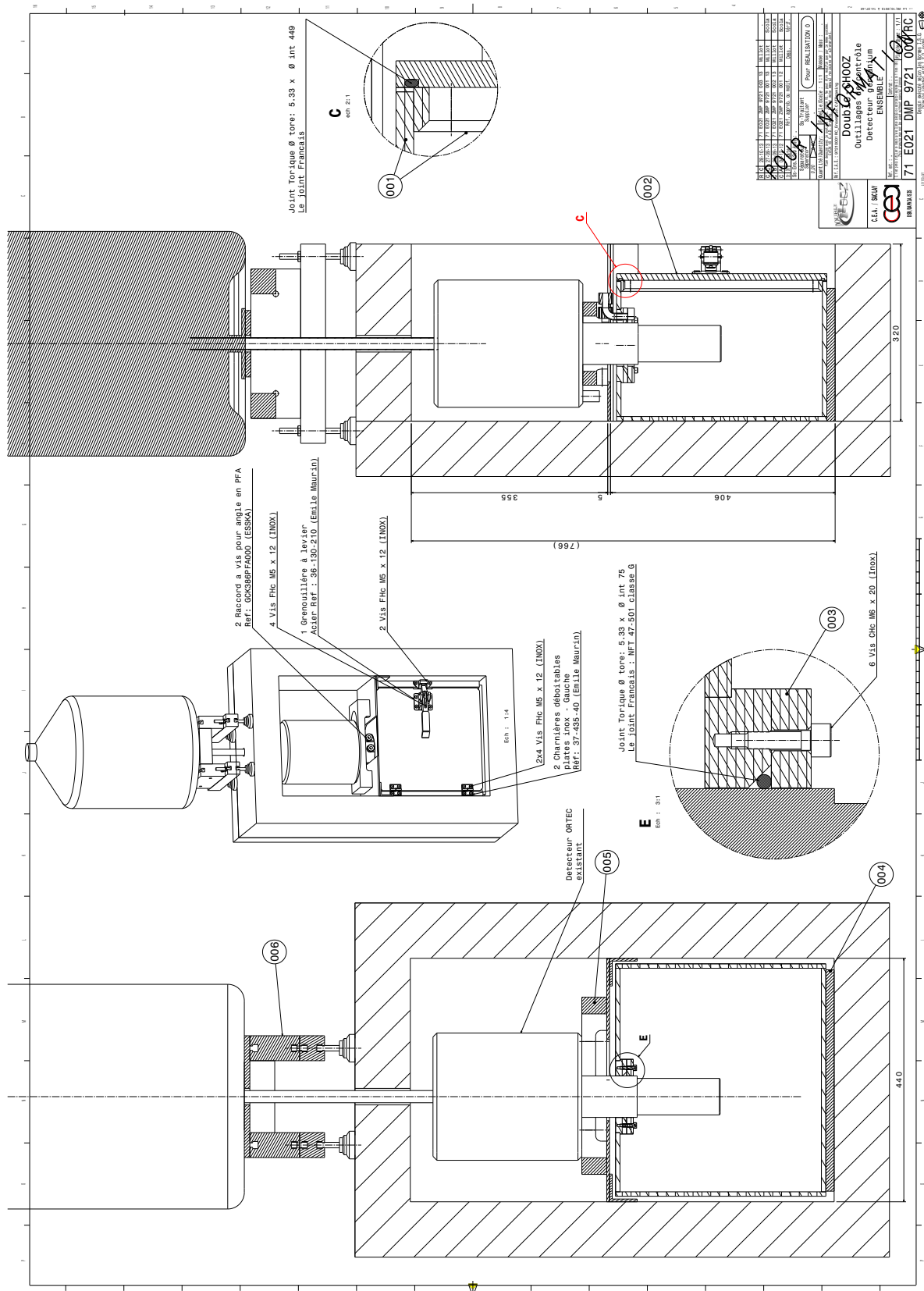Figure D.2: *Scheme of the detector as given by industry and technical services*

Figure D.3: *Map of the environment of the detector.*
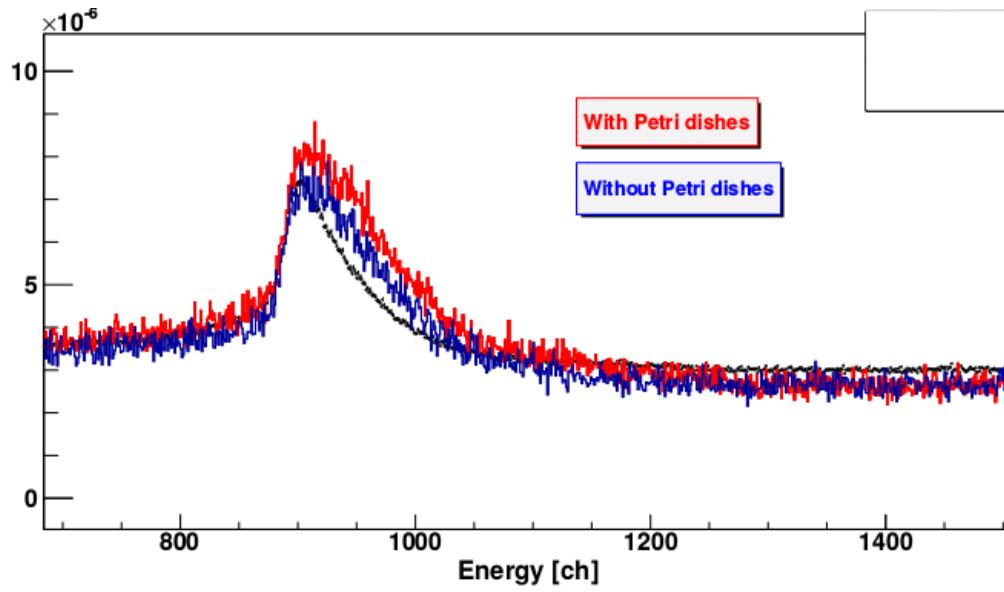
Petri dishes influence on shape

Figure D.4: *Petri dishes influence on the backscattering peak.*

Appendix E

Contamination study

| ^{Z}N | E_γ [keV] | $\mathcal{B}_R$ [%] | Données ^{144}Ce | MC: ^{144}Ce+^{Z}N | |
			MDA [Bq/kg]	$\mathcal{A}_{^ZN}$ [Bq/kg]	$\mathcal{A}_{^ZN}/\mathcal{A}_{^{144}Ce}$
^{250}Bk	989	0.4500	28.53	501.02	1.98019e-05
^{250}Bk	1031	0.3560	36.34	515.91	1.85196e-05
^{249}Cf	388	0.6600	53.36	90.52	6.59041e-05
^{249}Cf	333.8	0.1460	253.36	0.00	6.29702e-05
^{244}Am	743.971	0.6600	20.37	23.80	1.37922e-05
^{244}Am	897.8	0.2800	35.32	36.23	1.3248e-05
^{243}Cm	228.18	0.1060	388.63	552.72	0.000286879
^{243}Cm	277.599	0.1400	267.24	630.91	0.000282703
^{154}Eu	591.8	0.0499	424.02	372.88	0.000376622
^{154}Eu	873.2	0.1227	104.08	126.30	0.000130051
^{154}Eu	1004	0.1801	53.33	105.08	0.000118548
^{154}Eu	1274.44	0.3513	48.97	127.40	0.000116128
^{153}Gd	172.85	0.0004	100498.00	159777.00	0.212318
^{152}Eu	964.079	0.1461	85.77	133.72	4.96266e-05
^{152}Eu	1085.87	0.1021	131.87	134.47	5.31133e-05
^{152}Eu	1112.07	0.1364	100.45	133.39	5.07518e-05
^{150}Eu	333.971	0.9600	38.49	72.91	3.36723e-05
^{150}Eu	439.401	0.8040	43.27	57.34	2.99646e-05
^{146}Pm	453.88	0.6500	53.91	123.75	4.84681e-05
^{144}Pm	618.01	0.9860	20.17	48.50	2.0767e-05
^{143}Pm	741.98	0.3900	24.23	63.28	2.99193e-05

Table E.1: *Results from the MC method generalised to any contaminant [1/2],*

^{Z}N	E_γ [keV]	$\mathcal{B}_R$ [%]	Données ^{144}Ce MDA [Bq/kg]	MC: ^{144}Ce+^{Z}N $\mathcal{A}_{zN}$ [Bq/kg]	$\mathcal{A}_{zN}/\mathcal{A}_{^{144}Ce}$
^{137}Cs	661.657	0.8510	15.62	18.73	3.92251e-05
^{134}Cs	795.864	0.8553	10.91	24.49	8.09636e-06
^{133}Ba	356.017	0.6205	57.91	153.73	6.25339e-05
^{125}Sb	427.874	0.2960	116.88	283.06	7.61688e-05
^{106}Rh	621.93	0.0990	197.61	620.44	0.000253453
^{102}Rh	475.06	0.3611	55.04	288.27	5.03433e-05
^{101}Rh	325.23	0.1183	223.03	1140.10	0.000178118
^{101}Rh	197.99	0.73	47.0375	1140.10	0.00018484
^{68}Ga	1077.35	0.0300	315.41	808.23	0.00031491
^{63}Zn	962.06	0.0650	137.77	393.94	0.000174563
^{60}Co	1332.5	0.9999	15.60	47.88	1.96294e-05
^{60}Co	1173.24	0.9997	15.34	46.03	1.97055e-05
^{54}Mn	834.85	0.9998	9.04	31.98	1.40725e-05
^{53}Fe	377.88	0.4200	59.90	129.93	6.97999e-05
^{44}Ti	146.212	0.0009	26167.70	107972.00	0.156159
^{22}Na	1274.53	0.9994	17.22	45.18	5.09449e-05
^{228}Th	238.6	0.4330	94.71	189.11	0.000139974
^{228}Ra	968.971	0.1580	57.76	88.13	3.00335e-05
^{228}Ra	911.204	0.2580	48.07	126.96	2.71992e-05
^{209}Po	896.3	0.0047	2594.12	4577.24	0.00113018
^{207}Bi	569.702	0.9774	23.68	44.63	1.88447e-05
^{195}Au	211.41	0.0001	274153.00	507284.00	0.638391
^{194}Ir	328.46	0.1310	281.09	839.96	5.24192e-05
^{194}Au	328.46	0.6130	60.07	155.04	5.24192e-05
^{192m}Ir	155.16	0.0097	3327.17	23369.20	0.00915292
^{178m}Hf	574.215	0.8830	18.17	39.88	1.56205e-05
^{172}Hf	1093.63	0.6300	21.44	52.60	1.94908e-05
^{174}Lu	1241.85	0.0514	229.62	446.28	0.000177623
^{173}Lu	272.105	0.2120	130.87	313.92	0.000210662
^{158}Tb	944.189	0.4390	28.36	56.75	2.08525e-05
^{158}Tb	962.126	0.2030	44.11	55.20	2.08506e-05
^{155}Eu	146.07	0.0005	64723.80	183820.00	0.433011
^{235}U	185.715	0.5700	47.71	75.16	2.94361e-05
^{230}Th	253.73	0.00011	365131.00	553789.00	0.303642
^{230}Th	143.87	0.00049	67032.90	235186.00	0.178019
^{230}Th	186.05	0.00009	259769	235186.00	x

Table E.2: *Results from the MC method generalised to any contaminant [2/2].*

Résumé: Le détecteur Borexino, situé au laboratoire souterrain du Gran Sasso (LNGS), mesure les neutrinos solaires depuis 10 ans. Parmi les neutrinos solaires, le spectre continu du ^{8}B jusqu'à 17 MeV permet de tester la zone de transition de l'effet de résonance dans la matière dit effet MSW. Cette nouvelle analyse augmente d'un ordre de grandeur la statistique par rapport à la précédente mesure de Borexino publiée en 2011. Pour ce faire, l'ensemble du volume scintillant a été inclus dans l'analyse, aucune coupure géométrique n'ayant été effectué au dessus de 5 MeV. Cela a permis l'identification d'un nouveau bruit de fond non pris en compte précédemment. L'ensemble des bruits de fond au dessus de 3 MeV est maintenant compris et la composante neutrino peut-être extraite d'un fit radial du détecteur.

Afin de tester l'existence d'un neutrino stérile léger, une source de 3-5,5 PBq de ^{144}Ce sera installée sous Borexino au début de l'année 2018 pour un an et demi de prise de données : c'est l'expérience CeSOX. Cette source est produite par PA MAYAK par purification de combustible nucléaire usagé, par conséquent les potentiels contaminants radioactifs sont très nombreux et peu contraints. Pour tester l'hypothèse stérile, une mesure en flux, une mesure en forme et une mesure combinée seront effectuées dans l'ensemble du détecteur Borexino. Ces mesures sont fortement dépendantes de la connaissance intime de la source (composition, forme du spectre beta du ^{144}Ce, énergie moyenne ^{144}Ce et ^{144}Pr). A cette fin, un spectromètre gamma a été spécifiquement étalonné et entièrement simulé au CEA, Saclay. De même un spectromètre beta a été dessiné, assemblé, simulé et est en cours d'étalonnage. Finalement, des mesures de spectrométrie alpha et de masse seront réalisés sur des échantillons représentatifs envoyés au CEA, Saclay afin de contraindre au mieux la composition de la source de ^{144}Ce de SOX.

Abstract: Located in the Gran Sasso underground laboratory (LNGS), Borexino measures solar neutrinos for 10 years. Among solar neutrinos, ^{8}B continuous spectrum (up to 17 MeV) enables to test the transition zone between vacuum and matter regime of the MSW effect. This new measurement increases by one order of magnitude the exposure with respect to previous Borexino publication. To do so, the entire active volume is considered in this analysis above 5 MeV. A new background has been identified and a radial fit is done above 3 and 5 MeV enabling to extract the neutrino component.

Existence of a light sterile neutrino would have important consequences on astrophysics and cosmology. SOX is the only experiment aiming at testing this hypothesis using a punctual radioactive source. A 3-5.5 PBq ^{144}Ce source is actually under production and will be positioned under Borexino in 2018. Precise knowledge of the source is one of the main challenge of this experiment, based on rate and shape neutrino measurement. Two critical parameters are the heat released by the source for activity measurement and the expected neutrino spectrum in the detector. We first describe the SOX experiment insisting on ^{144}Ce source production. Then, we focus on Saclay installations dedicated to constrain radioactive contamination inside the source using representative samples. Alpha, gamma and mass spectroscopy calibration and simulation are discussed and competitive constrains are derived. A status on ^{144}Ce beta shape measurements is done as well as presentation of future measurement.